An Experimental Investigation of Reacting and Nonreacting Coaxial Jet Mixing in a Laboratory Rocket Engine

by

Stephen Alexander Schumaker

A dissertation submitted in partial fulfillment
of the requirements for the degree of
Doctor of Philosophy
(Aerospace Engineering)
in The University of Michigan
2009

Doctoral Committee:

Professor James F. Driscoll, Chair
Professor Werner J. A. Dahm
Professor David R. Dowling
Professor Wei Shyy
Assistant Professor Matthias Ihme

© Stephen Alexander Schumaker
All Rights Reserved 2009

Dedicated to my incredible wife Hyce, who's love, support and encouragement made this work possible.

ACKNOWLEDGEMENTS

It is hard for a Buckeye to admit, but my time at Michigan has given me some of the best experiences of my life. These wonderful experiences are due almost entirely to the exceptional people with whom I have had the pleasure to work. First and foremost is Prof. Driscoll, who was everything one could ask for in an advisor and more. His approach of not pushing anyone into a project and giving one a chance to explore the nuances of an experimental issue even if they were "slightly" off topic were invaluable learning experiences and greatly helped me grow as a researcher. Without Prof. Driscoll's technical expertise, knowledge, and guidance who knows where this work would be today. Discussions with him over good food and wine might not have always increased productivity but were always educational. Hopefully, someday he will recover from the mistake of taking me and Danny to an all you can eat Brazilian steak house and forgive me for lying about meeting my parents for dinner to get him to his surprise birthday party. A manager I interviewed with might have said it best when he called Prof. Driscoll "the nicest guy in all of the Combustion Institute." It truly has been a privilege working with Prof. Driscoll.

While at Michigan I also had the honor of working with Prof. Dahm. Discussions with Prof. Dahm helped shape a number of the theoretical concepts in this work. The incredible work he has done over the years on mixing in turbulent shear flows and accounting for heat release in such flows is the foundation on which this study was built. For these discussions and teaching me the true beauty of turbulence

and a tall glass of beer, I'm extremely thankful. In addition, having the Air Force Chief Scientist as a reference when applying for a job with the Air Force Research Laboratory is pretty sweet. I would also like to thank the rest of my committee members Prof. Dowling, Prof. Ihme, and Prof. Shyy for their efforts in helping this work reach its full potential. I also owe a great deal to Jeff Donbar, who's guidance while I worked as a Co-op with AFRL illustrated the importance of graduate school and convinced me to go to Michigan and work for Prof. Driscoll.

Success and enjoyment in graduate school is largely tied to the fellow graduate students one works with during the day and has a little bit of fun with on the nights and weekends. I was fortunate that Prof. Driscoll somehow managed to bring Adam, Danny, and I into his group at the same time. I'm sure that he is relieved that we are leaving with FXB still standing. Besides the endless conversations about how to fix the world sports and on occasions work, the endless barbecues, broom ball games, and football Saturdays would have made this four and a half year endeavor worth it even if I did not earn a degree. From Adam I learned how to smoke large pieces of meat, drink properly, and that a lost Canadian can always find his way back in his home country. From Danny I learned that bacon grease does make everything better, that fireworks are strictly an outdoor activity and to always be on the lookout for tasers. I also will never forget the making of the Turguduckenhen, cabin smashing at Indian lake, learning to SCUBA dive, and road trips to Andy's wedding and Montreal. As a new graduate student it is important to have some grandfathers in the group to show you the ropes and Jeff, Chad, Zac and Sulabh did not disappoint. I owe a huge debt to these four for teaching me about laser diagnostics, conducting research and to always leave time for some fun. I especially would like to thank Jeff, who convinced me that the NASA CUIP project was a good opportunity to build

a new facility and take some great fundamental measurements. Another graduate student that was always there to lend a hand in the lab, eat cake and go run around was Andy. I especially enjoyed the use of his hand built inlaid laundry folding table over the past year. The Pi Dog House also has a very special place in my heart for the many memorable football Saturdays and other events over the years. I really cannot believe that Kristina, Prashant, and Ellie kept letting us come back week after week with the amount of cleanup required each Sunday. I also greatly enjoyed the friendly debates over wine, scotch and good food with Prashant and Elena. I'm also thankful they did not let me starve to death when Hyce went out of town. Last but not least, I would like to thank Erin for her constant advice on my wardrobe.

Experimental studies can be made on the efforts of technicians and I was extremely fortunate to have the help of four of the highest caliber. Terry taught me the proper way to do tolerances so my many rocket components would actually fit together in the end. I also appreciate his accommodating my sometimes harebrained schemes where adding or removing some piece of metal would fix all of my problems. Dave taught me just enough about circuits to be dangerous and found a way to ignite a rocket using parts from a Ford F-150. Finally Eric and Tom helped with all of the building modifications necessary to make the experiment work not to mention a number of other small projects that greatly helped along the way. I would also like to acknowledge all of the administrative staff that have helped with the tedious but necessary paperwork for all of the purchasing that had to be done to build the facility. I would especially like to thank Denise for keeping me on the right track and the almost endless supply of free food.

I would not be where I am today without the love and support of my family. From an early age my parents pushed me to work hard and to choose a career that made

me happy: that more then anything propelled me to keep going in my education. Aerospace was the only engineering field I ever considered and I think that has came from my love of airplanes and spacecraft passed down from my father. At a young age my dad put me on the back of his bike and took me to watch the planes take off at the Springfield Air National Guard Base. He would also take me down to the Air Force Museum so we could look at the P-47 Razorback like the one my grandfather flew in World War II. I'm very thankful for these experiences because without them I never would have found a field I enjoyed as much. I'm also thankful I received my mom's math ability instead of my dad's; otherwise this would have been a very short endeavor. Most importantly I would like to thank Hyce for her constant love, support and putting up with all of my craziness during prelims and the writing of this thesis. The sacrifices she has made to come to Michigan and now on to California are something that I will never be able to repay. I'm looking forward to the years ahead as we go together through the journey of life.

TABLE OF CONTENTS

LIST OF FIGURES

Figure

LIST OF TABLES

Table

LIST OF APPENDICES

Appendix

CHAPTER I

Introduction

Coaxial jets are utilized in a number of devices throughout the world. These applications include propellent injectors in rockets and industrial furnaces, components of pumps and ejectors, and perhaps most visibly, the exhaust of modern large bypass ratio turbofan engines. In all of these applications the complex near field mixing structure of coaxial jets plays a critical role in determining how well the system performs. For example, in turbofan engines the bypass ratio is set by the overall operational performance but the exit nozzle can be shaped to produce a coaxial jet with an outer to inner area and velocity ratio which minimizes exhaust noise to meet ever tightening noise standards at airports worldwide. Another example is a rocket propellent injector for which the near field mixing not only sets the length of the flame and consequently the size of the chamber, but also plays an important role in the stability of the engine.

Since the dawn of the space age coaxial jets have been used in rocket engines as propellent injectors to mix fuel and oxidizer, due to both the simplicity of the geometry and the rapid mixing that they provide. When the outer jet is fuel and the inner jet is oxidizer, the outer fuel annulus acts as a protective envelope which encases the oxidizer. This greatly reduces combustion chamber wall oxidation. In

addition, such a design results in a relatively short flame. Rockets of note that use coaxial jets as injectors include the SSME on the Space Shuttle (Sutton and Biblarz 2001) and the Vulcain engine of the Ariane 5 (Juniper et al. 2000). In these engines the coaxial jet injector is typically used for airblast atomization. The gaseous high speed outer jet (fuel) is used to blast apart a dense liquid core (oxidizer). However, interest exists in developing engines using a full flow staged combustion cycle. The full flow of the oxidizer and fuel are run through preburners to drive the turbopumps, resulting in complete gaseous injection into the main combustion chamber (Farhangi et al. 1994 and Jensen et al. 1995). Recent studies also have indicated that liquid core coaxial jets operating at supercritical conditions (which are common in modern rocket engines) scale in a similar-manner as single-phase coaxial jets (Davis et al. 2006). Consequently, studying the mixing properties of gas/gas coaxial jets can provide insight into the processes that are occurring in the supercritical case and has the added advantage of being able to apply certain experimental methods and having well defined fluid transport properties.

Since coaxial injectors already are used in legacy engines and posses a simple geometry yet a complex flow field, they are ideal for validating the next generation of modeling tools. Using gas/gas injection has the advantage that the mixing and combustion models can be exercised without the added complexity of a droplet breakup model. Also, by obtaining reacting and nonreacting experimental results, issues with the mixing model can be explored separately from the combustion model. These reasons and the desire to increase the basic understanding of the complex interaction between turbulent shear flows, have motivated the present systematic study of reacting and nonreacting turbulent coaxial jet mixing.

1.1 Understanding Coaxial Jet Mixing

Three distinctly different types of jets commonly appear in the literature: simple jets, coflowing jets, and coaxial jets. Each has different mixing pattern. The simple jet is the most common and is characterized by a single stream of fluid that is injected into a still environment. A coflowing jet is characterized by a single stream of fluid that is injected into an environment that has a bulk velocity in the same direction as the injected fluid and which, for the purposes of mixing, extends to infinity. A coaxial jet is a single jet surrounded by an annular jet which does not extend to infinity; therefore two mixing layers exist in the near field which interact. The three types of jets are sketched in Fig. 1.1.

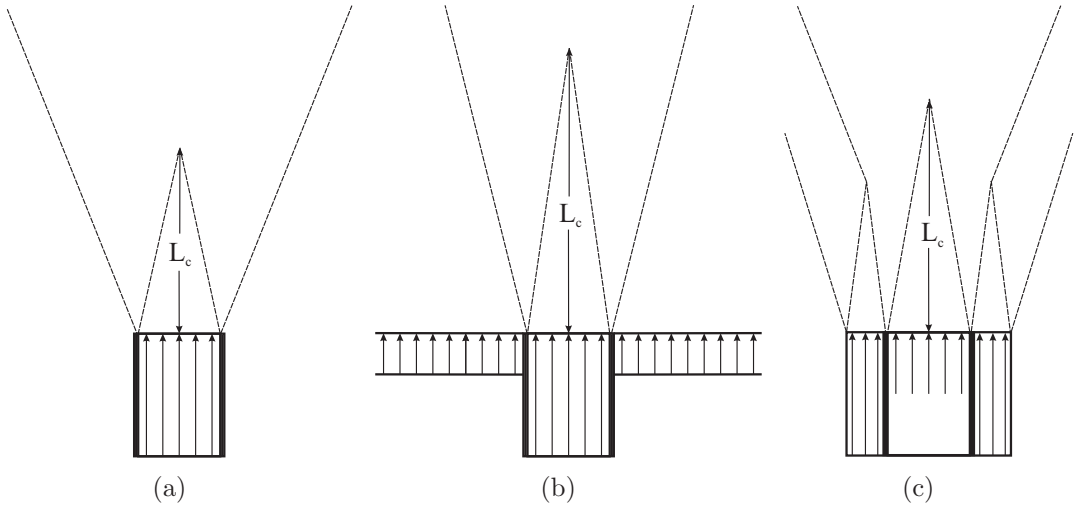

Figure 1.1: Shear layer development and potential core length in (a) simple jet, (b) coflowing jet, and (c) coaxial jet.

In simple jets, the near field is characterized by well-established shear layer growth equations. In the far field dimensional reasoning, conservation of momentum, and self-similarity of velocity and conserved scalar profiles provide simple scaling laws that predict the growth of the jet, velocity decay, and decay of the conserved scalar (Ricou and Spalding 1961). The same is true for coflowing jets, except that the far

field solution depends on whether one is looking at region in the "jet-like" limit, the "wake-like" limit or in the transition regime (Maczyński 1962). For coaxial jets the far field solution is the same as a simple jet, since the far field is governed only by the total momentum and therefore the injector geometry does not play a role. However, in the near field the interactions of the two mixing layers make the flow very complex. A more detailed sketch of the near field and transitional region of a coaxial jet is shown in Fig. 1.2. The outer mixing layer in Fig. 1.2 lies between the ambient fluid and the outer jet and the inner mixing layer lies between the inner and outer jet. The growth, interaction and the structures that make up these layers are discussed throughout this work.

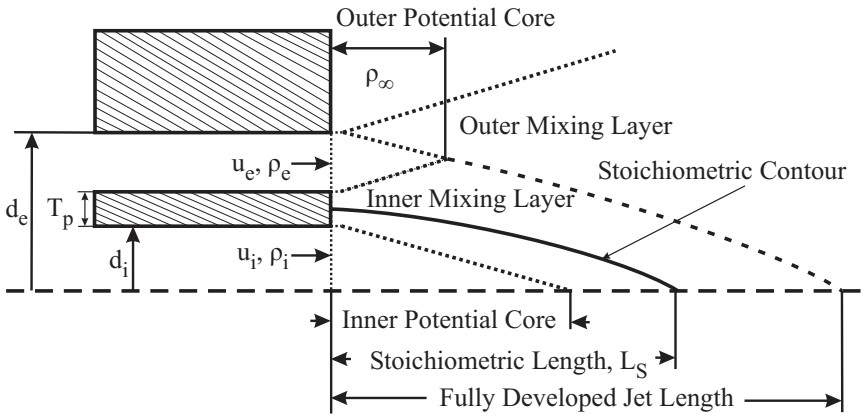

Figure 1.2: Schematic of a coaxial jet injector with the inner and outer mixing layers and the different mixing regimes labeled.

1.2 Literature Review

Since coaxial jet mixing occurs in rockets and in the exhaust of turbofan engines, they have been a subject of active research since the late 1950s. This concise review of previous studies is divided into two sections which describe nonreacting and reacting coaxial jets, respectively. Only studies that quantified mixing in the near field or

transitional region are considered. In addition, only coaxial jets and flames which are "single-phase" are considered. Single-phase means that all three fluids (inner, outer, and ambient) are the same phase, either gas or liquid. Supercritical fluids were not considered.

1.2.1 Nonreacting Coaxial Jets

One of the first experimental studies of a coflowing jet was that of Forstall and Shapiro (1950), who seeded helium into the inner jet and used a gas sample probe to measure gas concentration and a Pitot probe to measure velocity. Williams et al. (1969) studied air/air coaxial jets in order to decrease the noise from jet engines. In Williams work the velocity ratio (r_u) was 0.72 and 1.04. The velocity ratio r_u is defined to be the ratio of the outer jet bulk velocity to the inner jet bulk velocity. Results showed that for a constant inner jet velocity, increasing the outer jet velocity increased the inner jet potential core. However, the length of the inner jet potential core never exceeded five times the outer jet diameter, which is what would be expected from a simple jet of the same diameter.

Theoretical analysis of Morton (1962) proposed that a differential equation method based on the conservation of mass and momentum could predict the concentration and velocity profiles. This method makes a number of major assumptions. First, the ratio of the mean inflow velocity at an average edge of the jet to the mean velocity along its axis is constant. A result of this assumption is that at any downstream location the inner and outer jet velocity profiles are different, but uniform in each jet. Second, density is assumed to be uniform. Due to these assumptions, experimental agreement with this model were poor.

Chigier and Beer (1964) experimentally studied the near-field of air/air coaxial

jets for velocity ratios (r_u) above and below one (∞, 2.35, 1.17, 0.235, 0.117, and 0.024). Pressure measurements were made using an impact tube with a disk-type static probe from which velocity profiles were obtained. Concentration measurements were made by seeding CO_2 into the outer jet, heating the inner jet to 50 K above room temperature and simultaneously measuring the temperature and gas concentration. An unique aspect of this work was the large post thickness (T_p) of 1.65 cm. This is significant compared to the inner jet diameter (d_i) of 2.5 cm and the outer jet diameter (d_e) of 9.7 cm. Results indicated that as the velocity ratio was increased, both the velocity and concentration on the centerline decreased. Therefore they concluded that the potential core length decreased as the velocity ratio increased.

Champagne and Wygnanski (1971) expanded on the work of Chigier and Beer (1964) by measuring the mean velocities, turbulence intensities and shear stresses for coaxial jets with velocity ratios between 0 and 10 using two linearized constant temperature anemometers. As in most nonreacting coaxial jet studies, a sharp contoured nozzle was used. The outer to inner nozzle area ratio was varied between 1.28 to 2.94. They showed that the widths of the outer and inner potential cores decrease approximately linearly with downstream distance and that the length of the outer potential core is largely independent of the velocity ratio. The inner potential core length was found to depend on both the velocity ratio and the injector area ratio. When the velocity ratio was less than one the inner potential core length was found to be longer than that of a single jet and it increased with increasing velocity ratio (r_u). For r_u values greater then one, the potential core length was found to decrease with increasing velocity ratio. Decreasing the outer to inner area ratio was found to decrease the inner potential core length. This was argued to be due to the increase in the static pressure gradient as a result of the decrease in the outer jet thickness. The

higher pressure gradient bends the outer jet towards the inner jet, which increases the mixing.

In addition coaxial jets with swirl have been studied. Using a hot-wire anemometer to measure mean velocity, Reynolds stresses, and velocity fluctuations, Ribeiro and Whitelaw (1980) investigated coaxial jets with and without swirl. Swirl was added to the outer jet for $0.65 \leq r_u \leq 1.5$. Results showed that the non-swirling coaxial jet reached a self-similar state much faster than a round jet of the same outer diameter and the same total mass flow due to vortex shedding from the injector post. Swirling coaxial jets were found to develop at an even faster rate than the non-swirling case.

In an effort to understand the underlying vortical structures in the near-field of coaxial jets with velocity ratios less than one (0.3, 0.5 and 0.7), Ko and Kwan (1976) and Kwan and Ko (1977) utilized a pressure probe, hot-wire, and microphone spectra. They were able to show that there are two vortex trains, one in the outer mixing layer that lies between the ambient and outer jet fluid, and one in the inner mixing layer that lies between the outer and inner jet fluid. The merging and the relative strength of these vortex trains were shown to be a function of the velocity ratio. The velocity profiles were shown to be self-similar in a number of regions. These regions include the outer and inner mixing region in the initial merging zone between the injector exit and the end of the outer potential core. The fully merged zone that occurs after the inner and outer mixing layers have merged was found to be self similar up to the end of the inner potential core. Similarity was not achieved across the whole flow, but only in the pockets of fluid between the potential cores, the outer core and the edge of the jet, and between the edge of the jet and the inner potential core above the outer potential core. Each of these regions had different

similarity profiles.

Ko and Au (1985) and Au and Ko (1987) expanded the work of Ko and Kwan to velocity ratios greater than one ($1 \leq r_u \leq 6.67$) using the same experimental setup. Different vortical patterns were found depending on the velocity ratio. When the velocity ratio fell below 1.25, the vortices were found to shed from the injector lip with alternating direction, which is an indicator of a "wake-like" mode. When the velocity ratio exceeded 2, the inner vortices were found to rotate towards the inner-jet. Comparison with other experimental studies suggested that for velocity ratios greater than one, the length of the inner potential core is inversely proportional to the velocity ratio. This is the first instance in the literature where the velocity ratio was shown to govern the inner potential core length. The outer potential core length was found to be independent of the velocity ratio, but was related to the area ratio.

Based on the coaxial jet work up to the late 1980's it is clear that the structure of the vortex patterns and the dynamics of their interactions play an important role in the near field mixing of coaxial jets and that the velocity ratio plays a role in determining these interactions. However, experimental studies up to this point had only indirectly measured the vortical structures using two-point cross-spectral techniques to determine the phase relationships between velocity components and pressure. Dahm et al. (1992) directly imaged the vortex structures and dynamics using two-color Planar Laser Induced Fluorescence (PLIF). In a water jet with a constant area ratio and a sharp injector, they seeded the inner jet with Rhodamine B dye and the outer jet with disodium fluorescein dye. They used an argon laser to excite the dyes. The different color fluorescence from the two dyes was then imaged at 60 Hz. Dahm et al. argued that the complex inlet velocity profile of a coaxial jet can be viewed as being comprised of a wake component and a shear-layer

component. These components are the symmetric and antisymmetric parts of the profile, respectively. In the mixing layers the mixing is said to be "wake-like" if the vortex structures have both positive and negative circulation and "shear-like" if they primarily have only one sign of circulation. At velocity ratios less than one (0.59 and 0.71) their results show that the outer layer is "shear-like" while the inner layer does not roll up before being consumed by the outer mixing layer structures. At a velocity ratio of one, the inner mixing layer becomes "wake-like", while the outer mixing layer continues the shear layer roll up. As the velocity ratio is further increased to 1.14 the inner layer starts to become more "shear-like". Finally as the velocity ratio is further increased (2.56 and 4.16) both layers become shear-like and an interlocking between the inner and outer vortical structures is observed. The percentage of time the locking between the structures in the two layer's structures is observed increases with velocity ratio, up to the point where they are essentially locked continuously. These results suggest that once the layers become fully "shear-like" and locked, a simple relation in terms of the velocity ratio should be able to predict the potential core length. This agrees with the finding of Ko and Au (1985).

Additional work on coaxial jets has focused on the difference between a blunt or sharp injector post. Buresti et al. (1998) studied air/air coaxial jets with a 5 mm thick injector post and a sharp post with an outer to inner area ratio of 2.06 at velocity ratios of 1.5 and 3.3. Laser Doppler Anemometry (LDA) and hot-wire measurements were used to obtain velocity statistics. Results showed that the sharpening of the injector post reduced the radial velocity fluctuations and the Reynolds stresses in the near field. However, all differences disappeared beyond the potential core. LDA also has been used to verify a number of the pitot probe results from previous studies (Warda et al. 1999). These include that the inner potential core length is a function

of the velocity ratio while the outer potential core is insensitive to r_u. For velocity ratios less than one, self-similarity is not reached by 25 inner jet diameters. For velocity ratios greater than one, mixing is faster than for velocity ratios less than one.

The infinite velocity ratio limit corresponds to the case of zero inner jet velocity. The inner jet becomes a bluff-body so a recirculation zone forms. This greatly truncates the length of the inner potential core. Rehab et al. (1997) explored this limit in water/water coaxial jets using LDV, PLIF, and pressure probes. They used a knife edge injector post and a diameter ratio of 1.4. Their results showed that for velocity ratios between 1 and 7 the inner potential core length was inversely proportional to the velocity ratio. Above velocity ratios of 7, a recirculation zone was observed at the end of the inner potential core. The recirculation zone was observed to cause oscillations that are convected downstream at a frequency related to the Strouhal number. Using a mixing layer argument and the pressure drop across the mixing layer, they proposed that the criterion for the onset of recirculation is $r_u > 7$. They also speculated that for variable density jets the governing parameter is not the velocity ratio, but the outer to inner momentum flux ratio (M) which is the density ratio (S) times the square of the velocity ratio (r_u). Their predicted criterion for recirculation in the variable density case is $\sqrt{M} > 7$. Rehab et al. (1998) continued to study the effects of nozzle geometries and the initial exit velocity profiles on the potential core length and the criterion for the onset of recirculation. They found that increasing the gap width (the distance between the edge of the outer jet and the outside edge of the injector post) increased the inner potential core and moved the onset of recirculation to higher velocity ratios. It also was found that as the inlet velocity profiles become more parabolic (compared to a top hat exit profile) the

inner potential core length becomes shorter and the recirculation initiated at lower velocity ratio values. However, both of these effects were small and were considered secondary compared to the velocity ratio dependence.

In another paper Villermaux and Rehab (2000) used a simple entrainment argument to formalize the scaling of the potential core with the inverse of the velocity ratio. This formulation allowed the method to be extended to centerline concentration values beyond the potential core. Also, using the result of Hill (1972), the method was extended to variable density jets by replacing the velocity ratio with the momentum flux ratio, however, this was not experimentally verified.

While the density ratio ($S = \rho_e/\rho_i$) is an important characteristic of coaxial jets used as propellent injectors, only two previous studies have reported measurements of these effects. One such study is by Favre-Marinet et al. (1999), who varied the density ratio (S) over a wide range for velocity ratios (r_u) greater then one. They considered air/air (S = 1), air/SF_6 (S = 0.21) and He/air (S = 0.14) cases, and the near field entrainment was investigated using LDV, laser-sheet visualizations, and a multi-wire probe which could detect flow reversal. A knife edge injector with an injector diameter ratio of 1.35 was used. Results showed that the dynamics of variable density jets are governed by the momentum flux ratio and also suggested that the criterion for the formation of recirculation zones is $M \approx 50$.

Continuing their work on variable density coaxial jets, Favre-Marinet and Camano-Schettini (2001) utilized an aspirating probe to measure density in the same injector that was previously studied. These results showed that for velocity ratios greater the one and density ratios less than one, the potential core length is inversely proportional to the square root of the momentum flux ratio and confirmed that recirculation occurs at $M \approx 50$.

1.2.2 Reacting Coaxial Jets

In comparison to nonreacting coaxial jets, very little systematic work has been done on reacting gas/gas turbulent coaxial jets. A majority of reacting work with coaxial jets has been focused on jets with gaseous outer jets and liquid inner jets, since this is the common configuration in liquid propellant rocket engines (Beisler et al. 1994, Juniper et al. 2000, Yeralan et al. 2001, and Singla et al. 2006). The outer jet typically is in the gaseous state because the cryogenic liquid fuel is heated as it is used to cool the rocket nozzle and the combustion chamber walls.

A great deal of reacting gaseous turbulent coaxial jet work has been done at the Propulsion Engineering Research Center at the Pennsylvania State University (Santoro 1998). All of this work was carried out in a single-element laboratory rocket engine similar to the experimental setup used in this study. Some of the first work done with coaxial jet flames in this group utilized OH PLIF and PIV measurements to characterize the flame structure and velocity field (Moser et al. 1993). These diagnostics were applied to two H_2/O_2 coaxial jet flames. The velocity ratio for case 1 was 3.4 and 9.7 for case 2, with inner to outer area ratios of 1.18 and 0.41 respectively. In both cases the post thickness was 0.89 mm and the chamber pressure was 1.31 MPa. Results indicated that the oxygen potential core stays intact well downstream of the injection location and that the turbulent intensities and unsteady nature of the flame were similar to turbulent jet diffusion flames at atmospheric conditions. Velocity measurements indicated the complex nature of the near field mixing region. Moser et al. (1995) expanded on this work by obtaining planar laser light scattering (LLS) images of seed particles for the same case 1 conditions that were previously studied. The scattered light signal was argued to be related to fuel or oxidizer concentration depending on which flow was seeded. However, the only

result of this study was to say LLS can be used to study mixing in gaseous coaxial injectors.

In the same single-element laboratory injector as used in previous studies, Foust et al. (1996b) used Raman spectroscopy to obtain mole fraction profiles of the major combustion species (O_2, H_2, H_2O, and N_2). Nitrogen was introduced into the flow next to the windows as a purge gas to keep the windows from over heating. Profiles were obtained for case 1 at a number of downstream locations. Results show that H_2 and O_2 only coexist for small distances, indicating that thin reaction zones occur. The outer H_2 jet also prevents the inner O_2 jet from significantly diffusing outwards, whereas the H_2 does rapidly diffuse outward and fills the test section. Also, as would be expected, the water mole fraction peaks near the intersection of the H_2 and O_2 mole fraction profiles. In another paper (Foust et al. 1996a) these results were compared to a computational fluid dynamics (CFD) RANS calculation. Reasonable agreement between the experimental and computational results were found, and differences between the two were attributed to measurement inaccuracy and due to insufficient data to fully determine an average value. Lastly, Marshall and Pal (2005) added fuel and oxidizer preburners to a new experimental rocket engine of similar design but with a smaller cross sectional area and obtained benchmark wall heat transfer measurements for CFD model validation. Unfortunately, no attempt was made to say anything about the structure of the turbulent coaxial jet flame from these measurements. Additional work performed on reacting coaxial jets includes a study of a H_2/O_2 coaxial jet flame with a velocity ratio of 2 and an injector geometry with a diameter ratio 2.26 and a post thickness of 1.15 mm at chamber pressures of 0.93, 2.5, and 3.8 MPa (Vaidyanathan et al. 2007). Diagnostics included OH PLIF and wall heat flux transducers. OH PLIF measurements provided the average

location of the flame and the wall heat transfer was found to significantly increase with chamber pressure, as would be expected.

Work outside of the Propulsion Engineering Research Center on reacting gaseous coaxial jets has been more limited but not without interesting results. Ghosh et al. (2007) studied flame-acoustic interactions in a two-dimensional coaxial injector for a number of density, velocity and momentum flux ratios. The flame-acoustic interaction was found to be relatively insensitive to velocity ratio changes but very sensitive to density ratio changes. Selecting the optimum density ratios to extend the combustion stability regime was suggested. Nicoli and Haldenwang (2003) performed direct numerical simulations of two-dimensional gaseous H_2/O_2 coaxial jet flames over a range of velocity ratios of 3 to 30, a range of density ratios of 0.02 to 0.125, and momentum flux ratios of 0.6 to 36. An ad hoc equation of state was used that allowed the density ratio to be varied while one-step H_2/O_2 chemistry was assumed throughout. Due to limited computational time the Reynolds numbers were quite low, however unsteady flapping was observed in all cases. Increasing the momentum flux ratio and the Reynolds number resulted in more complex structures and increased amplitude of the flapping. Using the O_2 mole fraction as a marker of the potential core, potential core lengths were found to follow the momentum flux ratio scaling suggested by Villermaux and Rehab (2000) for nonreacting cases but the reacting flow data had a different constant than the nonreacting case.

For the case of fuel in the inner jet and oxidizer in the outer jet, Sautet et al. (2001) and Ditaranto et al. (2001) studied oxygen/natural gas combustion from a coaxial jet injector with velocity ratios between 0.8 and 4 and momentum flux ratios between 0.5 to 2.5. Using OH* chemiluminescence as a marker of the flame, the unsteady structures of the flames were characterized. In addition, LDV was used

to obtain velocity statistics. Two instability modes were observed in the near field: a sinusoidal and a radial mode. The preferred mode was shown to depend on the momentum flux ratio. Also, large burning pockets were observed to break off from the main flame and convect downstream especially at low momentum flux ratios. Finally, the flame lengths calculated from the chemiluminescence images were shown to decrease with the momentum flux ratio.

1.3 Motivation and Objective

Because of their relation to rocket injectors, turbulent coaxial jets with properties typical of such injectors are investigated in this work. These properties include outer to inner velocity ratios (r_u) greater than one and outer to inner density ratios (S) typically much less than one. An outer fuel jet surrounds an inner oxidizer jet for all cases considered here. The injector has a relative post thickness that is representative of an actual engine. This work also focuses on fuel-oxidizer combinations common in rockets and industrial furnaces. For such combinations, the stoichiometric mixture fraction based on inner jet fluid (f_S) is relatively large; specifically, $f_S = 0.97$ for hydrogen-air, $f_S = 0.89$ for hydrogen-oxygen and $f_S = 0.80$ for methane-oxygen. Thus the distance to mix to stoichiometric on the centerline (L_S) is typically only slightly larger than the jet potential core length. As a consequence the stoichiometric mixing length in the nonreacting coaxial jets, and the flame length in the reacting coaxial jets, both are dominated by the mixing in the near field.

With these points in mind the main objectives of this work are as follows:

- obtain the first average and instantaneous planar mixture fraction fields in variable density coaxial jets,

- expand the range of density ratios that have been systematically varied in nonreacting coaxial jets by a factor of two lower than has previously been considered,
- explore near field scaling concepts and evaluate their ability to predict the measured potential core lengths in coaxial jets,
- extend promising near field scaling methods to predict the stoichiometric mixing length (L_S) in nonreacting coaxial jets for fuel/oxidizer combinations of interest,
- investigate the effect of velocity ratio, density ratio, velocity difference, injector geometry, confinement and Reynolds number on the mixing length (L_S),
- image OH fluorescence of reacting coaxial jet diffusion flames to locate the average and instantaneous flame front and the flame length,
- use OH fluorescence and cinema chemiluminescence diagnostics to study the structure and instabilities of turbulent coaxial diffusion flames,
- relate nonreacting stoichiometric mixing lengths and coaxial jet flame lengths using recently proposed scaling methods that account for heat release effects,
- produce a high fidelity data set of nonreacting and reacting coaxial jets for use in model development and validation.

1.4 Outline of the Dissertation

In Chapter II, theoretical methods to predict the inner potential core length and the stoichiometric mixing length of nonreacting turbulent coaxial jets are described.

Particular attention is paid to the strengths and shortcomings of each prediction method. The existing theory that describes the effect of heat release on the stoichiometric mixing length and hence the flame length is discussed in Chapter III. In particular, the of Tacina and Dahm (2000) is described which accounts for the effect of heat release on the experimentally measured mixing length for the reacting coaxial jets. Chapter IV gives a description of the experimental facilities that were built and used for this study. Also described are the planar laser-induced fluorescence (PLIF) techniques utilized to obtain mixture fraction fields in nonreacting coaxial jets and OH contours in the reacting jets. In Chapter V the measured mixture fraction fields for nonreacting coaxial jets are reported and are used to obtain stoichiometric mixing lengths (L_S) which are than compared against the models described in Chapter II. Then the effects of velocity ratio, velocity difference, density ratio, diameter ratio, injector post thickness, and Reynolds number are explored. Inner potential core length obtained in this work are compared to experimentally obtained values that are in the literature. Next, OH PLIF images from the reacting jet experiments are presented in Chapter VI and are used to show the structure of reacting turbulent coaxial diffusion flames. From these images flame lengths (L_S) are measured, and the equivalence principle of Tacina and Dahm (2000) is used in an attempt to collapse the flame lengths and nonreacting stoichiometric mixing lengths to a single curve. Finally, the main conclusions are summarized in Chapter VII.

CHAPTER II

Nonreacting Mixing Length Models

As noted in Chapter I, a main objective of this work is to obtain scaling laws for reacting and nonreacting turbulent coaxial jets. In this chapter, four previously-proposed mixing length models are described for nonreacting turbulent coaxial jets. For fuel-oxidizer combinations that are commonly found in rockets and industrial furnaces, the stoichiometric mixture fraction based on inner jet fluid is relatively large. Specifically $f_S = 0.97$ for H_2/air, $f_S = 0.89$ for H_2/O_2, $f_S = 0.94$ for CH_4/air, and $f_S = 0.80$ for CH_4/O_2, where the oxidizer is the inner jet fluid. Thus the stoichiometric mixing length (L_S) is typically only slightly larger than the jet potential core length, which suggests that mixing in these cases is controlled by near field mixing and not far field mixing. Why far field scaling is not valid also is discussed. Particular attention is paid in this chapter to the assumptions in each of these models for coaxial jets.

2.1 Shear Layer Scaling

One of the more common ways to look at mixing in the near field of simple jets or coflowing jets is to apply planar shear layer theory, where the growth rate and

entrainment flux ratio equations are used to approximate the axi-symmetric shear layers of jets (Clemens and Paul 1995 and Chehroudi et al. 2002). Early work on variable density planar shear layers was actually motivated by the desire for a simplified method to study shear layers in simple jets (Brown and Roshko 1974). The near field of coaxial jets have additional complexity, compared to simple or coflowing jets due to the interaction of two shear layers. However, the mixing length of a coaxial jet can be related to the length of the inner potential core formed by the merging of the axi-symmetric inner shear layer. Using a semi-empirical argument, Dimotakis (1986) was able to derive entrainment and growth rate equations for planar shear layers. This derivation, as it applies to coaxial jets, is discussed below.

Note firstly that compressibility effects can be ignored, since all jets studied in this work have inner and outer Mach numbers less than 0.3. Also, assuming that the flow is at a sufficiently high Reynolds number such that the only affect of viscosity is to set the inner turbulence scale, then the only flow properties that affect the outer scale variables, U_{out} and δ, are u_e, u_i, ρ_e and ρ_i. Subscript i corresponds to the low speed side and e the high speed side of the shear layer. This nomenclature is consistent with the labeling of coaxial jet properties presented in this work, since the high speed fluid is always the outer jet and the inner jet is always the low speed fluid. U_{out} is the difference between the high and low speed fluid velocities, which is typically assumed to be constant along the downstream direction x in the shear layer, as shown in Fig. 2.1. However, taking U_{out} to be a constant may be a poor approximation, since the outer shear layer affects the velocity at the edge of the inner shear layer. Nevertheless, if this approximation is accepted, then when dimensional reasoning is applied to the governing parameters of the problem a total of three

dimensionless groups are possible, namely

$$\frac{\delta}{x}, \frac{u_e}{u_i}, \frac{\rho_e}{\rho_i}. \tag{2.1}$$

Here δ/x u_e/u_i is the velocity ratio (r_u) and ρ_e/ρ_i is the density ratio (S). The shear layer growth rate is thus a function of r_u and S, namely

$$\frac{\delta}{x} = f(r_u, S). \tag{2.2}$$

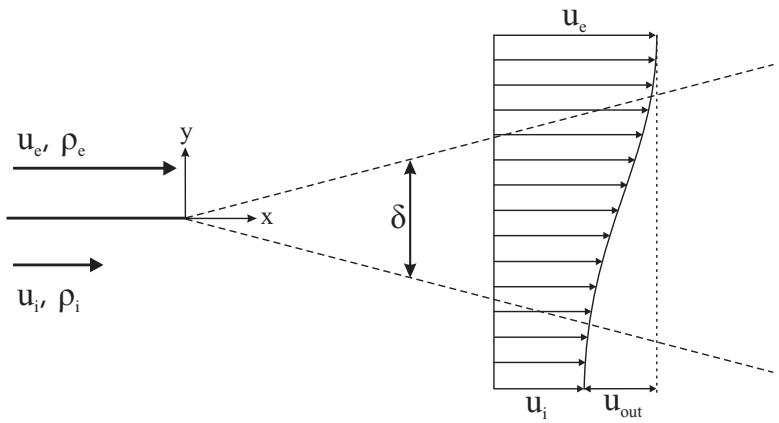

Figure 2.1: Diagram of planar shear layer showing far field velocity profile and shear layer thickness.

Following Dimotakis (1986), to determine this function of r_u and S, the shear layer is viewed in a vortex-fixed frame, in which the splitter plate used to create the shear layer appears to be moving to the left at the vortex convection velocity (u_c), as illustrated in Fig. 2.2. In the vortex-fixed frame, there exists a stagnation point between any two neighboring vortices which is surrounded above and below by newly entrained nearly irrotational fluid. Hence, Bernoulli's equation can be applied on a streamline that extends through the stagnation point into both the unperturbed high and low speed fluids,

$$P_e + \frac{1}{2}\rho_e \left(u_e - u_c\right)^2 = P_i + \frac{1}{2}\rho_i \left(u_c - u_i\right)^2. \tag{2.3}$$

Assuming that $P_e = P_i$, or else the shear layer would deflect, Eq. 2.3 can be solved for the vortex convection velocity ratio ($r_c = u_c/u_e$),

$$r_c\,(r_u, S) = \frac{1 + (r_u S^{1/2})^{-1}}{1 + S^{-1/2}}. \tag{2.4}$$

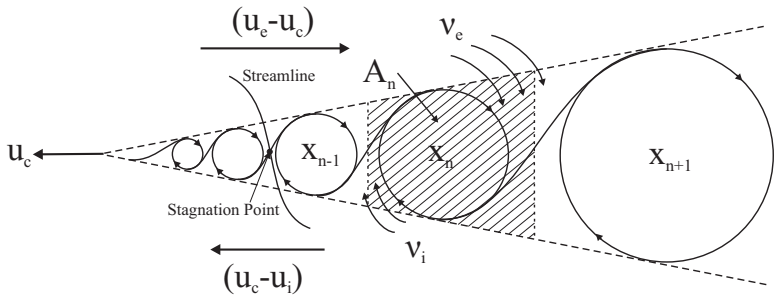

Figure 2.2: Diagram of shear layer in vortex fixed frame.

Entrainment velocities defined on the high and low speed side of the layer, v_e and v_i respectively, are expected to be a function of the dimensionless parameters of the problem and proportional to the velocities of the high and low speed streams in the vortex rest frame (Dimotakis 1986). It is then assumed that the functional relationship for both nondimensional entrainment velocities are equal, namely

$$\frac{-v_e}{u_e - u_c} = \frac{v_i}{u_c - u_i} = f(r_u, S). \tag{2.5}$$

Using Eq. 2.5 the volume entrainment ratio can be written as

$$E_v = \frac{-v_e\,(x_{n+1} - x_n)}{v_i\,(x_n - x_{n-1})} = \frac{(u_e - u_c)\,(x_{n+1} - x_n)}{(u_c - u_i)\,(x_n - x_{n-1})}, \tag{2.6}$$

where the difference in x values is the distance between vortices through which fluid is entrained. From dimensional reasoning, the mean spacing (l) between the vortices scales with x, and thus E_v can be written as

$$E_v = s^{-1/2}[1 + (l/x)], \tag{2.7}$$

where the ratio of velocity differences in Eq. 2.5 is equal to the inverse of the density ratio, which is a result of Bernoulli's equation (Eq. 2.3). Note that l/x is related to x_n, the position of the n^{th} vortex, by a geometric progression, $x_{n+1} = (1 + l/x)x_n$.

The mean spacing of the vortices (l) can be related to r_u and S by using the experimental correlation of Koochesfahani and Dimotakis (1985) which relates l/x to the shear layer vorticity thickness,

$$l/x = 3.9\,(\delta/x)\,. \tag{2.8}$$

The shear layer growth relation from Brown and Roshko (1974) for uniform density shear layers,

$$\frac{\delta}{x} = 0.17\frac{1 - r_u^{-1}}{1 + r_u^{-1}}, \tag{2.9}$$

allows l/x to be written in terms of r_u,

$$\frac{l}{x} = 0.68\frac{1 - r_u^{-1}}{1 + r_u^{-1}}. \tag{2.10}$$

Equations 2.8 and 2.9 are obtained for uniform density shear layers, however Eq. 2.10 is believed to be not a function of S, based on experimental observations by Konrad (1976). The vortex spacing also has been observed to be independent of S in reacting flows (Clemens and Paul 1995). Using Eqs. 2.7 and 2.10 the volume entrainment ratio can be written as

$$E_v(r_u, S) = S^{-1/2}\left(1 + 0.68\frac{1 - r_u^{-1}}{1 + r_u^{-1}}\right). \tag{2.11}$$

The volume entrainment ratio easily can be related to the mass entrainment flux ratio by $E_m = E_v S$.

$$E_m(r_u, S) = S^{1/2}\left(1 + 0.68\frac{1 - r_u^{-1}}{1 + r_u^{-1}}\right). \tag{2.12}$$

While the above analysis applied to entrainment ratios, the total entrainment into a shear layer can be derived in a similar manner. This derivation is done by

equating the growth of an area A_n,

$$A_n \approx \frac{1}{2}\delta_n \left(x_{n+1} - x_{n-1}\right), \tag{2.13}$$

which contains a single vortex (Fig. 2.2), to the change in A_n as entrained fluid is added,

$$\frac{A_n}{t} = \epsilon \left[\left(u_e - u_c\right)\left(x_{n+1} - x_n\right) + \left(u_c - u_i\right)\left(x_n - x_{n-1}\right)\right]. \tag{2.14}$$

Equating A_n in Eqs. 2.13 and 2.14, using results from Eqs. 2.10 and 2.4, and lastly transforming back into laboratory coordinates, results in a shear layer thickness that is given by

$$\frac{\delta}{x} = \epsilon \left(\frac{1 - r^{-1}}{1 + S^{-1/2} r^{-1}}\right)\left[1 + S^{-1/2} - \frac{1 - S^{-1/2}}{1 + 2.9(1 + r^{-1})/(1 - r^{-1})}\right], \tag{2.15}$$

where ϵ is a constant with a value of 0.17.

The simplest method to predict the potential core length in coaxial jets, using Eq. 2.15, is to simply set $x = L_c$, which is the length of the core, when $\delta/2 = d_i/2$ and then solve for L_c/d_i. However, this method ignores the fact that the shear layer does not grow at the same rate into the low and high speed streams due to the unequal entrainment, that was demonstrated by Eq. 2.6 and was shown graphically in Fig. 2.4. This unequal shear layer growth can be accounted for by assuming that the amount of fluid entrained from either stream is equal to the mass flow rate that would cross a vertical plane equal in height to the penetration depth of the shear layer into the undisturbed flow as depicted in Fig. 2.3. The ratio of the mass flow rates across the shear layer can be written as

$$\frac{\dot{m}_e}{\dot{m}_i} = E_m = \frac{\rho_e u_e \tan\alpha_e}{\rho_i u_i \tan\alpha_i}. \tag{2.16}$$

The ratio of the volume flow rates across the shear layer could also have been used without altering the results. From Fig. 2.3, it can be seen that the total shear layer

growth is given by

$$\frac{\delta}{x} = \tan\alpha_e + \tan\alpha_i. \tag{2.17}$$

In the present study, the low speed side is always the inner jet, the corrected definition for L_c becomes $d_i/2L_c = \tan\alpha_i$. Using this criterion and Eqs. 2.16 and 2.17, the potential core length for a coaxial jet using planar shear layer theory can be written as

$$\frac{L_c}{d_i} = \frac{1}{2}\left(\frac{\delta}{x}\right)^{-1}\left(1 + \left(r_u S^{1/2}\right)^{-1}\left(1 + 0.68\frac{(1 - r_u^{-1})}{(1 + r_u^{-1})}\right)\right), \tag{2.18}$$

where δ/x is obtained from Eq. 2.15.

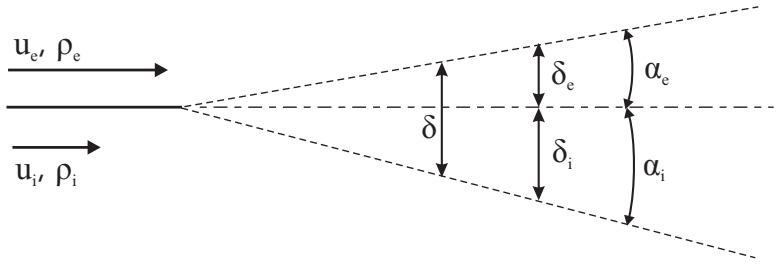

Figure 2.3: Diagram of unequal growth into the high and low speed streams of a shear layer.

Conditions under which the shear layer growth is equal are limited. If $S = 1$ then the shear layer growth is only equal when $r_u = 1$ which corresponds to a growth rate of zero for both sides. If $S > 1$ then the growth rate can never be equal since at $S = 1$ the high speed side always has a smaller growth rate and making the fast speed side denser further decreases the growth rate compared to the slow speed side. Last, if $S < 1$ for every density ratio there exists one r_u where the growth rates are equal and as S decreases the corresponding r_u value where equal growth occurs becomes larger.

2.1.1 Applicability of Planar Shear Layer Ideas to Coaxial Jets

In the derivation of the planar shear layer equations, there are three assumptions which are of a questionable nature for coaxial jets. One such assumption is that the velocities in the free stream are constant in the x direction. In a coaxial jet the velocity is nearly constant until the end of the outer potential core. After the end of the outer potential core the velocity starts to decay. A method outlined by Murakami and Papamoschou (2002) to correct for this effect is discussed in §2.2. An additional assumption states that the entrainment velocities in the coaxial jet when normalized by their respective free stream velocities in the vortex fixed frame, are equal to the same functional dependence of r_u and S as in the planar shear layer. In the single shear layer case this ansatz is justified by showing the final results for shear layer growth and entrainment match well with the experimental data of Brown and Roshko (1974). However, in coaxial jets the inner shear layer is confined. The mere presence of the outer shear layer, which is also trying to entrain fluid, can hinder the inner shear layer from entraining fluid since it must compete with the outer shear layer. In addition, for the case for which the outer jet is much faster then the inner jet a static pressure gradient is formed and a pressure force directed towards the center of the jet can reduce entrainment by retarding shear layer growth.

One reason that the derivation leading to Eq. 2.15 is semi-empirical is the use of an empirical relationship to relate l/x to δ/x (Eq. 2.8). While this relationship appears to work well for the case of a single shear layer, when a second shear layer is present a coupling exists that is based on whether the inner or outer jet dominates. The coupling of these shear layers was shown by Dahm et al. (1992). If the functional relationship (Eq. 2.8) is altered by this coupling, the shear layer growth equations would have to be altered, but if only the scaling constant is affected the new constant

could be obtained using a best fit with coaxial jet results. Adjusting the constants also accounts for varying definitions of the shear layer thickness.

To further investigate how the planar shear layer results apply to coaxial jets, the entrainment ratios, defined on mass and volume basis, for planar shear layers are plotted versus velocity ratio in Fig. 2.4. Figure 2.4 shows that for a unity density ratio, both volume and mass entrainment favor the high speed fluid. As S is increased the mass entrainment ratio also increases while the volume entrainment ratio decreases. The total entrainment into the shear layer is directly related to the shear layer growth rate (Eq. 2.15). Assuming that the shear layer growth rate into the outer and inner jets are equal, Fig. 2.5*a* shows that decreasing the density of the outer (high speed) jet relative to the inner (low speed) jet shortens the potential core, causing a larger growth rate and mixing rate. This decrease is consistent with jet and coflow jet theory for which the high speed fluid is the inner jet. Increasing the inner fluid density lengthens the jet. However, this is opposite of what is expected in coaxial jets based on the work of Favre-Marinet and Camano-Schettini (2001) who showed that a decrease in the potential core length occurs as the density ratio is increased. Of course their assumption that the shear layer grows equally into both jets is incorrect. When the unequal growth is accounted for (Fig. 2.5*b*) the density dependency reverses for velocity ratio values between one and approximately three, but remains unchanged for velocity ratio values above three. To summarize, the equations for planar shear layers predict that decreasing the density of the high speed fluid enhances mixing.

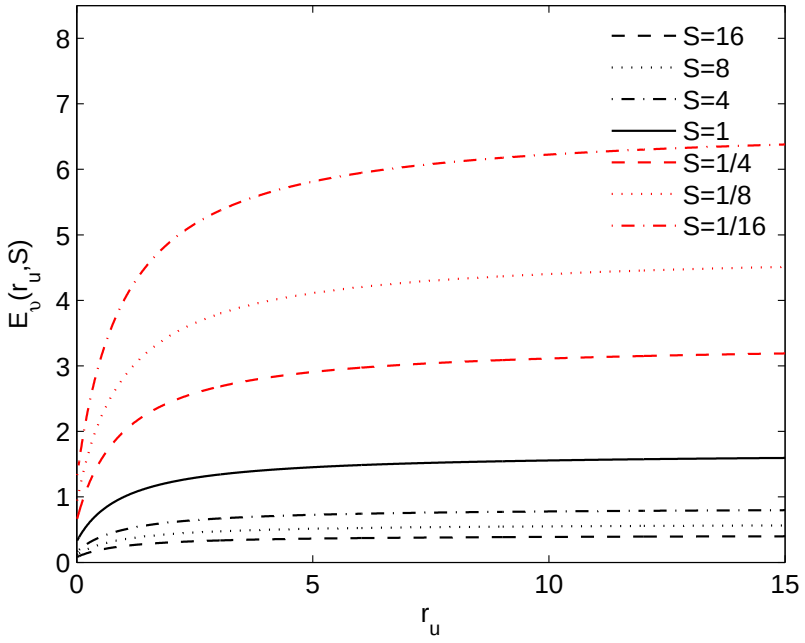

(a) Volume flux entrainment ratio

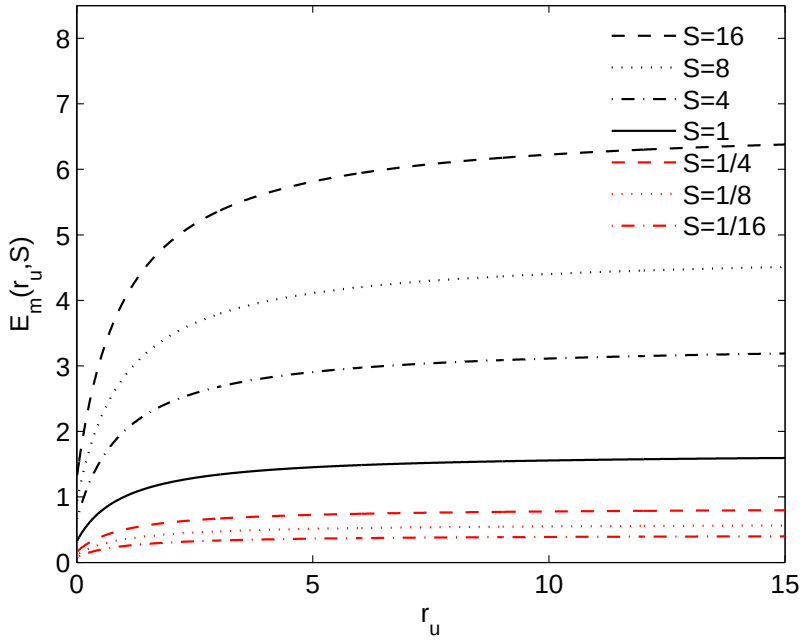

(b) Mass flux entrainment ratio

Figure 2.4: Planar shear layer (a) volume (Eq. 2.11) and (b) mass (Eq. 2.12) entrainment ratios as defined in the text. S = density ratio; r_u = velocity ratio

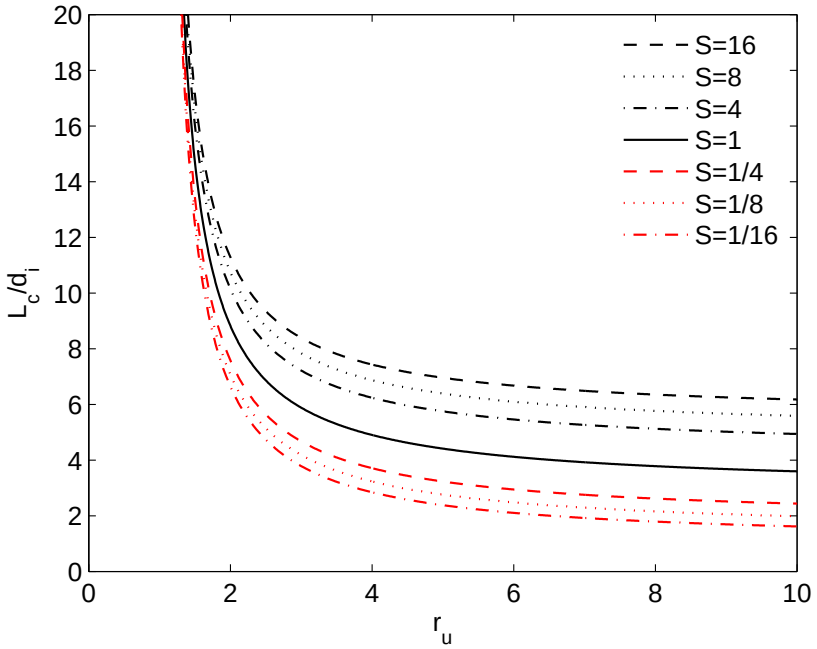

(a)

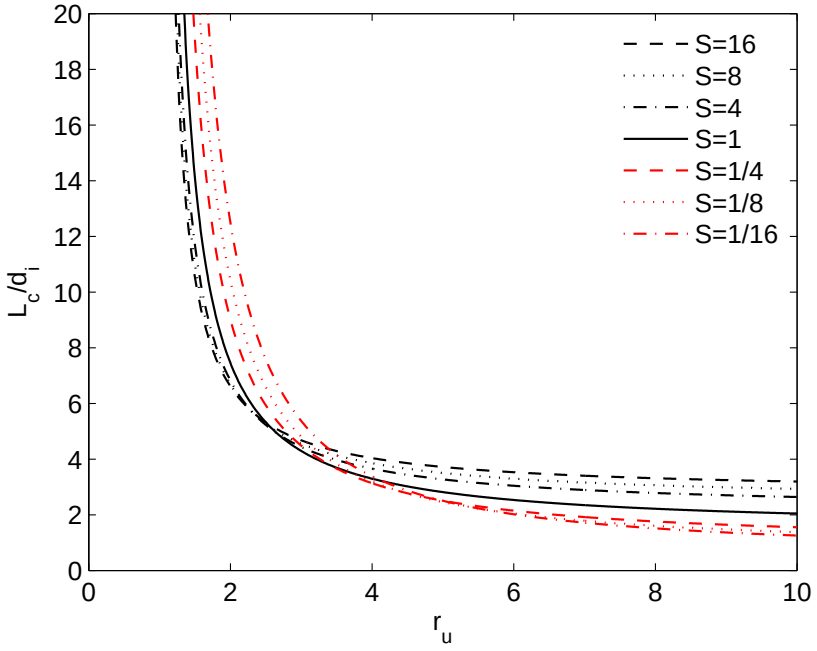

(b)

Figure 2.5: Potential core length as a function of r_u and S for (a) shear layer growth equally into both inner and outer fluid (Eq. 2.15), and (b) unequal shear layer growth (Eq. 2.18).

2.2 Modified Shear Layer Scaling

One of the assumptions that was stated in §2.1.1 to be questionable for coaxial jets is that coaxial jets are analogous to planar shear layers that have upper and lower free stream velocities that are constant in the downstream direction. In an attempt to correct for this assumption, Murakami and Papamoschou (2002) divided the inner potential core region into two parts: the first section being defined between the jet exit and the end of the outer potential core, and the second being between the end of the outer potential core and the end of the inner potential core. The first section, protected by the outer potential core, can be considered a coflowing jet with an outer velocity equal to the outer jet exit velocity, while in the second region the outer jet velocity is considered zero and the inner potential core grows like a single jet. The argument then states that the length of the potential core of a coaxial jet lies somewhere between the length of a single jet and the length of a coflowing jet. However, this argument can become problematic in cases where $r_u > 1$ since at large enough values of r_u the coflowing jet length can become shorter than the single jet. The method of Murakami and Papamoschou (2002) is described below with compressibility corrections ignored. A method then is outlined to account for the case of a coflowing core length that exceeds that of a single jet.

Using the planar shear layer growth equation (2.15) the length of the potential core of a single jet can be written as

$$\frac{L_{single}}{d_i} = \left[\epsilon\left(1+\sqrt{\frac{\rho_\infty}{\rho_i}}\right)\right]^{-1}, \tag{2.19}$$

where ρ_∞ is the density of the ambient fluid. For the case of an enclosed combustor this ambient fluid consists of products and any excess fuel or oxidizer. For a non-reacting fluid in a chamber, the ambient fluid is the result of the mixing of the two

injected fluids. Also note that Murakami and Papamoschou (2002) use an ϵ value of 0.14 while Dimotakis (1986) uses a value of 0.17. The actual value is likely somewhere in between and can be adjusted in this range to improve the correlation of the data. The second limit on the length of the coaxial jet potential core is that of a coflowing jet and is identical to the potential core length obtained using the equation for shear layer growth in §2.1 (Eq. 2.15). Murakami and Papamoschou (2002) take the last term in Eq. 2.15 to be negligibly small as S or r_u approaches 1. This is acceptable in their work since S and r_u are nearly unity, but inadvisable in the present study because both ratios are typically far from unity.

It is necessary to divide the potential core of the coaxial jet into two sections: one is upstream and the other is downstream of the end of the outer potential core. The outer potential core length is proportional to the average growth rates of the shear layers which surround it,

$$\frac{L_{out}}{H} \sim \left(\delta_{coflow} + \delta_{out}\right), \tag{2.20}$$

where H is the gap thickness $(d_e - (d_i + 2T_p))$, δ_{coflow} is the growth rate of the inner shear layer (Eq. 2.15), and δ_{out} is the growth rate of the outer shear layer. The growth rate of the outer shear layer is identical to Eq. 2.19 except ρ_i is replaced with ρ_e. L_{out} can now be written in terms of the coflowing potential core length L_{coflow},

$$\frac{L_{out}}{d_i} = \alpha \frac{H}{d_i}\left[\frac{L_{coflow}/d_i}{\delta_{out} L_{coflow}/d_i + 1}\right], \tag{2.21}$$

where α is a constant of proportionality reported by Murakami and Papamoschou (2002) to be 2.8, however a reprocessing of the results in their work of secondary core lengths by the author suggests α is 2.4 for $\epsilon = 0.14$.

Consider now the case for which the secondary potential core is longer than the inner potential core. The inner core would have a length of L_{coflow}. As the secondary

potential core becomes shorter, L_c will approaches L_{single}, hence L_c should lie between L_{single} and L_{coflow} depending on the value of L_{out}. The model suggested by Murakami and Papamoschou (2002) that meets these requirements is

$$L_c = L_{single} + \left[f\left(\beta L_{out}/L_{coflow}\right)\right]\left(L_{coflow} - L_{single}\right), \tag{2.22}$$

where β is a constant and f is a function that increases asymptotically from $f(0) \rightarrow 0$ to $f(\beta) \rightarrow 1$. A hyperbolic tangent meets this criteria so Eq. 2.22 becomes:

$$\frac{L_c}{d_i} = \frac{L_{single}}{d_i} + \tanh\left(\beta \frac{L_{out}}{L_{coflow}}\right)\left(\frac{L_{coflow} - L_{single}}{d_i}\right). \tag{2.23}$$

Murakami and Papamoschou (2002) suggest that $\beta = 2.8$, while a reprocessing of their data by the author suggests this is an error and that a value of 1.6 is correct.

For the case of $r_u >> 1$ the core length of the coflowing jet can actually become shorter than the core of a single jet. This reduction in core length is one reason coaxial jets are preferred over single jets to achieve rapid mixing. Of course for these conditions Eq. 2.23 is invalid. Figure 2.6*a* shows core lengths versus velocity ratio for core lengths calculated using the single jet formulation (Eq. 2.19), as represented by horizontal straight lines. The coflowing jet formulation is represented by the curved lines. From this plot it is clear that L_{coflow} becomes smaller than L_{single} at approximately $r_u > 3$ for $S < 1$. The simplest method to account for L_{coflow} becoming smaller than L_{single} is to reverse the limiting cases in Eq. 2.23,

$$\frac{L_c}{d_i} = \frac{L_{coflow}}{d_i} + \tanh\left(\beta \frac{L_{out}}{L_{single}}\right)\left(\frac{L_{single} - L_{coflow}}{d_i}\right). \tag{2.24}$$

It is not clear that for the case of $r_u > 1$ the use of L_{single} in Eq. 2.24 is accurate. When $r_u < 1$ the outer jet quickly decays after the end of the outer potential core, while for $r_u > 1$ a longer decay process takes place and the outer velocity might not be near zero by the time the outer potential core ends. It is likely that conditions

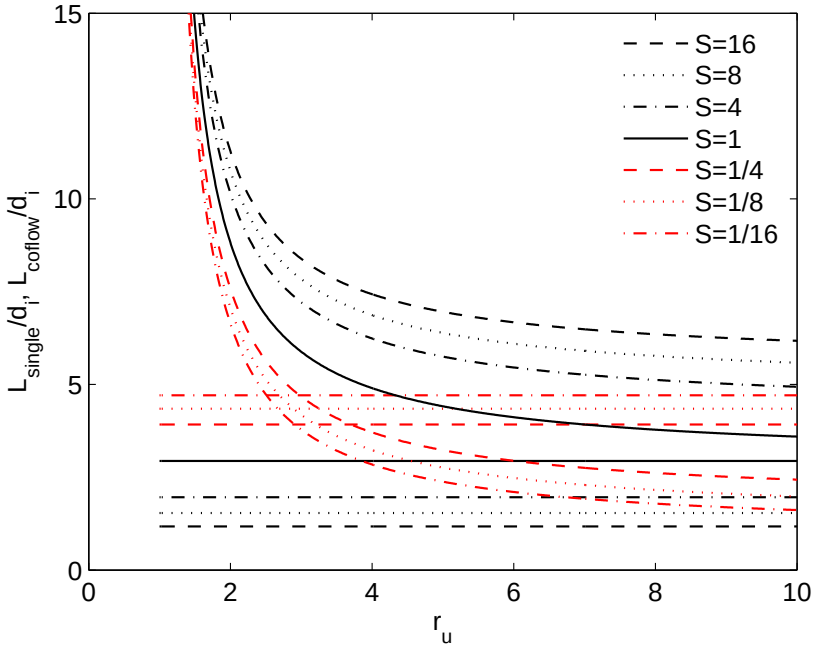

(a)

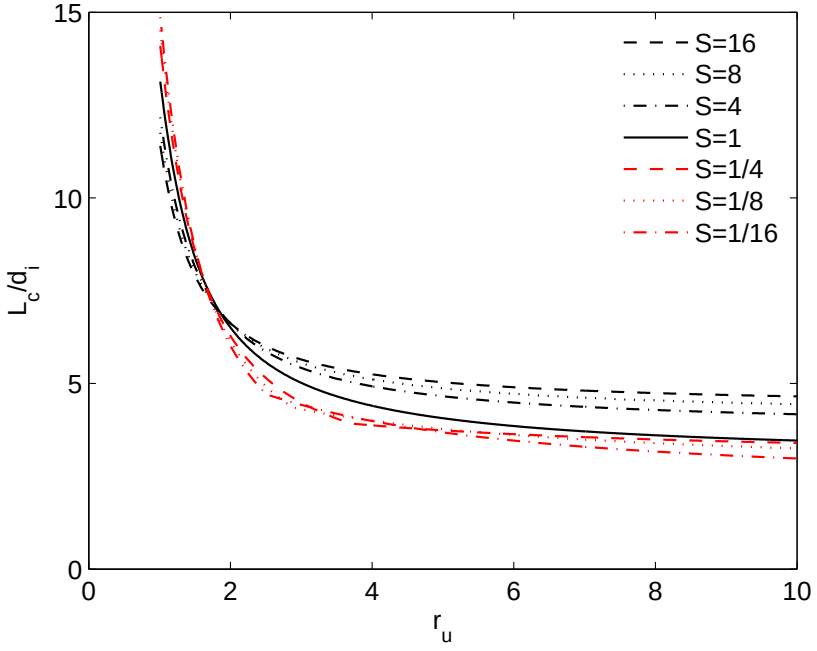

(b)

Figure 2.6: Jet lengths computed using the modified shear layer formulas of Murakami and Papamoschou (2002) for single and coflowing inner jets (a) and for core lengths (b). In (a) horizontal lines are for single jets while curved lines correspond to coflowing cases.

will occur for which the inner and outer velocity are nearly equal, however this will depend on the flow parameters H, r_u, S, and d_i. The largest core length is predicted to occur at $r_u = 1$, but this limit is unrealistic since shear layer theory predicts that the core length will approach infinity. However, for the case where H is small the outer jet decays quickly and this limit would be finite. Figure 2.6*b* shows that this method, which assumes that planar shear layer formulas apply to coaxial jets, fails to predict the trends caused by varying the density ratio that are measured for coaxial jets. So while this method does help to correct one of the poor assumptions any improvements in accuracy are expected to be minimal.

2.3 Momentum Flux Ratio Scaling

Another method to predict the stoichiometric mixing length (L_S) of nonreacting coaxial jets is based on a global mass entrainment argument (Villermaux and Rehab 2000). First consider the volume of the inner jet fluid that is contained in a cylinder as illustrated in Fig. 2.7. There is a constant entrainment velocity (u_{ee}) on the cylinder surface. The length of a cylinder required to entrain a stoichiometric amount of outer jet fluid is L_S. Therefore the ratio of the volume per second of inner jet fluid through the cylinder to the volume per second of fluid entrained across the cylindrical surface is

$$\left(\pi u_i (d_i/2)^2\right) / \left(\pi d_i L_S u_{ee}\right) = X_S, \tag{2.25}$$

where X_S is the mole fraction of inner jet fluid in a stoichiometric mixture. Data for variable density jets (Hill 1972 and Favre-Marinet and Camano-Schettini 2001) indicate that

$$u_{ee} \sim S^{1/2} u', \tag{2.26}$$

where u' is a turbulent velocity fluctuation.

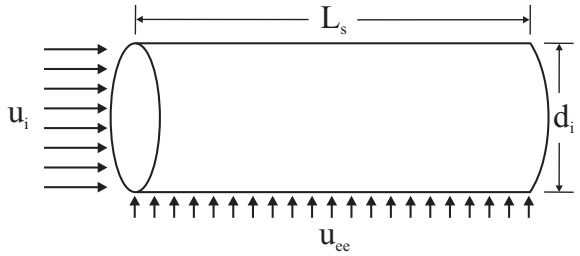

Figure 2.7: Stoichiometric contour of a coaxial jet that is modeled as a cylinder with a constant entrainment velocity (u_{ee}) on the surface.

For the case of $r_u >> 1$, previous studies show that the turbulence level at the inner jet boundary is controlled by the outer jet velocity, hence $u' \sim u_e$ (Dahm et al. 1992 and Villermaux and Rehab 2000). Inserting Eq. 2.25 into Eq. 2.26 and solving for L_S yields the fundamental scaling relation:

$$\frac{L_S}{d_i} = C_1 \left(M^{1/2} X_S\right)^{-1}, \tag{2.27}$$

where C_1 is a scaling constant and M is the momentum flux ratio. The work of Davis et al. (2006), includes a review of all potential core lengths in single phase coaxial jets that are reported in the literature. His work indicates that $C_1 = 5$. It will be shown in Chapter V that a better fit to the data can be obtained if a constant vertical offset C_2 is added to Eq. 2.27. The momentum flux scaling can then be written as

$$\frac{L_S}{d_i} = C_1 \left(M^{1/2} X_S\right)^{-1} + C_2. \tag{2.28}$$

Unfortunately the constant C_2 is likely not universal but a weak function of the inlet velocity profiles and the shape of the injector post. It is noted that X_S is related to the stoichiometric mixture fraction (f_S) by

$$X_S = \left(\frac{MW_i}{MW_e}\left(f_S^{-1} - 1\right) + 1\right)^{-1}. \tag{2.29}$$

2.3.1 Momentum Flux Ratio Applicability

The momentum flux ratio scaling obtained in Eq. 2.27 has a number of advantages over the shear layer methods discussed in § 2.1 and 2.2. As shown in Fig. 2.8, the momentum flux scaling correctly predicts the general density ratio trend reported in the literature, core length decreases as S is increased for $r_u > 1$. Experimental data is presented in §5.2 that agrees with this model. An additional advantage is that the core length does not approach infinity as r_u approaches one which is the nonphysical prediction of shear layer models. This method provides a simple way to study the mixing downstream of the potential core whereas the shear layer methods require additional terms to account for the distance between the end of the potential core and the location where stoichiometric conditions occur.

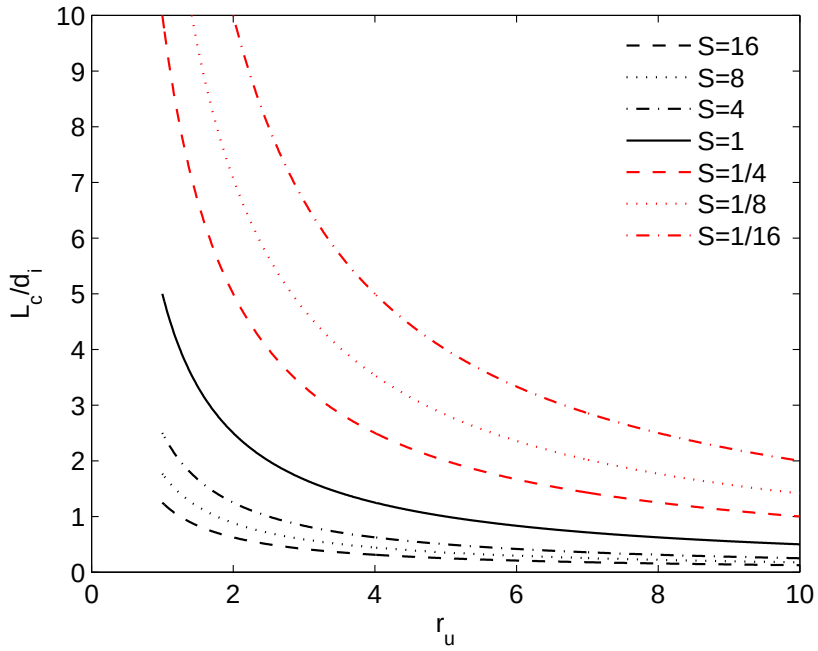

Figure 2.8: Normalized potential core length versus velocity ratio (r_u) for varying density ratio (S) using the momentum flux ratio scaling (Eq. 2.27) with $C_1 = 5$ from the work of Davis et al. (2006) and $C_2 = 0$.

2.4 Far Field Scaling

In most turbulent shear flows, far field scaling arguments are used to predict the growth rate of the outer length scale and the centerline decay of velocity and conserved scalar. However, a number of assumptions in the far field analyses are not valid in the near field of a coaxial injector. All far field analysis are based on at least two of the following assumptions. First, the flow of interest is sufficiently far from the source that any details of the source are not relevant and only integral quantities such as the jet momentum are relevant. Second, velocity and conserved scalar profiles are self-similar, hence when they are plotted against the proper variables the profiles collapse to a single curve. Lastly, in the far field enough ambient fluid has been entrained such that the density in the shear flow is approximately equal to the ambient density.

In the context of coaxial jets there are two far field scalings that warrant consideration. The first is the scaling of a simple jet and the second is the scaling of a coflowing jet. At some point downstream any coaxial jet will achieve the far field scaling of a simple jet. The jet width will grow linearly with downstream distance and the centerline velocity will decrease with the inverse of downstream distance, as was first proposed by Thring and Newby (1953) and later was experimentally verified by Ricou and Spalding (1961) for variable density turbulent jets. However, due to the assumptions discussed above, at a location where this scaling is achieved the inlet velocity values and density values are no longer the relevant parameters. For far field scaling to be valid, the density field has to be uniform and equal to the ambient value. In short, the two separate streams are already completely mixed by the time far field scaling is reached and further mixing occurs only with the ambient

fluid. Before far field scaling is achieved, velocity and mixture fraction profiles are not self-similar due to the bimodal nature caused by the two streams. They only become self-similar after they fully mix. Hence the far field scaling is not a valid method to obtain the mixing length of the present coaxial jets because all three assumptions listed above are invalid and therefore far field scaling will not be explored further in this work.

2.5 Comparison of Mixing Models

To obtain an understanding of how the different mixing models for nonreacting coaxial jets relate to each other, potential core lengths for three models are plotted for two density ratios ($S = 1$ and $1/8$) in Fig. 2.9. The three models are called "uneven shear" (Eq. 2.18), "modified shear" (Eq. 2.24), and "momentum flux" (Eq. 2.24). From Fig. 2.9 it is clear that at large r_u values all models asymptotically approach a constant value, but at small values of r_u their dependance on S differs. The uneven shear and modified shear models both have a trend that is opposite to the measured trend as S is varied. The measured trend is for L_c to decrease as the density ratio (S) increases. The momentum flux model has the correct trend as S is varied and predicts a finite mixing length at $r_u = 1$ which is reasonable. The final test of these models with experimental data is described in §5.2.

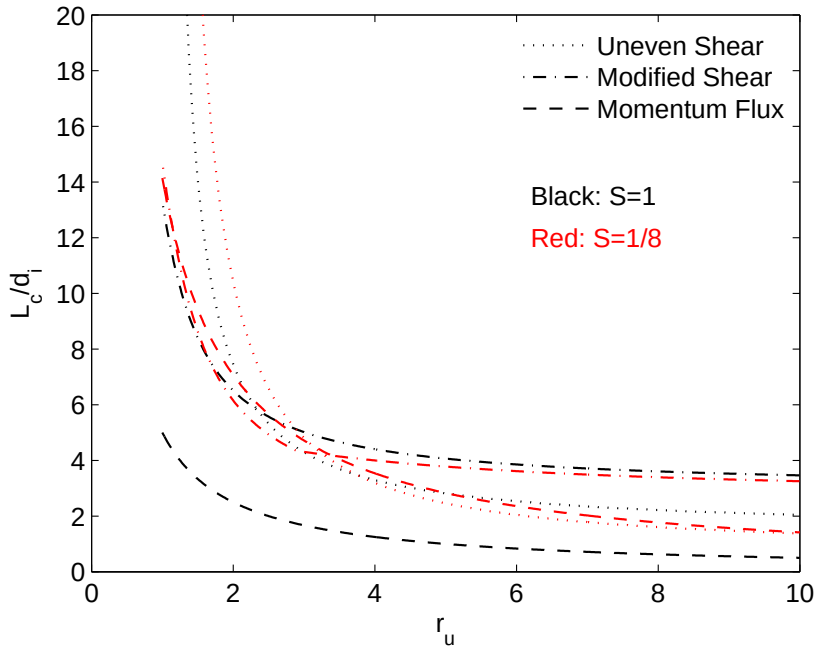

Figure 2.9: Predicted length of the potential core versus velocity ratio (r_u) for density ratios $S = 1$ and $S = 1/8$ for three nonreacting mixing models; uneven shear (Eq. 2.18), modified shear (Eq. 2.24), and momentum flux (Eq. 2.27).

CHAPTER III

Model for Reacting Coaxial Jet Flame Length

To relate reacting and nonreacting flows, the effects of heat release must be considered. Previous studies demonstrated that heat release effects dramatically alter flow structures and hence mixing and entrainment properties even in the absence of buoyancy effects (Clemens and Paul 1995). This idea has led some to conclude that reacting and nonreacting flows are fundamentally different and cannot be compared (Beer and Chigier 1983). However, due to the additional expense and complexity of both experimental and computational combustion studies compared to nonreacting studies, simple methods to fundamentally relate the two are still an area of active research (e.g., Tacina and Dahm 2000, Dahm 2005, Muniz and Mungal 2001, Han and Mungal 2001).

One of the major objectives of this study is to obtain a physical model that can accurately predict the flame length of coaxial-jet diffusion flames for a variety of fuel/oxidizer combinations and hence heat release rates. Flame lengths, like many other flow properties such as heat release distributions and induced flow fields, are determined by entrainment and mixing rates and consequently a model that takes into account heat release effects on these properties is needed. If turbulent shear

flows are considered, of which coaxial jets are a subset, and with the assumption that the heat release does not cause the flow to become transitional or laminar, then the conservation of mass and momentum indicate there are four main effects which must be considered:

(i) inertial effects caused by changes in the density field,

(ii) body force effects such as buoyancy,

(iii) diffusive effects caused by changes in the viscosity field,

(iv) dilatation effects caused by the divergence of the velocity field caused by changes in the density field.

In this chapter the previous theoretical concepts of Tacina and Dahm (2000) and Dahm (2005) are described, which attempts to account for heat release effects related to the density field. In the coaxial jets studied in this work, changes in the density field are argued to be the dominant effect. In addition, theoretical methods are used to show that the effects of buoyancy are small in all cases considered in this study. Diffusive effects also are briefly discussed. Inertial effects of heat release related to the density field are accounted for by utilizing the "general equivalence principle" of Tacina and Dahm (2000) which relates the reacting flow field to that of the simple mixing of two nonreacting fluids. The equivalence principle has previously been shown to accurately predict the effects of heat release in turbulent planar and axisymmetric simple jets in both the near and far field and in turbulent reacting shear layers, but not in turbulent coaxial jet flames. In the prior works of Tacina and Dahm (2000) and Dahm (2005), the application of the equivalence principle has been limited to cases where the equilibrium temperature state relation is essentially linear and has

not been applied to cases where dissociation effects are substantial such as in oxygen enriched combustion. In §3.1 the equivalence principle is outlined for coaxial jets. An extension of this method is proposed where the effective outer fluid density $(\rho_e)_{eff}$ is calculated directly from the inner fluid equilibrium density field which accounts for heat release in flows with non-piecewise linear equilibrium state relations. Consistent with the experiments performed in this study, three fuel/oxidizer combinations are considered; H_2 / O_2, H_2 / air, and CH_4 / O_2.

3.1 Density Effects Due to Heat Release

In the absence of buoyancy and assuming that the Reynolds number is large enough so that the reacting flow stays fully turbulent, then reductions in the inertia of the flow due to the density changes will be the largest effect of heat release. In a coaxial jet this reduction in the density field leads to a decrease in the mass entrainment and accordingly an increased stoichiometric mixing length compared to the nonreacting case. This density change due to heat release can in concept be quantitatively accounted for by the "general equivalence principle" of Tacina and Dahm (2000). In this section the equivalence principle is applied to explain the difference between the stoichiometric mixing lengths of reacting and nonreacting coaxial jets.

In turbulent shear flows, entrainment, mixing properties and scaling laws are primarily determined by mass and momentum conservation. Consequently, if the profile of momentum flux density $(\rho * u)$ of a nonreacting flow is made to match as close as possible the profile from a reacting flow then both flows will have the same entrainment and mixing properties and therefore the same scaling laws. The concept

behind the general equivalence principle of Tacina and Dahm (2000) is that setting the density of one of the jet fluids in a coaxial jet to some equivalent density will result in a nonreacting jet that has mixing properties similar to that of a reacting jet. The general equivalence principle then reduces the problem to determining the proper equivalent density that best matches the density profile of the reacting case over the portion of the flow where $\rho * u$ is largest. The equivalence principle matches the density profile by making use of the piecewise linear form of the equilibrium state relations with respect to propellent mole fraction and equating the reacting density field to that of the simple nonreacting mixing between two fluids at different temperatures and densities.

Consider the simple mixing of two fluids (i and e) and assume the fluids are calorically perfect, then the conservation of enthalpy states that temperature field is everywhere related to the propellent mole fraction. Any nonlinearity in this relation is due to the difference in molar specific heats of the fluids (Fig. 3.1a). Whereas mass specific heat differences are usually large, molar specific heat differences are typically small and this relation in most situations is essentially linear. If a typical exothermic reaction is considered, for which the activation energies are large enough such that the reaction is significant only for conditions that are nearly stoichiometric, then the equilibrium temperature state relation will be piecewise linear (Fig. 3.1b). Each linear side of the temperature state relation can then be viewed as the result of the simple mixing between the appropriate actual fluid and a new "effective" fluid. In Fig. 3.1b, the equilibrium temperature state relation for $X > X_S$ is the result of the mixing between two fluids at T_i and $(T_e)_{eff}$. In a similar manner the second part of the state relation $X < X_S$ can be viewed as the result of the mixing between two fluids at T_e and $(T_i)_{eff}$. This same method can be applied to

the equilibrium molecular weight state relation to obtain $(MW_e)_{eff}$ and $(MW_i)_{eff}$. The effective density values can then be obtained from the effective temperature and molecular weight values by applying the ideal gas law. Note that unlike the aforementioned work on the equivalence principle in simple jets and shear layers (Tacina and Dahm 2000, Dahm 2005), in the present study the effective molecular weight ratio contribution to $(\rho_e)_{eff}/\rho_e$ is significant. The final question is which side of the equilibrium state relations (i.e. the rich side or the lean side) should be approximated using this procedure.

3.1.1 Choice of Effective Fluid

The underlining theory of the equivalence principle of Tacina and Dahm (2000) is that the $\rho * u$ profile in the hypothetical nonreacting jet needs to be matched as closely as possible to the actual $\rho * u$ profile in the reacting jet by changing the fluid density of either the inner or outer jet of the hypothetical nonreacting case. In simple jets if the scaling upstream of the flame tip ($X_i > X_S$) is of interest, then the density profile of the jet fluid must be altered since the velocity is highest in this region and this is where the inertial effects of heat release are most important. For this situation the ambient fluid is the effective fluid. Downstream of the flame tip, X_i is always less then X_S and hence all of the momentum and inertial effects are related to the ambient fluid and the effective fluid is the jet fluid. Since most turbulent shear flow scaling laws have a density ratio dependence, it is clear that the choice of effective fluid can have a profound impact. Switching the effective fluid typically produces the opposite effect of heat release. For example, in simple jets the equivalence principle predicts a decrease in the centerline velocity decay below the flame tip in reacting jets compared to nonreacting jets. Above the flame tip the

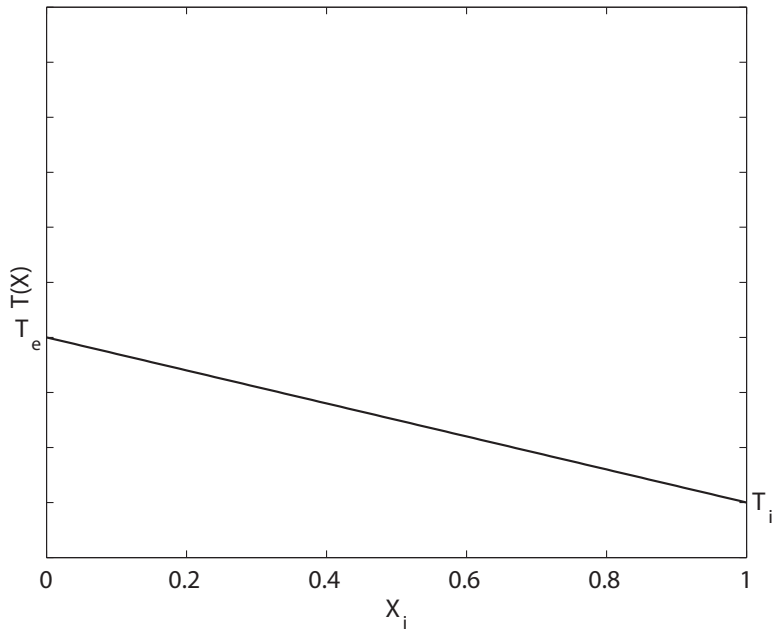

(a)

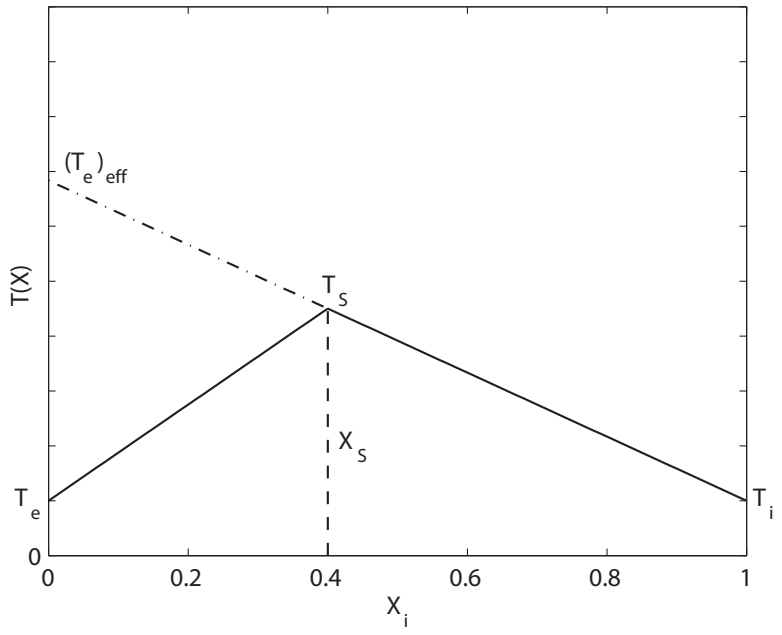

(b)

Figure 3.1: Schematic diagram of the equilibrium temperature state relation for the mixing of two nonreacting fluids at different temperatures T_e and T_i (a) and two reacting fluids at temperatures T_e and T_i (b). $(\rho_e)_{eff}/\rho_e$ is the effective density ratio calculated using the general equivalence principle of Tacina and Dahm (2000). X_i is the mole fraction of the inner jet fluid.

equivalence principle predicts an increase in centerline velocity decay in the reacting jet compared to the nonreacting jet. Consequently this method is likely to perform poorly when the total momentum flux density is evenly divided between the rich and lean conditions. This occurs near the flame tip in a simple jet (Tacina and Dahm 2000) and in shear layers when the combination of density ratio, velocity ratio, and X_S produce equal momentum flux density on the rich and lean side of the shear layer (Dahm 2005).

In coaxial jets, either the density of the outer jet (ρ_e) or that of the inner jet (ρ_i) of the hypothetical nonreacting case must be adjusted to match the momentum flux density profile of the reacting case as nearly as possible. As for the case of the simple jet, selecting either the inner jet or the outer jet fluid as the effective fluid will have different effects on the stoichiometric mixing length. For the values r_u and S investigated here ($r_u > 1$ and $S < 1$), selecting the outer jet as the effective fluid results in a longer mixing length, while selecting the inner jet as the effective fluid results in a shorter mixing length, as compared to the nonreacting case. Results in Chapter VI will show that for all cases examined in this work, the stoichiometric mixing length in reacting jets is observed to be larger than that of their nonreacting counterparts. Therefore, it is assumed that the inner jet is the main contributor to the $\rho * u$ profile of interest so the outer jet fluid should be selected to be the effective fluid.

3.1.2 Application to Coaxial Jets

Based on the above argument, it was decided to investigate whether the actual mixing in the reacting coaxial jets could be represented by the mixing in a hypothetical nonreacting coaxial jet having an outer jet fluid at an effective density $(\rho_e)_{eff}$.

If it is assumed that the state relation between temperature and the mole fraction of inner fluid (X_i) is piecewise linear, then the effective temperature of the outer jet fluid is given by Tacina and Dahm (2000) to be

$$(T_e)_{eff} = T_i + \frac{T_S - T_i}{1 - X_s}, \tag{3.1}$$

as graphically illustrated in Fig. 3.1*b*. Similarly the outer effective fluid molecular weight is given by

$$(MW_e)_{eff} = MW_i + \frac{MW_S - MW_i}{1 - X_s}. \tag{3.2}$$

This method to calculate $(T_e)_{eff}$ and $(MW_e)_{eff}$ will be referred to as method 1. To apply the equivalence principle the effective density of the outer fluid $(\rho_e)_{eff}$ is obtained from the perfect gas law

$$\frac{(\rho_e)_{eff}}{\rho_e} = \left(\frac{T_e}{(T_e)_{eff}}\right)\left(\frac{(MW_e)_{eff}}{MW_e}\right). \tag{3.3}$$

This method of calculating $(\rho_e)_{eff}/\rho_e$ is accurate only if the temperature and molecular weight equilibrium state relations are piecewise linear. However, realistic equilibrium state relations are affected by dissociation that leads to nonlinear state relations. This is especially true for the case of oxygen enriched combustion. Method 1 contains large errors in these situations and a better method is to calculate the effective fluid density $(\rho_e)_{eff}$ based on the average slope of the inner jet profiles of T and MW far from the stoichiometric value. Following Tacina and Dahm (2000), in such cases it is appropriate to define T_S in Eq. 3.1 as

$$T_S = T_i + \left\langle -\frac{dT}{dX_i}\bigg|_{X_i \gg X_S} \right\rangle (1 - X_S), \tag{3.4}$$

and MW_S in Eq. 3.2 as

$$MW_S = MW_i + \left\langle -\frac{dMW}{dX}\bigg|_{MW \gg MW_S} \right\rangle (1 - X_S). \tag{3.5}$$

This method to calculate $(T_e)_{eff}$ and $(MW_e)_{eff}$ will be referred to as method 2. As will be shown in §3.1.3, this method also does not guarantee that the inner fluid density profiles of the hypothetical nonreacting case and the actual reacting case will be accurately matched because the slopes dT/dX_i and dMW/dX_i in Eqs. 3.4 and 3.5 are approximate curvefits to the nonlinear state relations and not the density relation.

An additional method to obtain $(\rho_e)_{eff}$ is to ignore the individual equilibrium temperature and molecular weight state relations and use a best fit procedure, such as least squares, to solve for $(T_e)_{eff}$ and $(MW_e)_{eff}$ directly from the equilibrium state relation for gas density (ρ) versus X_i. A suitable linear fitting function is found to be given by

$$\rho(X)|_{X>X_S} = \frac{P_C\left[((MW_e)_{eff} - MW_i)(1-X) + MW_i\right]}{R_u\left[((T_e)_{eff} - T_i)(1-X) + T_i\right]}, \tag{3.6}$$

where P_C is the chamber pressure and R_u the universal gas constant. This method, referred to as method 3, provides the best agreement between the inner fluid density profiles of the nonreacting hypothetical jet and the reacting actual jet. However, it does not give the best agreement for the temperature and molecular weight profiles. In the case of perfectly piecewise linear equilibrium state relations for temperature and molecular weight all three methods will produce identical values of $(\rho_e)_{eff}/\rho_e$. However, for cases of nonlinear relations, very different values are obtained.

To apply the equivalence principle to the general scaling law for mixing length, a new effective momentum flux ratio, (M_{eff}) is defined as:

$$M_{eff} = M[(\rho_e)_{eff}/\rho_e]. \tag{3.7}$$

Inserting this new momentum flux ratio into the cold flow momentum flux ratio scaling law (Eqn. 2.28) results in a modified scaling law which is valid for reacting

coaxial jets, namely

$$\frac{L_S}{d_i} = C_1 \left(M_{eff}^{1/2} X_S \right)^{-1} + C_2. \tag{3.8}$$

Note that for a nonreacting jet $M_{eff} = M$.

3.1.3 Actual Effective Density Ratios

The three fuel/oxidizer combinations considered in this work produce different values of $(\rho_e)_{eff}/\rho_e$ due to differences in their chemistry. The effective density ratio also is a function of chamber pressure. As pressure increases, the degree of dissociation decreases. The decrease in dissociation causes the equilibrium state relations to become more linear compared to the lower pressure relations. This also causes T_S to increase. This effect is shown for the three chamber pressures studied for H_2 / O_2 turbulent coaxial jet flames in Fig. 3.2. While the molecular weight ratio only varies slightly over the pressure range from 0.98 to 8.49 atm, the increase in T_S is 9%. In addition the large amount of nonlinearity in the equilibrium temperature state relation (Fig. 3.2*a*) is clearly visible. The relation becomes more linear as pressure increases. All state relations were calculated using the chemical equilibrium code CEA (McBride and Gordon 1996), however the equilibrium code in Chemkin (Kee et al. 2006) with the GRI-Mech chemical mechanism set was found to produce nearly identical results in all cases.

The effective density ratio of the outer fluid was obtained from the equilibrium state relations for the five reacting data groups listed in Table 4.5. Values of $(\rho_e)_{eff}/\rho_e$ were calculated using all three methods described in the last section. The inner jet density profile then was obtained using $(\rho_e)_{eff}/\rho_e$ for all three methods and compared to the density relation obtained from equilibrium chemistry. The closer the inner jet density profile obtained using the equivalence principle matches

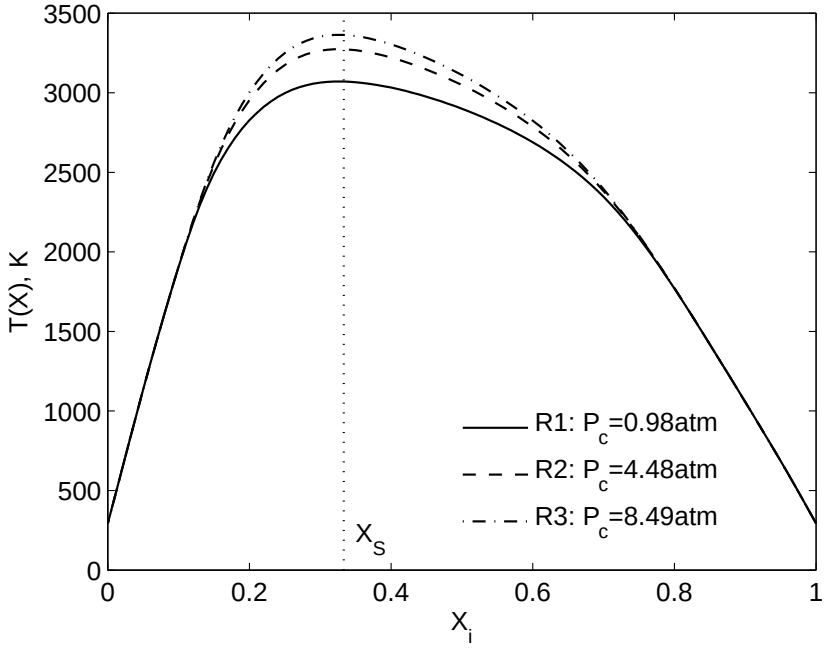

(a)

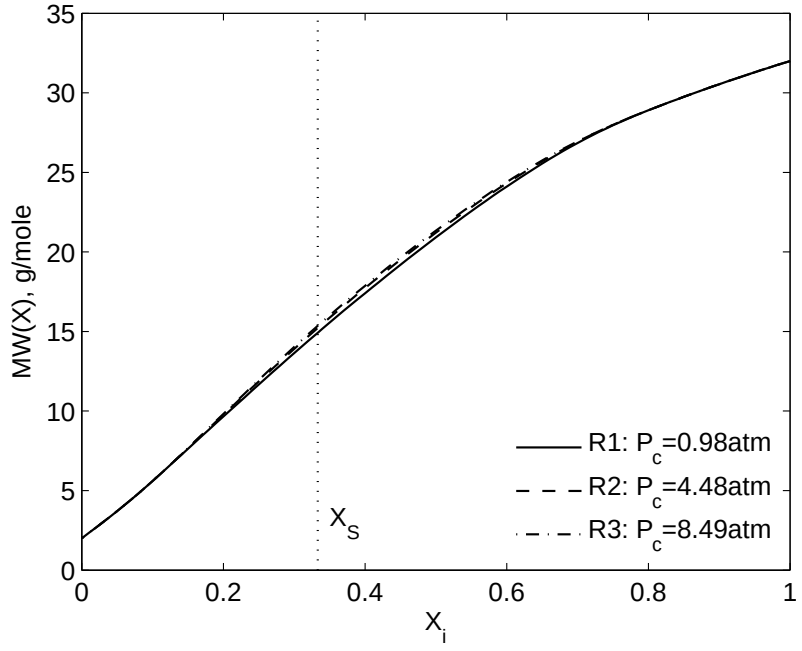

(b)

Figure 3.2: Effect of pressure on equilibrium H_2 / O_2 chemistry for the temperature vs. inner fluid (oxidizer) mole fraction profile (a) and molecular weight vs. inner fluid mole fraction profile. The stoichiometric mole fraction is 1/3. Computed using CEA chemical equilibrium code (McBride and Gordon 1996).

the one from equilibrium chemistry the better the method should account for heat release.

Figure 3.3 shows the equilibrium state relations for H_2 / O_2 at a chamber pressure of 4.5 atm. Note that due to the minimal change in the equilibrium state relations due to pressure this figure is also representative of the results obtained for chamber pressures of 0.98 and 8.49 atm. Due to the large curvature of the temperature relation method 1 greatly under predicts the temperature and molecular weight profiles (Figs. 3.3*a*-*b*) over the inner fluid mole fractions ($X > X_S$) and hence over predicts the equilibrium density profile over this range (Fig. 3.3*c*). Overpredicting the density profile should result in the effect of heat release being under predicted. Method 2 does better, but still underpredicts the molecular weight profile and underpredicts the density profile which should lead to over correcting for heat release effects. Method 3 overpredicts both the temperature and molecular weight profiles, but reproduces the inner fluid side density profile almost exactly and accordingly should take into account the effect of heat release the most accurately of the three methods.

Figure 3.4 shows the equilibrium state relations for H_2 / air at a chamber pressure of 4.8 atm. Unlike the H_2 / O_2 case, the temperature and molecular weight relations are nearly piecewise linear. However, some nonlinearity is still present for X_i values near X_S. Since the case is nearly piecewise linear, method 1 and 2 produce nearly identical results. Method 3, however, produces a very different effective molecular weight ratio which is counteracted by a slight increase in effective temperature ratio. Figure 3.4*c* shows that all three methods approximate the inner jet density profile reasonably well, but again method 3 produces the closest approximation.

Figure 3.4 shows the equilibrium state relations for CH_4 / O_2 at a chamber pressure of 5.3 atm. Like the H_2 / O_2 case, a large amount of nonlinearity is seen in the

temperature and molecular weight equilibrium state relations. In addition a kink is seen in the temperature equilibrium state relation, which is caused by the formation of carbon on the fuel rich side of the profile. Due to these issues the simple mixing assumption of the equivalence principle is severely tested. As would be expected method 1 and method 2 do a better job then assuming $\rho(X_i) = \rho_i$. However, significant differences exist between these methods and the equilibrium inner fluid density profile. Even with the large nonlinearities, method 3 is able to do an excellent job of approximating the inner density profile.

The effective ratios calculated for all reacting data groups using the three methods are provided in Table 3.1. The ability of the equivalence principle using the three different methods to calculate $(\rho_e)_{eff}/\rho_e$ is assessed against experimental flame lengths in Chapter VI.

3.1.4 Limitations of the Equivalence Principle

The equivalence principle of only takes into account heat release effects that act on the flow properties through the density field. As noted by Tacina and Dahm (2000), method can fail when the assumptions on which it is based are violated. When buoyancy effects become important, the equivalence principle is expected to fail. However, it will be argued in §3.2 that in the current study these effects are small and can be ignored.

An additional effect of heat release is to change the molecular transport properties such as the viscosity and diffusivities (Tacina and Dahm 2000). These can result in a reduction in the Reynolds number which may result in the flow becoming transitional or even laminar. However, if the Reynolds number is large enough that the flow remains fully turbulent then these properties only affect the smallest turbulent, the

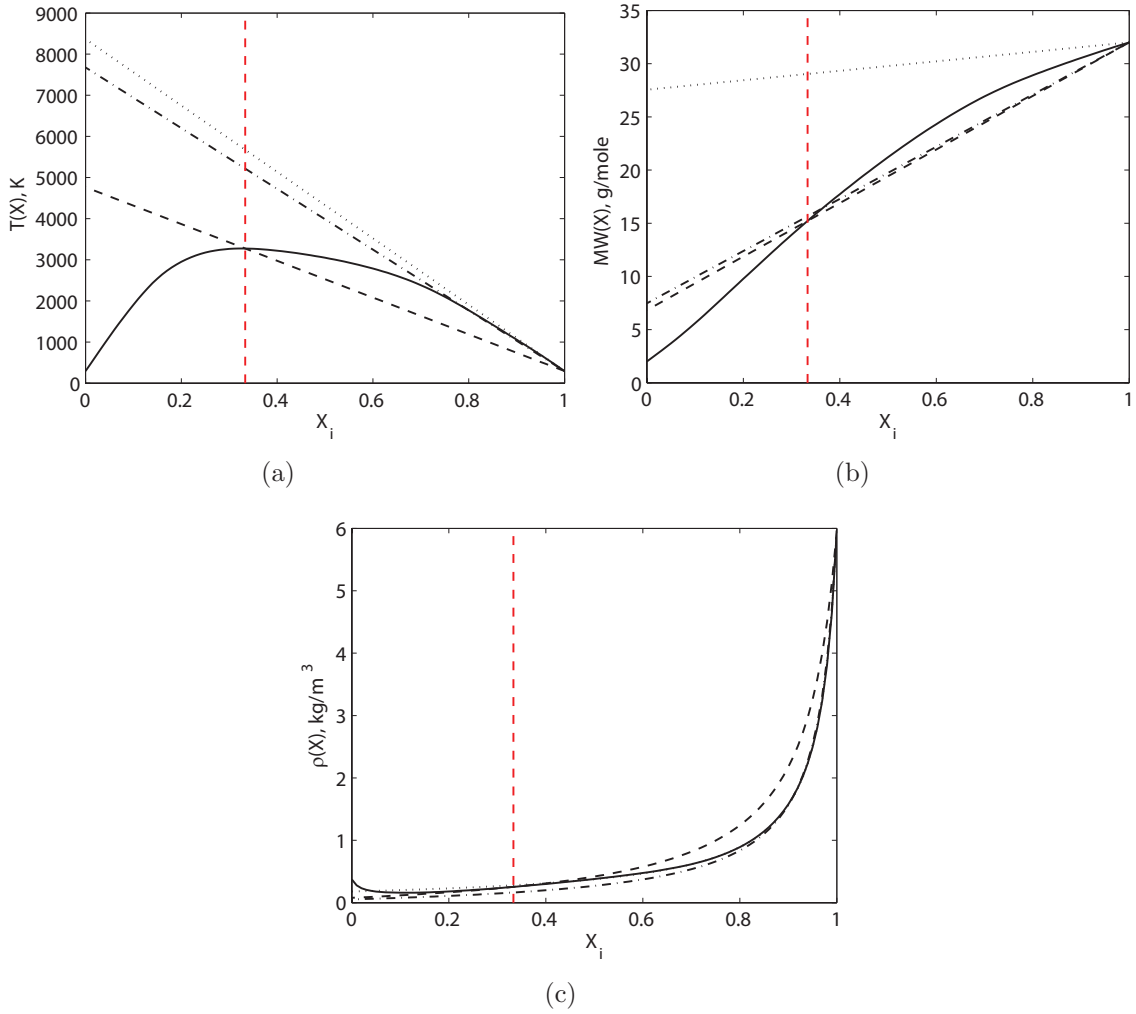

Figure 3.3: Equilibrium state relations (temperature (a), molecular weight (b) and density (c)) for H_2 / O_2 at $P_c = 4.5$ atm (R2). Solid line is calculated from equilibrium chemistry while broken non-vertical lines are calculated from the equivalence principle using methods 1 (- - - -), 2 ($- \cdot - \cdot$) and 3 ($\cdot \cdot \cdot \cdot$). Mole fraction is defined based on the inner jet fluid and hence the intersection of the broken lines with the $X_i = 0$ side of the plot correspond to the effective properties of the outer fluid calculated using the different methods; $(T_e)_{eff}$, $(MW_e)_{eff}$, and $(\rho_e)_{eff}$. The vertical line marks the stoichiometric mole fraction $X_S = 0.33$.

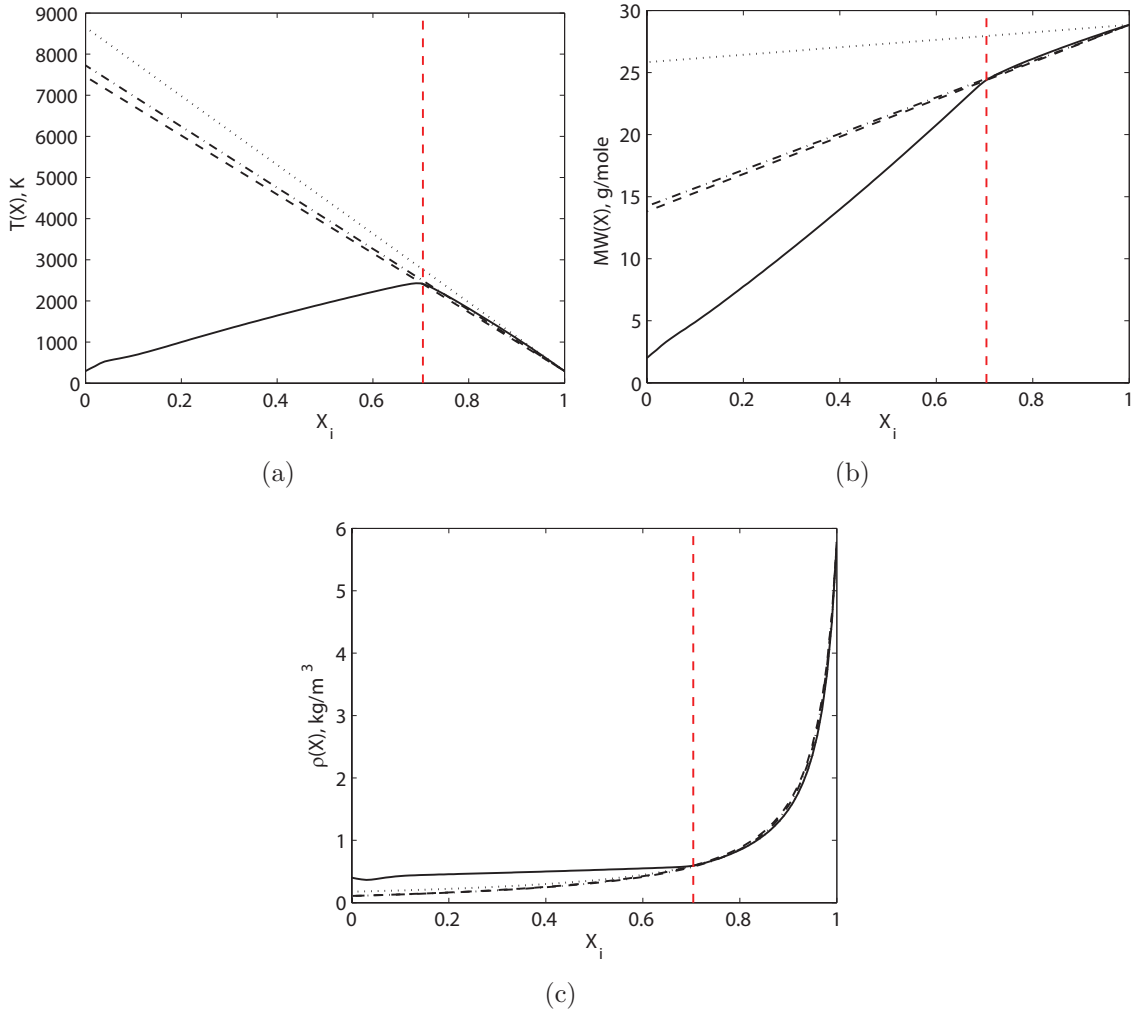

Figure 3.4: Equilibrium state relations (temperature (a), molecular weight (b) and density (c)) for H_2 / air at $P_c = 4.8$ atm (R4). Solid line is calculated from equilibrium chemistry while broken non-vertical lines are calculated from the equivalence principle using methods 1 (- - - -), 2 ($- \cdot - \cdot$) and 3 ($\cdot \cdot \cdot \cdot$). Mole fraction is defined based on the inner jet fluid and hence the intersection of the broken lines with the $X_i = 0$ side of the plot correspond to the effective properties of the outer fluid calculated using the different methods; $(T_e)_{eff}$, $(MW_e)_{eff}$, and $(\rho_e)_{eff}$. The vertical line marks the stoichiometric mole fraction $X_S = 0.71$.

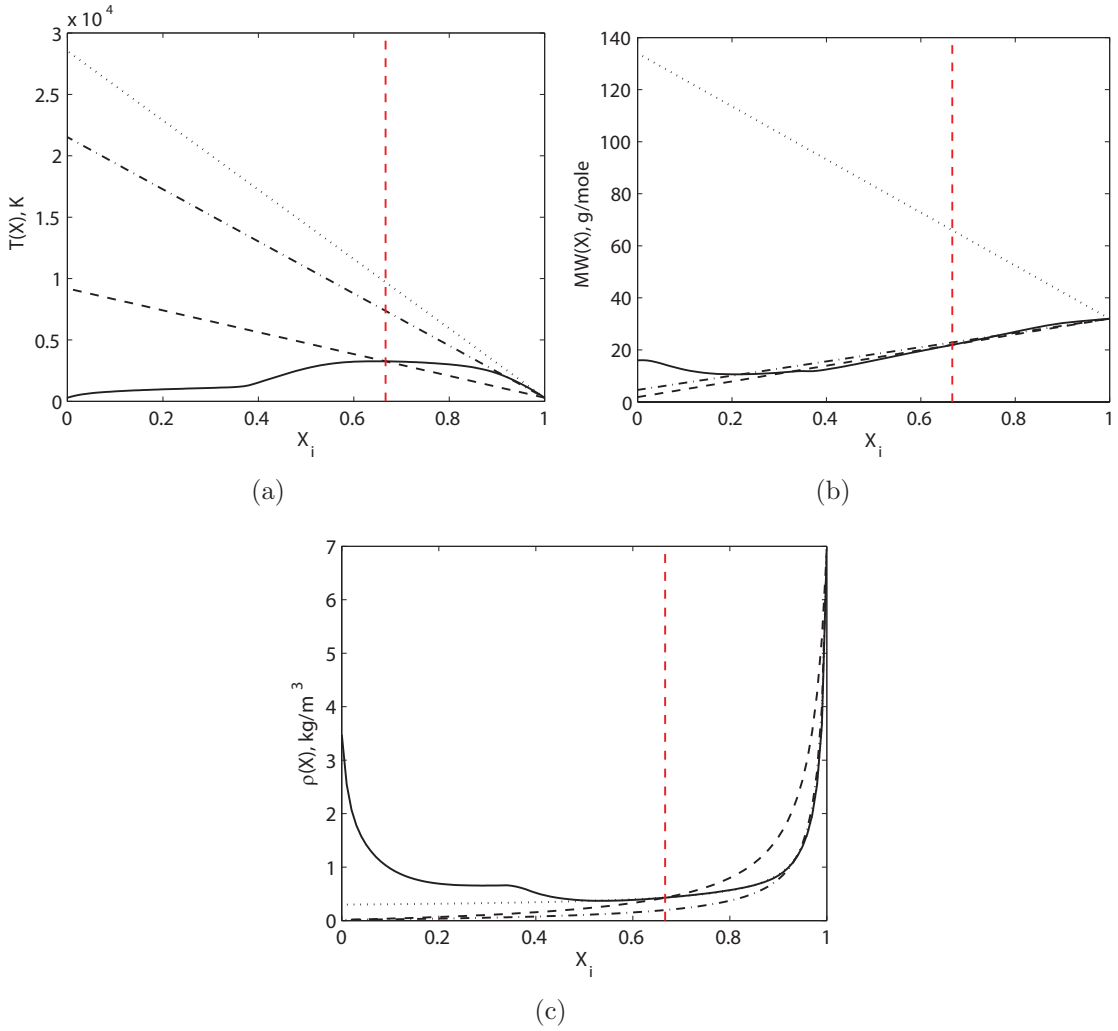

Figure 3.5: Equilibrium state relations (temperature (a), molecular weight (b) and density (c)) for CH_4 / O_2 at $P_c = 5.2$ atm (R2). Solid line is calculated from equilibrium chemistry while broken non-vertical lines are calculated from the equivalence principle using methods 1 (- - - -), 2 ($- \cdot - \cdot$) and 3 ($\cdot \cdot \cdot \cdot$). Mole fraction is defined based on the inner jet fluid and hence the intersection of the broken lines with the $X_i = 0$ side of the plot correspond to the effective properties of the outer fluid calculated using the different methods; $(T_e)_{eff}$, $(MW_e)_{eff}$, and $(\rho_e)_{eff}$. The vertical line marks the stoichiometric mole fraction $X_S = 0.67$.

Table 3.1: Outer fluid effective temperature, molecular weight, and density ratios calculated using the general equivalence method of Tacina and Dahm (2000) and the three methods outlined in the text.

				$(T_e)_{eff}/T_e$			$(MW_e)_{eff}/MW_e$			$(\rho_e)_{eff}/\rho_e$		
Group	P_c, atm	Fluids	X_S	M-1	M-2	M-3	M-1	M-2	M-3	M-1	M-2	M-3
R1	0.98	H_2 / O_2	0.33	15.2	26.1	28.8	3.19	3.56	14.9	0.21	0.14	0.52
R2	4.48	H_2 / O_2	0.33	16.3	26.2	28.6	3.42	3.74	13.8	0.21	0.14	0.48
R3	8.49	H_2 / O_2	0.33	16.7	26.2	28.5	3.52	3.81	13.3	0.21	0.15	0.47
R4	4.82	H_2 / air	0.71	25.4	26.4	29.5	6.91	7.11	12.9	0.27	0.27	0.44
R5	5.22	CH_4 / O_2	0.67	31.4	73.4	97.4	0.12	0.29	8.37	0.004	0.004	0.086

method is expected to remain valid.

A third way in which the equivalence principle could fail is if the temperature is no longer determined solely by the mole fraction field (Tacina and Dahm 2000). This can occur when the adiabatic assumption is violated due to large heat extraction. Differential diffusion also could cause the temperature to no longer be determined by the mole fraction. As long as the flow stays fully turbulent the differential diffusion effects are expected to be negligible.

Finally, the equivalence principle will fail when the density profile can no longer be accurately represented by the simple mixing of two fluids. However, for cases with large dissociation, method 3 was shown to accurately approximate the inner jet density profile. Also if one branch of the state relations does not account for a significant majority of the total momentum flux density, the inertial effect of heat release will not be accounted for accurately. The validity of these assumptions and limitations for turbulent reacting coaxial jets investigated in this study will be addressed in Chapter VI.

3.2 Buoyancy

One heat release effect that can cause the equivalence principle to fail in the current formulation is buoyancy. Buoyancy adds momentum to the flow and invalidates the conservation of momentum assumptions on which the method is based. A simple method to test for buoyancy effects is to invert the experimental setup and see if the flame length changes. However, due to limitations of the experimental apparatus this was impractical in the current setup. Instead the conditions for which the jet is momentum-dominated (and buoyancy is not important) are estimated using

semi-empirical methods. One such method for reacting simple jets is the Richardson number based method of Becker and Yamazaki (1978).

The Richardson number is the ratio of the buoyancy and input momentum flux,

$$Ri = \frac{\pi g(\rho_\infty - \rho)x^3}{4G_O}, \tag{3.9}$$

where g is the gravitational constant, x is the downstream distance, and G_O is the input momentum flux in newtons. For a simple jet to be momentum-dominated Ri has to be below a certain constant. Equation 3.9 can be simplified if the worst case is considered ($[\rho_\infty - \rho] \rightarrow \rho_\infty$) and the flow is assumed to grow linearly with downstream distance. Becker and Yamazaki (1978) then suggest that for a flame of length L_S, the jet is momentum driven up to,

$$(\pi g \rho_\infty / 4G_O)^{1/3} L_S = \epsilon_L < 2. \tag{3.10}$$

To use Eqn. 3.10 for coaxial jets a worst case scenario was utilized.

Coaxial jets involve three fluids; ambient, outer jet and inner jet fluids. Buoyancy forces between all of the fluids should be considered. The worst case scenario for a coaxial jet would be the lightest fluid being injected into an atmosphere of the densest fluid from the entire injector. Equation 3.10 already assumes that the lightest fluid has zero density and the densest fluid in this work is always the oxidizer. Since all cases are run fuel rich, the ambient fluid always has a density between the fuel and oxidizer density and hence ρ_∞ should be set to ρ_i. The input momentum flux G_O is set to the actual momentum flux of each coaxial jet. Using this method for all reacting coaxial jets investigated in this work values of ϵ_L were found to vary between 0.3 and 1.4 which is well below the limit of 2 that has been measured to mark the onset of the transition region between the momentum and buoyancy dominated regimes. Thus buoyancy effects are believed to be negligible in this study. Note that temperature

change due to the reaction was never taken into account since the light fluid density already was assumed to be zero and decreasing the ambient fluid density would have reduced the calculated ϵ_L values and not changed the conclusion. While buoyancy is believed to be negligible, the way by which buoyancy effects the flow should be considered. Buoyancy would add momentum to the less dense outer jet (compared to the denser inner jet) and accordingly decrease L_S. In the current study the case that gives the largest ϵ_L (1.4) is a H_2 / O_2 coaxial jet at $P_C = 8.5$ atm (R3) and a velocity ratio value of 2.67.

CHAPTER IV

Experimental Facilities and Diagnostics

Experimental measurements of nonreacting and reacting turbulent coaxial jets were obtained in The Michigan Single Element Injector Experiment. This experimental facility was designed and built as part of this thesis work. It is a laboratory scale rocket engine capable of chamber pressure up to 10 atmospheres. In addition, experimental PLIF techniques used to obtain mixture fraction in nonreacting cases and OH contours in reacting cases are outlined.

4.1 Michigan Single Element Injector Experiment

The Michigan Single Element Injector Experiment is a laboratory scale rocket engine with optical access so laser based and visual diagnostic techniques can be utilized. It was specifically designed and built for this investigation. The design and sizing of the rocket is based on work done at Penn State and NASA Marshall (Moser et al. 1993, Santoro 1998, and Hutt and Cramer 1996). The rocket experiment is of a modular design which allows a window section to be moved to various locations in the combustion chamber. The combustion chamber length also can be varied by the addition or removal of spacer sections. A schematic of the rocket is shown in Fig. 4.1

and a photo is shown in Fig 4.2. The rocket is comprised of sections including the nozzle assembly, injector assembly, window section, ignition block, and a number of spacer sections. This facility is capable of chamber pressures up to 10 atmospheres.

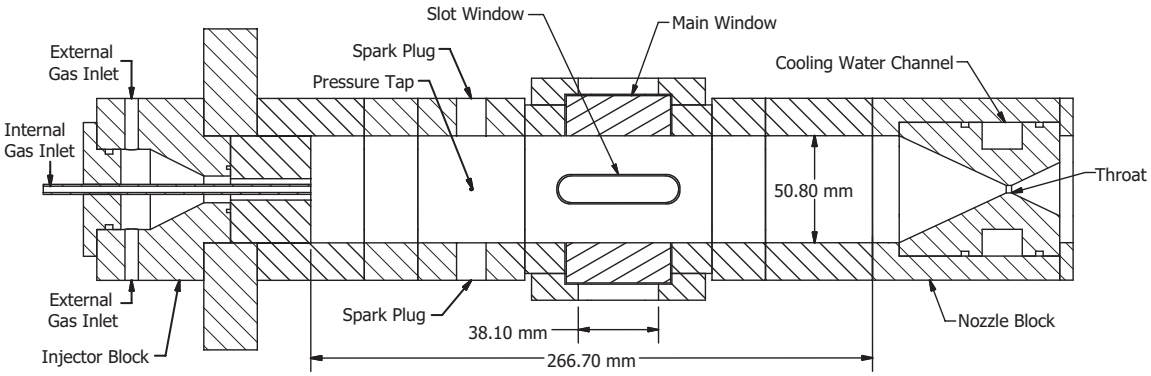

Figure 4.1: Schematic of the Michigan Single Element Injector Experiment.

Every section of the rocket is machined from C145 tellurium copper. The rocket is held together using four threaded brass rods that run the length of the assembly. Between each section, a 0.79 mm thick high temperature silicone gasket is used to seal the combustion chamber. The rocket is mounted in a vertical position on a unistrut test stand so the exhaust plume can directly enter the laboratory venting system.

The combustion chamber is 50.8 mm x 50.8 mm square with a 6.35 mm radius on the inner corners. In this work, a configuration with a combustion chamber length of 266.0 mm was utilized. The nozzle assembly consists of an outer sleeve and an inner nozzle. This provides a water cooling channel between the two pieces to prevent the throat from melting and for the inner nozzle diameter to be changed without requiring the machining of a new outer sleeve. Different nozzle sizes allow for the chamber pressure to be varied for the same mass flow rate of propellants. Two nozzle

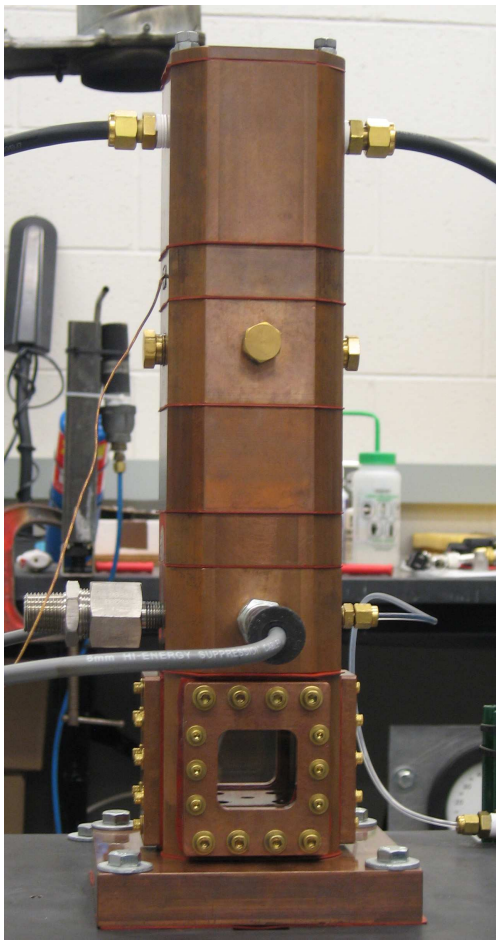

Figure 4.2: Picture of the Michigan Single Element Injector Experiment.

diameters were utilized in this investigation; a 2.16 mm diameter nozzle was used for all pressurized nonreacting cases and reacting H_2 / air and CH_4 / O_2 cases. In addition, a 3.56 mm diameter nozzle was used for all reacting pressurized H_2 / O_2 cases. Ignition of the rocket is achieved using two opposed spark plugs located in the ignition block. The ignition block also contains a rupture disk that is designed to prevent window blowout in case of chamber over-pressurization.

Optical access to the combustion chamber is provided by the 88.9 mm long window section. This section can be moved to any location in the combustion chamber, including the injector face. Two opposed 50.8 mm x 50.8 mm windows, with a 38.1

mm x 38.1 mm viewable area, provide optical access to the combustion chamber, while two opposed 12.7 mm x 57.15 mm, 6.35 mm x 50.8 mm viewable, slot windows provide access for laser sheets. All windows are 19.05 mm thick fused quartz.

The injector assembly contains a single shear coaxial injector. A typical coaxial jet face plate is shown in Fig. 4.3. Oxidizer flows through the center tube surrounded by an annulus of fuel. The injector is of a modular design that allows the inner tube and the injector face plate to be modified. In this work the inner diameter was varied between 3.0 and 3.7 mm, the outer diameter between 10.0 and 6.7 mm, and the post thickness (T_P) between 0.89 and 0.54 mm. The inner tube is set to be flush with the injector face plate for all cases.

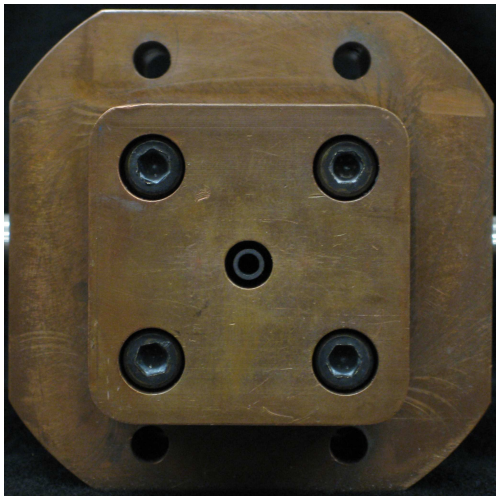

Figure 4.3: Picture of coaxial jet injector face plate where $d_e = 7.5$ mm, $d_i = 3.4$ mm, and $T_P = 0.72$ mm.

For both reacting and nonreacting cases, experimental measurements were taken at atmospheric chamber pressures, which in the current facility was typically 0.98 atm. Atmospheric chamber pressure was obtained by removing the nozzle section and leaving the end of the rocket open to the laboratory. The walls of the rocket remained, except for one nonreacting data set which is noted.

4.1.1 Propellent Delivery and Control System

When dealing with highly energetic propellents such as H_2 / O_2, it is paramount that a failure of any one component in the system does not result in a catastrophic failure of the whole system. The propellent delivery and control system for The Michigan Single Element Injector Experiment was designed with this basic principle in mind. The propellant delivery system supplies gaseous fuel and oxidizer to the rocket experiment using remotely operated solenoid valves which allow the experiment to be controlled from a control room located next to the laboratory. The fuel and oxidizer lines each have three solenoid valves. The first acts as a cut off to isolate the propellant supply from the rest of the system allowing a second valve to open and purge the system. The third solenoid valve is the fire valve which opens to start the delivery of propellants into the rocket. In addition to the solenoid valves, a number of relief and check valves are present in case of regulator failure, rocket over pressurization and to prevent any premixing of the propellants in the delivery system.

Mass flows are metered using calibrated choked orifices with pressure transducers and is controlled using a combination of regulators and needle valves. Due to a difficulty in setting the mass flow rates of the propellants when there is no flow through the system, an oxidizer vent valve and a fuel burner are integrated into the system that allow propellant to flow through the delivery system and bypass the combustion chamber. The utilization of this bypass allows the setting of a more accurate mass flow without forming a potentially dangerous combustible mixture in the rocket. The propellent delivery system is controlled by LabVIEW software, utilizing two LabJack U12 data acquisition and control devices. The first LabJack uses differential analog inputs to monitor and record pressure in the combustion

chamber, oxidizer line, and fuel line from Cooper Instruments PTG404 gage pressure transducers. The second uses digital I/Os to control the solenoid valves, ignition system and trigger any other data acquisition systems such as cameras and boxcar integrators. Due to the need for acetone seeding in the nonreacting work and an ignition torch in the reacting work two different delivery systems were utilized and are shown in Figs. 4.4 and 4.5 respectively.

In the work concerning turbulent nonreacting coaxial jets Acetone Planar Laser Induced Fluorescence (PLIF) was used to obtain mixture fraction fields. Acetone was seeded into the inner jet fluid by bubbling a known amount of air (always used as inner jet fluid in the nonreacting work) through a reservoir of acetone and mixing it with another known amount air. Using this method any desired acetone concentration up to the saturation point can be obtained. A heat blanket wrapped around the brass acetone bubbler was controlled by a PID controller which kept the acetone reservoir within plus minus one degree of the laboratory temperature of 20^oC. This heat blanket ensured that the acetone seeding level didn't change over the course of a run. After combining the two oxidizer streams, a long coil of tubing was used to insure complete mixing of the two flows before introduction into a fluorescence cell to obtain calibration constants for the PLIF measurement. Since heating was not an issue and combustible mixtures were never used in a pressurized chamber, remote operation was not needed in the nonreacting work. Therefore, manual operation of the valves through the LabVIEW interface was utilized, which allowed for run times on the order of ten's of minutes.

The turbulent reacting coaxial jet work utilized OH PLIF and therefore no additional seeding of either propellent stream was necessary. However, to aid in ignition in certain cases the acetone seeding line was converted into a torch line which was

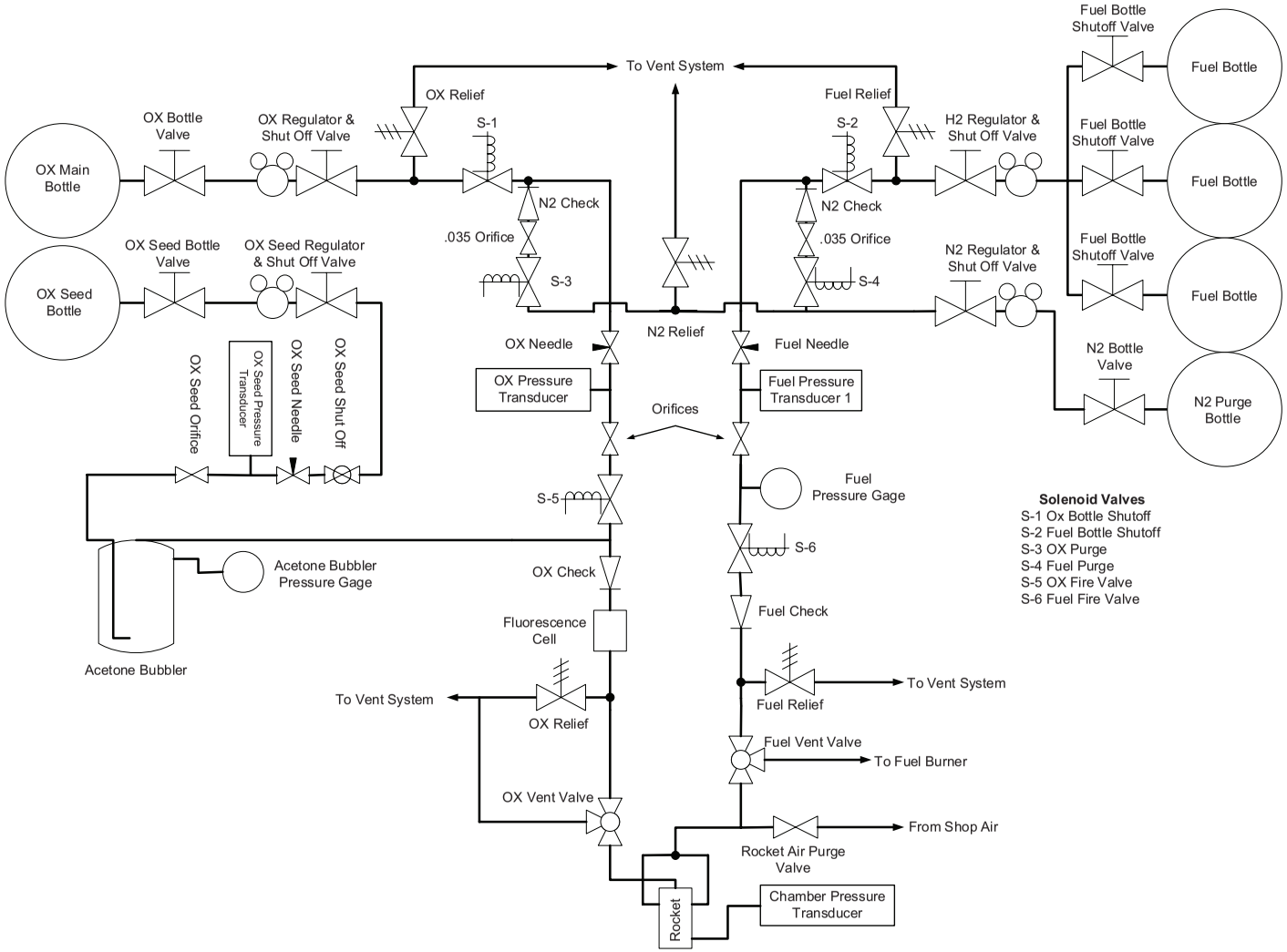

Figure 4.4: Piping diagram of the system used for nonreacting mixing studies.

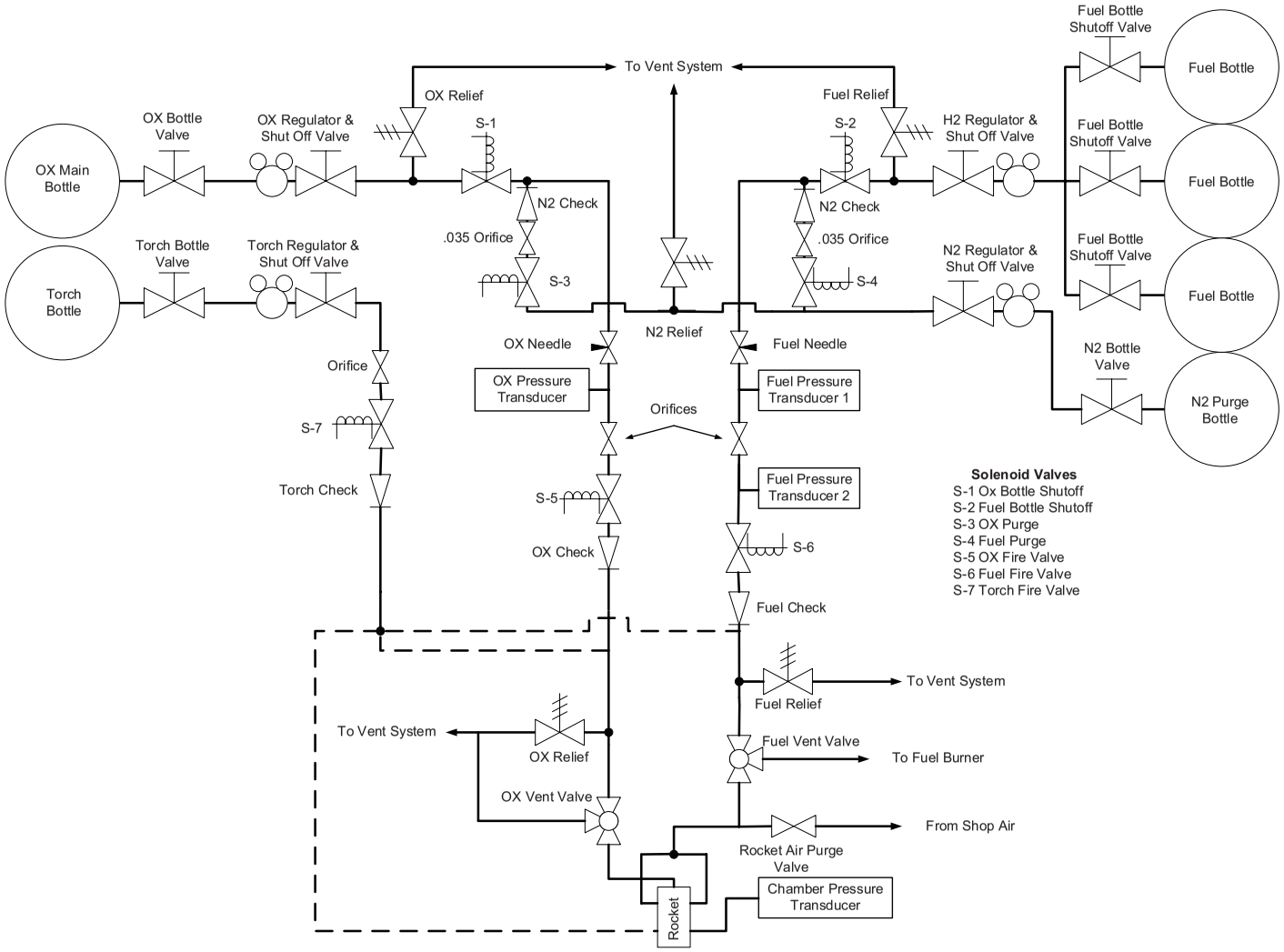

Figure 4.5: Piping diagram of the system used for reacting flow studies. Dashed line represents possible locations of torch feed which was moved depending on the propellents being studied.

moved to different locations of the rocket. The location of the torch depended on which propellent combination was being investigated. For H_2 / O_2, the torch line injected additional O_2 into the side of the injector block perpendicular to the spark plugs. This location of injection allowed the spark at the wall to propagate through what in certain cases was a very fuel rich mixture to the center of the test section where the coaxial jet would then ignite. Next , for H_2 / air, it was found that the easiest ignition occurred when O_2 was added directly to the air stream during the ignition phase. Last, for CH_4 / O_2 it was found the methane flame had difficulty flashing back and stabilizing on the injector post due to the relatively low flame speed in the large velocity ratio cases. This was overcome by using the torch line to add H_2 to the CH_4 stream during ignition.

Due to heating of the rocket during reacting cases, runs were limited to 18 seconds of which 15 were used for data acquisition. Timing was controlled by the LabVIEW program. The sequence starts when the control program turns on the torch and spark plug. After a delay of 0.1 sec, the flow of fuel is initiated. An additional 0.15 sec delay occurs before the oxidizer flow is started. The spark and torch are turned off after 2 sec and then for 1 sec the flow is allowed to stabilize before the 15 sec data acquisition window starts. After a run filtered shop air is run through the rocket to blow out any water which condensed inside, and to speed up the cool down process. The next run was started when a surface temperature of the rocket dropped to 40^oC.

4.1.1.1 Safety Considerations

To ensure safe operation of Michigan Single Element Injector Experiment, a number of safety mechanisms were designed into the system. First and foremost, the entire experiment is run from a control room located next to the laboratory so no

personnel are present during runs. In addition to a computer terminal from which the experiment is operated, the control room contains video surveillance of the experiment, a hardwired emergency shutoff switch, and combustible gas alarms. Operation procedures ensure correct startup and shutdown of the experiment.

The propellent delivery system also has a number of safety features. Numerous relief values are vented into the exhaust system in case of regulator failure or chamber over pressurization. To guard against chamber over pressurization a rupture disk is present on the rocket sidewall. Check valves insure that premixed fuel and oxidizer does not flow back into the delivery system. All components which touch O_2 are oxygen cleaned. In addition, O_2 piping was sized to keep the flow velocity below 10 m/sec for all cases which eliminates any possibility of fire in the lines due to a particle strike. The solenoid values automatically close and result in the flow being shutoff in the event of a power or system failure. Also the double solenoid valves in the line provide redundancy in the case that one would remain open after shutdown.

4.2 Acetone Planar Laser Induced Fluorescence

The use of Acetone Planar Laser Induced Fluorescence (PLIF) is well documented in the literature and has been used to measure concentration, temperature and as a general flow visualization tool (Bryant and Driscoll 2001, Thurber et al. 1998, and Yuen et al. 1997) in reacting and nonreacting flows. It has a large broadband absorption spectrum that is accessible to a number of commercial lasers, a high vapor pressure, and a fluorescence signal that is largely independent of temperature and gas composition. In addition since it is inexpensive and nontoxic, acetone is an ideal flow tracer (Lozano et al. 1992). In this section the acetone system and equations

used to obtain mixture fraction fields in nonreacting coaxial jets are discussed.

4.2.1 Acetone PLIF System

An illustration of the quantitative acetone PLIF setup is shown in Fig. 4.6. Acetone fluorescence was excited near the peak of its absorbtion spectrum at a wavelength of 266 nm. Fluorescence was produced by sending the second harmonic (532 nm) from a Spectra-Physics GCR-130 Nd-YAG laser into an external BBO doubling crystal. The 266 nm laser beam then was split to send 90 percent of the energy into the sheet forming optics. The other 10 percent was used for secondary measurements. The fluorescence from the test section was collected between 400 nm and 700 nm on a scientific grade CCD (Sony XCD-710) camera using a Nikon f/1.4 50 mm lens. No filter was used since the BK7 glass lens effectively blocked the 266 nm excitation wavelength. The usable portion of the CCD in the Sony XCD-710 is 1,024 by 768 pixels. However, a subset of this CCD (584 by 756 pixels) was used that corresponded to an imaging window of approximately 28 by 31 mm with a pixel size of 41 μm square. Due to the small pixel area the limiting factor in the resolution is the sheet thickness (220 μm), which is defined at the full width half max (FWHM) of the sheet. Note that air was always used as the inner jet gas, which allows the oxygen to quench the acetone phosphorescence and makes the use of a gated camera unnecessary. The second beam path then was further split using a glass flat to send beams to a photodiode (Thorlabs DET10A) and through a reference cell. The reference cell was plumbed inline with the inner jet to allow the acetone-seeded air to pass through the reference cell just before being injected into the test section. A photo-multiplier tube (Hamamatsu R636-10) was used to measure the fluorescence of the pure acetone/air mixture. This measurement then was used to normalize the

test section fluorescence and to correct for shot-to-shot power variations. A second photodiode was placed at the beam exit from the reference cell and was used in combination with the first photodiode to perform an absorbtion spectroscopy measurement from which the acetone seeding level could be calculated. A nominal 18 percent by volume acetone seeding level was used for all atmospheric cases. Acetone seeding was adjusted at other chamber pressures to maintain the same fluorescence signal level as that achieved at one atmosphere. Acetone-seeded air was produced by bubbling a known flow rate of air through liquid acetone and combining it with another known flow rate of air. This allows any acetone concentration, up to the saturation value, to be produced. Acetone temperature was maintained at 20^o C using a thermal blanket on the brass bubbler and a PID controller with a K-type thermocouple. Image corrections and relating acetone signal mixture fraction are discussed in §4.2.3.

4.2.2 Acetone PLIF Timing

Timing of the acetone PLIF system was based on the internal clock of the Nd:YAG laser that fires at 10 Hz. Due to a slow shutter and long exposure time of the camera, the flashlamp output trigger was used to trigger a DG535 time delay generator which then provided a delay to trigger the imaging camera and the data acquisition of the Stanford Research Systems SR250 gated integrator. To minimize noise in the PMT and the two photodiodes, the gated integrators (one for each device) were used to create tight integration windows around the laser pulse. Because of jitter in the flashlamp output trigger the Advanced Q-switch output trigger was used to trigger the integration windows. Data acquisition was initialized by placing a white card in the beam path and then flipping the manual switch which triggered both the

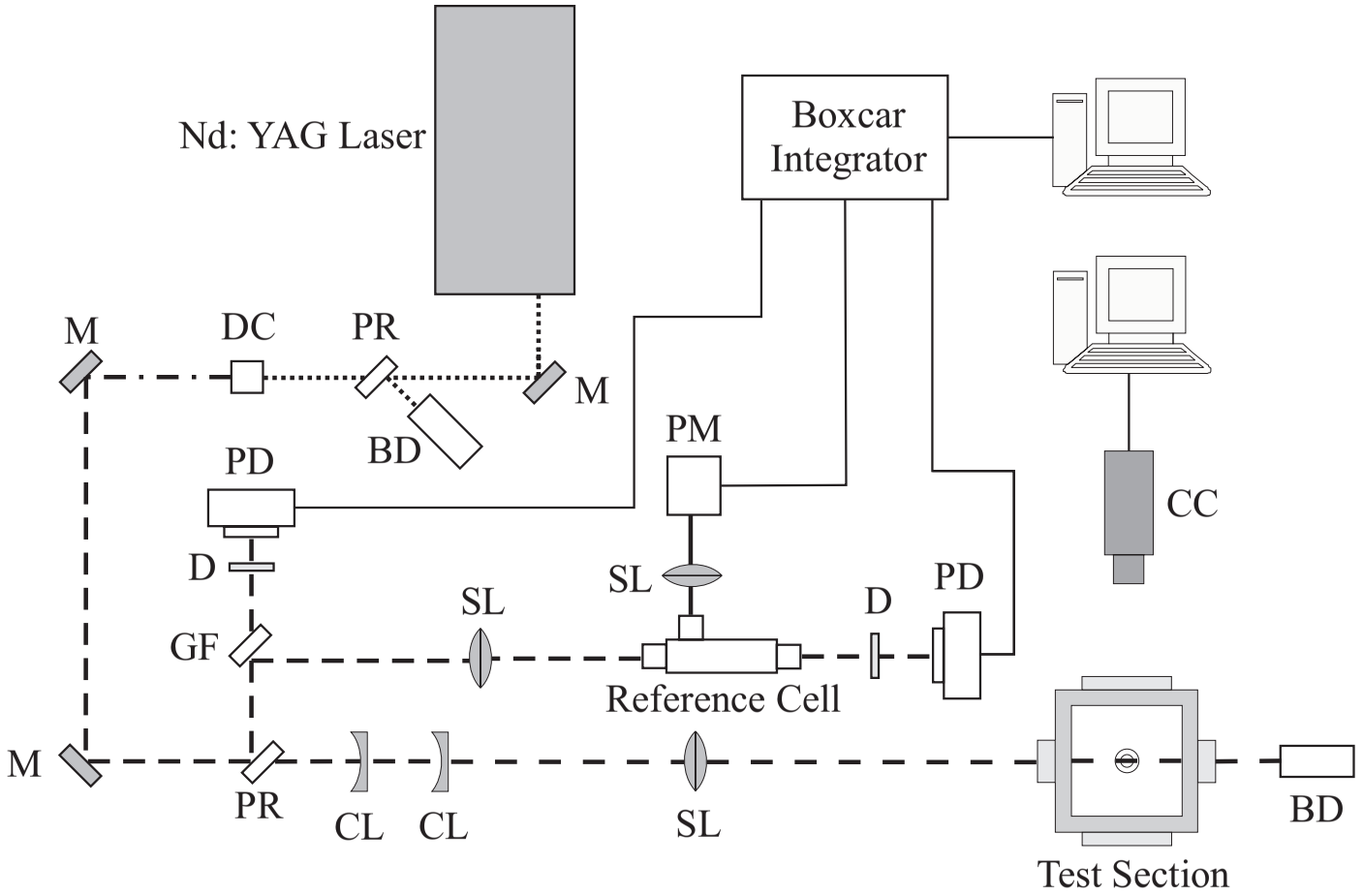

Figure 4.6: Laser and optical setup for quantitative acetone PLIF measurements. BD - beam dump, CC - CCD camera, CL - cylindrical lens, D - diffuser, GF - glass flat, M - mirror, DC - doubling crystal, PD - photodiode, PM - photo-multiplier tube, PR - partial reflector, SL - spherical lens. $(\cdots)$ - 532 nm , $(- - -)$ - 266 nm.

camera and boxcar integrator. After a few pulses the card was removed and data collected. The card was used to ensure the images from the camera and data from the integrators were synchronized since during testing of the system a one pulse difference was randomly observed. To better illustrate the timing system, a wiring schematic is presented in Fig. 4.7 and the sequence of timing events is shown in Fig. 4.8. It is important to note that while the camera exposure is 100 μs, the lifetime of the acetone florescence is on the order of 2 ns (Lozano et al. 1992) and the laser pulse width is approximately 9 ns. Given that the upper bound on velocity in these jets is 200 m/s, images obtained using this system are instantaneous measurements of the flow field. However, due to the slow acquisition rate (10 Hz) the sequence of images are obtained only at random instances in time and are not time resolved.

4.2.3 Fluorescence Equation

The acetone PLIF signal recorded on the CCD camera can be converted to acetone mole fraction (X_{ace}) by applying the fluorescence equation after some corrections are made. For weak excitation (not saturated), the fluorescence signal from acetone PLIF is given by

$$S_f = \frac{E}{hc/\lambda}\eta_{opt} dV_c \left[\frac{X_{ace}P}{kT}\right] \sigma(\lambda, T)\phi(\lambda, T, P, \sum X_i), \tag{4.1}$$

where E is the laser fluence, hc/λ is the energy of a photon at wavelength λ, η_{opt} is the collection optics efficiency, dV_C is the collection volume, σ is the molecular absorption cross-section and ϕ is the fluorescence quantum yield. To be in the linear fluorescence regime where Eq. 4.1 is applicable, Lozano et al. (1992) suggest, for excitation at 266 nm with a sheet of thickness 220 μm (FWHM) and a height of 30 mm, as used in this study, that saturation will not occur until pulse energies on the order of 6 J

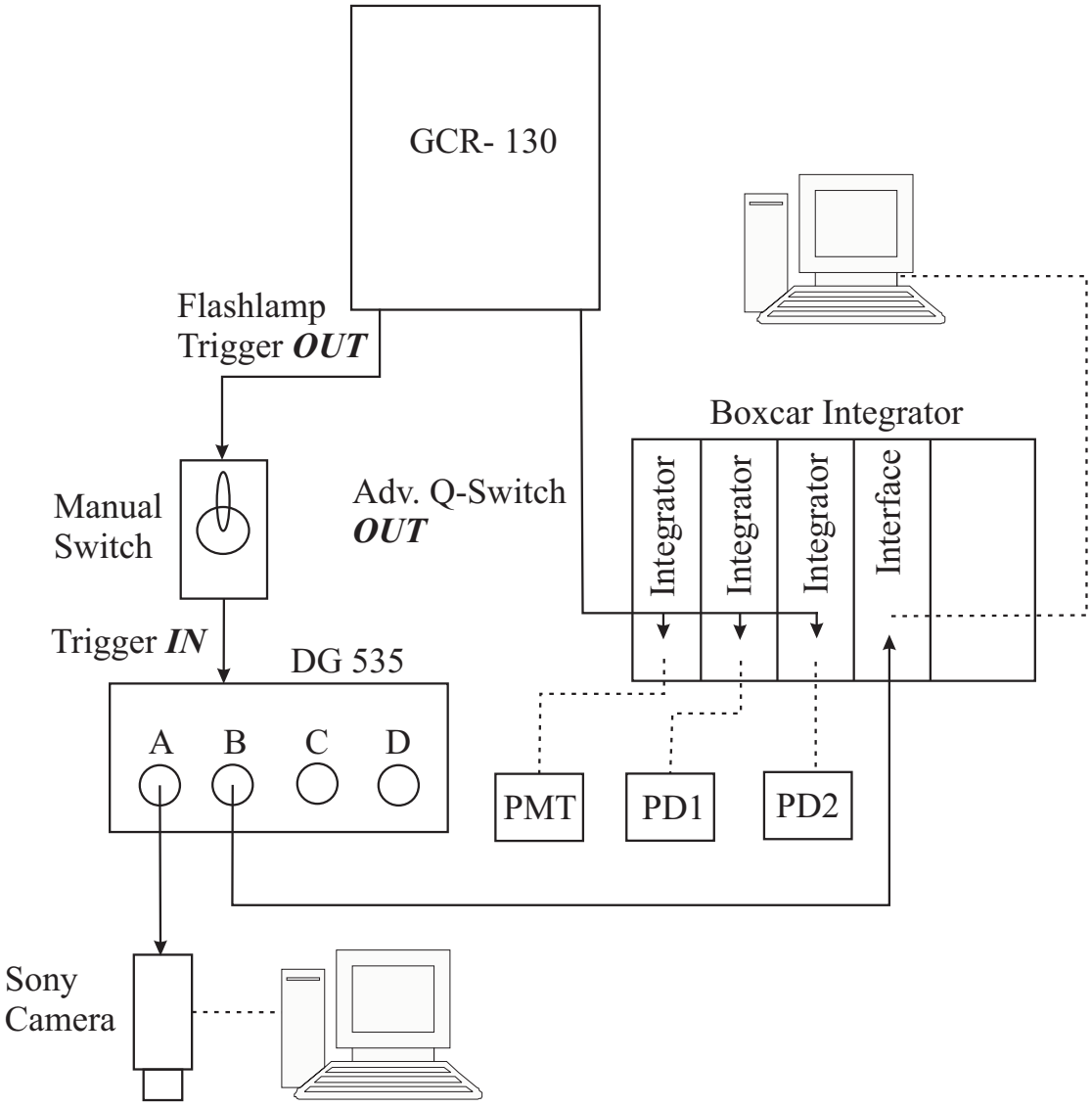

Figure 4.7: Schematic of the wiring used to synchronize acetone PLIF imaging camera and boxcar integrator with Nd: YAG laser firing at 10 Hz. After initialization of the boxcar integrator and the camera using their respective computer systems, flipping the manual switch started data acquisition. PMT and PD are photo-multiplier tube and photodiode respectively.

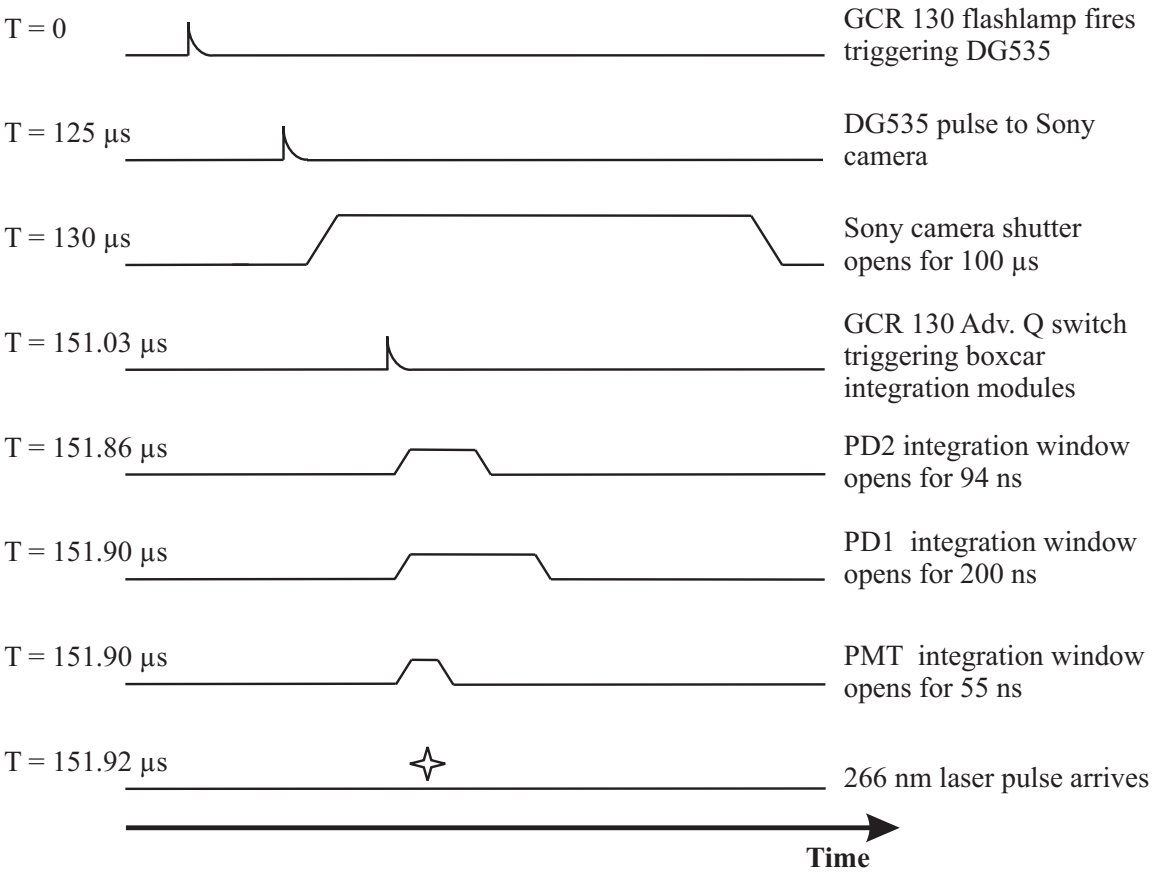

Figure 4.8: Diagram of the timing used to synchronize the camera, PMT and two PDs with the laser pulse for Acetone PLIF measurements.

are reached, which is well above the 20-30 mJ used in this work. However, to ensure linearity both from a fluorescence standpoint and from the fluorescence measuring devices (camera, PMT, and photodiodes) pulse energy was varied and the response was measured for $X_{ace} = 0.18$ (Fig. 4.9*a*). The linearity achieved for a set pulse energy and varying mole fraction is shown in Fig. 4.9*b*. The camera signal is the integrated value from all pixels in the field of view after the field is corrected for absorption. The PMT signal also is corrected for absorption.

Returning to Eq. 4.1 the only nonconstants are X_{ace}, ϕ, and E. The molecular absorption cross-section (σ), which is a function of λ and T, is a constant since the same excitation wavelength is used and all nonreacting coaxial jets tested are isothermal and nearly isobaric. To eliminate the issue of variable laser fluence, a normalization condition is needed. Normally this is done by using a region of the flow where the measured signal is known to correspond to a mole fraction of one, such as in the potential core. However, depending on the location of the moveable window section, the potential core is not always in the field of view. Instead, a PMT is used to make a florescence point measurement in a reference cell that contains the acetone seeded air before it enters the test section. Thus the ratio of the florescence signals from the camera and PMT provide the value of the constant θ, which is

$$\frac{S_f^C}{S_f^P} = \frac{E^C \eta_{opt}^C dV^C}{E^P \eta_{opt}^P dV^P} = \theta(x,y) = constant. \tag{4.2}$$

Superscripts C and P correspond to camera and PMT values respectively. Note that the camera signal varies in the image plane and therefore so does θ. Since the partial reflectors used to split the laser beam split the same percent of laser energy regardless of total laser energy, it is easily shown that E^C/E^P is a constant. By filling the test section and the reference cell with the same acetone mixture before

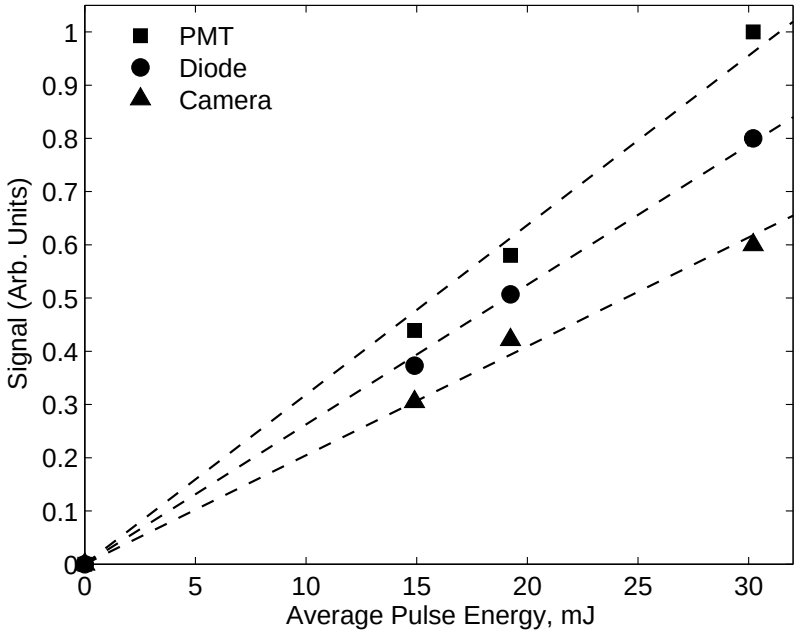

(a)

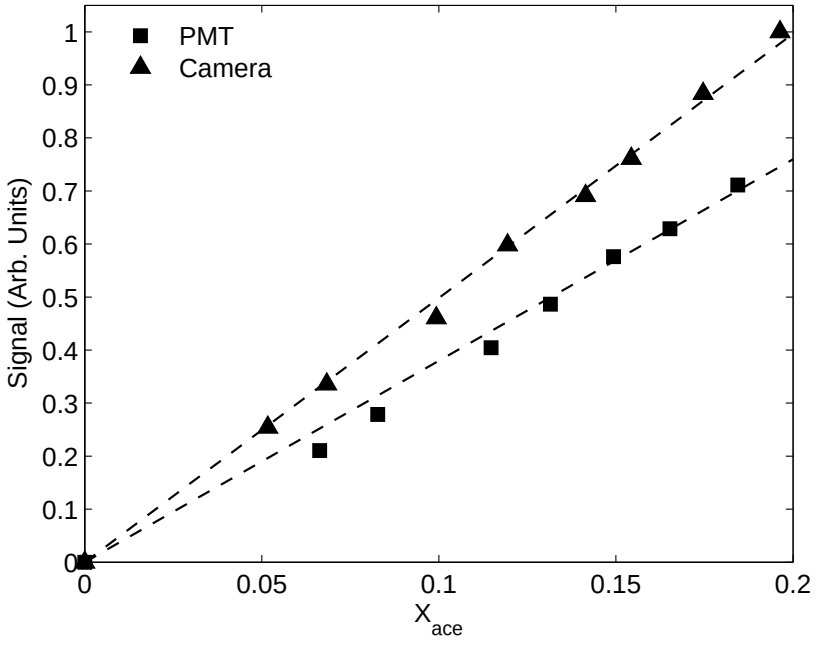

(b)

Figure 4.9: Test of the linearity of imaging devices used in acetone PLIF system. Linearity of the diode, PMT, and camera as a function of pulse energy is shown in (a). Linearity of the PMT and camera as a function of mole fraction is shown in (b).

a run and imaging the fluid, $\theta(x, y)$ is obtained. The normalized fluorescence signal can now be written as,

$$\frac{S_f^C}{S_f^P} = \theta(x, y)\frac{X_{ace}^C}{X_{ace}^P}\frac{\phi^C}{\phi^P}. \tag{4.3}$$

The desired final result from this analysis is to obtain the mole fraction field based on the inner jet fluid (X_i). To relate X_i to X_{ace}^C/X_{ace}^P all mole fractions can be written in terms of total moles,

$$X_{ace}^C = \frac{n_{ace}^C}{n_{ace}^C + n_{air}^C + n_e^C}, \quad X_{ace}^P = \frac{n_{ace}^P}{n_{ace}^P + n_{air}^P}, \quad X_i^C = \frac{n_{ace}^C + n_{air}^C}{n_{ace}^P + n_{air}^P + n_e^C}. \tag{4.4}$$

The ratio X_{ace}^C/X_{ace}^P in terms of moles is given by,

$$\frac{X_{ace}^C}{X_{ace}^P} = \frac{n_{ace}^C + \frac{n_{air}^P}{n_{ace}^P} n_{ace}^C}{n_{ace}^C + n_{air}^C + n_e^C}. \tag{4.5}$$

Assuming that acetone is a perfect tracer and differential diffusion is dominated by turbulent mixing, then the ratio of the moles of air to acetone never changes, so:

$$\frac{n_{air}^P}{n_{ace}^P} = \frac{n_{air}^C}{n_{ace}^C}, \tag{4.6}$$

and the ratio of acetone mole fraction can be written as the inner fluid mole fraction,

$$\frac{X_{ace}^C}{X_{ace}^P} = \frac{n_{ace}^C + n_{air}^C}{n_{ace}^C + n_{air}^C + n_e^C} = X_i^C(x, y). \tag{4.7}$$

Inserting Eq. 4.7 into Eq. 4.3 and solving for X_i^C results in

$$X_i^C(x, y) = \frac{S_f^C}{S_f^P}\frac{1}{\theta}\frac{\phi^P}{\phi^C}. \tag{4.8}$$

The only unknown in Eq. 4.8 is the ratio of the quantum yields (ϕ^P/ϕ^C) since ϕ^P/ϕ^C is a function of concentration and pressure and a variable concentration field exists in the test section. In this work, the ratio of quantum yields is assumed to be 1. The errors caused by this assumption is determined to be less than 8% for He/air and

H_2/air , as discussed in §4.2.7. The inner jet mole fraction can easily be converted to mixture fraction using

$$f = \frac{X_i^C MW_i}{(X_i^C MW_i + (1 - X_i^C) MW_e)}, \tag{4.9}$$

where MW_i and MW_e are the molecular weight of the inner and outer fluids at injection respectively.

4.2.4 Image Correction

Acetone images were corrected for background noise, dark noise, white field variations, and sheet intensity variations as outlined by Clemens (2002). In his formulation the desired signal (S_e) can be related to the actual signal ($S_{tot}(x, y)$) through;

$$S_e(x, y) = \frac{S_{tot}(x, y) - [w(x, y) S_{back}(x, y) + S_{dark}(x, y)]}{w(x, y) L(x, y)}, \tag{4.10}$$

where $w(x, y)$ is the white-field correction, $L(x, y)$ is the sheet correction, $S_{dark}(x, y)$ is the dark signal, and $S_{back}(x, y)$ is the background signal. If the same camera and exposure time are used to take a background image as the actual images then this image will also have the same dark noise and white field response as the actual image. In this situation the noise term can be written as a single correction,

$$S_e(x, y) = \frac{S_{tot}(x, y) - S_{correction}}{w(x, y) L(x, y)}. \tag{4.11}$$

Since θ in Eq. 4.8 is obtained by imaging a uniform acetone mixture and the same sheet is utilized, the white field and sheet intensity corrections are already accounted for and therefore an additional correction is not needed. Due to the large acetone concentration used in this study, the mixture at least somewhere in the coaxial jet flow field was not optically thin and hence an absorption correction is needed.

The absorption of laser energy across an uniform fluid is described by Beer's Law. For the case of a single absorber and a uniform fluid, Beer's law states that the ratio of the laser energy after the beam pases through the fluid to the initial energy is:

$$\frac{I_1}{I_0} = e^{-\sigma N d}; \tag{4.12}$$

where σ is the molecular absorption cross section ($4.4 \times 10^{-20}\,\mathrm{cm}^2$ for acetone excited at 266 nm), d is the distance the beam travels through the fluid, and N is the number density of the absorbing molecule. The flow field of a coaxial jet is not uniform, and so a predictor corrector scheme (van Cruyningen et al. 1990) along with Beer's law must be used to correct for absorption. This method sums the energy loss in all previous pixels, corrects the value in the new pixel, and then calculates the energy loss across the new pixel. This is repeated until a conversion criteria is met. Since the sheet travels through a part of the test section that is not imaged, the acetone seeding level in this part is estimated from the measured flow rates and the measured value of X_{ace}.

4.2.5 Obtaining Acetone Concentration

The acetone mole fraction of the inner jet fluid (X_{ace}) is needed to calculate MW_i so the inner jet mole fraction can be converted to mixture fraction using Eqs. 4.8 and 4.9. Historically acetone mole fraction has been calculated by assuming that the fluid leaving the bubbler is at the saturation limit. To ensure the mixture is at saturation, a series of bubblers in an ice water bath are used (Thurber et al. 1998). However, using an ice bath greatly reduces the saturation concentration. To eliminate these problems, the acetone concentration was directly measured in two different manners.

The first method was to image the test section filled with an uniform acetone/air

mixture. The average absorption profile across the test section was then fit to Beer's Law (Eq. 4.12) by solving for the X_{ace} value which provided the best fit. In all cases the difference between the measured absorption profile and the best fit to Beer's Law was less then 1.5%. In atmospheric test cases this value then could be used to determine the seeding level because starting the flow of the outer jet did not alter the pressure or temperature in the test section or the bubbler. Therefore the seeding level did not change between the calibration and data runs. However, for pressurized test cases, starting the outer fluid flow increased the pressure in the test section and the bubbler, changing the seeding concentration.

To calculate X_{ace} for pressurized cases, the absorption in the reference cell was measured using the two photodiodes. To obtain a scaling constant related to this system, a calibration experiment was performed at atmospheric pressure and temperature and the ratio of the diode signals was plotted against X_{ace} that was measured in the test section using the camera. The results of this calibration experiment are shown in Fig. 4.10.

The results that are plotted in Fig. 4.10 follow a curve that agrees with Beer's Law, but the constant in the exponent differs from the expected value. The constant in the exponent (13.36) is related to the amount of light the partial reflector sends to the diode before the cell versus through it. This depends on the molecular absorption cross section, the absorption distance, and the conversion from number density to acetone mole fraction which is a function of temperature and pressure. The acetone molecular absorption cross section (σ) was calculated using the measured value of 13.36. The resulting value of σ is 5.28×10^{-20} cm^2 which is 20% different from the agreed upon value of 4.4×10^{-20} cm^2. This difference is believed to be due to the beam focusing in the fluorescence cell for the PMT measurement and losses off of

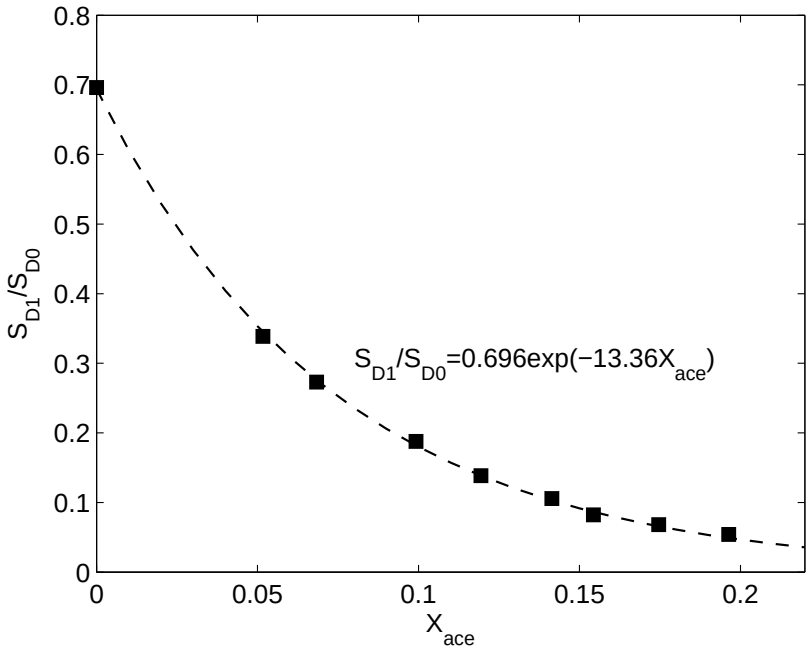

Figure 4.10: Ratio of diode signals before (D0) and after (D1) fluorescence cell compared to acetone mole fraction at atmospheric pressure and temperature with best fit exponential curve.

the cell windows. This method of calculating X_{ace} was used for all pressurized cases.

To check these methods, measured X_{ace} values were compared to the saturation values calculated from the measured mass flow rates and temperature and pressure in the bubbler. The measured values were found to be within 15% of the saturation values but always were lower, indicating that the bubbler flow was not fully saturated at the exit. It also was found that as the level of liquid acetone in the seeder was increased and the air mass flow rate through the seeder was decreased the measured value approached the saturation value as expected.

4.2.6 Imaging and Correction Procedures

The exact imaging and correction procedures used to obtain mixture fraction fields in nonreacting turbulent coaxial jets are briefly outlined below. The imaging

procedure was as follows. First, the test section and florescence cell were allowed to fill with an uniform acetone/air mixture. After a few minutes equilibrium was reached, so images and signal measurement in the reference cell were taken. From these measurements, $\theta(x, y)$ was calculated. Then the outer flow was turned on and set to the correct flow rate. After 30 seconds steady conditions were obtained and images of the nonreacting coaxial jet were collected along with the normalization values from the reference cell. The outer flow was turned off and the uniform acetone/air mixture again was allowed to fill the chamber. Measurements of the uniform field again were taken to insure that nothing had changed over the course of the run. Lastly, the line from the acetone bubbler was closed off, the flow rate of air in the main line was increased to approximately the same total flow rate as with the bubbler line and the outer flow was also turned on. After all acetone was purged from the system, a background image set was taken. All data sets consisted of 180 images.

The image correction procedure was applied in the following manner. First, the background image was subtracted from the uniform acetone field and the background signal from the PMT measurement. Beer's law then was used to correct for absorption. Using the measured X_{ace} value, the PMT measurement was corrected for absorption. The ratio of these corrected signals were used to calculate $\theta(x, y)$. Secondly, the background image and background PMT signal were subtracted from the jet images and corresponding PMT measurements. The ratio of these signals were then averaged and the θ correction applied. Thirdly, Beer's law and a predictor corrector method were used to correct for absorption in the final average image. Lastly, a 4 pixel by 4 pixel median filter was applied to reduce any remaining noise, yet preserve the sharp edges in the image. This method was typically used on average images from which mixing lengths were calculated. However it also was applied

in the same manner to instantaneous coaxial jet images.

4.2.7 Mixture Fraction and Mixing Length Uncertainty

To determine the actual measurement uncertainty it is necessary to have both the measured value and the true value of what is being measured. With the exception of calibration experiments the true value is almost always unknown. Instead the uncertainty of a derived quantity has to be estimated from the uncertainty of the variables from which it is calculated. Using the root-sum-square (RSS) combination method, Moffat (1988) estimates the uncertainty of a derived quantity as

$$\delta R = \left\{ \sum_{i=1}^{N} \left(\frac{\partial R}{\partial Z_i} \delta Z_i \right)^2 \right\}^{1/2}, \tag{4.13}$$

where R is the derived quantity, Z_i are the independent variables used to calculate R, δZ_i is the uncertainty of each independent variable, and N is the total number of independent variables. In the case where the function of the derived quantity R can be written in product form (Moffat 1988),

$$R = Z_1^a Z_2^b Z_3^c \cdots Z_N^n \tag{4.14}$$

Eq. 4.13 can be expressed as

$$\frac{\delta R}{R} = \left[\left(a \frac{\delta Z_1}{Z_1} \right)^2 + \left(b \frac{\delta Z_2}{Z_2} \right)^2 + \cdots + \left(n \frac{\delta Z_N}{Z_N} \right)^2 \right]^{1/2}. \tag{4.15}$$

To obtain the mixture fraction and mixing length uncertainty, the uncertainty in the inner fluid mole fraction X_i has to be obtained first. Applying the form of Eq. 4.15 to the relation for X_i (Eq. 4.8) the error in mole fraction can be estimated as

$$\frac{\delta X_i}{X_i} = \left[\left(\frac{\delta S_R}{S_R} \right)^2 + \left(\frac{\delta \theta}{\theta} \right)^2 + \left(\frac{\delta \phi_R}{\phi_R} \right)^2 \right]^{1/2}, \tag{4.16}$$

where S_R is the ratio of the camera to PMT signal and ϕ_R is the ratio of the PMT to camera fluorescence quantum yield. The uncertainty of each term in Eq. 4.16 was calculated as outlined below.

The uncertainty of the calibration constant θ is a function of the errors in the ratio of the camera and PMT signals and the absorption correction to the uniform acetone field. The error in the signal ratio can be estimated from the standard deviation (σ) of this ratio in an uniform low signal region of the flow. Using this method a maximum value of 6.6% was obtained for σ. In the case where average values are used the uncertainty of R is related to the standard deviation by $\delta R/R = 2\sigma/\sqrt{Q}$, where Q is the total number of instances averaged. Theta is obtained from the average of 360 images. Therefore the uncertainty of the signal ratio in θ is estimated to be $\pm 0.70\%$. The other component of uncertainty in θ is the absorption correction. Due to non-uniformities in the imaging field due to the white field response of the camera and the variable intensity sheet, the uncertainty of the absorption correction was estimated at $\pm 1.5\%$. This was estimated from the curve fit of the average profile across the image to Beer's law (Eq. 4.12). Using the RSS combination method to combine these two values, the uncertainty of θ ($\delta\theta/\theta$) is $\pm 1.7\%$. The uncertainty in the absorption correction can also be used to estimate the uncertainty in X_{ace} which is used to convert from mole to mixture fraction. An uncertainty of $\pm 1.5\%$ in the ratio of signals in Beer's laws (Eq. 4.12) results in an uncertainty of $\pm 3.25\%$ in X_{ace}.

The ratio of the camera to PMT signal uncertainty is obtained in a similar manner to that of θ. Using the same standard deviation as in the θ calculation the uncertainty in the ratio of the signals is $\pm 1.0\%$ due to the smaller set of images used to create the average field (180 versus 360). The error due to the absorption correction in the main image was estimated by making a simulated radial acetone profile that corresponded

to the experimental test case with the highest overall acetone concentration which results in the largest absorption effects and therefore the largest error. Beer's law was then used to simulate what the profile would look like after absorption. The correction method used in the image possessing software to correct for absorption was then applied with X_{ace} at it's uncertainty limits. Using this method the total uncertainty in S_R was estimated to be $\pm 1.3\%$.

The final component uncertainty needed to calculate the uncertainty in X_i is that of the fluorescence quantum yield (ϕ). Equation. 4.1 shows ϕ to be a function of the excitation wavelength, the temperature, the pressure, and the local concentration. Since the local concentration varies between the reference cell and different locations in the test section this ratio will deviate from the assumed value of one. The error related to this assumption can be estimated from the acetone fluorescence quantum yield model of Thurber and Hanson (1999). This ia a quantitative multistep decay model which has additional terms to account for the quenching effects of oxygen on the fluorescence. Using this model (ϕ_R) was calculated for four cases that correspond to the fuel/air-acetone combinations, chamber pressures, and acetone seeding levels used in the nonreacting work. These cases include He/air at chamber pressures of 0.98, 3.86 and 5.40 atmospheres with injection acetone mole fraction (X_{ace}) values of 0.18, 0.05, and 0.037, respectively. The fourth case was CH_4/air at 0.98 atm with $X_{ace} = 0.18$. Jets with hydrogen were also studied in this work. Unfortunately constants for hydrogen bath gases are not available in the literature. However, since the molecular complexity of helium and hydrogen are similar and the fluorescence yield is only weakly dependent on molecular weight, the helium results are believed to be a good approximation of ϕ for a hydrogen bath gas. Figure 4.11 shows the ratio of quantum yields for the four run conditions. At a mixture fraction of one the

ratio is also one since the reference and test section conditions are the same. The pressure difference between the two was always less then 0.02 atm and consequently had a negligible effect on the results. The maximum error for the He/air cases was limited to 8.2% and was greatly reduced as the chamber pressure increased. The error at the stoichiometric condition ($f_S = 0.89$) was 3.0%. In the nonreacting work the stoichiometric condition was defined assuming the fuel plus oxygen chemistry. In the case of helium outer jets H_2/O_2 chemistry was assumed. The error was much greater for the CH_4/air with a max error of 18% but a more modest error of 7.1% at the stoichiometric condition $f_S = 0.80$. The method of Thurber and Hanson (1999) can be used to correct the mixture fraction field for the effect of quantum yield, however in this work this was not done since constants were not available for a hydrogen bath gas and it was desirable to keep the correction procedure the same for all cases. Making this correction with unknown constants could result in increasing instead of decreasing the error. Instead the maximum error for each case was used as the uncertainty for the ratio of quantum yields. Using Eq. 4.16 and the uncertainties for each component, the uncertainty of X_i can be obtained. These are listed with all other estimated uncertainties in Table. 4.1.

Finding the uncertainty of the mixture fraction (f) is more difficult since the functional relationship (Eq. 4.9) can not be written in simple product form. In such situations Moffat (1988) suggests sequentially perturbing the inputs by their uncertainly and using RSS to combine the uncertainty caused be each input. The mixture fraction equation only has two inputs that have uncertainties associated with them, X_i and MW_i. Applying this method, the max uncertainty and the uncertainty at the stoichiometric condition were obtained for each case and are listed in Table. 4.1. Results in Chapter V will show that the momentum flux ratio scaling (Eq. 2.27) does

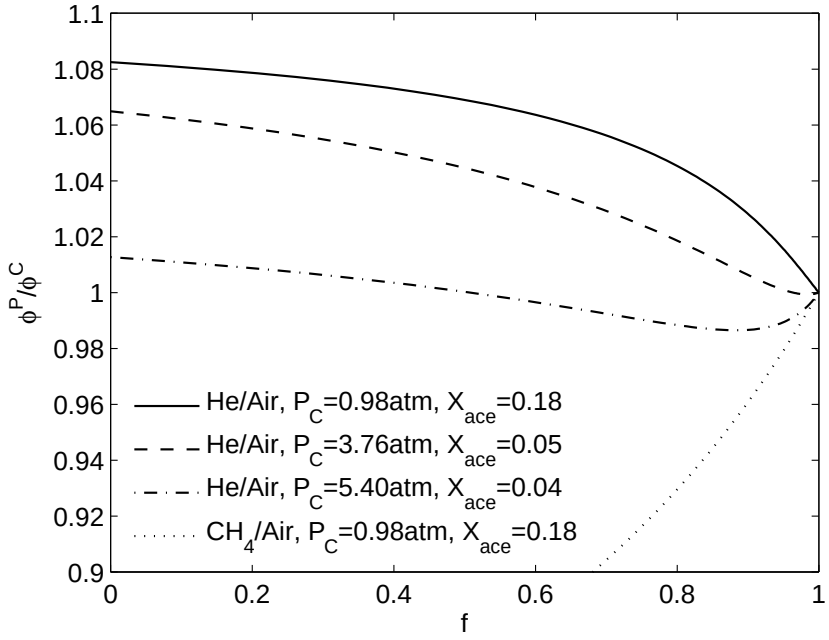

Figure 4.11: Ratio of the reference to actual quantum yields versus mixture fraction for four nonreacting run conditions. Calculated using the model of Thurber and Hanson (1999).

an excellent job of predicting the stoichiometric mixing lengths. Since this scaling is inversely proportional to the stoichiometric mole fraction (X_S) a good estimate of the uncertainty in the mixing length is the uncertainty in (X_i). To provide a conservative estimate of error, the maximum uncertainty in X_i is used to set the error bars on the measured stoichiometric mixing lengths in Chapter V.

4.3 OH Planar Laser Induced Fluorescence

Fluorescence of combustion radicals is a popular technique to gain insight into the location and structure of flames (Tanahashi et al. 2005 and Bryant and Driscoll 2001). In certain cases, PLIF of a combustion radical can be made quantitative and concentrations can be obtained (Everest et al. 1997). In addition, two line methods can be used to obtain temperature in reacting flows (Lucht et al. 1982). In a review

Table 4.1: Estimated uncertainties for acetone PLIF results. Subscript S is the value at stoichiometric condition and m is the max value in the flow field.

Outer Gas	He	He	He	H_2	CH_4
P_C, atm	0.98	3.76	5.40	0.98	0.98
Component	Percentage Uncertainty				
$\left(\frac{\delta\theta}{\theta}\right)$	1.7	1.7	1.7	1.7	1.7
$\left(\frac{\delta S_R}{S_R}\right)$	1.3	1.3	1.3	1.3	1.3
$\left(\frac{\delta\phi_R}{\phi_R}\right)_m$	8.2	6.5	1.4	8.2	18.0
$\left(\frac{\delta\phi_R}{\phi_R}\right)_S$	3.0	0.7	1.4	3.0	7.1
$\left(\frac{\delta X_i}{X_i}\right)_m$	8.5	6.8	2.5	8.5	18.1
$\left(\frac{\delta X_i}{X_i}\right)_S$	3.7	2.2	2.5	3.7	7.4
$\left(\frac{\delta f}{f}\right)_m$	2.3	1.9	0.7	2.2	7.4
$\left(\frac{\delta f}{f}\right)_S$	1.1	0.7	0.8	1.0	3.3

a LIF techniques in combustion environments, Eckbreth (1996) lists six diatomic combustion radicals that are of interest in combustion and which are excited at wavelengths within the reach of current laser technology. These include CH, OH, CN, C_2, NH and NO. Each of these marks an unique region of the flame or post combustion gases depending on several factors: where it is produced, its lifetime, and the range of temperature over which it is stable. The only radical which exists in all three of the reactions of interest in the work (H_2 / O_2, H_2 / air, and CH_4 / O_2) is OH. Fortunately, OH has been shown to be a good marker of the flame front in turbulent diffusion flames (Seitzman et al. 1990 and Donbar et al. 2000) and it provides a comparison of the stoichiometric contours obtained in the nonreacting acetone PLIF work to those obtained in the reacting cases. One might be tempted, as in the nonreacting mixing study, to use a tracer as a flame marker. However most

tracer molecules, such as acetone, break down at temperatures far below the flame temperature and hence are a marker of a temperature isocontour and not the flame.

4.3.1 OH PLIF System

OH fluorescence was obtained by taking the 532 nm beam of a Nd:YAG laser (Spectra-Physics Quanta-Ray Lab 150) and passing it through a dye laser (Lumonics HD-500) containing Rhodamine 590 dye to produce a yellow beam at 566.02 nm with a linewidth of 0.06 cm^{-1}, based on manufacture specification. Using a doubling crystal the 566.02 nm beam was doubled to 283.01 nm and had a pulse energy of approximately 5 mJ. This beam excited the $Q_1(6)$ transition of the $A^2\Sigma^+ \leftarrow X^2\Pi(1,0)$ band of OH. The selection of this band is discussed in §4.3.2. The wavelength was verified using a wavelength meter (HighFinesse WS-6). After expanding the 283.01 nm beam with a 2:1 Galilean telescope, a cylindrical lens followed by a spherical lens was used to produce a sheet with a height of 35 mm and a thickness of 210 μm (FWHM).

Fluorescence was collected using a 16-bit intensified CCD (Princeton Instruments PI-MAX Gen II) camera. Images were taken at 5 frames per second with a 105 mm Nikkor UV lens operating at f/4.5. OH fluorescence was collected from the A-X(1,1) and (0,0) bands around 310 nm. The imaging portion of the CCD was reduced from 512 x 512 pixels to 400 x 300 pixels which correspond to an imaging window of 40 by 30 mm. The imaging window was further reduced during post processing. This camera setup resulted in a spatial resolution of 100 μm per pixel. A 100 ns gate was used along with WG-295 and UG-11 Schott glass filters to block scattering and flame luminosity. A diagram of the OH PLIF system is shown in Fig. 4.12.

Instantaneous sheet corrections were made by splitting off a portion of the sheet

and imaging the sheet in a cell filled with an optically thick mixture of Rhodamine 590. The distance between the splitter plate and the center test section and the splitter plate and dye cell were identical and therefore the sheet had the same thickness at both locations. To ensure that the dye mixture and CCD camera (Sony XCD-X710) used to image the sheet responded linearly to pulse energy a calibration measurement was performed. Figure 4.13 shows that the sheet measurement does respond linearly with pulse energy.

4.3.1.1 OH PLIF Timing

Due to heating of the experimental test section, runs were limited to 18 seconds during which 15 seconds were used to collect 75 images. Since the rocket run procedure was automated a timing system that could be initiated by the rocket control system was needed. The timing was accomplished by using a DG535 signal delay generator firing at 10 Hz to trigger both the flashlamps and Q-switch in the Nd: YAG laser. A third line from the DG535 was used as a trigger for the intensified camera. This DG535 line, however, had an electronic switch which the rocket control program opened after the ignition and stabilization of the rocket. After receiving the trigger pulse, the intensified camera sent out it's own trigger pulse to the sheet camera and then used an internal delay to open the gate for image acquisition. A second DG535 was used to condition the output pulse from the intensified camera so the sheet camera could be triggered. Due to limitations on readout time in the intensified camera at the CCD size used in this experiment, the intensified camera was only able to run at 6 Hz and consequently ignored every other trigger pulse. This limitation resulted in an imaging rate of 5 Hz. Triggering the sheet camera from the intensified camera ensured that the sheet camera was synchronized with

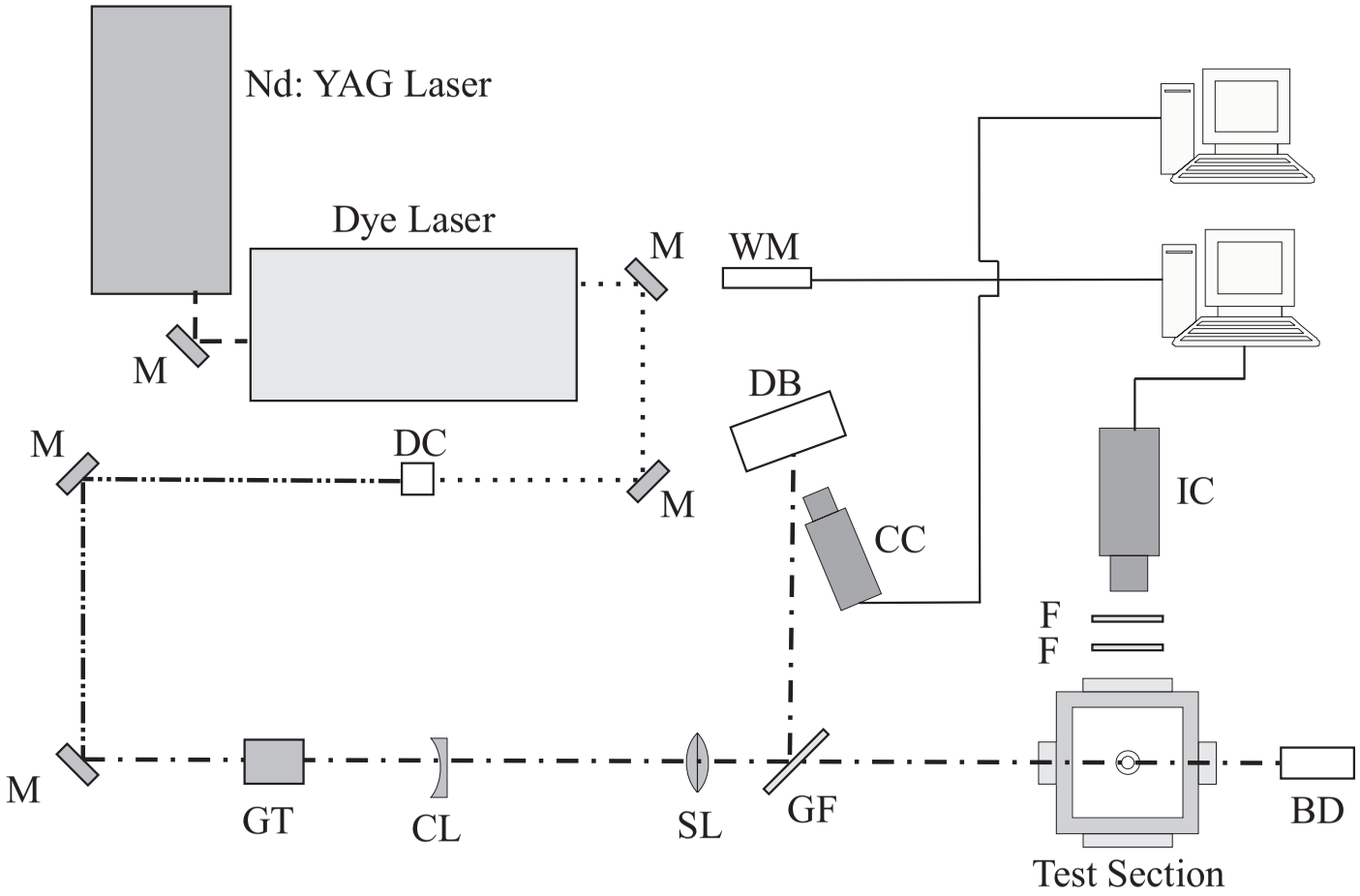

Figure 4.12: Laser and optical setup for OH PLIF measurements. BD - beam dump, CC - CCD camera, CL - cylindrical lens, DC - doubling crystal, DB - dye cell, F - filter, GF - glass flat, GT - Galilean telescope, IC - intensified camera, M - mirror, SL - spherical lens, WM -wavelength meter. $(- - -)$ - 532 nm , $(\cdots)$ - 566 nm, $(- \cdot -)$ - 283 nm.

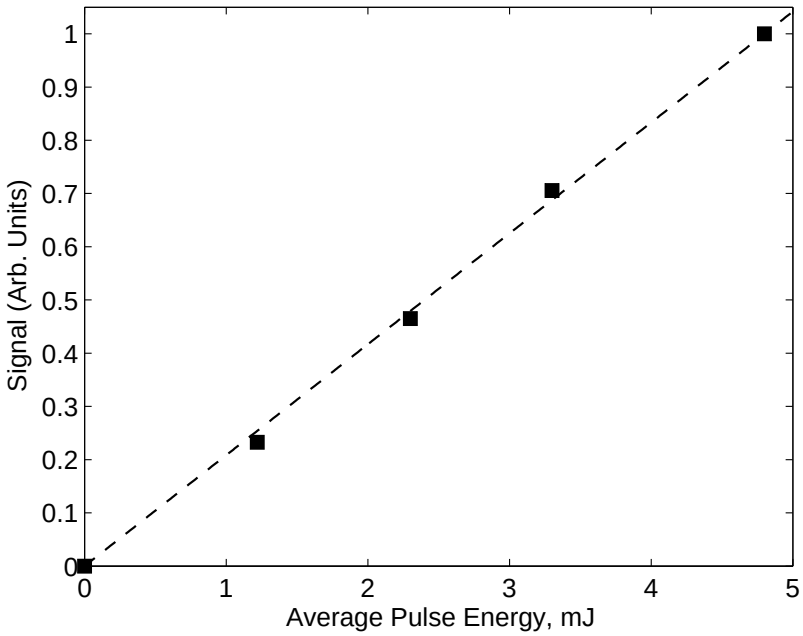

Figure 4.13: Signal calculated by integrating the sheet image in the dye cell versus averaged pulse energy showing the linearity of the optically thick mixture of Rhodamine 590 dye with increasing laser pulse energy.

the 5 Hz rate of the intensified camera. A wiring schematic of the timing system is illustrated in Fig. 4.14 and the corresponding timing diagram is shown in Fig. 4.15.

4.3.1.2 Correction Procedure

Images of OH signal were corrected in same manner as in the acetone PLIF work. Using Eq. 4.10, corrections were made for background signal, white field variations and variable sheet intensity. The background signal correction consisted of one image taken with the laser sheet blocked to capture any flame luminosity that is not blocked by the filters. A second image was taken with the laser firing but no flame present to capture any background light scattering. The white field correction was applied to each of these images which were summed to create a single background image. A dark noise image then was subtracted from this background image since otherwise in

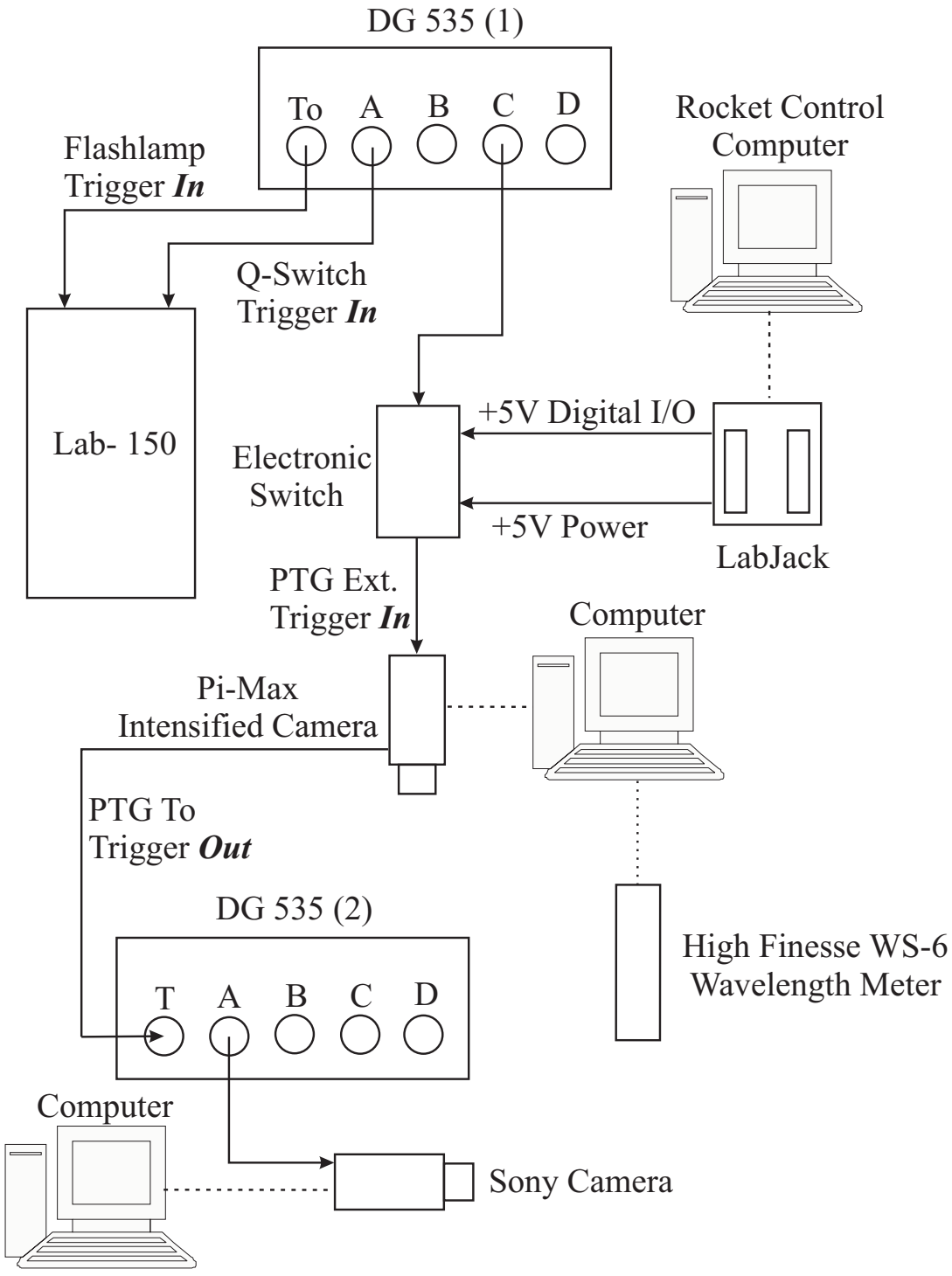

Figure 4.14: Schematic of wiring to synchronize the OH PLIF system. A DG535 firing at 10 Hz triggers the Nd: YAG laser and Intensified camera. A second DG535 is used to convert the output signal of the intensified camera to trigger the sheet imaging camera.

the final corrected image the dark noise would have been accounted for twice. The white field correction was obtained by imaging a frosted piece of glass using the room lighting which was found to produce a very uniform field. The dark noise correction was obtained by taking an image set with the lens cap on and using the same camera settings. Lastly, the sheet correction was obtained by integrating the signal across the imaged sheet to produce a sheet profile. This sheet profile then was transformed on to every column of pixels in the OH image by using another image for which the sheet was clipped on both ends well within the field of view of both cameras and using the sharp cutoff as reference points.

4.3.2 OH Line Selection and Relating the OH Signal to the Flame Front

When performing OH PLIF measurements it is important to select a transition that not only gives a large signal to noise ratio but also is relatively insensitive to gas temperature so the peak PLIF signal corresponds to the max OH value. This can be accomplished by choosing a higher ground state rotational level which tends to have a temperature insensitive Boltzmann distribution over the temperature range where OH exists (Singla et al. 2006). However, this is just half of the story. The quenching of OH also plays a large role in the temperature sensitivity of the band and has to be included as well. The quenching depends on the number density of collisional partners which is a function of the chemistry and therefore the strain rate. This is one reason why quantitative OH PLIF is so difficult unless simultaneous Raman scattering is used to measure the concentrations of the major species and the temperature. A method to evaluate the effect of the Boltzmann fraction and quenching is outlined for OH in a CH_4 / air flame by Barlow and Collignon (1991). This method was used to evaluate the $Q_1(6.5)$ transition of the $A^2\Sigma^+ \longleftarrow X^2\Pi(1,0)$

band used for the current OH measurements and the $Q_1(9.5)$ transition of the same vibrational band suggested by Singla et al. (2006) for LOX/GH_2 high pressure flames. In addition the OH quenching model of Garland and Crosley (1986) is compared with the Harpooned model of Paul (1994). Finally, a simulated PLIF signal is compared to the OH profile of a laminar strained counter-flow flame. Results showed that the $Q_1(6.5)$ transition is the best choice, especially for the current laser pulse energy. The method is outlined for H_2 / O_2 chemistry, but final results for H_2 / air and CH_4 / O_2 also are discussed.

4.3.2.1 Counter-Flow Flame Calculations

To calculate a simulated PLIF signal an accurate representation of the flame structure is needed, such as temperature and mole fraction profiles of all major species as a function of mixture fraction. One way to model the flame structure of a turbulent diffusion flame is to use a strained laminar flame in the form of a counter-flow flame calculation and vary the strain rate to correspond to the values found in the diffusion flame of interest. Strain rates (a) through out this section are defined at the stagnation point.

To meet the need for detailed knowledge of the flame, profiles of temperature and mole fraction for all major species and radicals were calculated using the OPPDIF code in Chemkin (Kee et al. 2006). Profiles were calculated for H_2 / O_2 chemistry at a pressure of 4.48 atm for a number of strain rates and are presented in Fig. 4.16. Equilibrium chemistry calculations are also included. Mixture fraction (f), as in the rest of this work, is defined to be unity in the oxidizer. The stoichiometric mixture fraction (f_S) is 0.89. Unlike most hydrocarbon reactions, H_2/O_2 chemistry is largely insensitive to strain rate as seen in Fig. 4.16. Because of this insensitivity to strain

rate, all calculations were performed using a strain rate of 192 inverse seconds.

4.3.2.2 Strategy for Evaluation of Transitions

In previous studies (Barlow et al. 1989 and Barlow and Collignon 1991), it has been shown that the linear fluorescence equation can be written for the OH concentration as

$$[OH] = C_{ref} C_Q C_f \left(\frac{\text{fluorescence signal}}{\text{laser energy}} \right), \tag{4.17}$$

where C_{ref} is a calibration constant based on a flat flame burner that approximates the adiabatic equilibrium flame condition and also accounts for PLIF system constants. C_f is the ratio of the ground-state Boltzmann population fraction at the adiabatic flame temperature to the ground-state Boltzmann population fraction at the local temperature in the turbulent diffusion flame. Also, C_Q is the ratio of the local quenching parameter over the quenching parameter at the adiabatic equilibrium flame condition.

To evaluate the different transitions a criterion is needed. The criterion used in this work is to minimize the difference between the strained laminar flame OH concentration profile and the simulated OH PLIF profile (Barlow et al. 1989). Using Eq. 4.17 the difference between the laminar flame concentration and the simulated LIF signal can be written as

$$\Delta[OH] = [OH]_{lf} - [OH]_{\text{uncorrected}} = [OH]_{lf} \left(1 - \frac{1}{C_Q C_f} \right), \tag{4.18}$$

where $[OH]_{lf}$ is the OH concentration from laminar flame calculations and the theocratical linear PLIF measurement or simulated PLIF signal that would be obtained if no corrections were applied is $[OH]_{\text{uncorrected}}$ (Barlow et al. 1989).

4.3.2.3 Calculation of C_f

As previously defined, C_f, the normalized Boltzmann distribution, is the percent of OH molecules that are at the proper vibrational and rotational ground energy level for excitation at the given wavelength. The method presented here to calculate the Boltzmann fraction follows the work of Lucht (2008). The Boltzmann fraction, f_B, can be written as

$$f_B = g_1 \frac{\exp\left[\left(\frac{\varepsilon_1}{hc}\right)\left(\frac{hc}{k_B}\right)/T\right]}{Z_{elec}Z_{vib}Z_{rot}}, \tag{4.19}$$

where $g_1 = 2J" + 1$ and J" is the ground rotational state and $\varepsilon_1/hc = B_0 J"(J" + 1) + \omega_e(V" + 1/2)$ where B_0 and ω_e are spectroscopic constants obtained from Luque and Crosley (1999) and where $V"$ is the ground state vibrational level. For all cases considered here, $V" = 0$. In addition, h is Planks constant, k_B is Boltzmann constant, c is speed of light and T is the absolute temperature. The partition functions for OH are

$$Z_{elec} = 4,\ Z_{Vib} = \frac{\exp\left(-\theta_{vib}/2T\right)}{1 - \exp\left(-\theta_{vib}/T\right)},\ Z_{rot} = \frac{k_B T}{hcB_0}, \tag{4.20}$$

where

$$\theta_{vib} = \frac{hc\omega_e}{k_B}. \tag{4.21}$$

Values for the spectroscopic constants are provided in Table 4.2.

Table 4.2: OH spectroscopic constants.

Name	Variable	Value	Units
Boltzmann Constant	k_B	1.38E-23	J/K
Planks Constant	h	6.63E-34	J*S
Speed of Light	c	2.998E10	cm/s
OH Spec. Constant	B_0	18.896	cm^{-1}
OH Spec. Constant	ω_e	3737.79	cm^{-1}

Singla et al. (2006) argue that the temperature sensitivity of the fluorescence signal is proportional to $f_B/\sqrt{T}$, and this inverse square root of temperature is related

to the collisional quenching in the fluorescence equation. Over the temperature range where OH exists (2500 K to 3300 K from Fig. 4.16), a difference of 25% and 38% was computed for J"=9.5 and J"=6.5 respectively as illustrated in Fig. 4.17*a*. However, using the method of Barlow and Collignon (1991) to calculate C_f and C_Q, the separate effects of Boltzmann fraction and quenching can be calculated. C_f is the same Boltzmann fraction calculated in Fig. 4.17*a* except that it is normalized by the Boltzmann fraction calculated at the reference condition. C_f is plotted against mixture fraction in Fig. 4.17*b*.

4.3.2.4 Calculation of C_Q

C_Q is defined as the local collisional quenching parameter divided by the collisional quenching parameter at the reference condition,

$$C_Q = \left(\frac{Q_{21}}{Q_{21,ref}} \right). \tag{4.22}$$

The quenching rate can be expressed as

$$Q_{12} = C_{CQ} \sum_i \left(X_i (T M_i)^{-1/2} \sigma_i(T)) \right), \tag{4.23}$$

where C_{CQ} is a constant, X_i are the collision partners mole fractions, M_i are the molecular weights and $\sigma_i(T)$ are the temperature dependent collisional quenching cross sections with OH. All parameters are known from the counter-flow flame calculations except the quenching cross sections. Two methods exist to calculate the collisional cross sections for OH. The first is by Garland and Crosley (1986) and the second is the Harpooned model of Paul (1994). The cross sections of H_2O, O_2 and H_2 for the two methods are plotted in Fig. 4.18.

Experimental data presented by Paul (1994) shows the Harpooned model performs slightly better then the Garland & Crosley models, but the experimental data

is scattered and not complete, which makes a comparison difficult. However, the Harpooned model is more physics based and was used for the calculation of C_Q in this work. It should be noted that Garland and Crosley state a 30-50% accuracy for their model and only a slight improvement should be expected for the Harpooned model though no error estimate is provided. Both methods assume that the OH is in the V'=0 vibrational state while the exited state used in the current measurement is V'=1. However, for H_2 / O_2 chemistry H_2O is the dominate quencher and results presented by Paul (1994) show the Harpooned method for V'=0 is in good agreement with V'=1 experimental results. This is also true for CH_4 / O_2 and H_2 / air. Neither method addresses OH as a self quencher which could be a source of error do to the large mole fractions of OH in the flame for H_2 / O_2 chemistry. For completeness, the curve fit for the Harpooned model is given as

$$\sigma_i \equiv P_A C_0 \{(1+h_c)\exp(-h_c) + C_1 h_c^{2/\alpha} \gamma(2-2/\alpha, h_c)\}, \tag{4.24}$$

where $h_c \equiv C_2 T_r/T$ and P_A, C_0, C_1, C_2, α and T_r are curve fit constants listed in Table 4.3 (Paul 1994). Collisional partners for CH_4 / O_2 and H_2 / air also are included. γ is the incomplete gamma function. The calculated C_Q profile is provided in Fig. 4.17*c*.

Table 4.3: OH quenching curve fit parameters from Paul (1994).

M	P_A	C_0	C_1	C_2	α	T_r
H_2O	1.120	15.955	2.251	4.302	3.12	300
H_2	0.330	12.848	1.360	3.079	3.50	300
O_2	0.537	14.892	1.327	3.866	3.95	300
H	1.038	13.763	1.347	1.399	4.00	300
O	1	13.959	1.452	2.067	5.20	300
CH_4	0.826	16.561	1.109	3.591	3.05	300
CO	0.846	14.536	1.664	6.206	4.60	300
CO_2	0.770	15.418	1.391	8.205	3.22	300

4.3.2.5 Line Selection Results

As previously stated, the criteria for selecting a transition is one that minimizes the distortion to the OH concentration profile (peak signal location matches max OH concentration location). In this spirit the difference between the simulated PLIF profile and the laminar flame profile normalized by the max OH concentration is shown in Fig. 4.19*a* for H_2 / O_2. From Fig. 4.19*a* the error for J"=6.5 is approximately 20% and 21% for J"=9.5. Hence, J"=6.5 appears to be the better choice, but the difference is so minimal the choice of transition comes down to experimental difficulty. With the current system a 60% loss in pulse energy was found between the J"=6.5 to J"=9.5 transition, making J"=6.5 the logical choice.

When looking at OH images and trying to determine the stoichiometric contour it is important to know how the PLIF signal relates to actual OH concentration profile, which is shown in Fig. 4.19*b* for H_2 / O_2. Fig. 4.19*b* again illustrates no real difference between the two transitions and shows a 16% increase in peak OH mole fraction and a shift of approximately 0.01 mixture fraction towards the lean side of the flame. This increase in peak value is arbitrary since the constant C_{ref} is unknown and assumed to be equal to one. However, the location and shape of the profile is correct and the stoichiometric contour occurs at 67% of the peak signal on the rich side of the flame.

In addition to looking at the effect of the excitation line on the PLIF signal for H_2 / O_2 chemistry, the same was done for H_2 / air at 5.3 atm and CH_4 / O_2 at 4.8 atm. Profiles for temperature, water and OH mole fraction for H_2 / air at varying strain rates were calculated and are shown in Fig. 4.20*a*-*c*. Unlike for H_2 / O_2, increasing strain rate does increase the OH mole fraction, but does not shift the peak location and therefore the relation of the peak signal to the stoichiometric value is indepen-

dent of the strain rate. The difference between the simulated PLIF profile and the laminar flame profile normalized by the max OH concentration demonstrates that the difference in error between J"=6.5 and J"=9.5 is small but J"=9.5 does better by about 1%. Again given the much higher pulse energy available at J"=6.5 this 1% better performance is not enough to use J"=9.5. Figure 4.20*e* shows that for H_2 / air the stoichiometric contour occurs at 94% of the peak signal on the rich side of the flame.

Like H_2 / O_2, CH_4 / O_2 chemistry is largely insensitive to strain rate over the mixture fraction range where OH exists (Fig. 4.21*a*-*c*). Again the difference in error between the two transitions is minimal and the choice of the J"=6.5 comes down to experimental considerations (Fig. 4.21*d*). Figure 4.21*e* illustrates that for CH_4 / O_2 the stoichiometric contour occurs at 74% of the peak signal on the rich side of the flame.

4.4 Cinema Chemiluminescence

Imaging flame chemiluminescence is one of the simplest optical diagnostics which can be applied to flames. Chemiluminescence is the result of heat release which excites combustion species or soot particles which then emit radiation. In H_2 / O_2 combustion, which contains no carbon, the only species which emit radiation are OH, O_2 and H_2O. H_2 / O_2 combustion was the only reaction investigated with this method. Unlike PLIF which is a planar method, chemiluminescence imaging results in a line of sight integration which provides some information about the three dimensionally of the flame.

In an effort to understand the breakup process at the tip of H_2 / O_2 turbulent

coaxial jet diffusion flames, cinema chemiluminescence was utilized. Chemiluminescence images were obtained using a Vision research Phantom v9.0 high speed CMOS camera operating at approximately 9,000 Hz with an exposure time of 21-31 μs. A 50 mm Nikkor lens operating at f/1.2 (non UV Grade) was used and therefore all wavelengths below approximately 400 nm were blocked. This eliminates OH* as a contributor to the chemiluminescence since the most intense bands of OH* are at 306.4 nm and 281.1 nm which are below the 400 nm limit (Gaydon 1994). Oxygen has six bands of medium intensity between 391 and 438 nm which contribute; however, the main portion of the chemiluminescence captured with the experimental setup is from H_2O, that has 26 distance bands between 570 and 810 nm captured within the range of the lens and camera (Gaydon 1957). Oxygen will be contained inside of the flame, however H_2O as a combustion product will exist on both the fuel and oxidizer side of the flame and in the recirculation zones radially outside the flame. Fortunately temperatures near the flame temperature are required for H_2O to emit. Results in §6.1.2 will show that the radial width of the chemiluminescence signal was approximately the same as that of the OH contours and gaps in the chemiluminescence signal (where the tip of the flame forms pockets of oxidizer) correspond to gaps seen in the OH contour images. Therefore the chemiluminescence signal is believed to be a good marker of the flame.

4.5 Experimental Conditions

Experimental test cases are divided into data groups. Within each group, data were taken for the same injectants, injector geometry, chamber pressure, and for either reacting or nonreacting cases, but the velocity ratio was varied. Each group

contains between three and six different turbulent coaxial jets. The symbols NR and R stand for nonreacting and reacting respectively. In the subsections below the properties of the groups for reacting and nonreacting conditions as a whole are listed along with the range in which the velocity ratio was varied. Subscript i is used to denote inner jet properties and e is used to denote outer jet properties. The thickness of the injector post is denoted as T_P. The Reynolds number (Re) is based on a theoretical jet with external jet fluid properties and a velocity that provides the same total momentum flux as the actual coaxial jet with the injector post thickness ignored,

$$\mathrm{Re} = \frac{\rho_e d_e u_e}{\mu_e} \times \left[1 + \frac{1-M}{M}\left(\frac{d_i}{d_e}\right)^2\right]^{\frac{1}{2}}. \tag{4.25}$$

4.5.1 Nonreacting Conditions

Test conditions for nonreacting cases are divided into 13 groups whose properties are listed in Table 4.4. Data groups were designed to vary one parameter at a time. Parameters which were varied include; density ratio, injector geometry, confinement, Reynolds number and absolute velocity difference. The notes column in Table 4.4 describes how each group was changed from the three baseline cases. Each baseline case has the same geometry but a different outer fluid (He, H_2, or CH_4). The inner jet fluid always is air that is seeded with acetone. Changes in the density ratio (S) for the same fluid indicate a change in the seeding level. This test matrix consists of 61 distinct jets. Results of varying these parameters in the nonreacting turbulent coaxial jet case are discussed in Chapter V. Experimental properties and mixing lengths for all 61 nonreacting coaxial jets are provided in Appendix A.

Table 4.4: Nonreacting coaxial jets: experimental data groups.

Group	Symbol	S	r_u	M	d_e, mm	d_i, mm	T_P, mm	X_s	Re	P_C, atm	Outer/Inner	Notes
NR1	■	0.118	10.3-1.1	12.6-0.14	7.5	3.0	0.89	0.49	3,200-3,700	0.98	He/air	Baseline He
NR2	○	0.118	4.6-1.5	2.5-0.28	7.5	3.0	0.89	0.49	2,400-5,700	0.98	He/air	Constant u_i
NR3	▲	0.118	4.8-2.4	2.7-0.69	7.5	3.0	0.89	0.49	4,300-4,700	0.98	He/air	Constant u_e
NR4	△	0.118	4.8-1.1	2.7-0.14	10.0	3.0	0.89	0.49	3,900-6,000	0.98	He/air	Large d_e
NR5	◇	0.119	4.9-2.4	2.8-0.72	7.5	3.7	0.54	0.49	3,700-6,500	0.98	He/air	Large d_i
NR6	□	0.119	11.0-1.1	14.4-0.14	7.5	3.0	0.89	0.49	3,200-3,700	0.98	He/air	Unconfined
NR7	◁	0.132	4.7-1.1	2.9-0.16	7.5	3.0	0.89	0.52	13,000-14,000	3.76	He/air	Pressurized
NR8	▼	0.133	5.1-1.1	3.4-0.16	7.5	3.0	0.89	0.52	18,000-20,000	5.40	He/air	Pressurized
NR9	▶	0.059	9.6-1.1	5.4-0.07	7.5	3.0	0.89	0.32	2,800-13,000	0.98	H_2/air	Baseline H_2
NR10	◀	0.059	9.5-1.9	5.3-0.21	6.7	3.4	0.72	0.32	4,400-8,300	0.98	H_2/air	Small d_e
NR11	▷	0.060	9.7-1.1	5.5-0.07	7.5	3.0	0.89	0.33	2,700-13,000	0.98	H_2/air	Unconfined
NR12	●	0.464	4.8-2.4	10.6-2.7	7.5	3.0	0.89	0.65	18,000-35,000	0.98	CH_4/air	Baseline CH_4
NR13	▽	0.471	1.9-1.4	1.7-0.88	6.7	3.4	0.72	0.65	12,000-14,000	0.98	CH_4/air	Small d_e

4.5.2 Reacting Conditions

Test conditions for reacting turbulent coaxial jets are divided into 5 groups, whose properties are listed in Table 4.5. Three fuel/oxizider combinations were explored; H_2 / O_2, H_2 / air, and CH_4 / O_2. For H_2 / O_2, three chamber pressure were studied; 0.98, 4.5 and 8.5 atmospheres; each corresponds to a different Reynolds number range. In addition, two different injectors were used; one for H_2 / O_2 and the other for H_2 / air and CH_4 / O_2. A discussion of the results of these experimental measurements is provided in Chapter VI. The reacting flow test matrix encompasses 20 distinct coaxial jets. Experimental properties and mixing lengths for each reacting case are provided in Appendix B.

4.6 Laser Doppler Velocimetry

In an effort to characterize the inflow boundary conditions, Laser Doppler Velocimetry (LDV) was used to measure the inlet velocity and turbulence intensity profiles. Using a Coherent Innova 90C argon laster operating at 514.5 nm and a TSI IFA655 digital burst correlator, measurements were made in two He/air coaxial jets ($S = 0.14$). Seeding was accomplished by using titanium dioxide particles in seeders installed in both the oxidizer and fuel lines. Seeding density was controlled by changing the percentage of the flow that bypassed each seeder. The LDV system was mounted on a translation stage so profiles could be obtained while the rocket was held stationary on its stand. Grooves were machined into the injector face plate in an attempt to get the interrogation volume within approximately $1d_i$ of the injection plane. The inner jet diameter (d_i) is 3.4 mm for both cases. Using photographic film, the intersection of the two beams was measured, which indicates that the in-

Table 4.5: Reacting coaxial jets: experimental data groups.

Group	Symbol	S	r_u	M	d_e, mm	d_i, mm	T_P, mm	X_s	Re	P_C, atm	Outer/Inner
R1	●	0.063	6.3-1.9	2.5-0.23	6.7	3.4	0.72	0.33	4,300-6,800	0.98	H_2/O_2
R2	■	0.063	8.4-2.5	4.4-0.41	6.7	3.4	0.72	0.33	30,000-52,000	4.5	H_2/O_2
R3	○	0.063	5.3-2.7	1.8-0.45	6.7	3.4	0.72	0.33	55,000-76,000	8.5	H_2/O_2
R4	◁	0.070	3.0-2.1	0.64-0.31	5.8	3.4	0.72	0.71	22,000-25,000	4.8	H_2/air
R5	◇	0.553	2.4-1.6	3.1-1.4	5.8	3.4	0.72	0.67	45,000-56,000	5.3	CH_4/O_2

terrogation volume is cubic with a side length of approximately 0.5 mm. Case 1 has a velocity ratio (r_u) of 5 with inner and outer average velocities of 17 and 86 m/s respectively. The average velocity profile for case one is shown in Fig. 4.22a and the turbulence intensity profile in Fig. 4.22b. Case 2 has a velocity ratio of 2 with absolute velocities of 31 and 62 m/s. The average velocity profile is shown in Fig. 4.22c and the turbulence intensity profile is shown in Fig. 4.22d. The dash-dot line in the average velocity profiles represent the turbulent pipe flow solution using the law of the wall as outlined by White (1991).

Average inlet velocity profile for both cases (Figs. 4.22a and b) illustrate that the inner jet velocity profile is well approximated by a fully-developed pipe flow profile. In addition, for both cases the outer jet velocity has already decreased from its peak value and has spread out beyond the injector, indicating that rapid mixing is already taking place $1d_i$ downstream of the injector exit. A word of caution is necessary when the profiles between the two jets and beyond the outer injector are examined. If the seeding levels of the two jets are not equal, the LDV measurement will be biased and will be closer to the velocity of the flow that is more heavily seeded. During data acquisition, efforts were made to try to keep the seeding level about the same in both flows, as verified visually but this is a vary imprecise measure. Near the outer edge of the outer jet, the ambient fluid does not have any seed and hence the velocity will be biased towards higher speeds. For this reason the velocity profile on the outer side of the annular jet in Fig. 4.22c is of questionable accuracy.

Average turbulent intensity profiles for both cases (Figs. 4.22c and d) indicate values of approximately 10% on the jet centerline. These values are higher than the values of 6 to 7% that are typically associated with turbulent pipe flow. Between the jets where the shear layer mixing is taking place, the turbulent intensity peaks

at 50% before falling to approximately 37% in the outer jet. The large values of turbulent intensity in the outer jet suggest that at $x = 1d_i$ intense mixing is already taking place.

Efforts were made to take additional LDV measurements with the windows on at elevated pressures. Particle seed adhered to the windows and the seeders pulsed at elevated pressures, which made these measurements unusable.

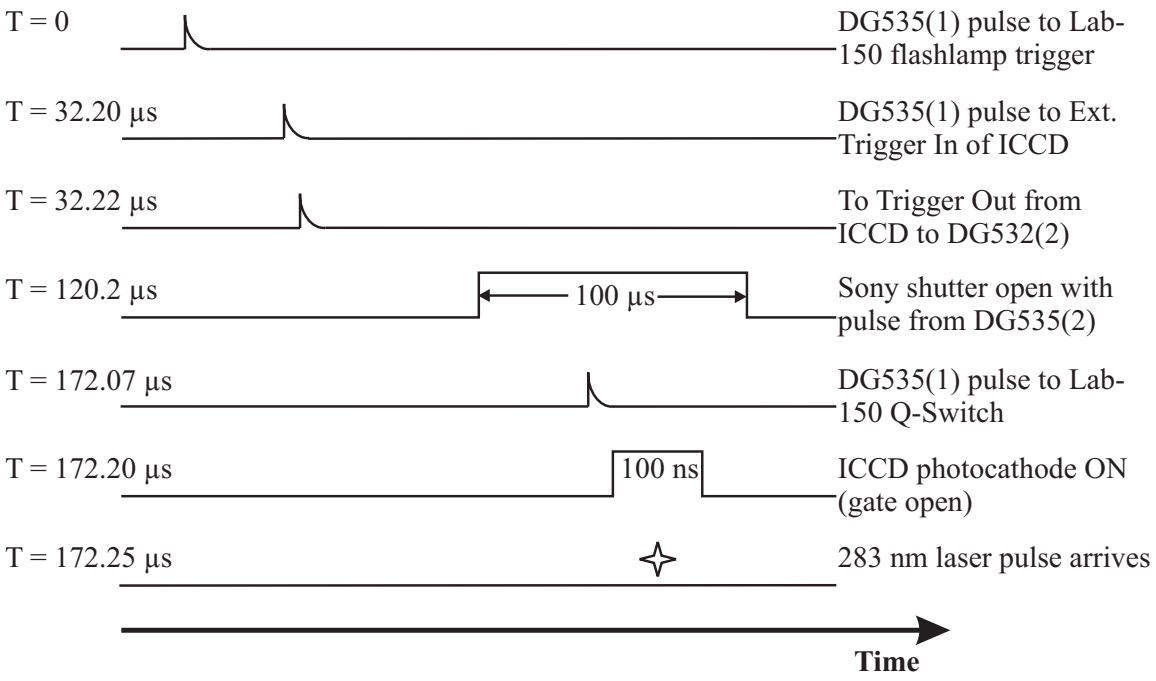

Figure 4.15: Timing diagram used to synchronize the intensified camera, sheet imaging camera and laser in the OH PLIF setup.

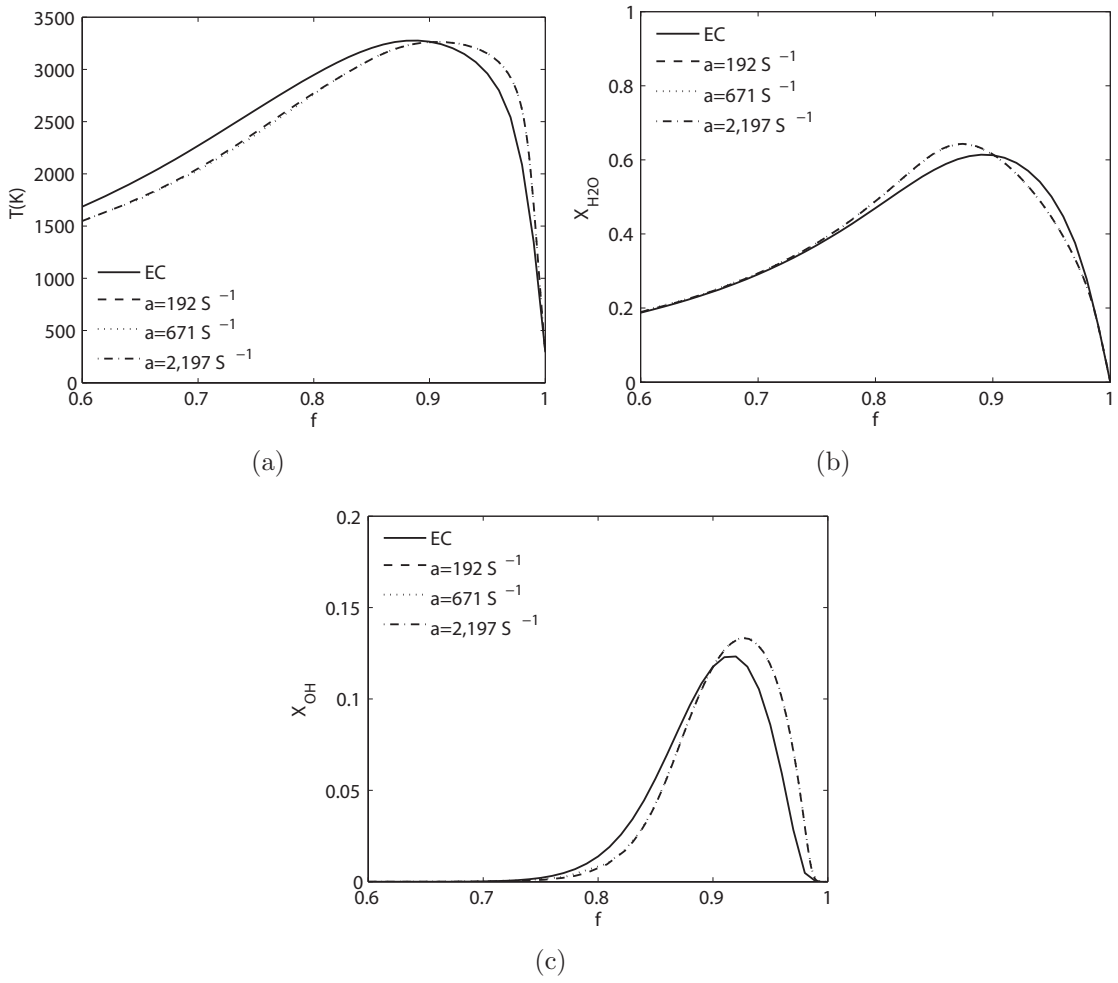

Figure 4.16: Calculated profiles of temperature (a), H_2O mole fraction (b), and OH mole fraction (c) versus mixture fraction for H_2 / O_2 chemistry at various strain rates (a) in a counter-flow flame and for equilibrium chemistry, EC.

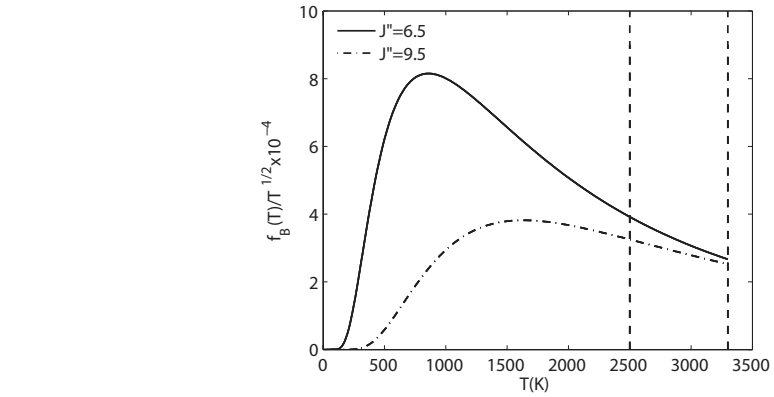

(a)

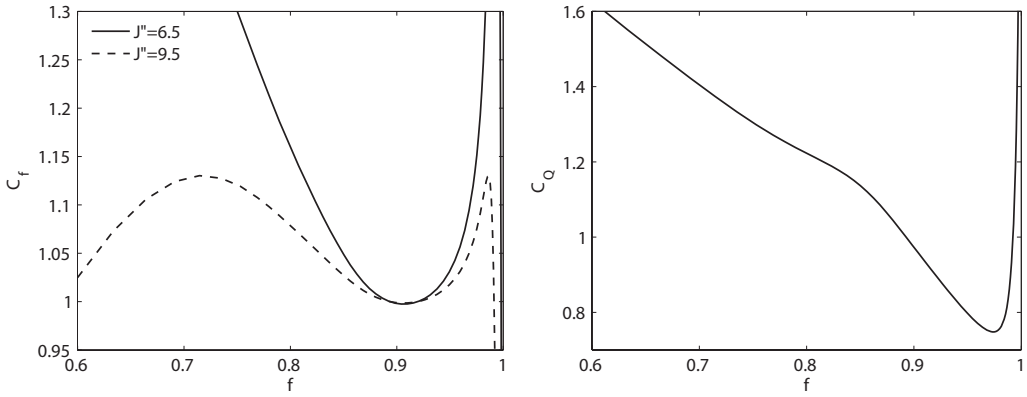

(b) (c)

Figure 4.17: Boltzmann fraction calculations for J"=6.5 and J"=9.5 divided by $\sqrt{(T)}$ (a) and normalized by the Boltzmann fraction calculated for the adiabatic flame condition, C_f (b). Calculated C_Q profile for H_2/O_2 chemistry using the Harpooned model for collisional cross sections (c).

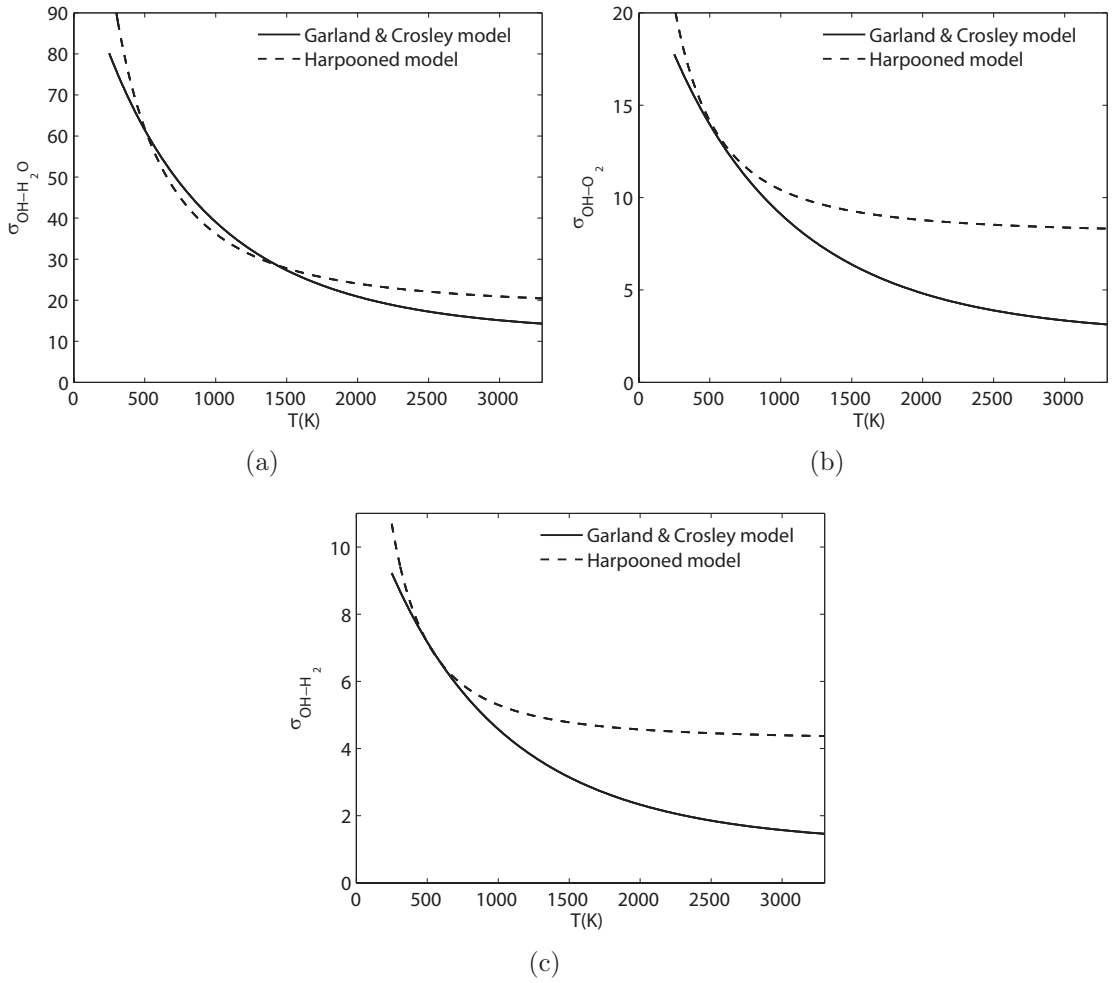

Figure 4.18: Collisional cross sections of OH with H_2O (a) , H_2 (b) and O_2 (c) calculated using the Harpooned and Garland & Crosley models.

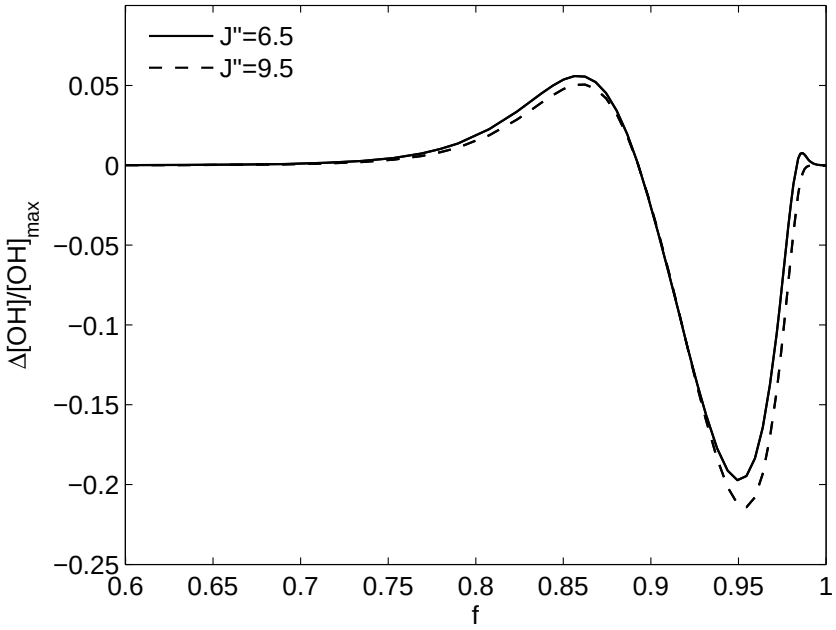

(a)

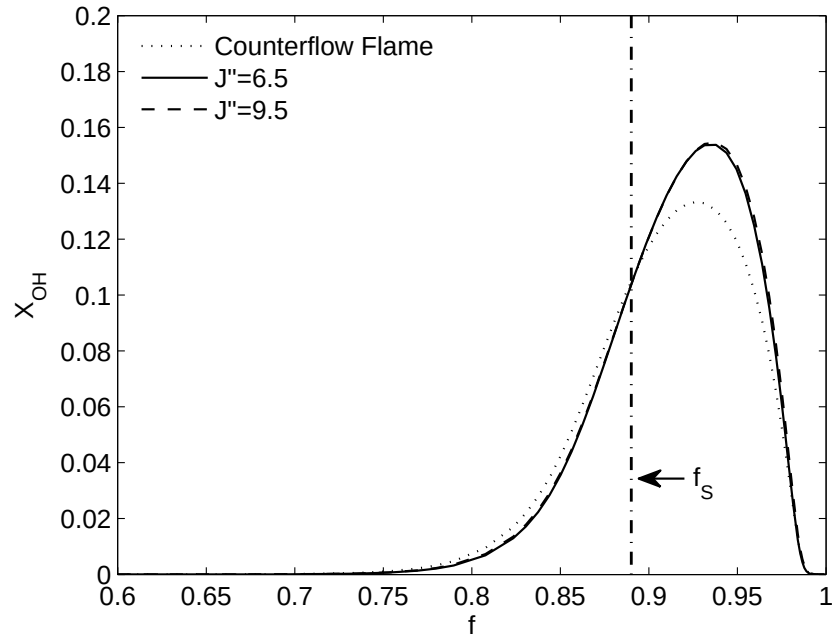

(b)

Figure 4.19: Profiles of $\Delta[OH]/[OH]_{max}$ for H_2/O_2 chemistry (a). OH mole fraction profiles for strained counter-flow flame and simulated PLIF signals for J"=6.5 and 9.5 transitions (b). Strain rate is 193 1/s.

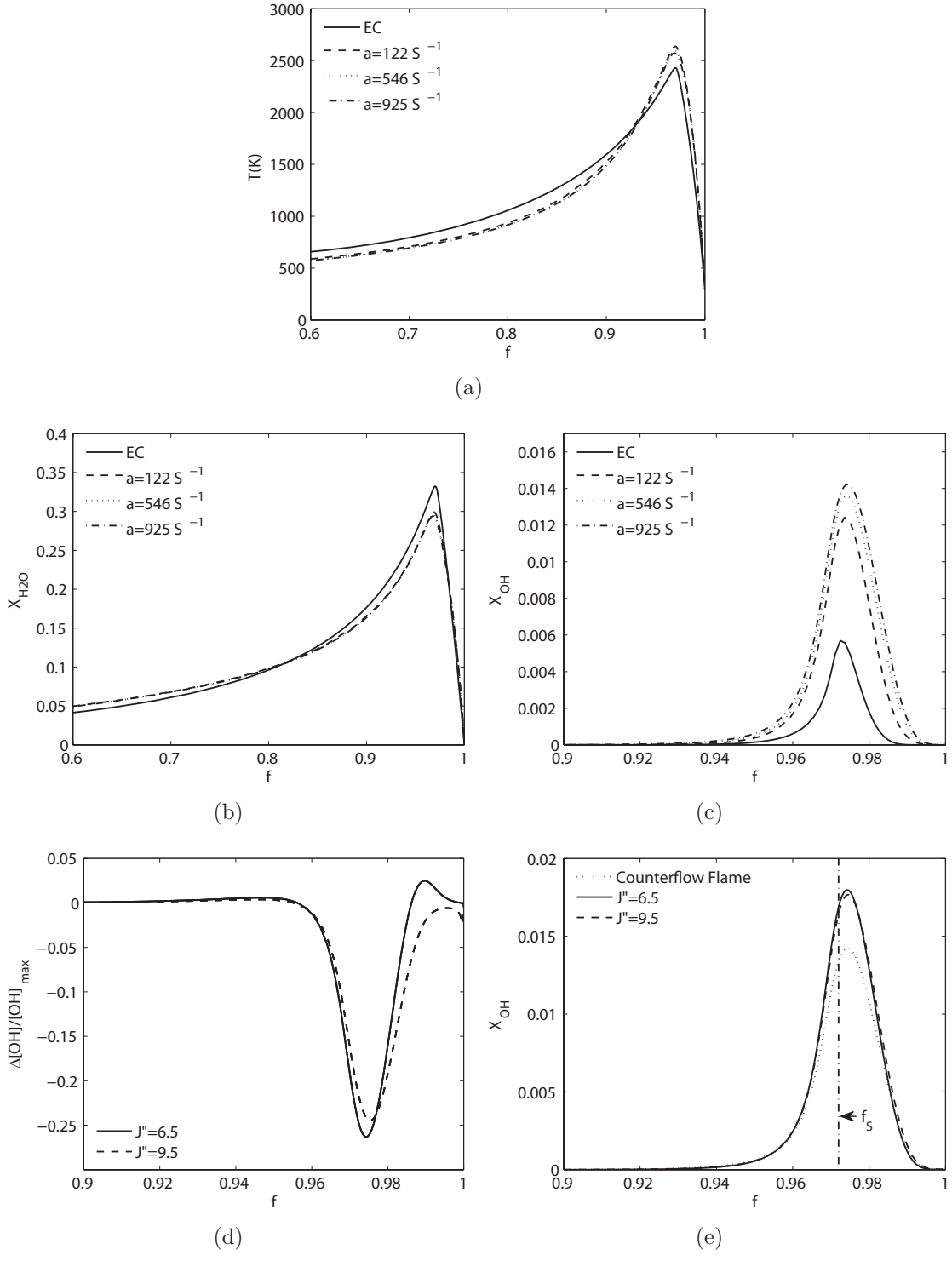

Figure 4.20: H_2 / air Calculated profiles of temperature (a), H_2O mole fraction (b), and OH mole fraction (c) versus mixture fraction at various strain rates in a counter-flow flame and for equilibrium chemistry, EC. Also profiles of $\Delta[OH]/[OH]_{max}$ (d) and OH mole fraction profiles for strained counter-flow flame and simulated PLIF signals for J"=6.5 and 9.5 transitions (e). Strain rate in (d) and (e) is 546 1/s.

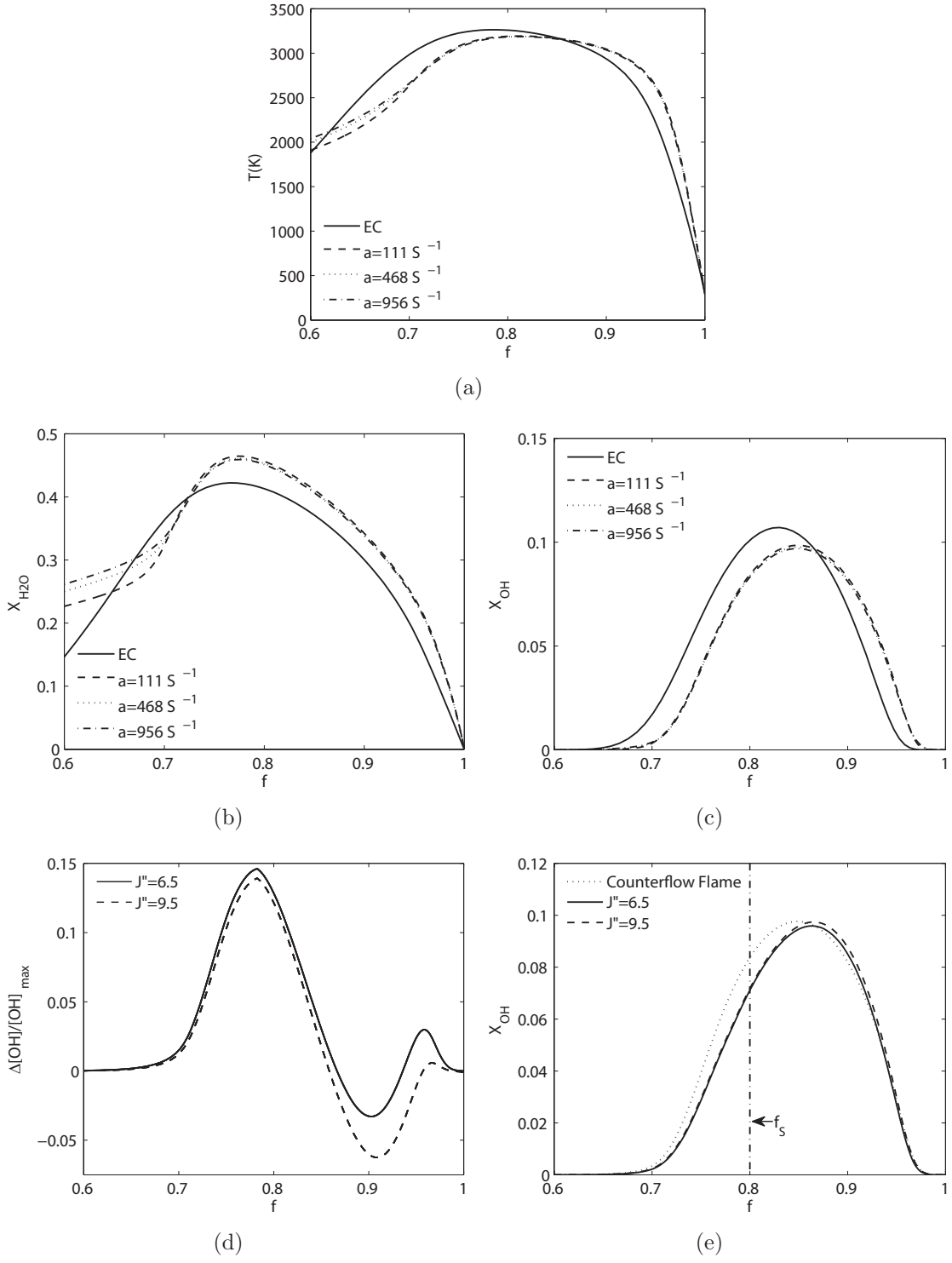

Figure 4.21: CH_4 / air Calculated profiles of temperature (a), H_2O mole fraction (b), and OH mole fraction (c) versus mixture fraction at various strain rates in a counter-flow flame and for equilibrium chemistry, EC. Also profiles of $\Delta[OH]/[OH]_{max}$ (d) and OH mole fraction profiles for strained counter-flow flame and simulated PLIF signals for J"=6.5 and 9.5 transitions (e). Strain rate in (d) and (e) is 468 1/s.

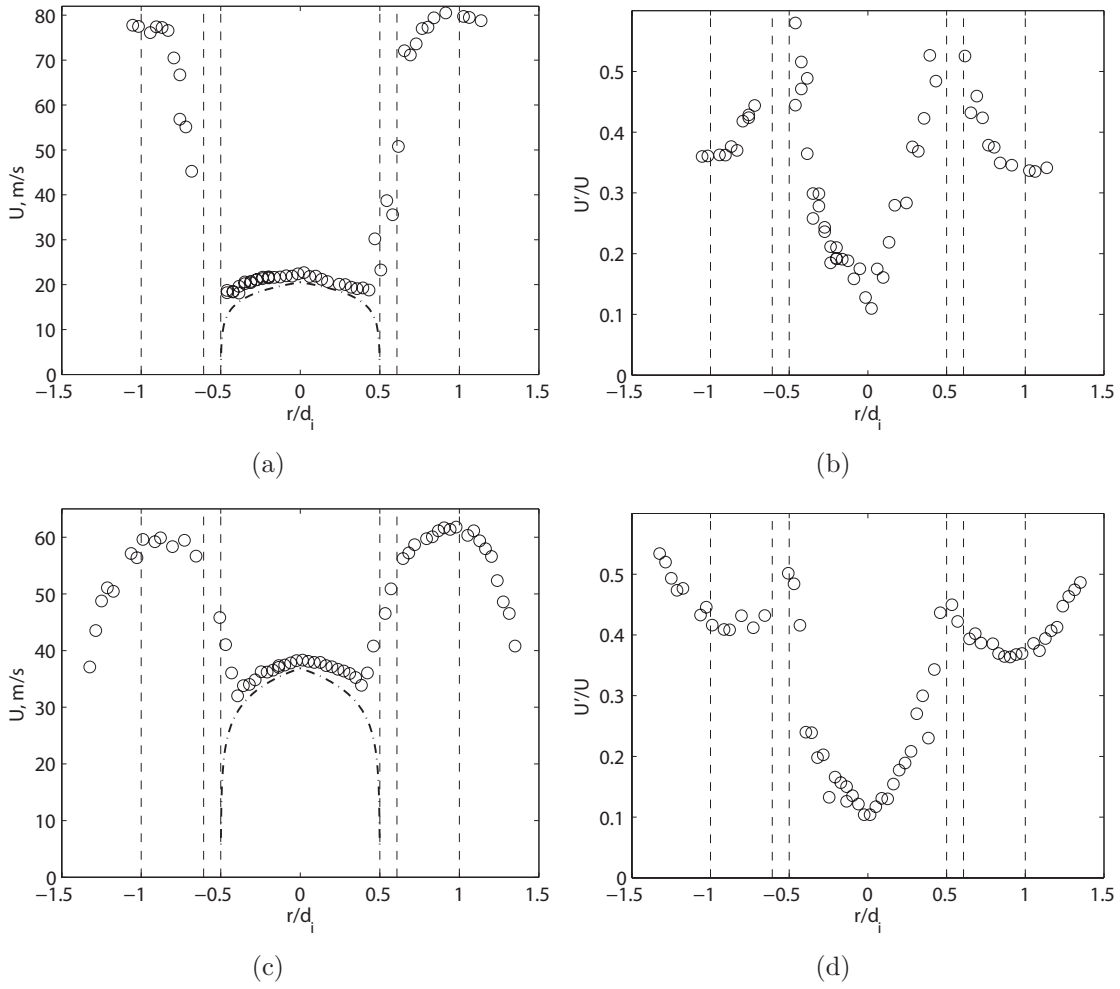

Figure 4.22: Inlet velocity and turbulence intensity profiles for two He/air coaxial jets with an injector geometry of $d_e = 6.73$, $d_i = 3.36$ and $T_P = 0.74$ mm at 0.98 atm. For case 1, (a) and (b), $r_u = 5$, $u_i = 17$ and $u_e = 86$ m/s. For case 2, (c) and (d), $r_u = 2$, $u_i = 31$ and $u_e = 62$ m/s. Vertical lines represent the injector geometry. The dash-dot line in the average velocity profiles represents the turbulent pipe flow solution.

CHAPTER V

Results for Nonreacting Turbulent Coaxial Jets

One major objective of this work is to obtain scaling relations for the stoichiometric mixing length of nonreacting coaxial jets, and to investigate whether those results can be rescaled based on fundamental principles to predict the flame lengths of reacting cases. Time-averaged and instantaneous mixture fractions fields were measured in coaxial jets using quantitative Acetone PLIF. The stoichiometric length (L_S) was defined as the axial distance at which the mixture fraction on the jet centerline had reached the stoichiometric value. Values of mixing length were used to test the mixing models described in Chapter II. Additionally, the effects of individual parameters such as the velocity ratio, density ratio, injector geometry, confinement, and Reynolds number on coaxial jet development and stoichiometric mixing length are explored. A comparison is made with coaxial jet core length data from prior studies. Best fit constants were determined for the momentum flux ratio mixing model along with a discussion of the limits at which the momentum flux ratio model is no longer applicable. The test matrix for the data used in this section is provided in Table 4.4.

5.1 Mixture Fraction Fields

Using the Acetone PLIF technique described in §4.2, average and instantaneous mixture fraction fields were obtained for nonreacting coaxial jets. Representative examples of average and instantaneous mixture fraction fields are shown in Fig. 5.1, with the examples shown corresponding to data group NR8 consisting of He/air coaxial jets (He outer and air inner) at a chamber pressure of 5.40 atm. The mixture fraction (f) throughout this work is defined as the mass fraction of the inner jet fluid, which in these experiments was always the oxidizer. The white line in these images represents the contour of stoichiometric mixture fraction $f = 0.89$ that corresponds to pure hydrogen and oxygen chemistry. Since this is a confined environment, the ambient fluid is a the f-value that corresponds to complete mixing of the two injectants. This value of f in the ambient fluid increases as the velocity ratio is decreased because relatively more inner fluid is injected.

The average mixture fraction field in Fig. 5.1 shows that the flow field is symmetric. The growth of both the inner and outer mixing layers can clearly be seen. Also from the average mixture fraction it is clear that the stoichiometric mixing length (L_S) is increasing as r_u approaches one. This agrees with the trend seen for the potential core in previous studies and with the mixing models presented in Chapter II. Instantaneous images of mixture fraction show a jet base with small wrinkles which grow as they progress downstream. Near the tip these wrinkles become large enough to break pockets of fluid from the main jet. In planar diagnostic methods such as PLIF, there is always the possibility that such pockets are not detached from the main jet but a part of the jet which has deflected out and then back into the measurement plane. However, chemiluminescence of reacting coaxial jets show

that portions of the main jet are detached from the flame tip and it is hypothized that the pockets seen in the images of Fig. 5.1 are the nonreacting equivalent since combustion does not fundamentally alter large scale mixing. It should also be noted that the images presented in Fig. 5.1 are a combination of images from two different window locations and hence in the instantaneous images the top and bottom sections of the image do not correspond to the same instance in time.

In the rest of this chapter average mixture fraction fields are used to define mixing lengths based on the centerline mixture fraction values. The effect of different flow field and geometric parameters are explored. Instantaneous images are used to obtain centerline and radial profiles of the RMS fluctuation of mixture fraction (f') and to explore if any difference exists between L_S calculated from the average flow field image and the average L_S of the instantaneous flow field images.

5.1.1 Average Mixing Length

In turbulent shear mixing, such as a coaxial jets, large scale turbulent structures play an important role in mixing. As these structures progress downstream their size increases. At some point downstream they become large enough that they can entrain large quantities of outer jet or ambient fluid to the centerline of the jet causing the local mixture fraction to decrease to a value below the stoichiometric value. Fluid downstream of this location which still has a mixture fraction value above the stoichiometric value then is cut off from the main jet. A pocket is formed, as shown in Fig. 5.1e. Since these pockets are infrequent and leave voids in the stoichiometric contour in an image of the average mixture fraction these pockets are averaged out and this results in a shorter mixing length than one that is determined by taking the average of instantaneous mixing lengths. To explore this effect, the stoichiometric

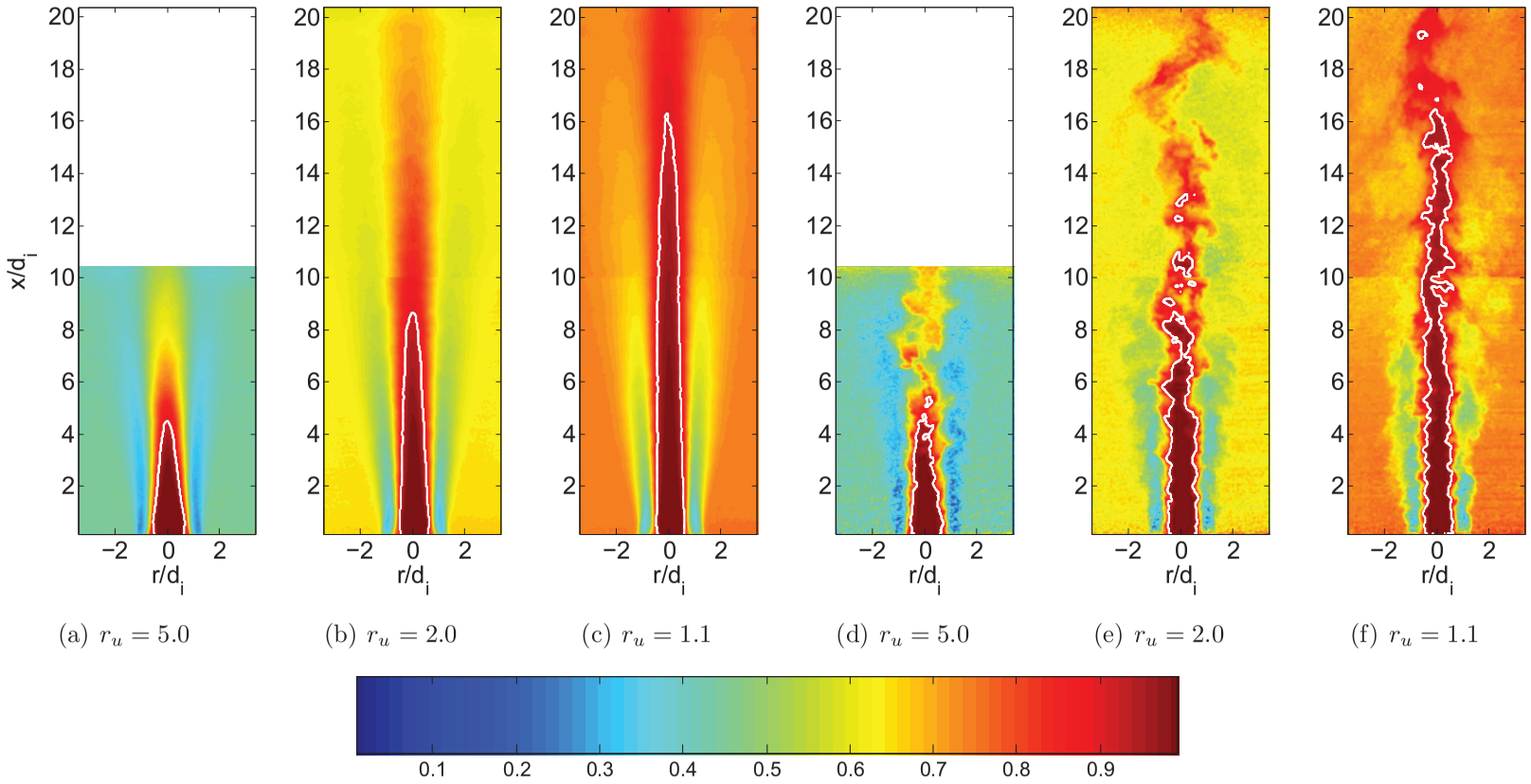

(a) $r_u = 5.0$ (b) $r_u = 2.0$ (c) $r_u = 1.1$ (d) $r_u = 5.0$ (e) $r_u = 2.0$ (f) $r_u = 1.1$

Figure 5.1: Time averaged (a)-(c) and instantaneous (d)-(f) mixture fraction fields of nonreacting turbulent coaxial jets for varying velocity ratios (r_u) obtained using acetone PLIF. Inner jet fluid is acetone seeded air and annular jet fluid is helium, corresponding to group NR8. Images from two window locations, (x/d=0-10 and x/d=10-20) are superimposed.

mixing lengths for three data groups (NR1, NR8 and NR9) were calculated from both the average mixture fraction and from the average of the instantaneous individual mixing lengths. A comparison of the calculated length for these two methods is presented in Fig. 5.2. The dashed line represents conditions for which the two measurements are equal, and the solid line is a best fit through the origin to the actual measurements. The same 180 images were used for both measurements.

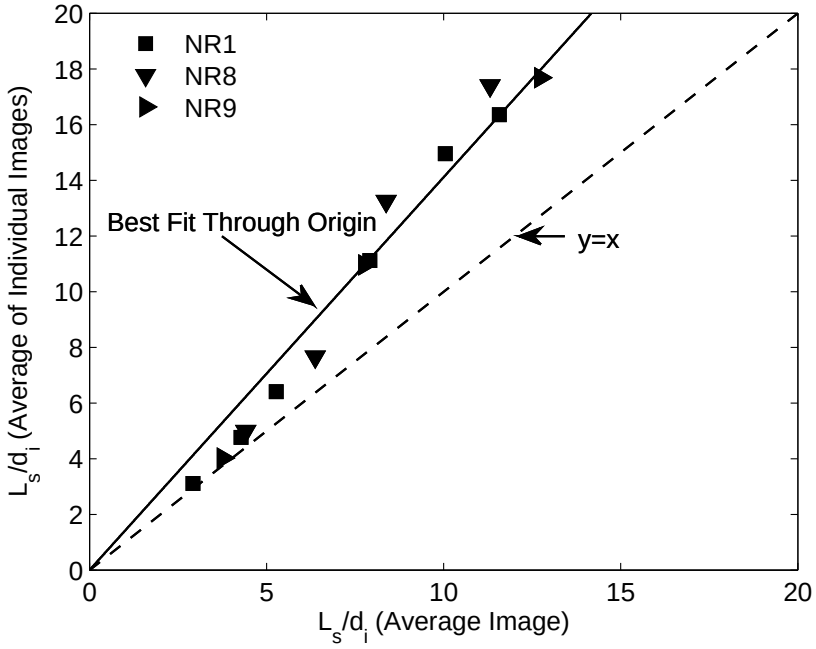

Figure 5.2: Comparison of L_S/d_i values calculated from the average flow field and the average of instantaneous L_S/d_i values. Lengths are calculated for jets from data groups NR1 (He/air, 0.98 atm), NR8 (He/air, 5.40 atm) and NR9 (H_2/air, 0.98 atm).

Figure 5.2 shows that for high momentum flux ratios and hence for short jets, the formations of these pockets is infrequent and the two averaging methods are approximately equal. However, the average of individual images always produces a longer mixing length. At lower momentum flux ratios and hence longer jets the difference in the measured lengths become significant. The mixing lengths presented

in the rest of this work are calculated from the average mixture fraction field. It should also be noted that coaxial jets used in combustion devices typically have large momentum flux ratios and hence short jets which fall into the range where the difference in the two averaging methods is minimal.

5.2 Comparison of the Data to the Mixing Models

In an effort to assess if the mixing models presented in Chapter II can be extended beyond their original formulations to predict mixing lengths in coaxial jets, these models are compared to experimentally obtained mixing lengths. The two experimental data groups used to assess these models are NR1 and NR9 which correspond to He/air and H_2/air respectively. These data groups allow the models to be tested for both velocity and density ratio trends, but geometric effects are not studied since the same injector is used for both groups. The three models tested are the uneven shear model (Dimotakis 1986), modified shear model (Murakami and Papamoschou 2002), and momentum flux ratio model (Rehab et al. 1998)). In Fig. 5.3*a* results from jet core lengths (L_C) predicted by the three models are compared to core lengths measured for data groups NR1 and NR9. The two shear layer based methods are formulated only to calculate the inner potential core length. The potential core lengths are defined as the distance downstream where the mixture fraction (f) is 0.95 on the centerline. From Fig. 5.3*a* it can be seen that both shear layer methods curve up at low r_u values which correspond to the shear layer growth rate going to zero at $r_u = 1$. They greatly over predict the experimental core lengths in this region. In addition, while the correct trend is predicted when the density ratio S is varied over part of the range, the overall effect of varying S is underpredicted. The one method that does match experimental data well is the momentum flux ratio method, which

accurately predicts the measured effect of both S and r_u. Note that the constants in all models were set using a best fit procedure to the experimental data that is presented in Fig. 5.3.

In addition to the jet core length, the stoichiometric mixing lengths (L_S) predicted by the momentum flux ratio model is compared to the measurements in Fig. 5.3*b*. The same trends that were seen in the core length data are repeated in the stoichiometric mixing length data and again the momentum flux ratio shows excellent agreement with the experimental mixing lengths. Therefore the momentum flux ratio scaling will be the only model utilized in the rest of this work. The constants C_1 and C_2 in the momentum flux model were set to 1.62 and 2.02 respectively. These were obtained from the collapse of all nonreacting coaxial jet data points at low Reynolds numbers in Fig. 5.22.

5.3 Centerline and Radial Mixture Fraction Profiles

To obtain a better understanding of the overall flow field, centerline and radial profiles were obtained from average mixture fraction fields. Instantaneous images were used to obtain profiles of the RMS fluctuations of mixture fraction (f'). Results in this section show that using the momentum flux ratio model collapses centerline profiles in the potential core region and in a transitional region beyond the potential core to a single curve. However, eventually the profiles do not collapse where the ambient fluid mixing becomes significant on the centerline and the flow transitions to a far field scaling. It also is shown that the radial profiles of mixture fraction are not self-similar and a true collapse is not possible. This is because of the bimodal nature or the radial profiles caused by the two different streams. Finally radial profiles of

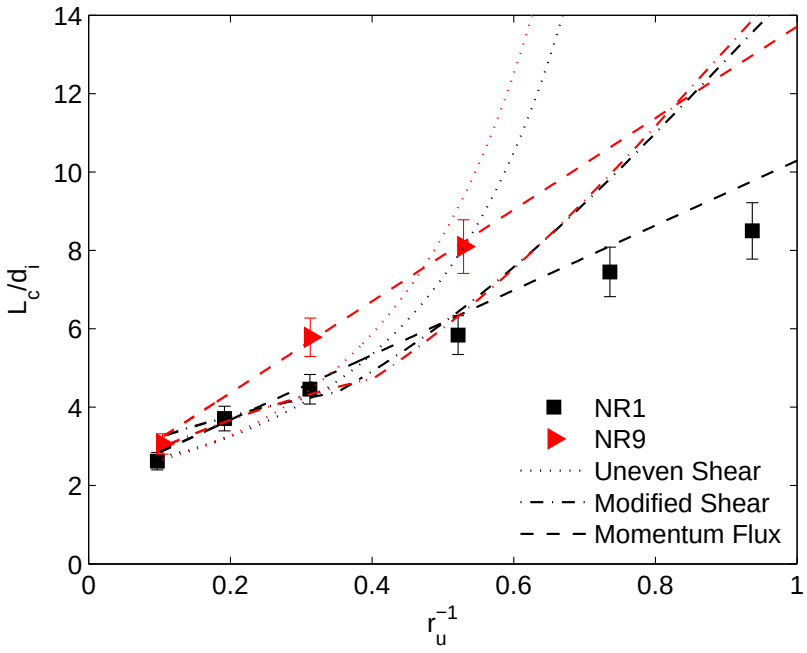

(a)

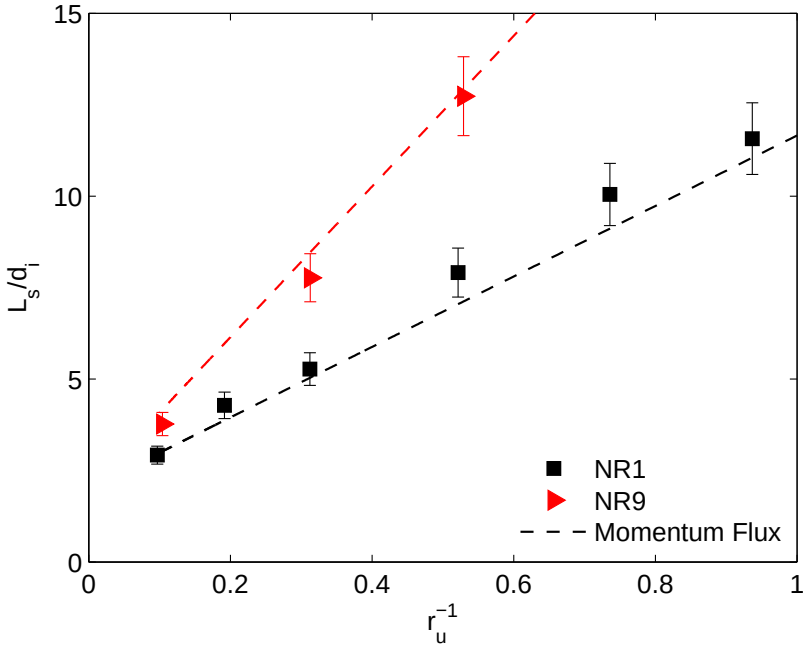

(b)

Figure 5.3: Comparison of nonreacting mixing models with experimental data groups NR1 and NR9 for He/air and H_2/air respectively. Part (a) is a comparison of the core length (L_c) and (b) is a comparison of (L_s) where $f_s = 0.89$ for both data groups. The momentum flux ratio model is the only model which accurately predicts both the S and r_u trends.

f' are used to study the regions of intense mixing.

5.3.1 Centerline Profiles of Average Mixture fraction

For the average mixture fraction field, centerline profiles as a function of normalized downstream distance were obtained. A representative set of centerline profiles corresponding to data group NR1 are shown in Fig. 5.4. As the velocity ratio is decreased, the length of the potential core increases which is the flat part of the profile where $f = 1$. The slope of the profile becomes less negative as r_u increases indicating that the jet becomes longer. Far downstream this region ends and the mixture fraction approaches the ambient value. Note that normally it would be excepted that in the far field the slope would approach negative one, which is the far field scaling for a simple jet. This, however, does not occur since the acetone PLIF system cannot distinguish between acetone from the inner jet and acetone from the ambient fluid. Since the momentum flux ratio model was shown to accurately predict both the core length and the stoichiometric mixing length for varying r_u and S, the centerline profiles should collapse over the region of the jet where this scaling is valid and diverge in the far field where this scaling breaks down.

Figure 5.5*a* shows the same centerline profiles as in Fig. 5.4, but the x-distance is now normalized using the momentum flux ratio for each case. Use of the momentum flux ratio does not collapse the profiles, however the slopes downstream of the potential core region are approximately equal. To fully collapse the centerline profiles to a single curve, the full momentum flux ratio model is needed (Eq. 2.28 with the constants C_1 and C_2 set to 1.6164 and 2.0247 respectively as shown in Fig 5.5*b*). The collapse in Fig 5.5*b* extends from $f = 1$ to $f \approx 0.75$ and the low r_u cases ($r_u = 1.1$ & 1.4) being the first to diverge. The break down in this collapse and hence the

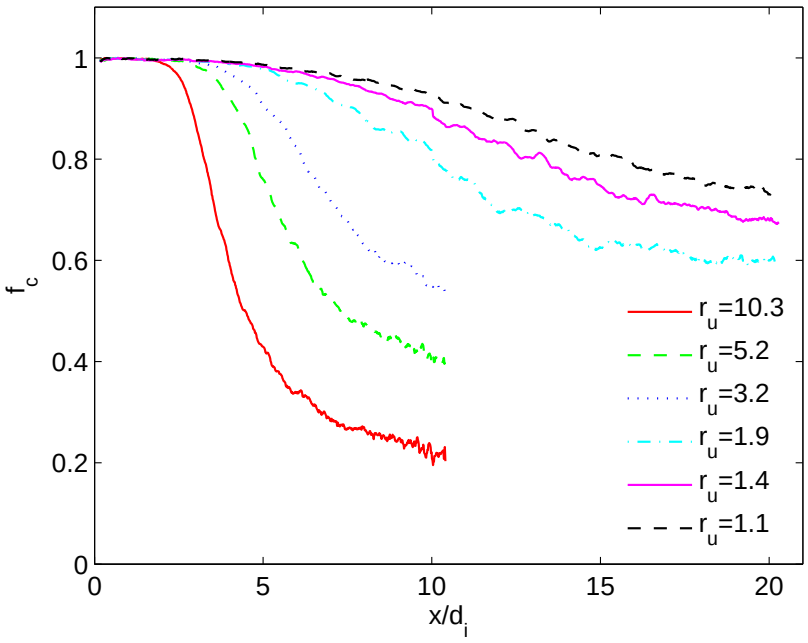

Figure 5.4: Centerline mixture fraction profiles versus normalized downstream distance for data group NR1 (He/air, S=0.118, and Re=3,200-3,700).

momentum flux ratio scaling is a result of the loss of the outer annular jet due to mixing which results in entrained ambient fluid reaching the centerline. This reduces the velocity that surrounds the inner jet at this location. Increasing the injector gap thickness (the initial thickness of the annular jet) will extend the region where the data will collapse. However when designing an injector, increasing the gap thickness has additional consequences. If the fuel/oxidizer ratio and d_i are held constant, an increase in gap thickness will decrease the velocity ratio which increases the mixing length.

The collapse of the data in Fig. 5.5 to a single curve occurs for other data groups as well. To illustrate this point, the collapse of centerline profiles are shown for data groups NR8 and NR9 in Fig. 5.6. For case NR8 He/air jets were run at 5.4 atm and high Reynolds numbers. For case NR9 H_2/air jets were run at 1 atm. The same features observed in Fig. 5.5*b* are seen in Fig. 5.6. The only difference is that for

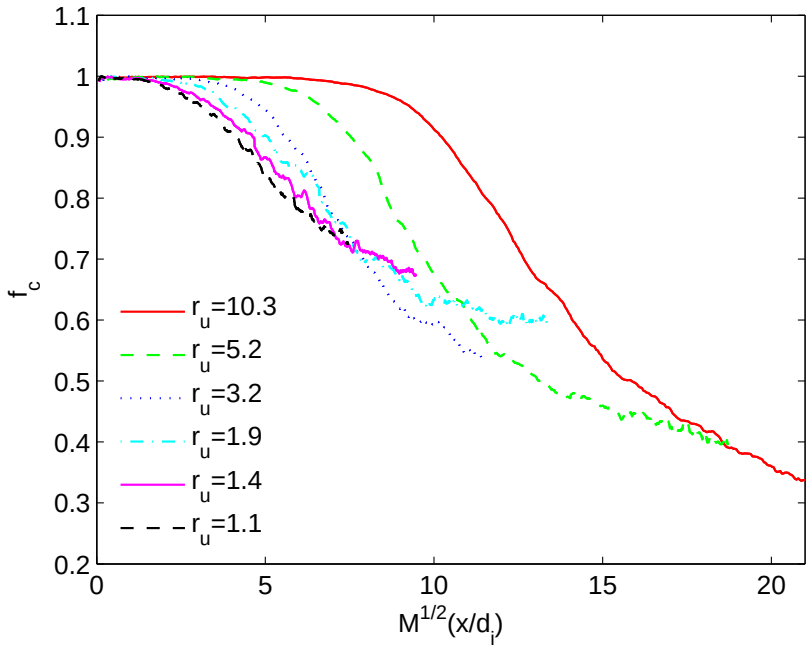

(a)

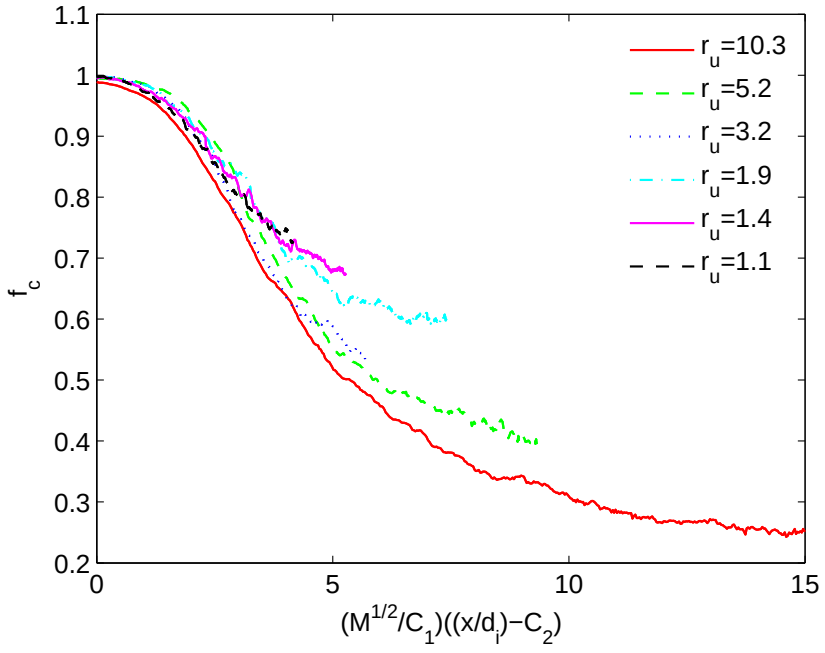

(b)

Figure 5.5: Measured Centerline mixture fraction profiles versus downstream distance for two normalization parameters. Data Group NR1 (He/air, S=0.118, and Re=3,200-3,700). C_1 and C_2 are 1.616 and 2.025 respectively.

data group NR8, different scaling constants are utilized. C_1 and C_2 are 2.70 and 1.19 respectively. Why different scaling constants are needed for high Reynolds numbers is discussed in §5.4.5.

Using the momentum flux ratio scaling and the correct constants, centerline mixture fraction profiles for all data groups collapse to a single curve for a significant distance beyond the potential core. To illustrate this point, the centerline profiles for NR1, NR8 and NR9 are plotted versus downstream distance in Fig. 5.7*a*. The downstream distance is normalized using the momentum flux ratio scaling Fig. 5.7*b*. When scaled using the momentum flux ratio all cases in this data groups collapse reasonably well. Profiles from NR9 (H_2/air) jets diverge from the rest of the data first, however they agree with the other data at $f = 0.89$ which is the stoichiometric value for H_2/O_2 and hence the farthest point downstream of interest. Note that since the air is seeded with acetone, the density ratio in this nonreacting case ($S = 0.059$) is approximately equal to that of H_2/O_2 ($S = 0.063$).

5.3.2 RMS Mixture Fraction Fluctuations: Centerline Profiles

In an effort to obtain a better understanding of how the inner mixing layer effects the mixing on the centerline, the RMS fluctuation of f was calculated. The RMS fluctuation of f was defined as:

$$f'(r,x) = \sqrt{\left\langle \left(f(t,r,x) - \overline{f(r,x)} \right)^2 \right\rangle}. \tag{5.1}$$

Figure 5.8*a* shows centerline values of f' for varying r_u in data group NR8 (He/air). In all cases f' is negligible in the potential core region where no mixing has occurred. Note that this value is not zero due to measurement noise. Downstream of the core sharp increases in f' are seen as the edges of the inner shear layer reach the centerline.

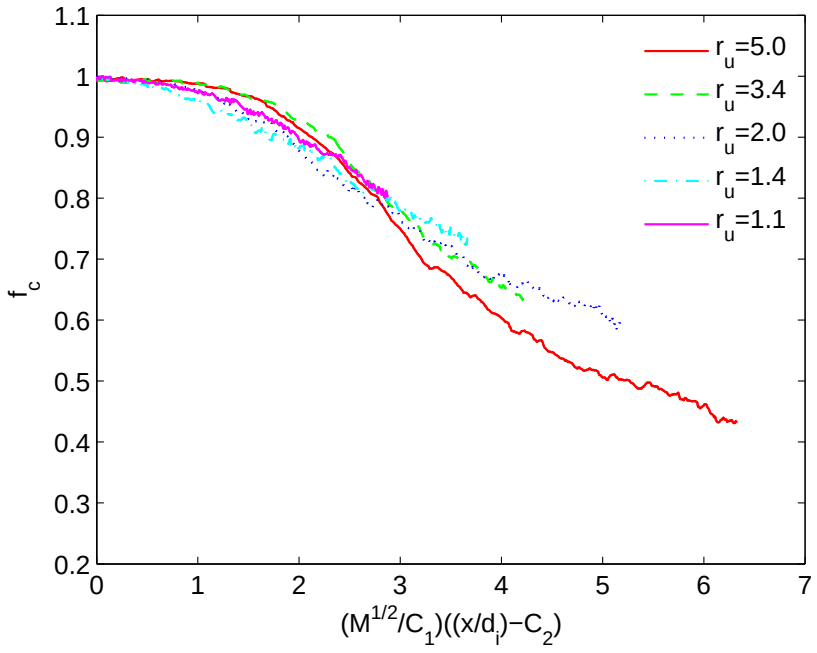

(a)

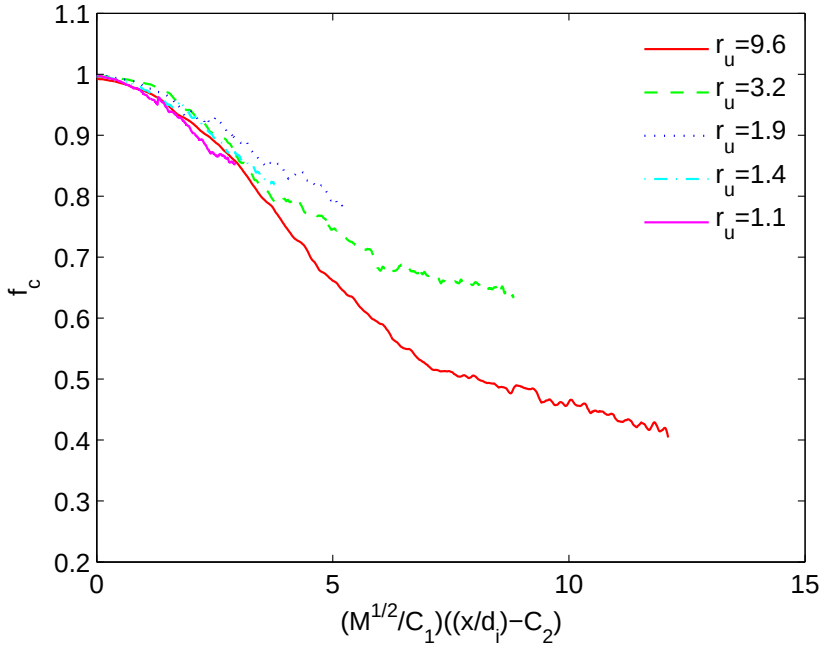

(b)

Figure 5.6: Centerline mixture fraction profiles versus downstream distance for a normalized parameter. Data group NR8 (a) (He/air, S=0.133, and Re=18,000-20,000) and NR9 (b) (H_2/air, S=0.059, and Re=2,800-13,000). C_1 and C_2 are 2.697 and 1.186 respectively for NR8 and C_1 and C_2 are 1.616 and 2.025 respectively for NR9.

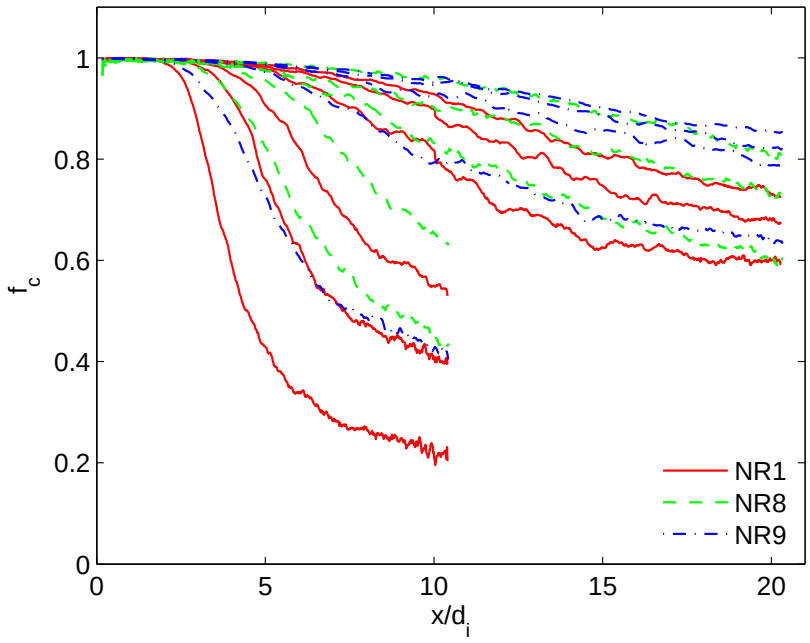

(a)

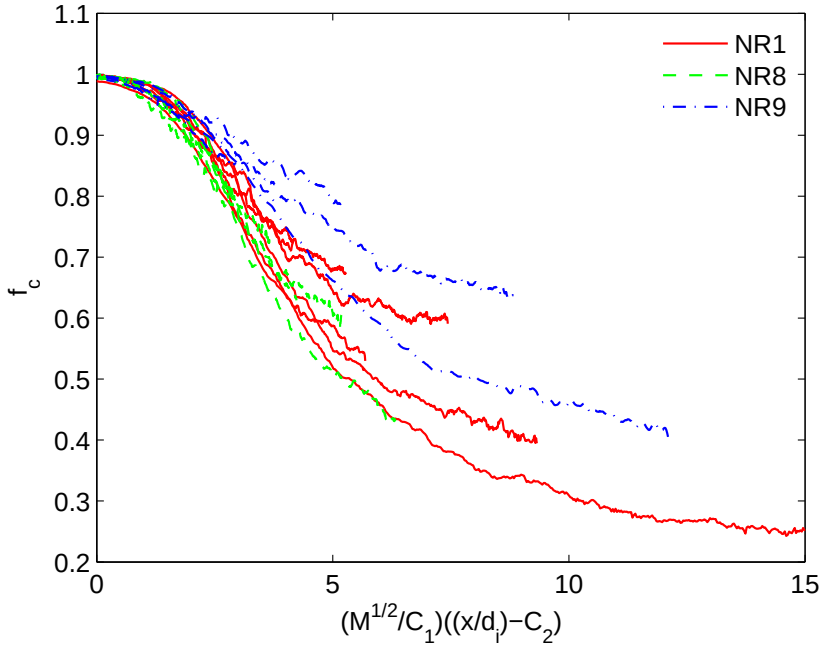

(b)

Figure 5.7: Measured Centerline mixture fraction profiles versus downstream distance for two normalization parameters. Data groups NR1, NR8, and NR9. Data groups NR1 and NR8 are He/air coaxial jets and NR9 are H_2/air. Velocity ratio values for these data groups are listed in Figs. 5.5 and 5.6.

Larger values of r_u result in steeper increases in f' and more rapid decreases in f' from the peak values. For lower values of r_u, f' tends to increase more gradually to a peak value, followed by a more gradual decrease. The peak value of f' is approximately constant for large values of r_u, but it decreases as r_u approaches 1. These profiles are in agreement with average mixture fraction centerline profiles. High intensity mixing occurs for large values of r_u and less intense gradual mixing for values of r_u close to one.

These same trends also can be seen in Fig. 5.8*b* for jets from data groups NR1, NR8, and NR9 with all have r_u values of approximately 3.3. NR1 and NR8 are the same except NR8 was taken at a chamber pressure of 5.4 atm and hence at a higher Reynolds number. While the profiles plotted in NR1 and NR8 have the same approximate momentum flux ratio ($M \approx 1.35$) the difference in Reynolds number does effect mixing and hence the f' profiles. The reasons for this difference are discussed in §5.4.5. As would be expected for the lower momentum flux ratio case ($M = 0.61$, NR9), the peak value of f' is relatively small and the peak of f' is spread out, which indicates that the jet is relatively long. Peaks and valleys in these profiles are due to statistics that are not converged, since only 180 images were used. These centerline profiles of f' are characteristic of all coaxial jets studied in this work.

5.3.3 Radial Profiles

To further understand how the mixing layers grow and combine in coaxial jets and to look for self-similarity, radial profiles of γ and f' were obtained from the mixture fraction fields. The nondimensional average mixture fraction γ is defined such that a value of one represents pure inner jet fluid and a value of zero represents

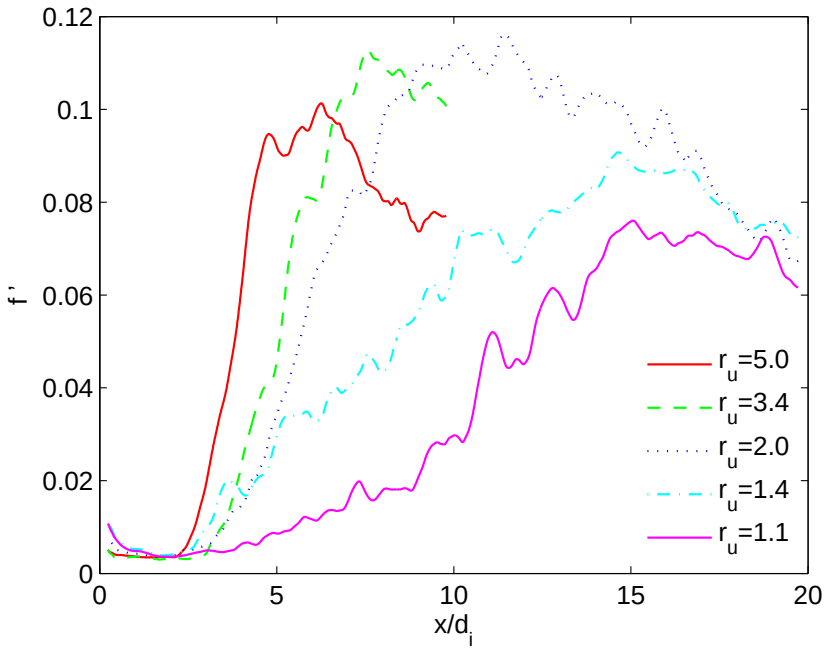

(a)

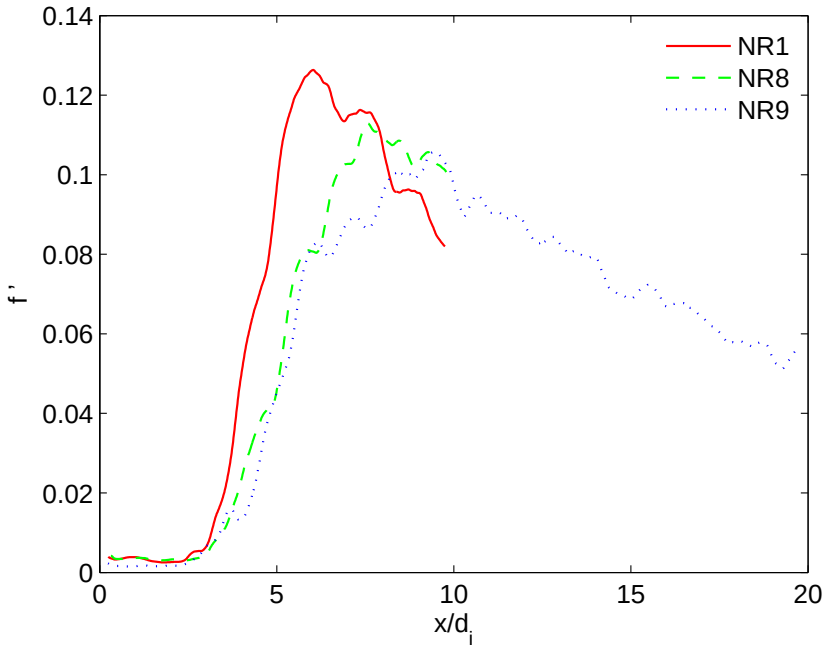

(b)

Figure 5.8: Centerline RMS mixture fraction fluctuations for NR8 (He/air, $Re = 18,000 - 20,000$) (a) and $r_u \approx 3.2$ from data groups NR1, NR8, and NR9 (b). f' profiles were calculated from 180 individual images.

pure ambient fluid;

$$\gamma(r,x) = \frac{f(r,x) - f_\infty}{1 - f_\infty}. \tag{5.2}$$

The centerline value of γ is γ_C. Figure 5.9 shows radial profiles of γ/γ_C and f' at five downstream locations for two cases for which $r_u = 10$. In Figs. 5.8*a*-*b* data are from group NR1 (He/air, $M = 12.6$ and $L_S/d_i = 2.9$). In Figs. 5.8*c*-*d* the data are from group NR9 (H_2/air, $M = 5.4$ and $L_S/d_i = 3.8$). In both cases $f_S = 0.89$. Profiles of γ/γ_C for both cases are very similar in the inner jet region and after $x/d_i = 1$ they collapse reasonably well. However where negative values of γ/γ_C occur a dramatic spreading is visible. It was not possible to collapse all of these profiles of γ in a self-similar manner.

The profiles of RMS fluctuations (f') in Fig. 5.9 show many interesting features. The inner Peaks centered around $r/d_i = 0$ are the inner mixing layer. Peaks also occur in the outer layer but they are only visible for small values of x/d_i and are characterized by double peaks. The rapid disappearance of the outer mixing layer is largely due to the low signals in both the ambient fluid and the outer jet. This can also be attributed to the large outer jet velocity and small gap thickness which results in the rapid mixing of the outer jet. As would be expected, for a shorter jet, the center line value of f' increases faster in the x-direction, as shown in Fig. 5.8*b* for $L_S/d_i = 2.9$, as compared to Fig. 5.8*d* for $L_S/d_i = 3.8$.

If the momentum flux ratio governs mixing in coaxial jets, then two cases with different values of r_u and S, but with the same value of M should have similar radial profiles of γ/γ_C and f' at a given downstream distance. To investigate this idea, radial profiles of γ/γ_C and f' for two cases with $M \approx 0.21$ are plotted in Fig. 5.10. The first case is a He/air jet with $r_u = 1.36$ from data group NR1 and the second case is a H_2/air with $r_u = 1.89$ from data group NR9. Profiles of γ/γ_C are very

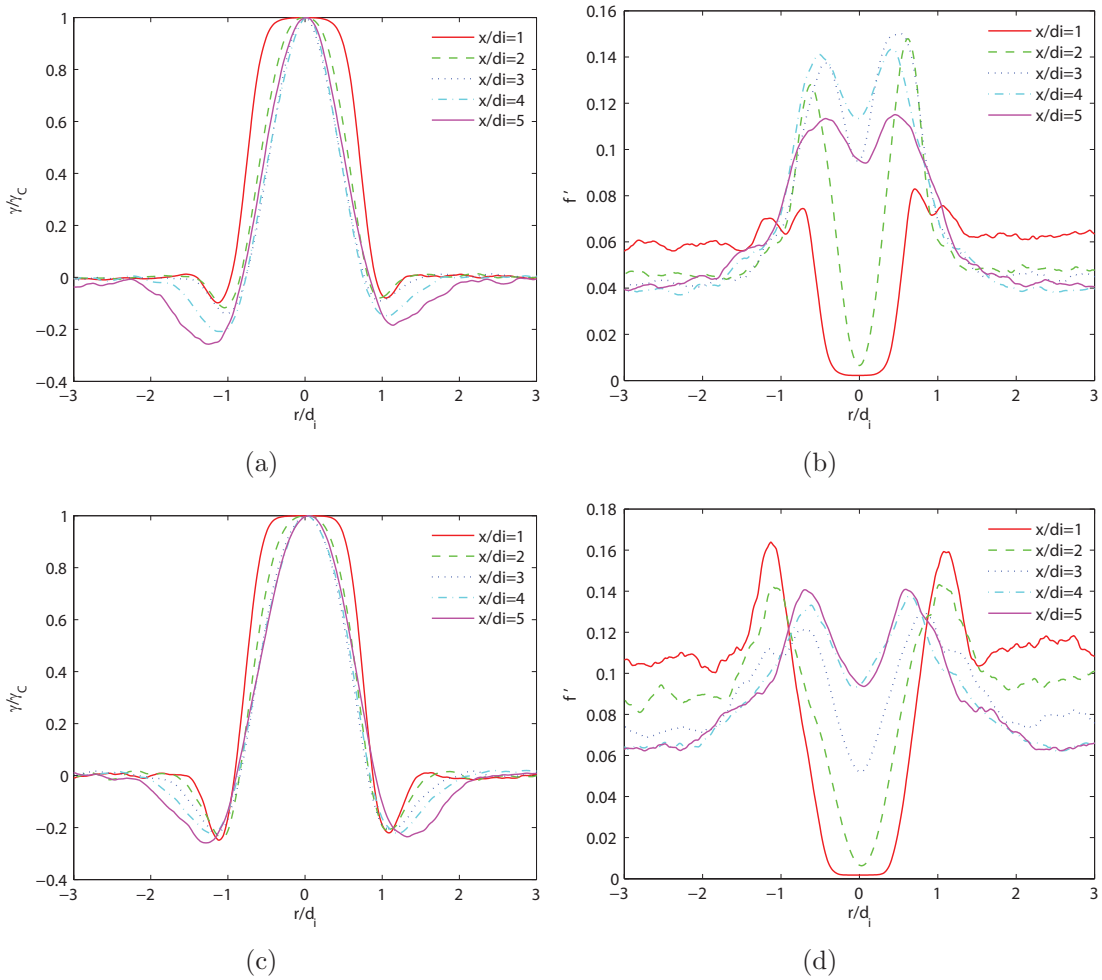

Figure 5.9: Radial profiles of normalized mixture fraction (γ/γ_C) and fluctuations f' for two cases for which $r_u = 10$. The first case is a He/air jet with $M = 12.6$ from data group NR1 (a and b). The second case is a H_2/air jet with $M = 5.4$ from data group NR9 (c and d).

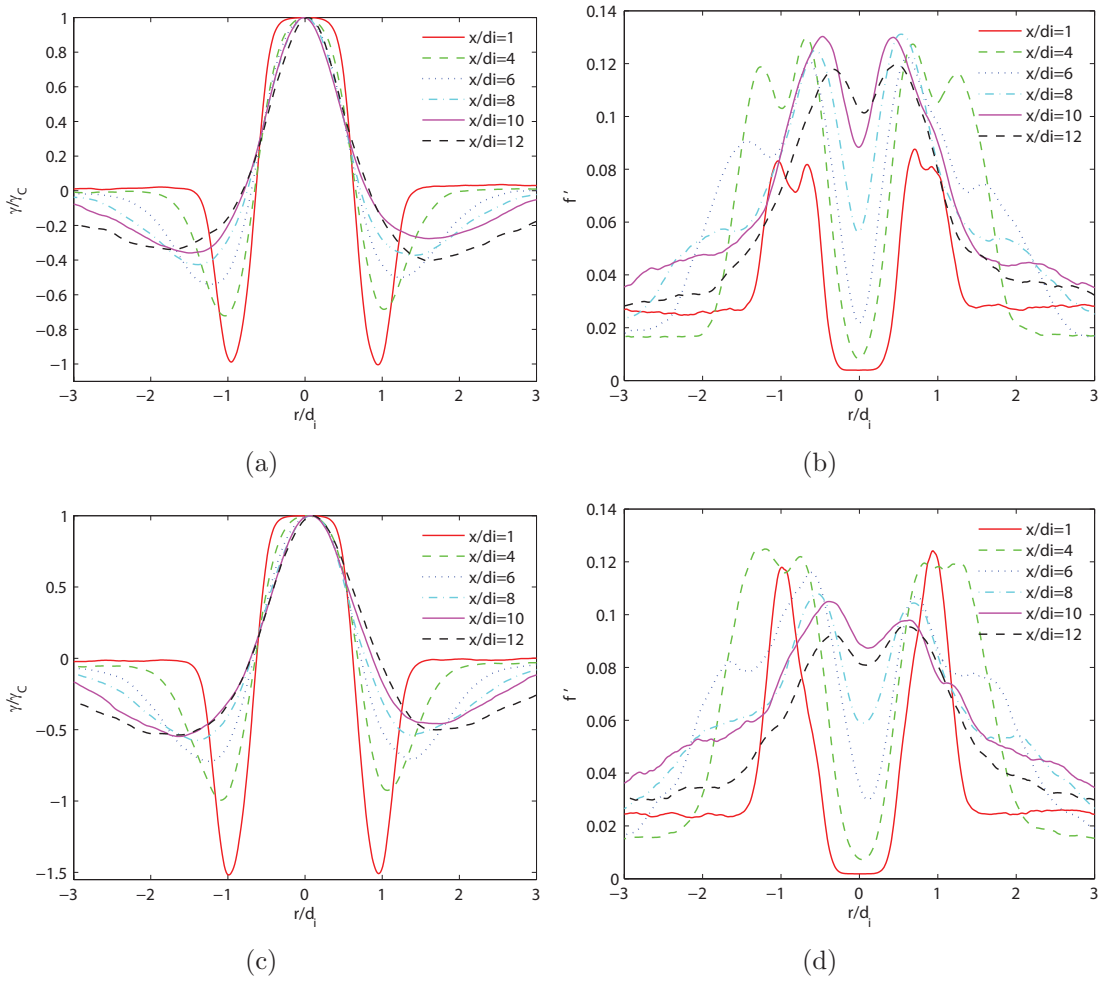

Figure 5.10: Radial profiles of normalized mixture fraction (γ/γ_C) and fluctuations f' for two cases where $M = 0.21$. The first case is a He/air jet with $r_u = 1.36$ from data group NR1 (a and b) and the second case is a H_2/air with $r_u = 1.89$ from data group NR9 (c and d).

similar. The only difference is the negative value that occurs in the annular jet region. This difference is due to the differences in f_∞ for the two cases. These profiles can not be made to collapse owing to the bimodal nature of the profile. To collapse the profiles, the similarity variable would have to account for the different growth rates of the mixing layers associated with the inner and outer jet. Hence there are too many variables to expect that a single similarity parameter will collapse the data. Downstream of where the inner and outer jets fully combine and mix, the problem becomes the same as the far field of a simple jet and the profiles do become self-similar.

RMS fluctuations for these two cases are shown in Fig. 5.10*b* and Fig. 5.10*d*. Centerline values and inner mixing layer peaks are similar in both cases. The outer peak, due to the outer mixing layer in the H_2/air case, takes longer to form and is never as pronounced as in the He/air case. At $x/d_i = 10$ and 12, the peak values of f' for the H_2/air case are relatively small. However the similarity between the profiles at the same x/d_i locations in these two plots is remarkable and suggests that the momentum flux ratio is the governing flow parameter.

5.4 Impact of Parameters on Mixing Length Scaling

Previous sections have shown that the momentum flux ratio model accurately predicts the effects of the velocity and density ratio on the core length and the stoichiometric mixing length. However a deeper understanding of these effects along with the effects of other injector parameters is needed. In this section the effects of r_u, S, injector geometry, confinement and Reynolds number are explored. In addition, the momentum flux ratio model has a lower limit for which it is valid. This limit is

explored in an effort to predict when the model fails.

5.4.1 Velocity Ratio

The good correlation of the data that was achieved using the momentum flux ratio parameter indicates that the velocity ratio, and not the absolute velocity difference $(u_e - u_i)$ determines the mixing length L_S. Further confirmation of this idea was obtained by examining three data groups that have a constant density ratio ($S = 0.118$) and a constant injector geometry. NR1 is the baseline He/air data set and r_u was varied by changing both the inner and outer jet velocities. In NR2 u_i was held constant at 21.1 m/s, while u_e was varied. For NR3 u_e was held at a constant value of 73.6 m/s and u_i was varied. Velocity differences ranged from 2.4 m/s to 76 m/s. Figure 5.11 shows that r_u is the governing parameter and the velocity difference $(u_e - u_i)$ is not.

5.4.2 Density Ratio

Coaxial jets used as injectors in rockets are characterized by small density ratios, yet, as mentioned in the introduction, very little work has been done on variable density coaxial jets. Figure 5.12*a* shows measured mixing lengths for three values of S which are 0.118, 0.059, and 0.464 and which correspond to He/air (NR1), H_2/air (NR9), and CH_4/air (NR12) respectively. Note that for NR1 and NR9 $f_s = 0.89$ was used and for NR12 $f_s = 0.80$ was used. The data in Fig. 5.12*a* do not collapse to a single line since the variable density ratio has not been accounted for. If however the momentum flux ratio parameter ($[M^{1/2}X_S]^{-1}$) is used, Fig. 5.12*b* shows that L_S collapses.

From Fig. 5.12*b* it is clear that a breakdown in the momentum flux scaling occurs

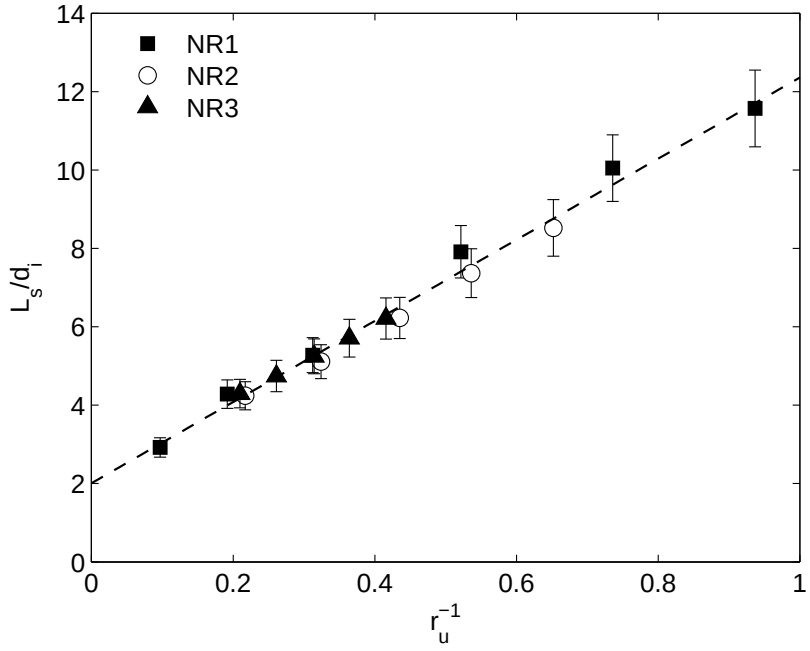

Figure 5.11: Test of velocity ratio scaling for stoichiometric mixing length for He/air coaxial jets ($f_s = 0.89$) with $d_e/d_i = 2.5$ and $P_C = 0.98$ atm. In data group NR1 both u_i and u_e are varied, in NR2 u_i is held constant and u_e varied, and in NR3 u_e is held constant and u_i varied. The dashed line is the best linear fit for the data shown.

at $(M^{1/2}X_s)^{-1} \approx 8$ as indicated by the two data points from NR9 which are well below the dashed line. These points fall far enough below the line that measurement uncertainty cannot be responsible. Furthermore, these two points correspond to H_2/air jets with r_u values of 1.37 and 1.06. The longest two jets from NR1 have similar velocity ratios of 1.36 and 1.07. Therefore the velocity ratio alone is not causing this deviation from the momentum flux ratio scaling. Two physical phenomena could cause this decrease in mixing length compared with the momentum flux ratio scaling and are buoyancy and a change in the structures of the mixing layers. In §5.4.2.1 it is argued that the effect of buoyancy is small and consequently unlikely to be causing the deviation from the scaling. In §5.4.2.2 a transition to a "wake-like" mixing regime is argued to be the likely cause.

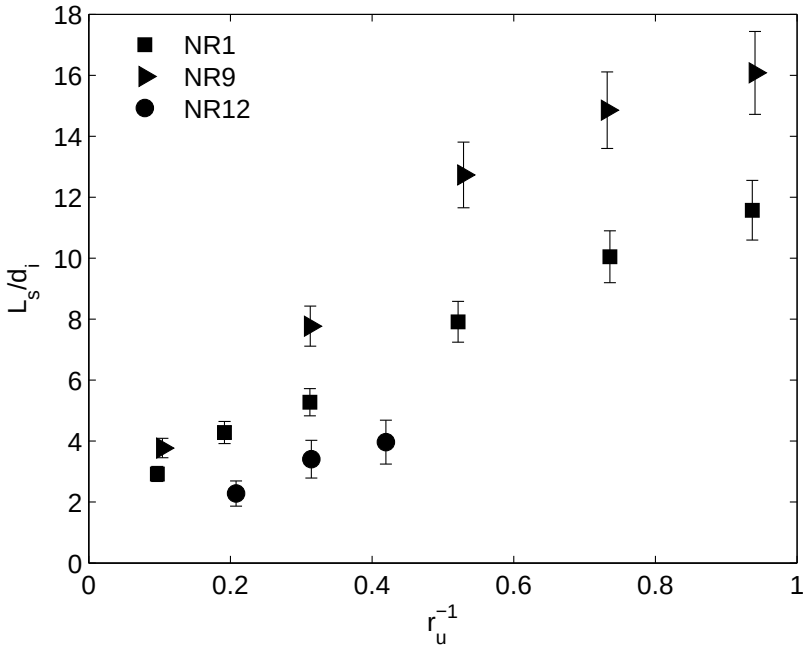

(a)

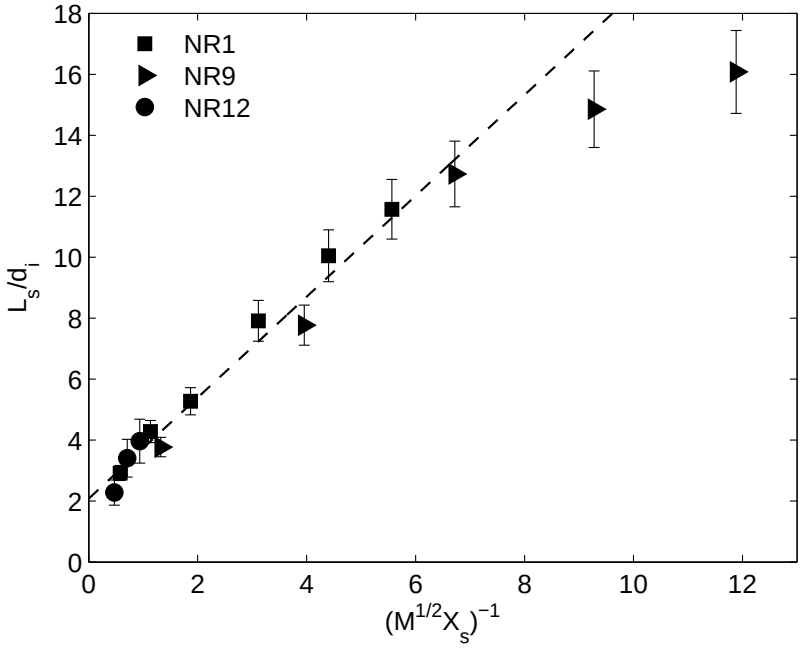

(b)

Figure 5.12: Determination of the proper parameter to scale the measured nonreacting mixing lengths (L_S) as velocity ratio (r_u) and density ratio are varied. Data plotted versus r_u^{-1} (a) and data plotted versus $(M^{1/2}X_S)^{-1}$ (b). Conditions are listed in Table 4.4. $d_e/d_i = 2.5$ and $P_C = 0.98$ atm.

5.4.2.1 Buoyancy

Since coaxial jets involve three fluids: (inner, outer and ambient), buoyancy forces between all fluids should be considered. The worst case for a coaxial jet occurs when the lightest fluid is injected from the entire injector into an atmosphere of the densest fluid. Under these conditions the Froude number method of Chen and Rodi (1980) for a round jet can be applied directly where the jet is dominated by inertia up to a distance of ξ from the injector exit and is defined as;

$$\xi = 0.5 d_e Fr_e^{1/2} S^{1/4}. \tag{5.3}$$

The Froude number in terms of outer jet properties can be defined as;

$$Fr_e = \frac{u_e^2}{g\frac{\rho_\infty - \rho_e}{\rho_e} d_e}, \tag{5.4}$$

where g is the gravitational acceleration constant. If this method is applied to the $r_u = 1.37$ and 1.06 cases of data group NR9 then ξ/d_i values of 16.6 and 13.0 are obtained respectively. This case is compared to L_S/d_i values of 14.9 and 16.1, which would seem to indicate that buoyancy could be playing a role in the $r_u = 1.06$ case. However, Favre-Marinet and Camano-Schettini (2001) inverted their experimental setup which had coaxial jets with a small density ratio of $S = 0.138$. They showed that the inertia dominated region extended beyond that predicted by Eqn. 5.3 by as much as 50%. In addition, in this work the ambient fluid is not pure air seeded with acetone, but a mixture of air, acetone, and hydrogen which has a density of 0.341 kg/m^3 compared to the 1.38 kg/m^3 used in the previous calculation. If this lower density is used, which is a better representation of the actual jet, in the $r_u = 1.06$ case the inertia dominated region is found to extend to 28.9 x/d_i which indicates that the jet is still in the inertial range. Also, the same decrease in jet length is

seen in the potential core length for $r_u = 1.37$ and 1.06 of NR9 as was seen for L_S. According to Eq. 5.3 using the larger outer density the potential core length for these two data points are well within the inertial range. For these reasons it is believed that buoyancy plays a minor role and is not causing the increase in mixing and hence the decrease in L_S for the two data points in Fig. 5.12*b* that fall below the line. However, due to the limitations of the experimental setup no inverted jet data was taken to experimentally verify this hypothesis. It should also be noted that these two points are the closest to the buoyant regime and consequently it is believed that it is valid to ignore buoyancy in all nonreacting results presented in this work.

5.4.2.2 Wake Versus Shear Instability

What makes coaxial jets different from other turbulent shear flows is the interaction between the inner and outer mixing layers. It is this interaction and coupling between the layers which causes the momentum flux ratio method to accurately predict L_S in some cases and fail in others. Dahm et al. (1992) argued that in a coaxial jet there is a velocity profile between which each mixing layer is formed that consists of a wake component and a shear component resulting from the symmetric and antisymmetric parts of the velocity profiles respectively. The wake component of the instability is characterized by vortex structures that have both positive and negative signs of circulations. The shear component of the instability is characterized by vortex structures that have the same sign of circulation. Dahm et al. (1992) were able to show that for $r_u >> 1$ a locking exists between the outer and inner mixing layer which are both dominated by a "shear-like" instability. Locking is used to describe the process by which the mixing layers no longer develop independently of each other. Instead the interactions of the vortices formed in the two mixing layers

create an instability other than the naturally dominant one (Dahm et al. 1992). This results in a set pattern being formed between the vortices in the two mixing layers.

This locking between both mixing layers is the explanation for the shear-layer based methods failure to predict the core lengths of coaxial jets. This failure is due to a change in both the passing frequency and vorticity thickness growth of the large scale vortical structures in comparison to a single planar shear layer. Empirical equations for both passing frequency and vorticity thickness growth (Eqs. 2.8 and 2.9 respectively) are built into the shear layer growth equations. To formulate the method for coaxial jets, these relations would have to be adjusted. Changing the constants in a curve fit to the data is not adequate, a change in the functional relationship would be needed.

As long as both the inner and outer mixing layers are dominated by a "shear-like" instability and locked together, the momentum flux ratio concept appears to explain the mixing. However, this locking breaks down as r_u approaches one and the "wake-like" instability starts to dominate in the inner shear layer, which again is demonstrated by Dahm et al. (1992). The effects of density ratio were not explored in their study because the density field is uniform in water jets. It is expected that the density ratio will play a role in determining when the transition between "wake-like" and "shear-like" in the inner mixing layer takes place. This explains why H_2/air coaxial jets experience this transition at higher values of r_u than He/air jets. The transition point is not at $M = 1$, since a number of cases in Fig. 5.12*b* are well below this value and still collapse using this scaling. The transition point is closer to $M = 0.1 - 0.2$. However, additional factors will play a role in setting this transition point such as injector post thickness and inlet velocity profiles. A thicker post and a less uniform inlet profile (larger viscous boundary layers) will cause this transition

to occur at higher values of M.

5.4.3 Injector Geometry

When studying injectors it is important to understand the effects of both flow parameters and geometry. In the experimental setup used in the study, three geometric features were investigated; the outer jet diameter (d_e), the inner jet diameter (d_i), and the inner post thickness (T_p). A fourth geometric feature, the post recess, always was set to zero in this work, but has been previously investigated in water coaxial jets (Rehab et al. 1997). Figure 5.13 plots L_S for four different injector geometry and two fuel/air combinations which span 5 data groups. NR1 and NR9 are He/air and H_2/air coaxial jets respectively with injector dimensions of $d_e = 7.5$ mm, $d_i = 3.0$ mm, $T_P = 0.89$ mm and represents the baseline nonreacting injector. Group NR4 are He/air cases taken with an increased d_e value of 10 mm. NR5 has a smaller post thickness ($T_p = 0.54$ mm) and a larger inner diameter ($d_i = 3.7$ mm) compared to the baseline case. Finally, NR10 are H_2/air coaxial jets and is the baseline injector used in reacting cases and has dimensions of $d_e = 6.7$ mm, $d_i = 3.4$ mm, $T_P = 0.72$ mm. Hence cases plotted in Fig. 5.13 represent a 61% reduction in post thickness, a 23% increase in d_i and a 33% increase in d_e over the baseline case.

Figure 5.13 illustrates that the momentum flux ratio scaling does an excellent job of collapsing L_S for all cases especially for $(M^{1/2}X_s)^{-1} < 5.5$. At the longest point for data group NR10 it appears that a slight deviation from the scaling occurs which is greater than the experimental uncertainty. It is possible this lengthening is due to the relatively small outer diameter for this case which may results in ambient fluid being entrained to the centerline. This lengthens the jet since the PLIF system cannot distinguish between acetone that originated in the inner jet and acetone that

is mixed into the ambient fluid. An important result of this investigation is that the injector post thickness has no effect on L_s over the range studied. Most experimental coaxial jet work has previously been done with contoured nozzles (sharp inner post) and consequently zero thickness. Typically in injectors for combustion devices a thickened post is used. However, it is possible that in a reacting coaxial jet the injector post thickness could play a large role in stabilizing the base of the flame and hence cannot be ignored in that context. Also note that while no effect was seen for these cases, the post thickness could play a role in determining the limits of applicability of the scaling.

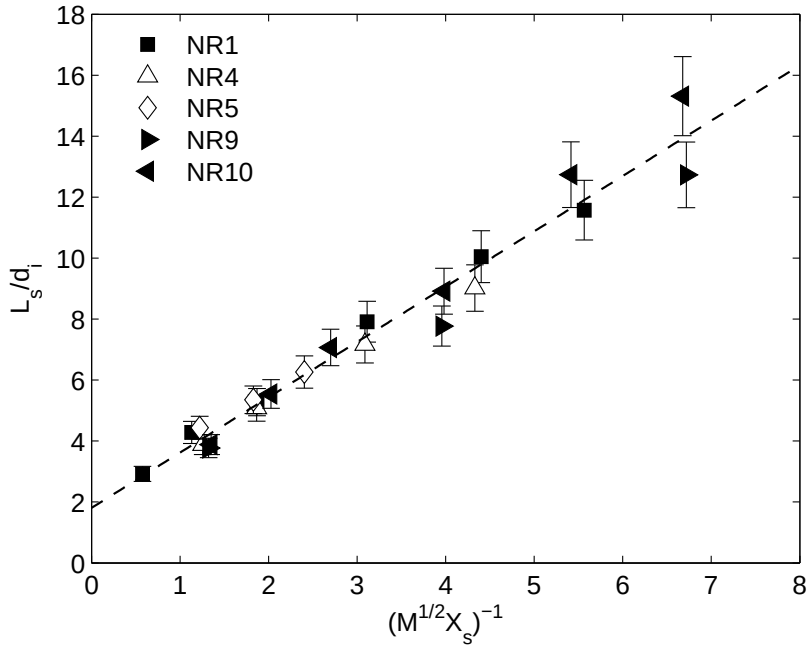

Figure 5.13: Effect of injector geometry on L_S for the momentum flux scaling at $P_C = 0.98$ atm for He/air (NR1, NR2 and NR3) and H_2/air (NR9 and NR10) coaxial jets. Data group NR1 and NR9 have dimensions of $d_e = 7.5$ mm, $d_i = 3.0$ mm, $T_P = 0.89$ mm, NR4 has dimensions of $d_e = 10$ mm, $d_i = 3.0$ mm, $T_P = 0.89$ mm, NR5 has dimensions of $d_e = 7.5$ mm, $d_i = 3.7$ mm, $T_P = 0.54$ mm,and NR10 has dimensions of $d_e = 6.7$ mm, $d_i = 3.4$ mm, $T_P = 0.72$ mm.

5.4.4 Confinement

When dealing with a closed combustion chamber recirculation zones can form which alter the mixing length. The chamber used in this study was 50.8 mm square with rounded corners. Thus the characteristic length scale of the confinement (D) was 50.8 mm. The largest injector diameter was 10 mm, so the confinement ratio (D/d_e) always was larger than 5. To investigate if this confinement ratio altered L_s, data were obtained at 1 atm with the chamber walls but the nozzle removed and with the chamber walls removed. This setup was used with both He/air (NR1 and NR6) and H_2/air (NR9 and NR11) coaxial jets using the baseline injector. Empty symbols in Fig. 5.14 correspond to unconfined jets while filled symbols represent confined jets. No effect of confinement is seen over the range of conditions in this study.

5.4.5 Reynolds Number

Coaxial jets used as injectors in combustion devices are not only characterized by small density ratios and large velocity ratios, but also by large Reynolds numbers. If the Reynolds number is sufficiently large, the mixing in any turbulent shear flow, including coaxial jets, should be independent of Re. To explore if any Re effects existed in the experimental data the range of Reynolds numbers for the baseline He/air configuration (data group NR1) was varied by increasing the chamber pressure from 0.98 atm to 3.76 atm to 5.40 atm. For nonreacting flows the only effect of increasing the pressure is to increase the Reynolds number (and the gas density) if the injection velocities are held constant. Due to this increase in pressure, the Reynolds numbers were 3,200-3,700 (NR1), 13,000-14,000 (NR7), and 18,000-20,000 (NR8). Stoichiometric mixing lengths for these three data groups are plotted in

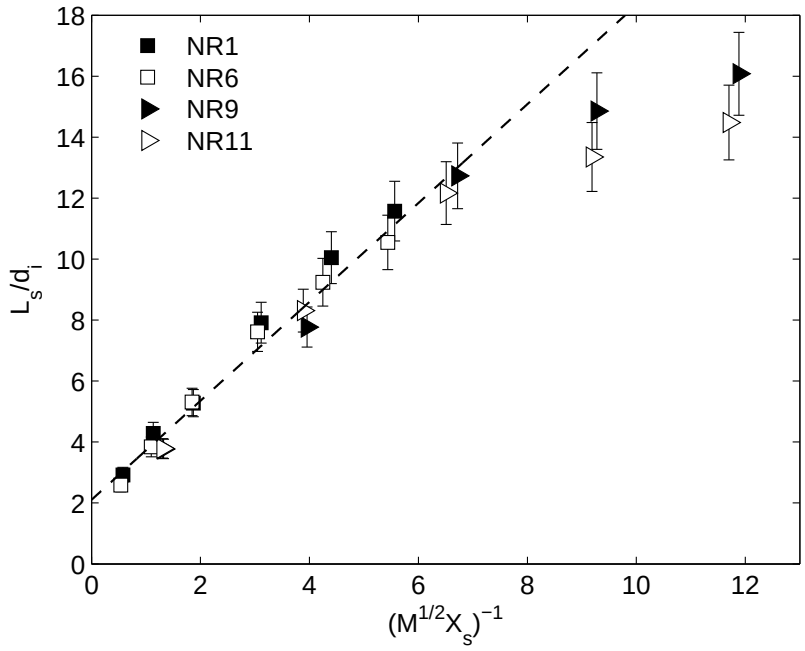

Figure 5.14: Test of the effect of confinement (with and without rocket sidewalls) at $P_C = 0.98$ atm. Filled symbols represent confined conditions and open symbols represent unconfined conditions. NR1 and NR6 are He/air ($S = 0.118$, $f_S = 0.89$) coaxial jets and NR9 and NR11 are H_2/air ($S = 0.059$, $f_s = 0.89$) coaxial jets.

Fig. 5.15. The data fall on two curves in Fig. 5.15. One curve corresponds to a low Reynolds number, and an atmospheric pressure. The other curve corresponds to a high Reynolds number and elevated pressure. Since increasing Re from 13,500 to 19,000 has only a minimal change on L_s it is believed that the upper curve is independent of Re and represents the large Re limit. The fact that the high Re curve lies above the low Re curve is opposite to what was expected.

An additional interesting point in Fig. 5.15 is results for low values of $(M^{1/2}X_s)^{-1}$ lie close to one another but the two curves in Fig. 5.15 differ at larger values of $(M^{1/2}X_s)^{-1}$. To understand the cause of this behavior Fig. 5.16 shows average and instantaneous images for the three data points that have velocity ratio values of 5 and that collapse in Fig. 5.15. In addition, Fig. 5.17 shows images for $r_u \approx 1.1$

which is where the largest difference exists in Fig. 5.15. In the low $(M^{1/2}X_s)^{-1}$ case (Fig. 5.16) L_S/d_i are approximately equal for the three values of Re. Instantaneous images show the wrinkleness of the stoichiometric contour to be similar in all cases. However what does clearly differ is the shape and growth of the outer mixing layer. For Re=3,500, the outer mixing layer does not start spreading till almost $2.5d_i$ and before it starts to spread a slight inward curving of the layer is visible. The inward curving is caused by the inward pressure force caused by the static pressure gradient formed between the high speed outer jet and the ambient fluid. As Re is increased from 3,500 to 14,000 the start of the spreading of the outer shear layer moves closer to the injector exit. At $Re = 20,000$ the outer shear layer begins to spread at the jet exit. This delay in spreading of the outer mixing layer greatly increases the length of the outer potential core which in turn protects the inner jet from the ambient fluid for a longer distance. This causes the outer jet velocity to decrease at a slower rate, which promotes a larger growth rate in the inner mixing layer. The result is better mixing between the two jets and a shorter mixing length. For $r_u \approx 5$, L_S is so short that this effect is negligible, however at $r_u \approx 1.1$ (Fig. 5.17) L_S is large so this effect is not negligible. The same differences in the spreading rate of the outer mixing layer are visible in Figs. 5.17 as seen in 5.16. At Re=19,000 for $r_u = 1.1$ the spreading starts very close to the injector exit, but unlike the $r_u = 5$ jet the increased growth rate causes the outer jet velocity to decrease faster resulting in less mixing in the inner mixing layer which in turn increases L_S.

From the above argument it is clear that Reynolds number independence is reached in the current configuration when the growth of the outer mixing layer starts at the injector exit. Note the absolute velocity of the outer jet also might play a role in determining when the shear layer growth starts since it determines the magnitude

of the pressure gradient which the outer mixing layer must overcome to grow. This *Re* effect also is not limited to nonreacting cases. The same effect is seen in reacting coaxial jets and is discussed is §6.3.

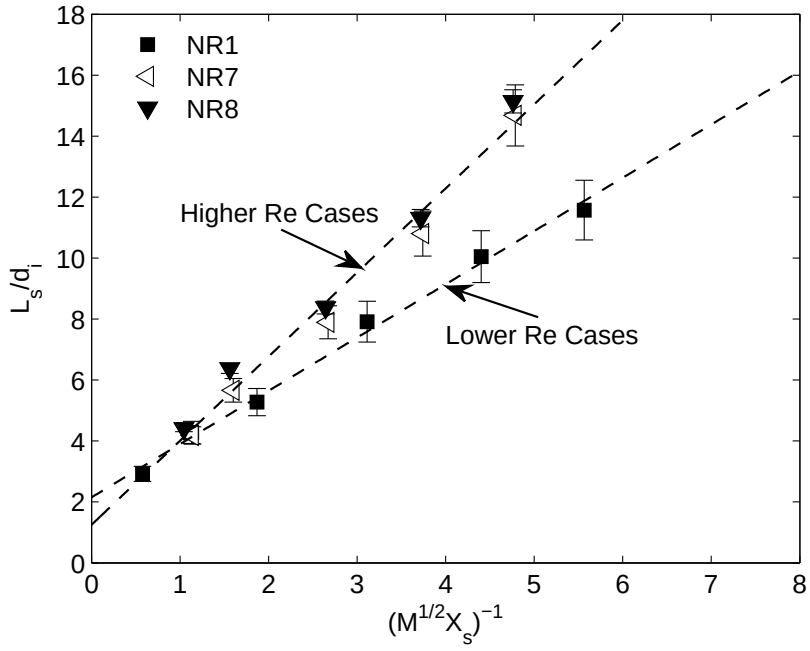

Figure 5.15: Effect of increasing pressure and therefore the Reynolds number on the stoichiometric mixing length for the momentum flux scaling. All jets are He/air coaxial jets ($f_s = 0.89$) with $d_e/d_i = 2.5$. NR1 cases are at $P_C = 0.98$ atm with a Re range of 3,200-3,700, NR7 cases are at $P_C = 3.76$ atm with a Re range of 13,000-11,000, and NR8 cases are at $P_C = 5.40$ atm with a Re range of 18,000-20,000.

5.5 Final Experimental Scaling

In this section mixing lengths for the nonreacting data groups are plotted on both linear and log-log graphs in order to obtain scaling constants for the momentum flux ratio scaling. Scaling constants are obtained for both low and high Reynolds number cases. Four mixing lengths were used to characterize different levels of mixing. The four mixing levels correspond to the locations where $f_s = 0.95$ (the end of the

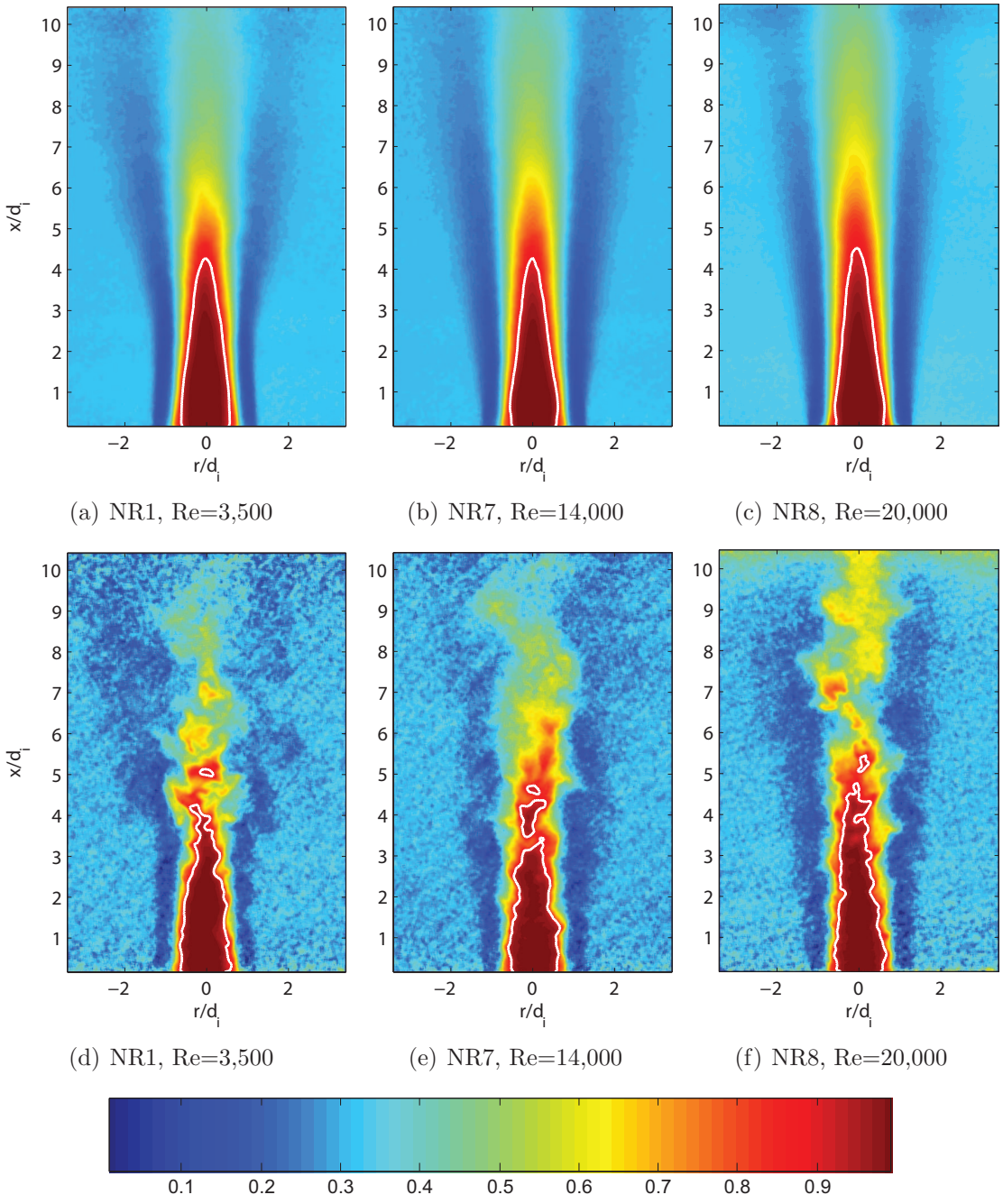

(a) NR1, Re=3,500 (b) NR7, Re=14,000 (c) NR8, Re=20,000

(d) NR1, Re=3,500 (e) NR7, Re=14,000 (f) NR8, Re=20,000

Figure 5.16: Average (a)-(c) and instantaneous (d)-(f) mixture fraction fields of He/air coaxial jets for $r_u \approx 5$ with varying Reynolds number. White line marks the stoichiometric contour, $f_s = 0.89$.

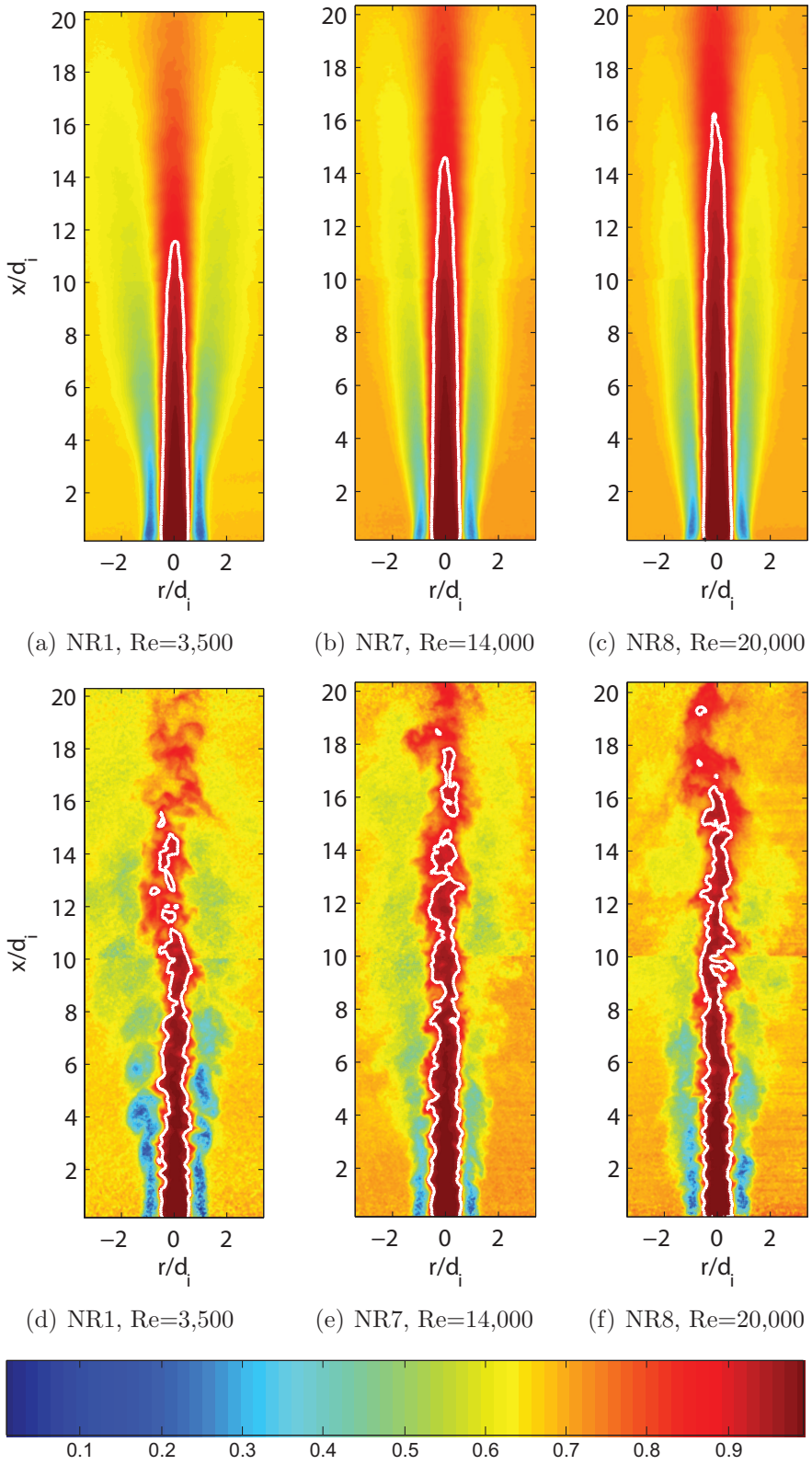

(a) NR1, Re=3,500 (b) NR7, Re=14,000 (c) NR8, Re=20,000

(d) NR1, Re=3,500 (e) NR7, Re=14,000 (f) NR8, Re=20,000

Figure 5.17: Average (a)-(c) and instantaneous (d)-(f) mixture fraction fields of He/air coaxial jets for $r_u \approx 1.1$ with varying Reynolds number. White line marks the stoichiometric contour, $f_s = 0.89$.

potential core), $f_s = 0.89$ (the stoichiometric mixture fraction of H_2/O_2), $f_s = 0.80$ (the stoichiometric mixture fraction of CH_4/O_2) and $f_s = 0.85$ (which falls between the latter two locations). The data are compared to potential core lengths reported in the literature along with a brief discussion on the limits of the momentum flux scalings.

5.5.1 Collapse of all Nonreacting Data

Figure 5.18 displays the stoichiometric mixing length for all cases in the thirteen nonreacting data groups. Both linear and log-log plots are shown. NR1-NR8 are He/air cases, NR9-NR11 are H_2/air and NR12-NR13 are CH_4/air cases. Note that $f_s = 0.89$ for H_2 and He cases and $f_s = 0.80$ for CH_4. From Fig. 5.18 it is clear that the momentum flux ratio parameter ($[M^{1/2}X_s]^{-1}$) can be used to correlate values of L_s in nonreacting coaxial jets. The deviation from this scaling in Fig. 5.18*a* are caused by the Reynolds number effect and the "shear-like" to "wake-like" transition that are discussed in §5.4.5 and §5.4.2.2 respectively. Four mixing lengths were measured for each case and they are plotted in Fig. 5.19. As expected, the same deviations are observed that were seen in Fig. 5.18.

Scaling constants C_1 and C_2 from the momentum flux ratio model (Eq. 2.28) were obtained for high Reynolds number and low Reynolds number cases using the four mixing lengths measured for each case. In addition, the scaling constant C_1 was obtained for the high Reynolds number data with the constant C_2 set to zero (Eq. 2.27). CH_4/air data, while taken at atmospheric pressure, had Reynolds number values between 18,000-35,000 and 12,000-14,000 for cases NR12 and NR13 respectively, and consequently was included in the high Reynolds number data groups. The other two data sets included in the high Reynolds number data group are NR7

and NR8 which correspond to elevated pressure He/air cases. Using a linear least squares best fit procedure, values of 2.7 and 1.19 were obtained for C_1 and C_2 respectively. High Reynolds number data groups and the corresponding curve fit are shown in Fig. 5.20. Using these constants, the difference between the data and the momentum flux ratio model (a straight line in Fig. 5.20) is 7%, for the high Re number data. In addition, the scaling constant C_1 was obtained with C_2 held at zero for the high Re number data and the fit to the data is shown in Fig. 5.21. A value of 3.06 for C_1 was found. While this model fits the large $(M^{1/2}X_s)^{-1}$ value mixing lengths well, the fit at small $(M^{1/2}X_s)^{-1}$ values is poor. This poor fit makes the use of C_2 necessary. Unfortunately the constant C_2 is likely not universal over all coaxial jets but a weak function of the inlet velocity profiles and the shape of the injector post. The results of Villermaux and Rehab (2000) suggest that in the case of a sharp injector post and uniform inlet velocity profiles C_2 will equal zero. However, for the injector geometries used in this C_2 is constant and should be thought of as analogous to the virtual origin in simple jets.

Using the same fitting procedure for the lower Reynolds number nonreacting data groups, the scaling constants C_1 and C_2 were found to be 1.62 and 2.02 respectively. Note that cases that lie in the "shear-like" to "wake-like" transition regime were removed since they are not expected to follow the scaling. The cases that were removed were those in groups NR9 and NR11 with r_u values of 1.06 and 1.37. A total of four data points were removed. Low Reynolds number data groups and the corresponding curve fit are shown in Fig. 5.22. For the low Reynolds number data, the difference between the data and the momentum flux ratio model (a straight line in Fig. 5.22) is 6%.

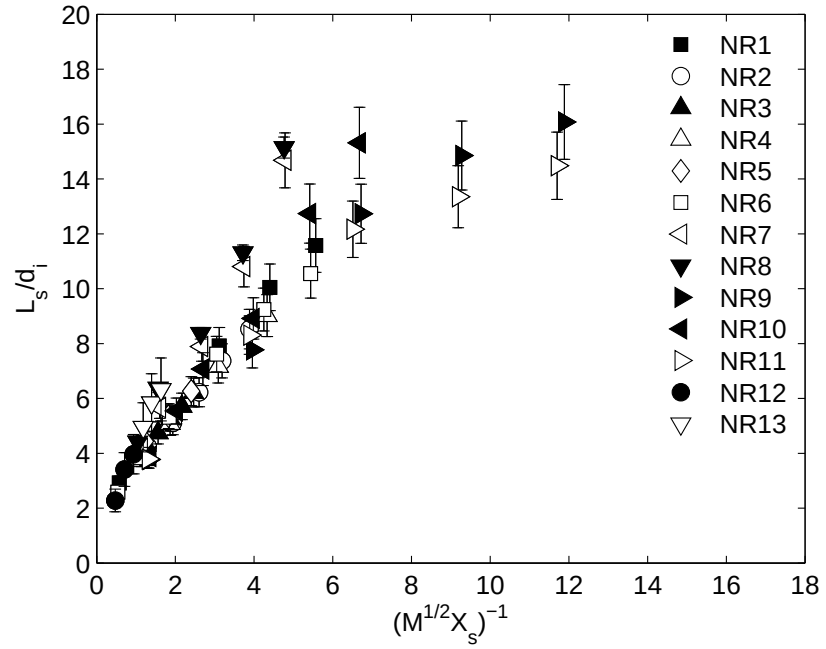

(a)

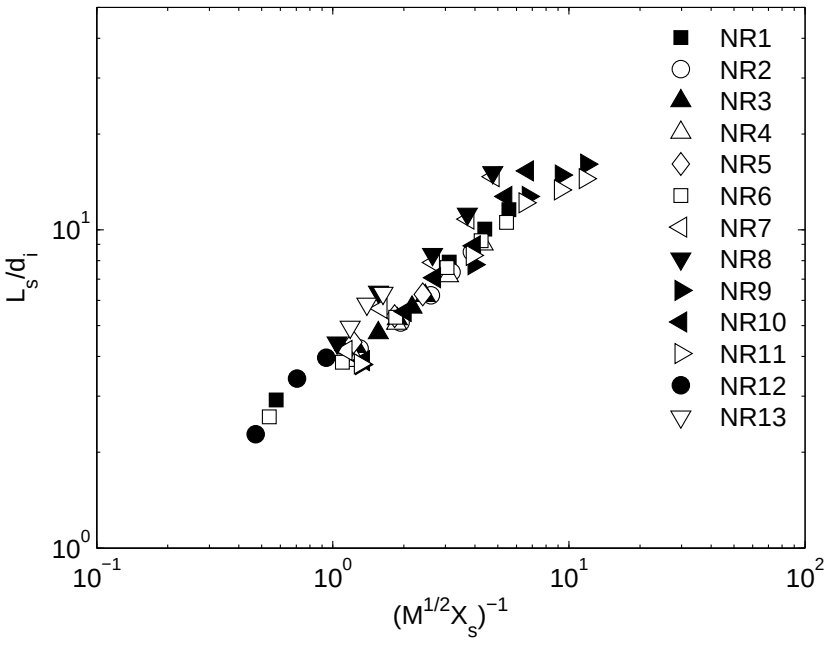

(b)

Figure 5.18: Stoichiometric mixing lengths for all nonreacting coaxial jets plotted against the momentum flux parameter for linear (a) and log-log (b) axes. NR1-NR8 are He/air, NR9-NR11 are H_2/air and NR12-NR13 are CH_4/air nonreacting coaxial jets.

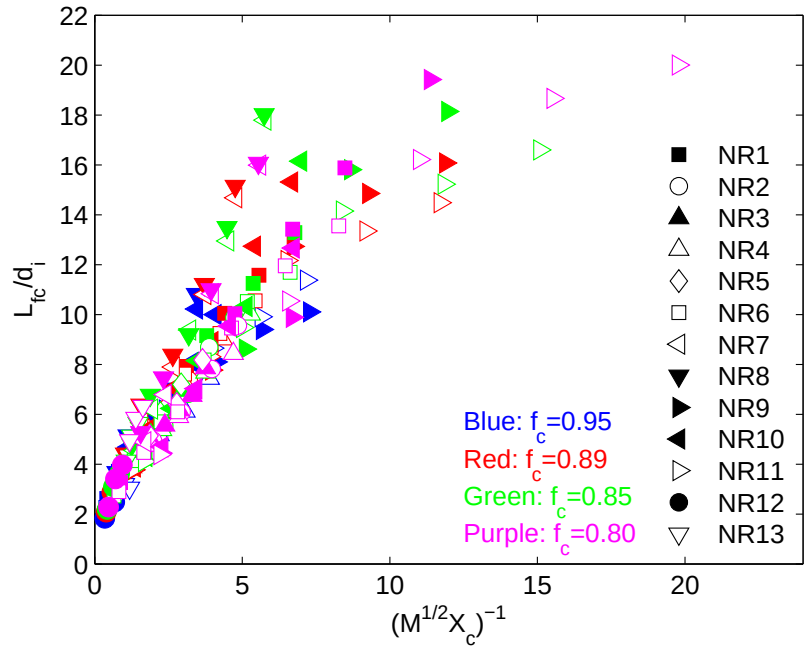

(a)

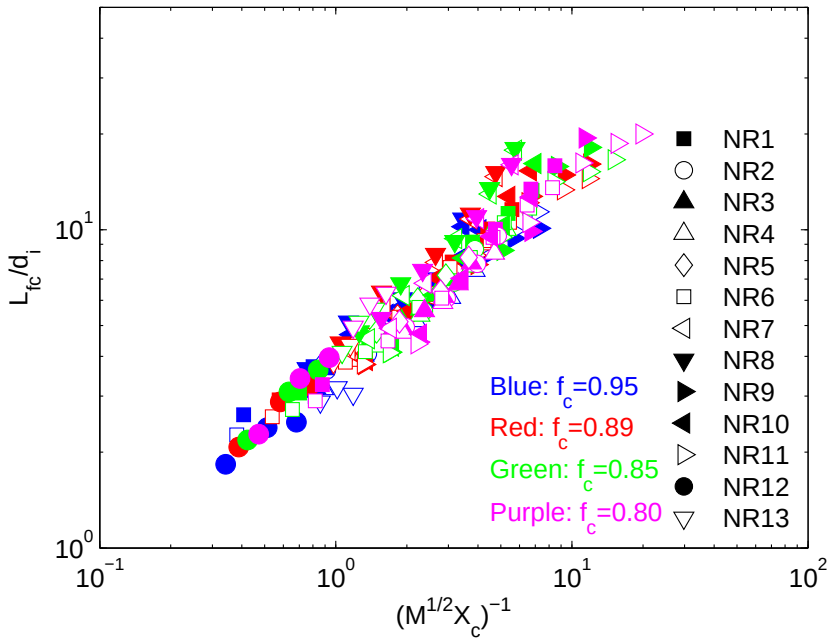

(b)

Figure 5.19: Mixing lengths plotted for all nonreacting coaxial jets against the momentum flux parameter for four values of mixture fraction (f_s =0.95, 0.89, 0.85, 0.80) in linear (a) and log-log (b) axes. NR1-NR8 are He/air, NR9-NR11 are H_2/air and NR12-NR13 are CH_4/air nonreacting coaxial jets.

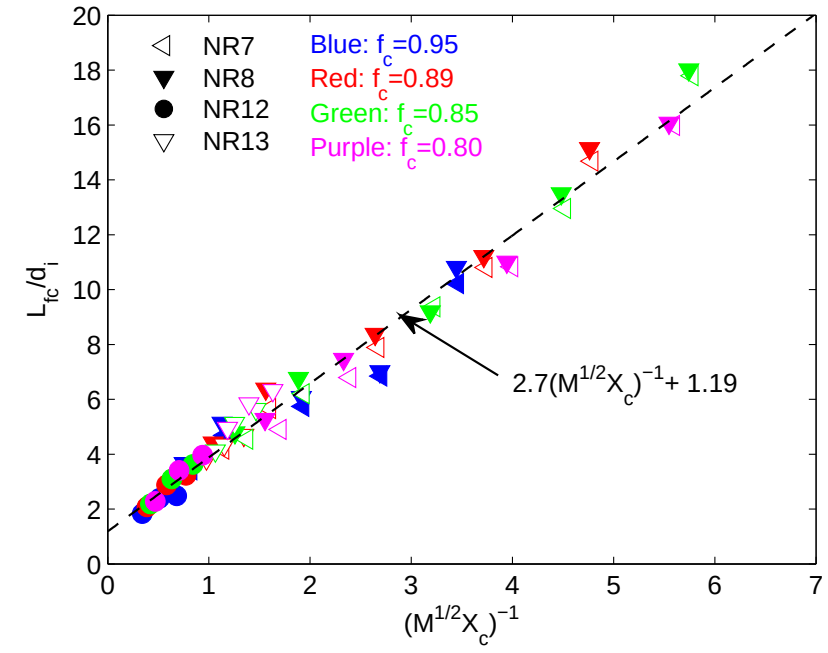

(a)

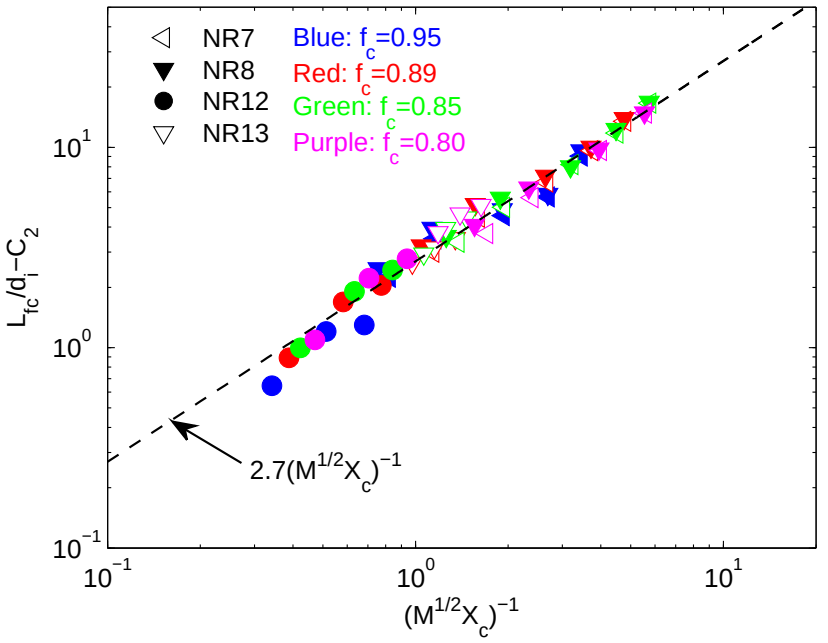

(b)

Figure 5.20: Mixing lengths for all high Reynolds number coaxial jets plotted against the momentum flux scaling for four values of mixture fraction (f_s =0.95, 0.89, 0.85, 0.80) in linear (a) and log-log (b) axes. NR7-NR8 are He/air and NR12-NR13 are CH_4/air nonreacting coaxial jets with Reynolds number ranges of 13,000-20,000 and 12,000-35,000 respectively.

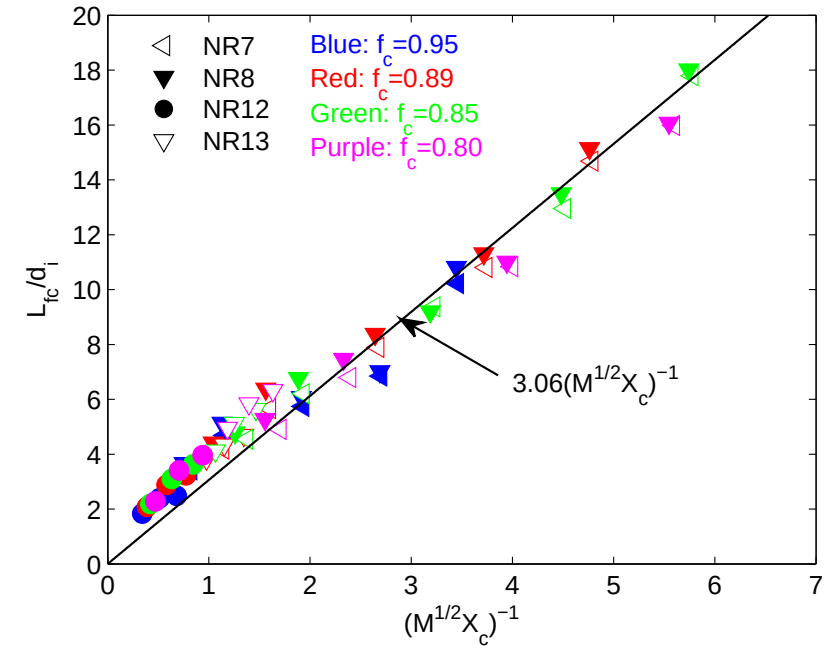

(a)

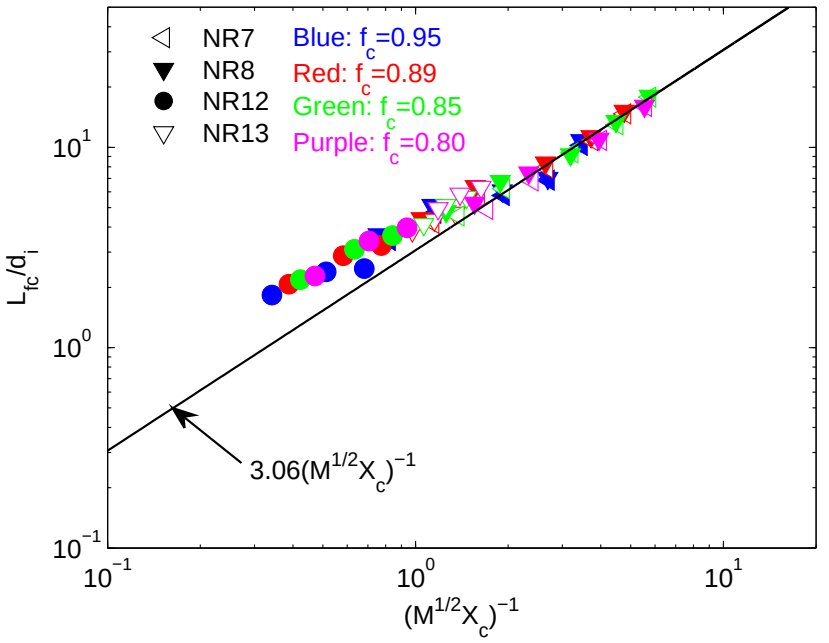

(b)

Figure 5.21: Mixing lengths for all high Reynolds number coaxial jets plotted against the momentum flux scaling with scaling constant C_2 set to zero for four values of mixture fraction (f_s =0.95, 0.89, 0.85, 0.80) in linear (a) and log-log (b) axes. NR7-NR8 are He/air and NR12-NR13 are CH_4/air nonreacting coaxial jets with Reynolds number ranges of 13,000-20,000 and 12,000-35,000 respectively.

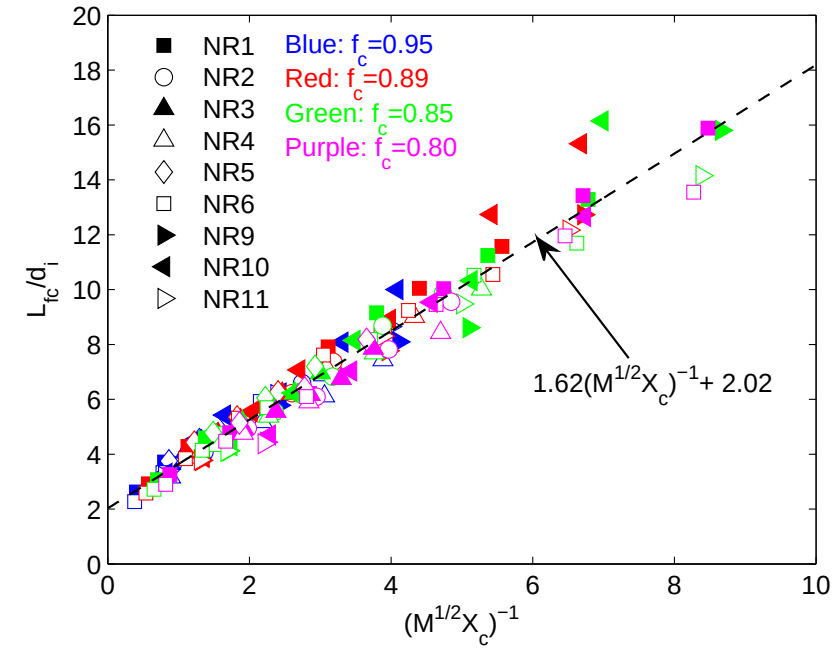

(a)

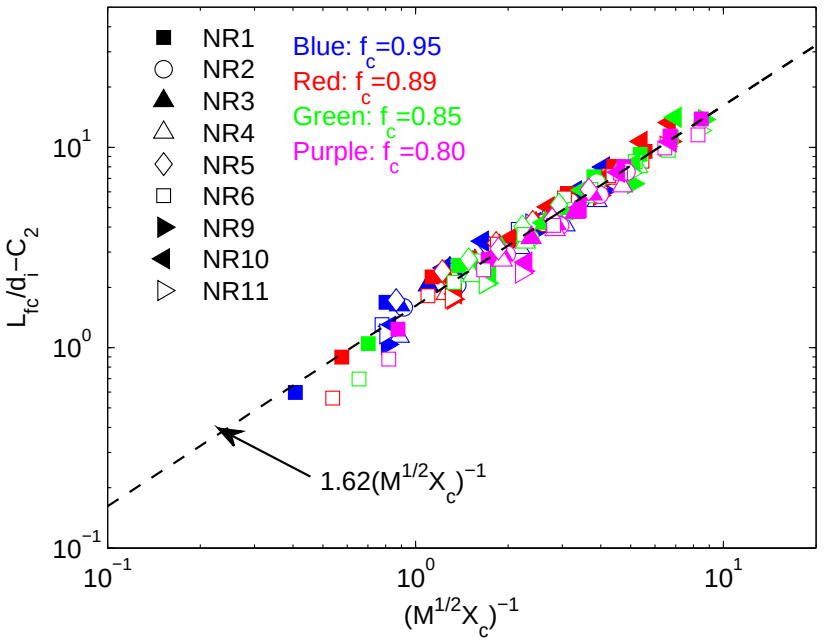

(b)

Figure 5.22: Mixing lengths for all low Reynolds number coaxial jets plotted against the momentum flux parameter for four values of the centerline mixture fraction ($f_s = 0.95, 0.89, 0.85, 0.80$) in linear (a) and log-log (b) axes. NR1-NR6 are He/air and NR9-NR11 are H_2/air nonreacting coaxial jets with Reynolds number ranges of 2,400-6,000 and 2,800-13,000 respectively.

5.5.2 Comparison with Prior Studies

Prior studies of coaxial jets have for the most part focused on the near field from the injector to the end of the potential core. Hence comparisons with data in the literature is limited to the potential core mixing length L_C. In this work the location $f_C = 0.95$ on the centerline is used to define the potential core length. It typically is located just after a rapid change in concentration at the end of the potential core. Previous results, which were used for comparison, comprise single phase coaxial jet data for which potential core lengths were reported. By single phase it is meant that the two fluids were either liquid-liquid or gas-gas at subcritical conditions. A list of such data obtained by the authors is provided in Table 5.1 and includes the original paper where it was first published, the fluids used, the diameter ratio (β), and the symbol used to represent the data set. Table 5.2 lists the same data sets, but includes values for S, r_u, M, and the injector geometry along with the paper and the number of the figure that contains the relevant data. These core length values along, with the present high Reynolds number core lengths and all core length values are plotted in Fig. 5.23*a* and Fig. 5.23*b* respectively. All black symbols represent lengths measured in this work, while all colored symbols represents lengths obtained from the literature. Is is seen that all of the data scales as $M^{-1/2}$ but the scaling constant does seem to differ slightly for the different studies. This is because the potential core lengths were obtained using a number of different measurement techniques and different definitions of the potential core. The difference in scaling constant is most notable in the results of Rehab et. al and Champagne and Wygnanski. A scaling constant of 5, which is recommended by Davis et al. (2006), fits all of the data reasonably well. The quantities that were measured were the density field using an aspirating probe (Favre-Marinet and Camano-Schettini 2001), PLIF emitted by a

fluorescent dye (Rehab et al. 1998 and Dahm et al. 1992), and finally velocity data (Au and Ko 1987, Champagne and Wygnanski 1971 and Chigier and Beer 1964).

5.5.3 Limits of the Momentum Flux Ratio Scaling

While most of the data collapse to a straight line in Fig. 5.23*b* the limits of the momentum flux ratio scaling are apparent. The upper limit is reported by Favre-Marinet and Camano-Schettini (2001) to be approximately 50. At this limit the ratio of the outer jet momentum to the inner jet momentum becomes large enough that a recirculation zone is formed on the centerline. Once this recirculation is formed the potential core becomes truncated and the momentum flux ratio scaling breaks down.

The second limit (the lower M limit) which this work did explore is the "shear-like" to "wake-like" transition. This limit was obtained only by reducing the momentum flux ratio (M) to an order of magnitude lower than previous studies; M was reduced from 1.0 to 0.1. The second limit occurs for M values of 0.1 to 0.2 as seen in Fig. 5.23*b*. However as discussed in §5.4.2.2 this limit can depend on injector post thickness and inlet velocity profiles. Ultimately between these two limits the momentum flux ratio scaling does an excellent job of correlating both potential core and stoichiometric mixing lengths for fuel oxidizer combinations of interest in rockets and oxy blast furnaces.

Table 5.1: Operating parameters for previous studies conducted on single phase coaxial jets with $r_u > 1$ and reported core lengths. Fluids used and the diameter ratio β are reported. All data taken at atmospheric pressure.

Data Set	Symbol	Inner Fluid	Outer Fluid	Ambient Fluid	β	Original Paper
Favre S=0.138 Air	□	Air	He	Air	1.35	Favre-Marinet and Camano-Schettini (2001)
Favre S=0.138 He	●	Air	He	He	1.35	Favre-Marinet and Camano-Schettini (2001)
Favre S=0.655	△	Air	He/Air	Air	1.35	Favre-Marinet and Camano-Schettini (2001)
Favre S=0.028	▲	SF_6	He	He	1.35	Favre-Marinet and Camano-Schettini (2001)
Rehab $\beta = 1.35$	○	Water	Water	Water	1.35	Rehab et al. (1998)
Rehab $\beta = 1.37$	■	Water	Water	Water	1.37	Rehab et al. (1998)
Rehab $\beta = 2.29$	◇	Water	Water	Water	2.29	Rehab et al. (1998)
Au and Ko	▽	Air	Air	Air	2.00	Au and Ko (1987)
Dahm	◁	Water	Water	Water	1.44	Dahm et al. (1992)
Champagne $\beta = 1.51$	▷	Air	Air	Air	1.51	Champagne and Wygnanski (1971)
Champagne $\beta = 1.98$	◀	Air	Air	Air	1.98	Champagne and Wygnanski (1971)
Chigier and Beer	▲	Air	Air	Air	2.56	Chigier and Beer (1964)

Table 5.2: Operating parameters for previous studies conducted on single phase coaxial jets with $r_u > 1$ and reported core lengths. Injector geometry, r_u, S, and M reported. All data at atmospheric pressure. NR stands for not reported and SP is for sharp point.

Data Set	S	r_u	M	d_e, mm	d_i, mm	T_P, mm	Data Taken From	Source Fig. #
Favre S=0.138 Air	0.138	32-2.7	146-1.0	27	20.0	SP	Favre-Marient (2001)	12
Favre S=0.138 He	0.138	32-8.2	146-9.2	27	20.0	SP	Favre-Marient (2001)	12
Favre S=0.655	0.655	8.1-1.2	42-1.0	27	20.0	SP	Favre-Marient (2001)	12
Favre S=0.028	0.028	70-18	200-9.0	27	20.0	SP	Favre-Marient (2001)	12
Rehab $\beta = 1.35$	1.0	5.7-2.3	33-5.2	NR	NR	NR	Rehab et al. (1998)	1
Rehab $\beta = 1.37$	1.0	5.7-2.3	33-5.2	NR	NR	0.3	Rehab et al. (1998)	1
Rehab $\beta = 2.29$	1.0	5.7-2.3	33-5.2	NR	NR	NR	Rehab et al. (1998)	1
Au and Ko	1.0	6.7-1.3	45-1.5	40	20.0	1.0	Rehab et al. (1998)	1
Dahm	1.0	4.2-2.6	18-6.7	76.5	53.3	1.3	Rehab et al. (1998)	1
Champagne $\beta = 1.51$	1.0	10-2.0	100-4.0	37.8	25.0	NR	Rehab et al. (1998)	1
Champagne $\beta = 1.98$	1.0	10-2.0	100-4.0	49.5	25.0	NR	Rehab et al. (1998)	1
Chigier and Beer	1.0	9.2-1.1	85-1.2	64	25.0	NR	Favre-Marient (2001)	1

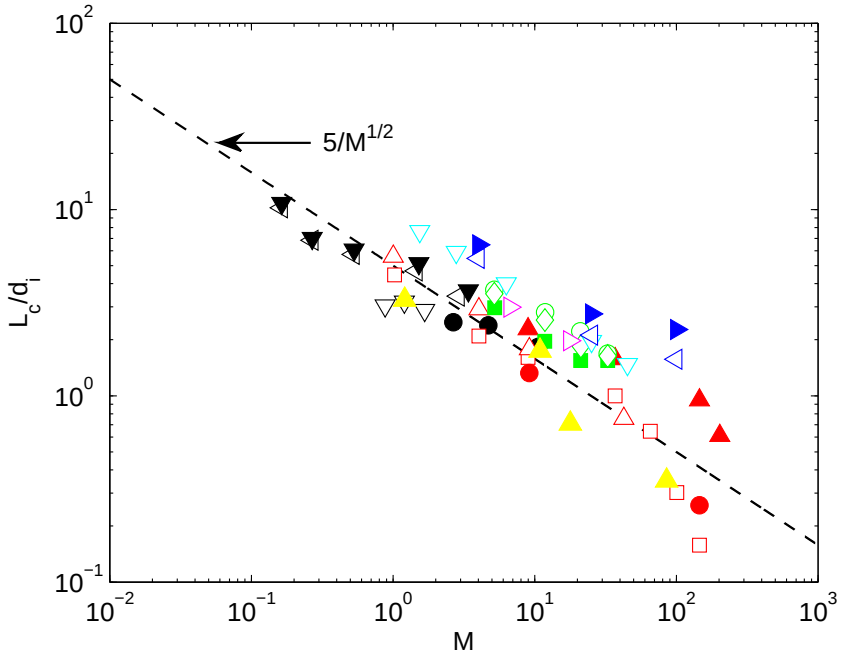

(a)

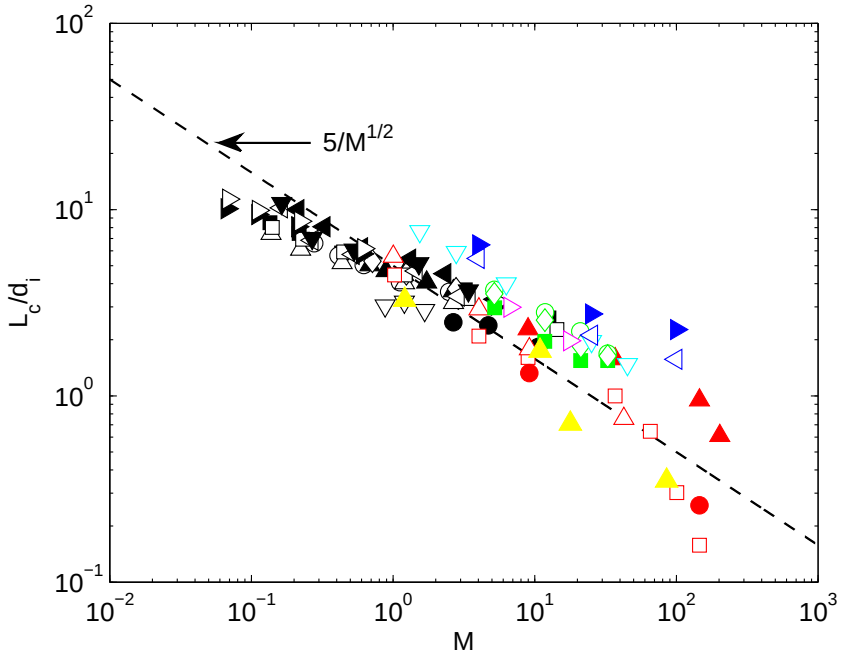

(b)

Figure 5.23: Length of jet core normalized by inner injector diameter versus momentum flux ratio (M) for all coaxial jet core lengths in the literature known to the author. Source, properties, and symbol legend of previous work provided in Table 5.1. In (a), only core lengths of high Reynolds number data from this study are included, while in (b) all core length data are included. All points from this study are black. Symbols can be found in Table 4.5.

CHAPTER VI

Reacting Turbulent Coaxial Jets Results

A main objective of this work is to compare reacting and nonreacting coaxial jets to gain an understanding of the effect that heat release has on the mixing field. To this end, OH radical contours obtained using OH PLIF were utilized as a marker of the flame location and hence the stoichiometric contour. From these combustion radical contours, flame lengths were obtained and compared to the nonreacting coaxial jet results of Chapter V. The three fuel/oxidizer combinations that were investigated were H_2 / O_2, H_2 / air, and CH_4 / O_2. In addition, for H_2 / O_2 three different chamber pressures and consequently three different Reynolds numbers ranges were studied. Experimental parameters for the five reacting data groups are given in Table 4.5. Additional insight into the convection of outer scale structures downstream was gained by looking at time resolved chemiluminescence images. An attempt is made to account for heat release effects on the reacting density field by applying the "general equivalence principle" of Tacina and Dahm (2000). Lastly, some minor effects of nonuniform pressure and temperature during data acquisition are addressed.

6.1 Structure of Turbulent Coaxial Jet flames

6.1.1 OH Radical Contours

A substantial amount of information about the general structure of turbulent coaxial jet flames can be gained from examination of average and instantaneous OH contours. A representative set of such images for H_2 / O_2 jets corresponding to data group R2 are shown in Fig. 6.1 for three cases with varying momentum flux ratio M. Instantaneous images show thin laminar like layers near the jet exit. As one moves downstream the wrinkling and thickness of the OH layers increases. At some downstream distance large-scale turbulent structures distort the flame enough to cause pockets to form, which then convect downstream before burning out. The average images indicate some of the same features observed in the instantaneous cases. Near the base of the flame the OH layers are thin, move and wrinkle little, and no OH is observed in the inner core region of the coaxial jet. At some location downstream the two sides of the jet start to merge, but two distinct sides are still viable. Finally the two sides completely combine creating a region of near constant OH which corresponds to where the large-scale structures have become large enough to highly distort the flame and cause flame tip breakup. From this area the average OH signal decreases as the frequency of burning pockets decreases. Also clearly visible in these average OH images is the increase in flame length that is caused by the decrease in momentum flux ratio as predicted by the cold flow turbulent coaxial jet analysis.

To accurately interpret these qualitative OH images, an understanding of what the OH signal actually represents is needed. Accordingly, an analysis was performed to relate the OH signal to the stoichiometric or flame front signal which is the same

in a high Damköhler number diffusion flame. This analysis requires quenching and populations effects on the OH molecular to be taken into consideration. Accounting for quenching effects requires that the temperature and relative mole fractions of all major collisional species be known. One way to accomplish this is to use strained laminar counterflow flame calculations to simulate the flame in our coaxial diffusion flames. The details of this analysis are discussed in §4.3.2, however the results show that the OH radical should form thin layers at the flame front and that the location of the stoichiometric value is 67%, 94%, and 74% of the local peak signal on the rich side of the flame for H_2 / O_2, H_2 / air, and CH_4 / O_2 respectively. In the case of H_2 / O_2, combustion or chamber pressure has a negligible effect on this value, but does effect the thickness of the layer. Given these results and the thin nature of the OH layers observed in Fig. 6.1, it is clear that OH is a good marker of the flame front and therefore the stoichiometric contour.

Of course the thickness of the OH layers is a function of both the chemistry of the reaction and the pressure at which the reaction takes place. To illustrate this point a representative instantaneous OH image from each reacting data group is shown in Fig. 6.1. The cases shown in this figure include CH_4 / O_2 at $P_c = 5.2$ atm (a), H_2 / air at $P_c = 4.8$ atm (b), and H_2 / O_2 at $P_c = 0.98$, 4.5, and 8.5 atm, (c), (d), and (e) respectively. In the H_2 / O_2 cases the OH layers thin with increasing pressure as would be expected from the diffusion reaction rate balance. In fact the OH layer in the atmosphere pressure case Fig. 6.2*c* is so thick and the wrinkling of the layer so minimal, it is questionable whether this case and others in the data set R1 can be viewed as fully turbulent ($Re = 4,900$). It can also be observed in Fig. 6.2*d* and more so in 6.2(e) that the signal strength decreases from the left layer to the right layer due to absorption of the laser sheet at higher chamber pressures. The OH

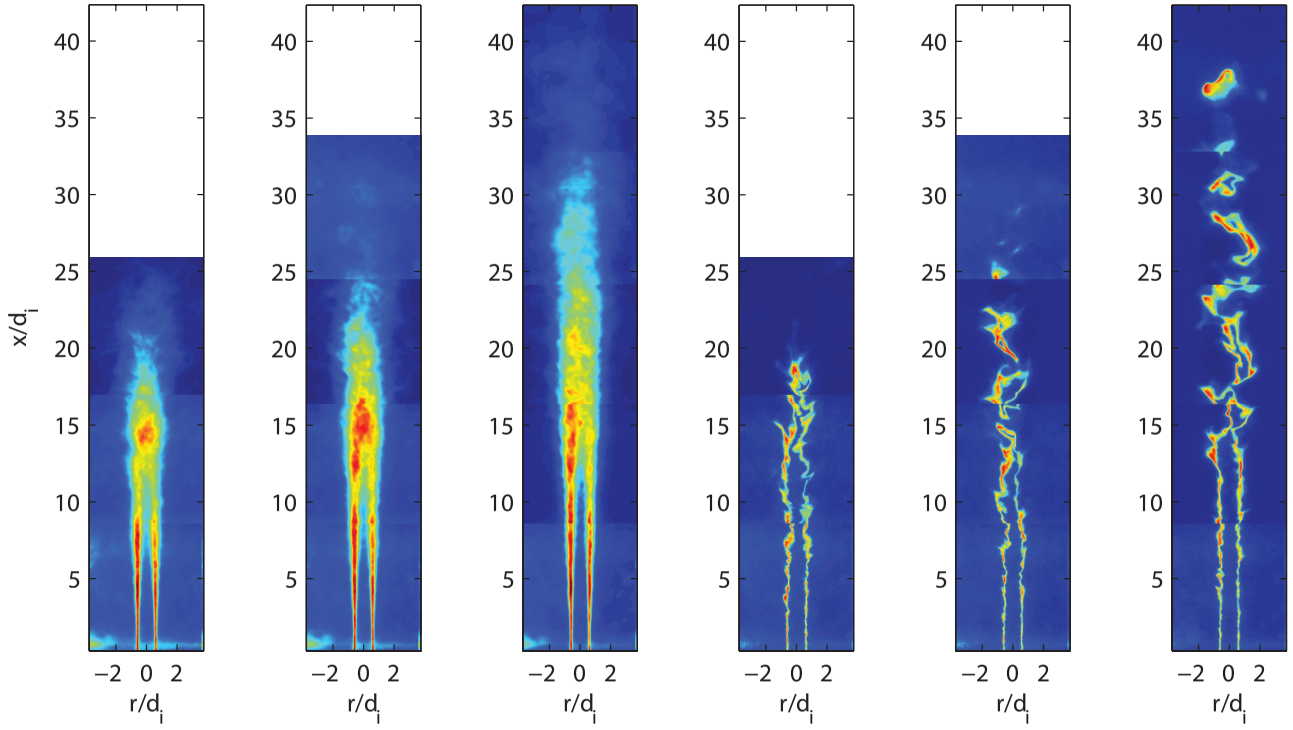

(a) $M = 4.4$ (b) $M = 3.3$ (c) $M = 1.9$ (d) $M = 4.4$ (e) $M = 3.3$ (f) $M = 1.9$

Figure 6.1: Time averages of thresholded instantaneous OH contours (a)-(c) and instantaneous OH contours (d)-(f) for H_2 / O_2 (outer/inner) turbulent coaxial jet flames with varying momentum flux ratios (M) from data group R2. Images from five window locations are superimposed.

layers seen in Fig. 6.2*b*, H_2 / air at $P_c = 4.8$ atm, are by far the thinnest even though the methane and middle H_2 / O_2 case have similar pressures. The thin layer in the H_2 / air case is caused by the OH radical existing over a much smaller mole fraction range in H_2 / air chemistry compared to oxygen enriched combustion. It should also be noted that the voids in the OH layers in the near field of this case are not due to extinction, but water droplets on the window interfering with image acquisition. Water droplets forming on the window at ignition were a common occurrence in most cases at the first window location. Typically these droplets were evaporated off within a second or two, but in lower heat release cases such as H_2 / air the droplets persisted the entire run. Figure 6.2*a* corresponds to CH_4 / O_2 at $P_c = 5.2$ atm and has medium thick layers again due to the chemistry of the reaction. One aspect of the CH_4 images which differed from the other reactions was interference in the images from polycyclic aromatic hydrocarbons (PAH), soot precursors. PAH broadband absorbs around 283 nm and fluorescence around 300-400 nm which is where the OH was excited and collected respectably (Smyth et al. 1997). Fortunately, a physical separation between the diffuse PAH signal, and the structured OH layers allowed a custom built program in Matlab to remove the PAH signal leaving just the OH layers. The presence of PAH in the recirculations zones of the rocket is not surprising since the recirculation zone is filled with hot products and excess fuel which is an ideal environment for the formation of PAH.

The structures observed here in our "inverse" coaxial diffusion flame appear to be consistent with the structures observed in simple turbulent jets (Mungal et al. 1991 and Mungal and O'Neil 1989) and "normal" coaxial jet diffusion flames (Sautet et al. 2001 and Ditaranto et al. 2001). Here "inverse" is used to denote a flame with oxidizer surrounded by fuel, which is the only arrangement investigated in this

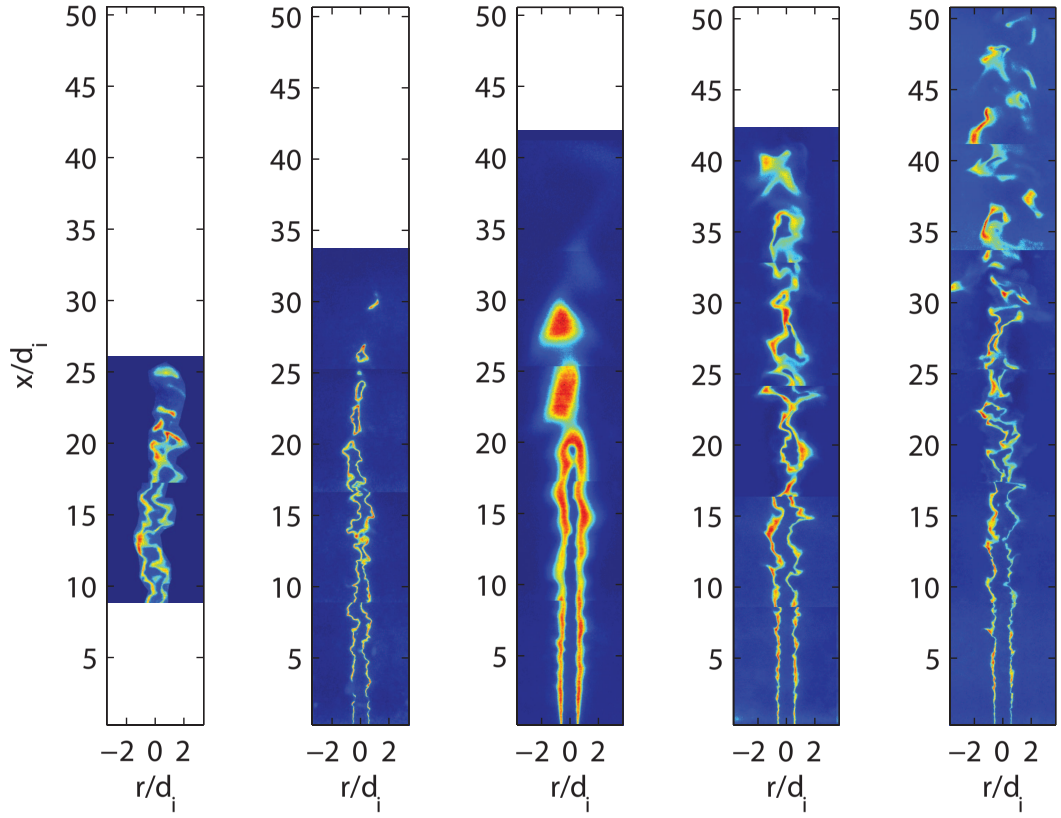

Figure 6.2: Comparison of instantaneous OH contours for all reacting data groups. (a) is from R5 and $M = 2.0$. (b) is from R4 and $M = 0.6$. (C) is from R1 and $M = 0.6$. (d) is from R2 and $M = 0.7$. Last, (e) is from R3 and $M = 0.8$.

work, versus the "normal" flame configuration where fuel is surrounded by oxidizer. With this in mind, a closer look at the near fields of the instantaneous images in Fig. 6.2 show that the OH layers are not perfectly straight but have very small ripples. Therefore large-scale structures are present, however they have not grown large enough to distort the flame at this location. This begs the question as to what form do these large-scale structures have in our reacting coaxial jet. Mungal and O'Neil (1989) report two instability modes associated with the underling vorticity field in their reacting turbulent jets. The modes were labeled axi-symmetric and asymmetric. The asymmetric mode is also referred to as a sinuous or helical mode in the literature to illustrate the three-dimensional nature of the instability. In the OH images the symmetric mode is characterized by wrinkles that have similar shape and size directly across from each other on the two sides of the flame. These wrinkles both bend towards or away from each other. This occurs when a vortex ring around the flame translates downstream wrinkling the flame. The asymmetric mode in the OH images is characterized by wrinkles that bend in the same direction across from each other and translate down the flame in a cork screw motion. This gives portions of the flame an "s" like shape.

Figure 6.3 shows five instantaneous images of the same flame, which correspond to H_2/O_2 with $M = 3.3$ (data set R2), at different instances in time. Both the axi-symmetric and asymmetric instability modes are visible in these images, however in the case shown and in all other flames the asymmetric instabilities are observed to occur much more frequently then the symmetric instability. The symmetric instabilities are observed to be mostly confined to the region just downstream of the jet exit, but do at times propagate farther downstream and play a role in flame tip break up. Of course these instability modes are important since if the symmetric instability

became the dominant instability the entrainment pattern would change altering the flame length.

One area of great interest is how the flame tip breaks up and the burning pockets are formed since this phenomena can greatly increase flame length. From the instantaneous images presented in Fig. 6.1, it is not clear what the primarily mechanism for break up is since at an image acquisition rate of 5 Hz these images can only be viewed as random in time and accordingly the structure of the flame before the breakup is unknown. Also with OH PLIF being a planar method it is impossible to rule out that the flame is not just bending out of the measurement plane. To fully understand the break up mechanisms a time resolved space integrated method such as high-speed chemiluminescence is needed.

6.1.2 Cinema Chemiluminescence

To obtain a deeper understanding of the flame tip break up process, chemiluminescence images of data set R2 (H_2 / O_2 at P_C = 4.5 atm) were taken at approximately 9,000 Hz which was fast enough to capture the break up process. Two processes by which the flame could locally extinguish and form pockets should be considered. First, the local strain rate on the flame is large enough to strain the flame out. This in the case of H_2 / O_2 combustion is very unlikely given the large strain rate needed to extinguish a H_2 / O_2 diffusion flame. Second, the large-scale structures strain the flame at a given location enough that over time the inner jet thins in a small area enough that the two sides of the flame burn together exhausting all oxidizer at that location resulting in local extinction.

To aid in evaluating the processes by which flame breakup occurs, four time sequences that illustrate flame break up for three different coaxial jets are shown

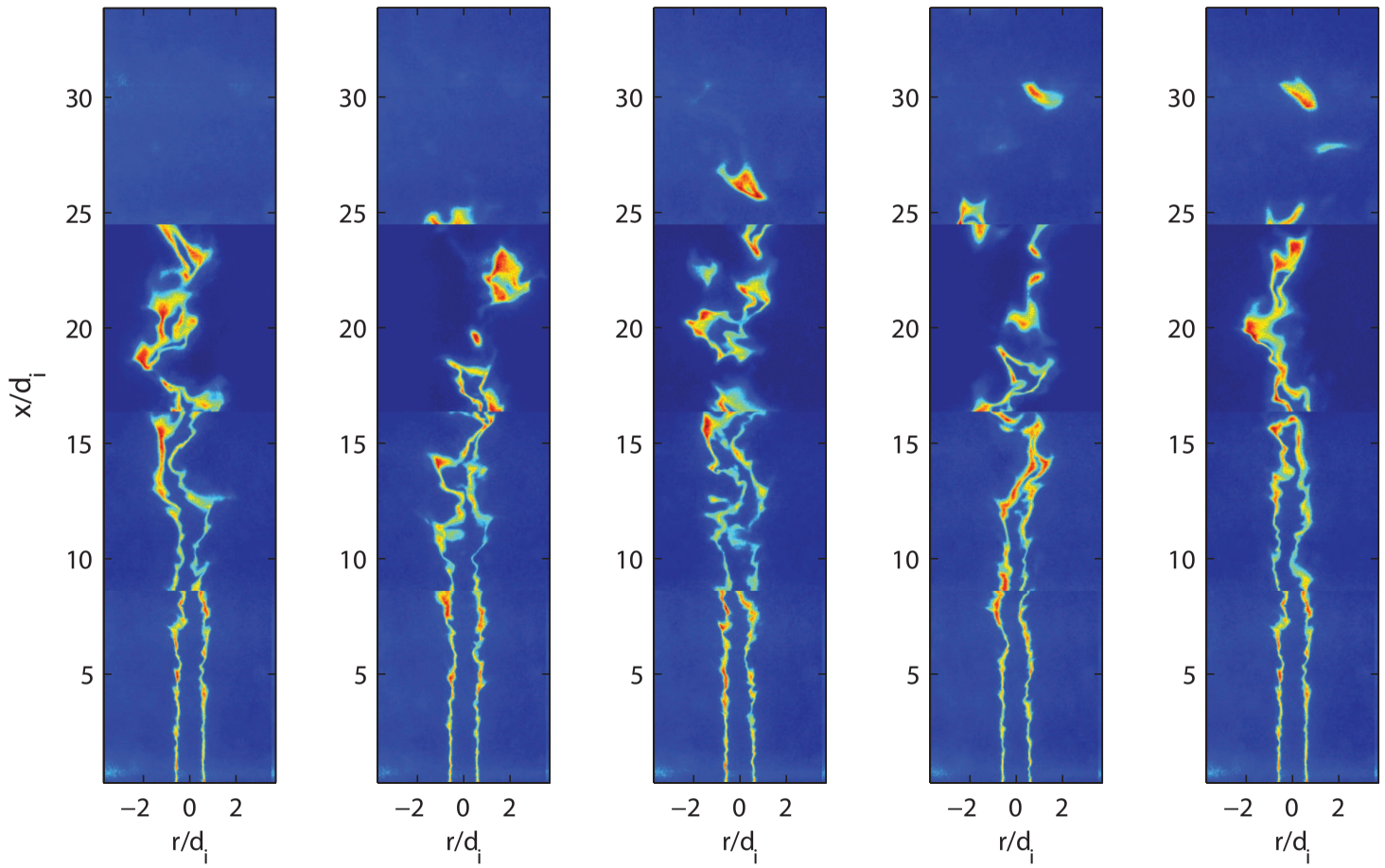

Figure 6.3: Instantaneous OH contours for H_2 / O_2 (outer/inner) turbulent coaxial jet flames with $M = 3.3$ from data group R2. Each image is made of 5 window locations each of which is a different instance in time.

in Figs. 6.4 and 6.5. The large-scale structures that interact with the flame front typically rotate towards the center jet since the high speed fluid is always the outer jet. In Fig. 6.4*a* on the far left the flame has a helical structure, characteristic of an asymmetric instability, with a small pocket already formed just past the tip that appears to be near burning out. As time progresses, two regions of the jet start to thin out leading to a three lobe shape. The bottom connector then starts to burn through and the two upper lobes separate and propagate downstream. It is expected that the flame separates at the second thin region, but this is not known for sure since the flame pocket propagates out of the field of view. The second time sequence, Fig. 6.4*b*, is taken at the same downstream location, but the momentum flux ratio has been decreased from 3.3 to 1.9. Again the flame is characterized by a helical structure in the far left. As the flame progresses in time an area below an area of high curvature thins out and then breaks apart. It was observed that the location of the break in the flame was usually just below a bend in the flame. Here it would appear that the flame just burns through at the thinnest location. This same phenomena is common in the instantaneous OH contour images where the flame below a pocket has a pinched shape such as in Fig. 6.4.

An important question to ask is, does momentum flux ratio affect the types or frequency of the structures in the flame and does this effect the break up process? In light of this question two time sequences from a case with $M = 0.8$ are shown in Fig. 6.5. The flame break up shown in Fig. 6.5*a* is very similar to the break ups show previously, where the flame burns through below an area of high flame curvature in a flame that appears to be dominated by an asymmetric instability. The second sequence, Fig. 6.5*b* shows a very different break up sequence. Here in the far left a symmetric instability has greatly thinned the inner jet and as time

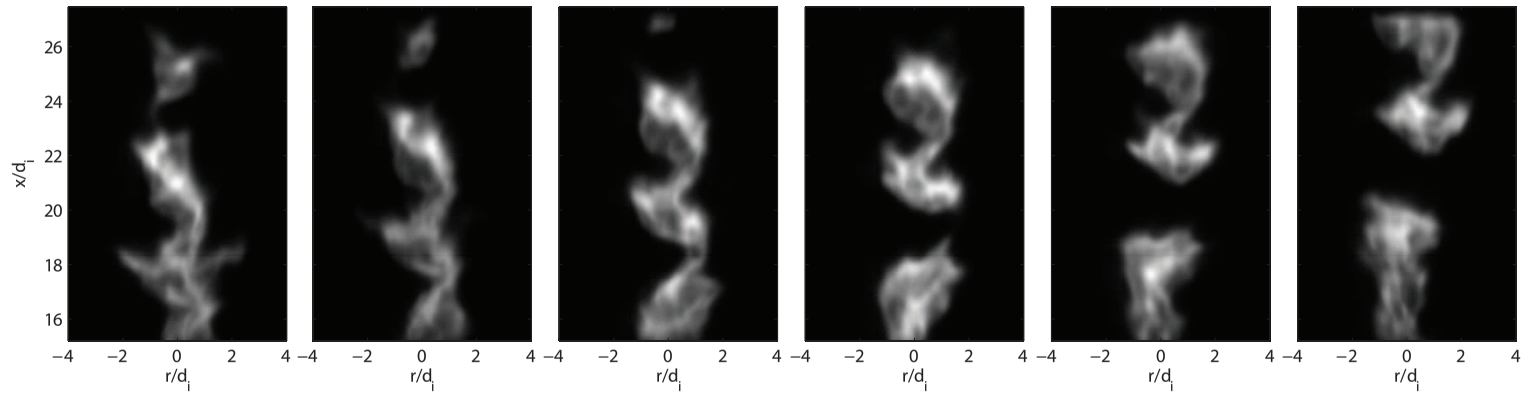

(a) $M = 3.3$

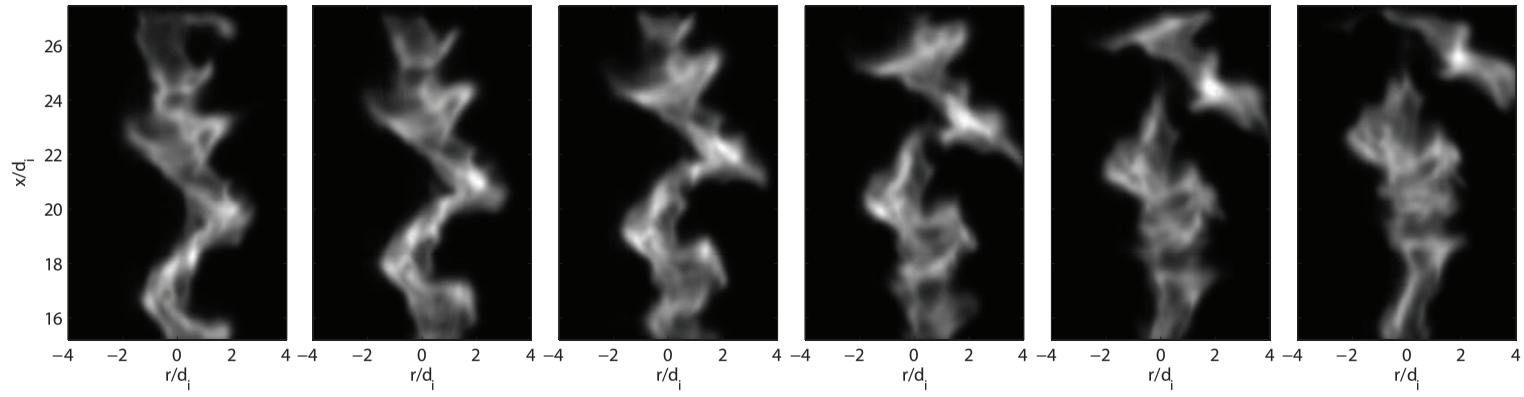

(b) $M = 1.9$

Figure 6.4: Time sequence of flame break up for H_2 / O_2 outer/inner fluids at $P_C = 4.5$ atm (R2). Two different cases are shown; $M = 3.3$ (a) and $M = 1.9$ (b). Exposure time was 31 μs and the time between frames was 111 μs or approximately 9,000 Hz.

progresses (moving to the right) this area continues to thin and then burns through. Therefore symmetric instabilities can also cause flame breakup. However, such a breakup was not found to occur more frequently in the two cases where $M < 1$ versus the $M > 1$ cases. This finding agrees with the results from the nonreacting work that the structure of coaxial jets does not change at $M = 1$, but at some much lower M value.

From these high-speed chemiluminescence the following conclusions can be drawn:

(i) flame pockets are the result of flame tip break up and not the result of the flame bending out of the measurement plane,

(ii) both symmetric and asymmetric instabilities can cause flame tip break up,

(iii) the relative occurrence of each type of instability does not seem to depend on whether the momentum flux ration(M) is above or below one,

(iv) asymmetric instabilities seem to be responsible for most instances of flame tip break up.

6.2 Flame Length Effects

6.2.1 Definitions of Flame Length

Producing a model which can accurately predict the flame length of turbulent coaxial jet flames is a primary goal of this work. However, first a definition of flame length must be decided upon. Having used the average stoichiometric mixing length in the nonreacting coaxial jets a definition that corresponds to the exact analog of this the reacting case is desirable. Since these diffusion flames operate in the high

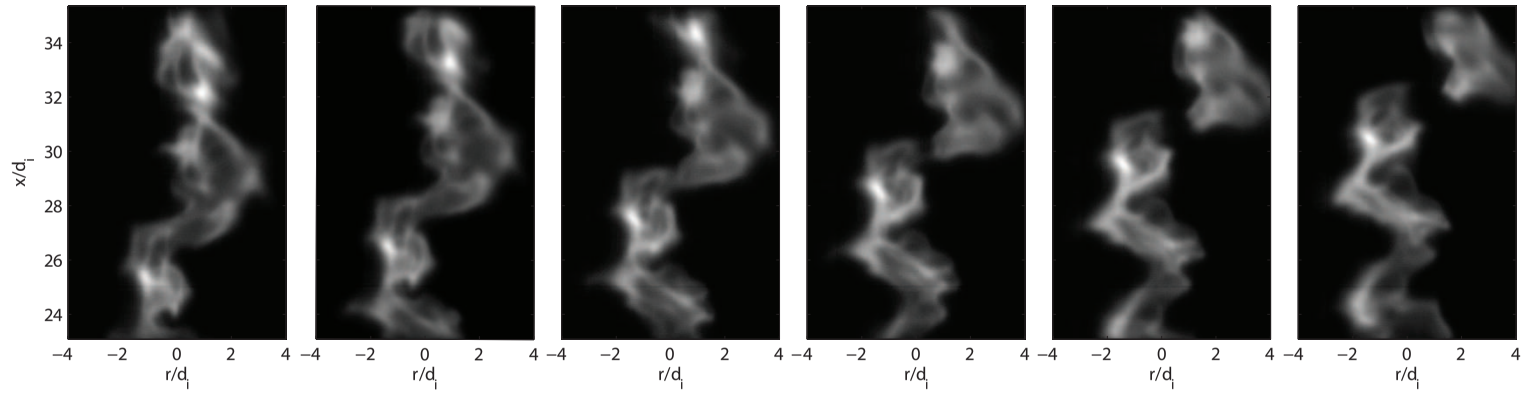

(a)

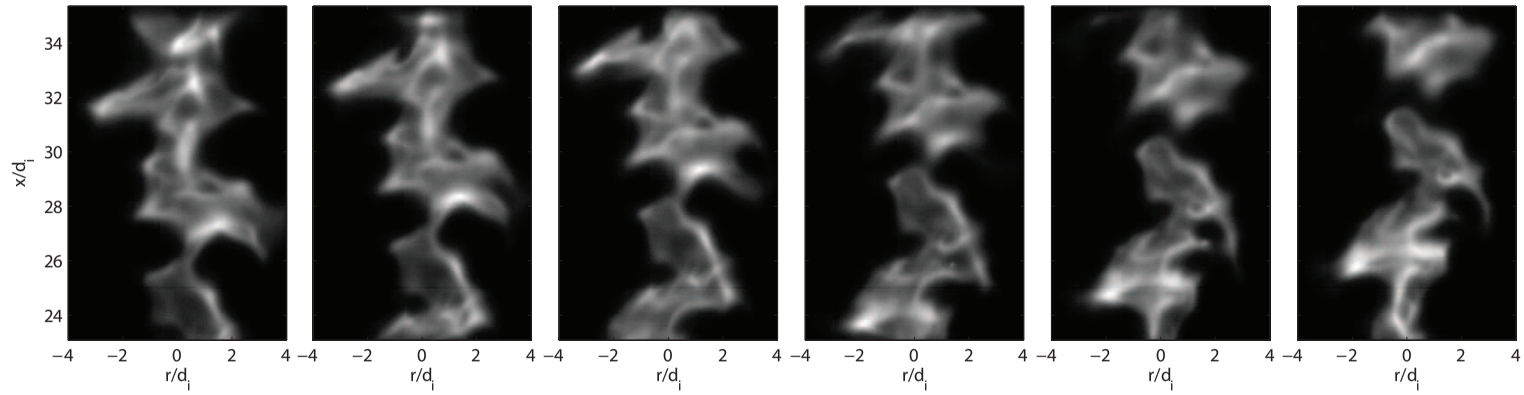

(b)

Figure 6.5: Time sequence of flame break up for H_2 / O_2 outer/inner fluids at $P_C = 4.5$ atm and $M = 0.8$ (R2). Two different break up events are shown. Exposure time was 21 μs and the time between frames was 111 μs or approximately 9,000 Hz.

Damköhler number limit, the downstream tip of the stoichiometric contour and the flame length are essentially the same. Defining flame length can be difficult due to the burning pockets described in the previous section. One common definition of flame length is "the furthest downstream point at which flaming gas is seen to dwell with an appreciable frequency" (Hawthorne et al. 1949). This could be extended to our instantaneous OH images to mean the top of the OH pocket that is observed farthest downstream. Such a definition would correspond with the average of individual images lengths discussed in §5.1.1 for nonreacting cases. This definition, however, was not the one used in the nonreacting work where the stoichiometric length of the average flow field was utilized. Also questions such as what size and signal level constitute a burning pocket make defining this length difficult. In addition, lengths calculated in this manner were found to extend in most cases across multiple window locations. From the upper window location the percent of time the flame was in this location and the average length when it was located here could be found, but when calculating the length of flame in the window below in most instances it was impossible to know if the flame had pockets beyond the field of view or not. The average of the instantaneous OH images does not directly correspond to our average mixture fraction field in the nonreacting case since signal only exists in thin layers around the flame in OH images and not the entire flow field as in the nonreacting mixture fraction fields. Also the local signal strength varies from location to location on the flame surface, but still marks the flame front and consequently the stoichiometric value.

It was decided to use a method that overcomes problems with different signal strengths. Local thresholding was applied to create a contour which marks the instantaneous reaction layer. Average images of these layers were created and the

flame length was defined based on centerline values. Due to the thin nature of the OH layers, the average of threshold images was deemed to be the most appropriate method. The length (L_s) was defined as the centerline location where the signal dropped to 50% of the OH signal strength that occurs above the core of the inner jet. This definition resulted in normalized centerline cutoff signal strengths of 30% for all H_2 / O_2 cases, 25% for all H_2 / air, and 35% for all CH_4 / air.

To ensure that this definition was consistent, the lengths of jets for which the average of individual flame lengths was calculated from the farthest downstream pocket were compared to the thresholded average length. Figure 6.6 shows that lengths (L_S) based on the two definitions differ only by a constant factor of 1.24. Therefore the two definitions are constant to within a proportionality constant.

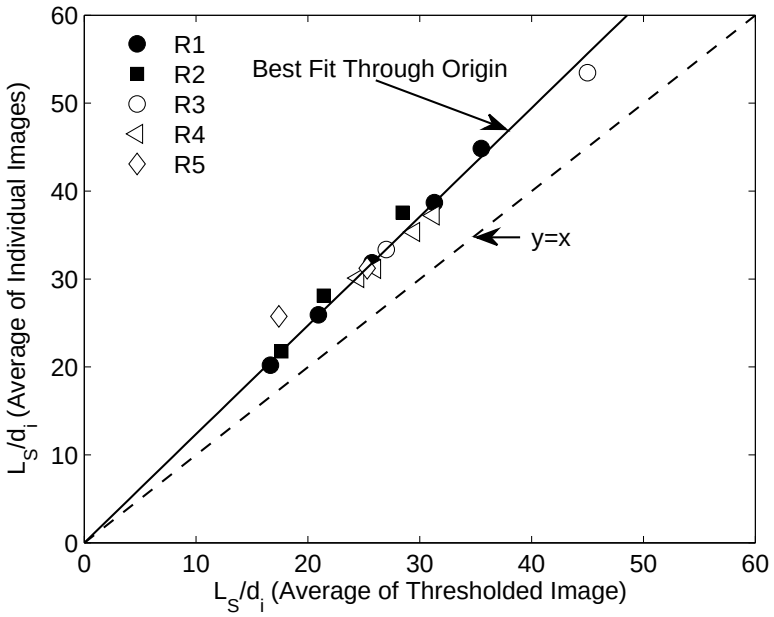

Figure 6.6: Comparison of values of L_S/d_i based on two definitions of L_S. Vertical axis: L_S calculated from the average thresholded image. Horizontal axis: L_S calculated from the average of individual L_S/d_i values. Cases for which the average of individual images were difficult to define due to the flame tip spanning multiple window locations are omitted.

The effect of the choice of the cutoff signal strength was tested for data set R2 (H_2/O_2 at $P_c = 4.8$ atm). Results are shown in Fig. 6.7. A normalized signal strength of 0.30 is the value that was chosen for H_2/O_2 data analysis. Figure 6.7 illustrates that changing the cutoff signal level between 0.20 and 0.35 results in small changes in the proportionality constant.

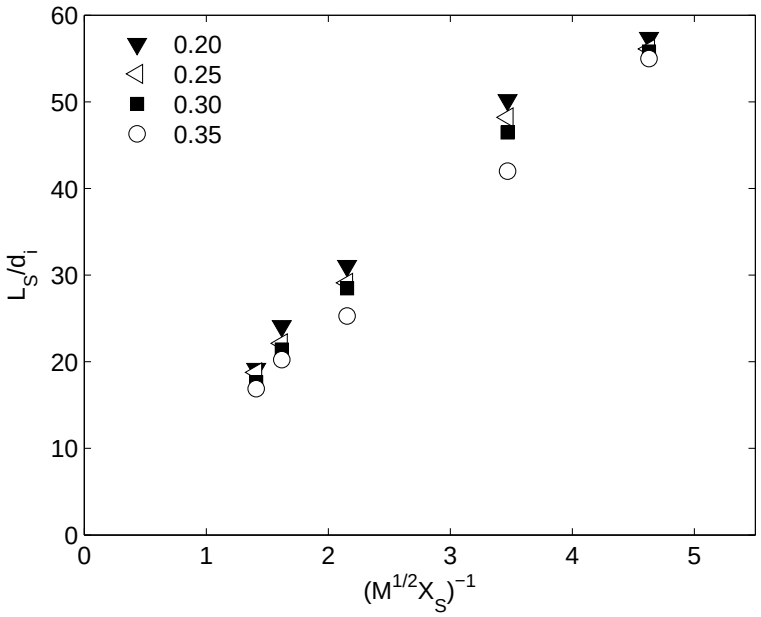

Figure 6.7: Effect of the cutoff signal level used to define flame length for data set R2 (H_2/air at $P_c = 4.8$ atm). A value of 0.30 was used for data analysis.

6.2.2 Effect of Increasing Pressure

During a typical run, the pressure inside the combustion chamber increases during the data acquisition time. Increases in pressure during the data acquisition were as large as 28% in some cases. The increase is defined as the difference between the pressure at the start and end times normalized by the average pressure during that window. A typical chamber pressure trace is shown in Fig. 6.8*a* with the data acquisition time clearly marked. To investigate if this increasing pressure had any

effect on flame length and consequently the mixing, images were divided into two groups based on if they were taken during the beginning or the end of the run with the middle five images removed. Flame lengths then were calculated from both groups and compared to the flame lengths calculated using all the images. Figure 6.8*b* shows that flame lengths calculated using the start and end groups are within 4.5% of each other. This collapse is excellent given that the start and end averages are based on approximately 65 images and some scatter in the data would be expected. Furthermore, it indicates that the momentum flux ratio or some other combination of the velocity and density ratio are the governing parameters since these ratios are unaffected by the change in chamber pressure, while the absolute values of density and velocity vary with chamber pressure.

6.3 Experimental Flame Lengths

In this section experimentally obtained flames length are compared to values predicted by the nonreacting coaxial jet momentum flux ratio scaling analysis. Results are divided into high Reynolds number and low Reynolds number cases, as was done for nonreacting results in Chapter V. A least squares best fit method is used to measure an effective density ratio which collapses each reacting data set to the nonreacting results.

6.3.1 High Reynolds Number Flame Lengths

Experimentally obtained stoichiometric mixing lengths (L_S) for all of the reacting and nonreacting high Reynolds number data sets are plotted in Fig. 6.9 for 28 cases and are compared to the predicted cold flow momentum flux ratio scaling (dashed

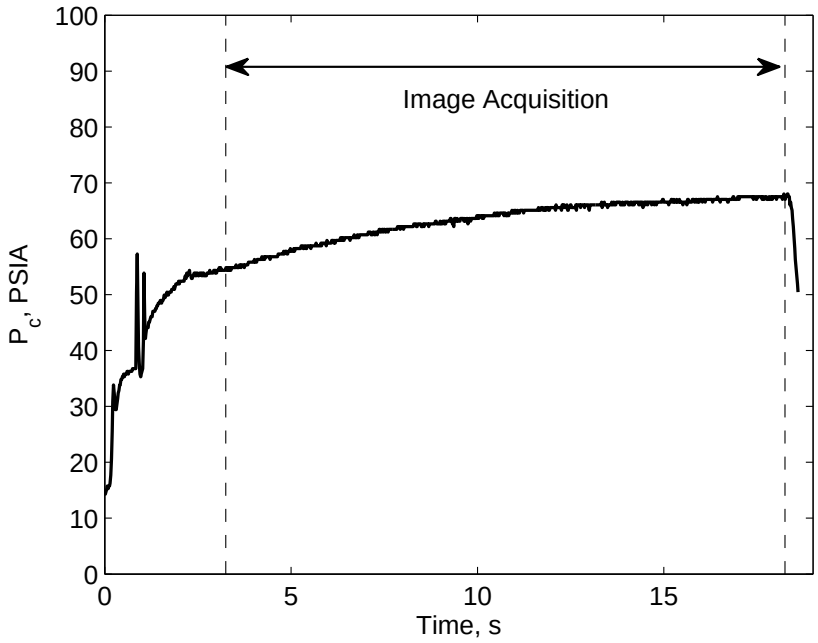

(a)

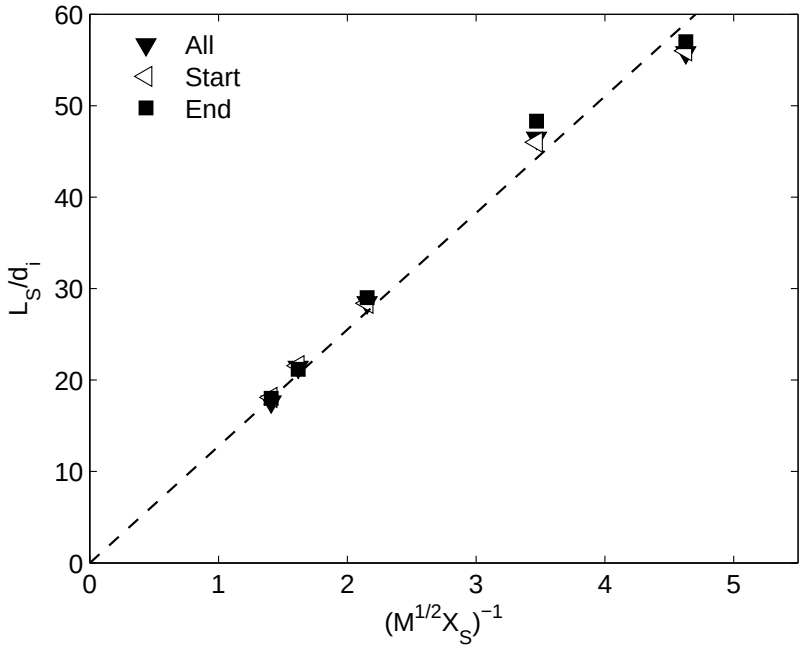

(b)

Figure 6.8: Typical run chamber pressure trace (a) and comparison of flame length calculated from the beginning half, ending half and all of the image acquisition time period for data set R2 (H_2 / air at $P_c = 4.8$ atm). Five images are removed from the middle in the half set calculations.

line). Black symbols correspond to nonreacting cases and red symbols correspond to reacting cases. The dashed-dot lines are best fits through the reacting data. The flow parameters for these data groups are provided in Tables 4.4 and 4.5 for nonreacting and reacting data sets respectively. Error bars are one standard deviation of the flame length calculated from the individual images where the farthest downstream OH pocket was used to define the length. Based on the sensitivity analysis and the inspection of flame length obtained from the individual images, it is believed that the true value of the flame length lies somewhere within those error bars. Data sets plotted in Fig. 6.9 include data sets NR7 and NR8 which are nonreacting He/air jets with chambers pressures of 3.76 atm and 5.40 atm and Reynolds number ranges of 13,000-14,000 and 18,000-20,000 respectively. NR12 are CH_4 / air coaxial jets with $P_C = 0.98$ atm and a Reynolds number range of 18,000-35,000. Reacting data sets include R2 and R3 which are H_2 / O_2 at $P_C = 4.5$ and 8.5 atm and Reynolds number ranges of 30,000-52,000 and 55,000-75,000 respectively. R4 are H_2 / air at $P_C = 4.8$ atm and a Reynolds number range of 22,000-25,000. R5 are CH_4 / O_2 at $P_C = 5.3$ atm and a Reynolds number range of 45,000-63,000. All Reynolds numbers are defined based on cold flow values.

Figure 6.9 shows the measured values of L_S for both the reacting and nonreacting case. All data scale linearly with $(M^{1/2}X_S)^{-1}$, but the slopes of the two curves (reacting and nonreacting) differ. The slopes between certain reacting data groups also differ. The difference in slopes and mixing lengths between the reacting and nonreacting data sets are expected due to the heat release. An interesting result is that the H_2 / O_2 data sets (R2 and R3) and the H_2 / air data set (R4) have similar stoichiometric mixing lengths and slopes even though they have very large differences in heat release and stoichiometric mixture fraction. The stoichiometric mixture fraction (f_S)

for H_2 / air is 0.97 compared to 0.89 for H_2 / O_2. For H_2/air much less entrained fuel is needed to reach a stoichiometric mixture and the reduced heat release would be expected to result in a smaller change in the density field than the H_2/O_2 case. Another important question is whether these results are Reynolds number independent. Data sets R2 and R3 are identical except for their Reynolds number ranges which are 30,000-52,000 and 55,000-75,000 respectively. This difference was accomplished by increasing the chamber pressure. Figure 6.9 shows an excellent collapse of these two data sets and therefore the results do appear to be independent of the Reynolds number. In addition the outer injector diameter was reduced from 6.7 mm in R2 and R3 to 5.8 mm in R4 and R5 to keep the overall equivalence ratio closer to one for the H_2/air and CH_4/O_2 data sets which aided in ignition. Changing the outer diameter did not alter the flame length which is consistent with the nonreacting results. If the outer diameter was made small enough, entrainment of ambient fluid before the end of flame would become important. In this situation, deviation from the momentum flux scaling would be expected. However, this was not observed.

In Chapter III, it was argued that the main effect of heat release was to alter the density field which results in decreased mixing and entrainment. The analysis of Tacina and Dahm (2000) suggests that this purely inertial effect of heat release could be accounted for by altering the definition of the density ratio in the momentum flux ratio (M). To test this hypothesis, least squares best fit methods were used to determine the effective density ratio $[(\rho_e)_{eff}/\rho_e]_{exp}$, which provided the best collapse of the reacting flow data with the nonreacting mixing length results. Subscript exp denotes values that were experimentally measured. Two different methods were considered; the linear best fit with an offset constant and a linear best fit with the offset constant set to zero. The method that involves zero offset is illustrated in

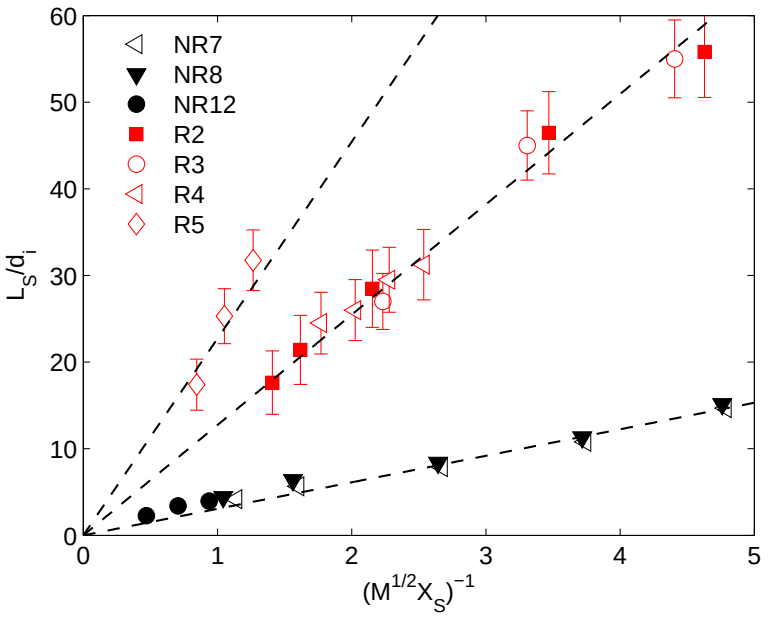

Figure 6.9: Measured nonreacting and reacting stoichiometric mixing lengths (L_S) for 28 cases (red symbols are reacting and black symbols are nonreacting) with high Reynolds numbers (13,000-75,000). Linear fits show that the momentum ratio parameter $(M^{1/2}X_S)^{-1}$ successfully correlates the data but different fits exist for reacting and nonreacting. Fits are also different for reacting data sets with different heat release.

Fig. 6.10*a* and the method that includes an offset is seen in Fig. 6.10*b*. The measured effective density ratios $[(\rho_e)_{eff}/\rho_e]_{exp}$ from the analysis are listed in Table 6.1. The effective density ratios calculated for the three H_2 / O_2 data groups differ; this can be explained by the fact that only a small number of data points were available and because the pressure varied between these cases, causing a decrease in dissociation which alters the heat release. Both methods result in remarkably good collapse of the reacting flame length data with the nonreacting fits, and thus accounting for heat release effects by altering the density ratio is fundamentally sound. However, the effective density ratios calculated here apply only to the propellents investigated and a theoretical based method to calculate $[(\rho_e)_{eff}/\rho_e]_{exp}$ is desirable so any propellent combination or dilution level could be compared. In §6.4 the equivalence principle

of Tacina and Dahm (2000) is evaluated against these experimental flame lengths in an effort to meet this requirement.

Table 6.1: Outer fluid effective density ratios calculated directly from experimental flame lengths for the linear best fit with offset and with a zero offset.

Group	P_c, atm	Fluids	$[(\rho_e)_{eff}/\rho_e]_{exp}$ Linear Fit	$[(\rho_e)_{eff}/\rho_e]_{exp}$ Zero Offset
R1	0.98	H_2 / O_2	0.074	–
R2	4.48	H_2 / O_2	0.048	0.059
R3	8.49	H_2 / O_2	0.048	0.057
R4	4.82	H_2 / air	0.048	0.057
R5	5.22	CH_4 / O_2	0.014	0.017

6.3.2 Low Reynolds Number Flame Lengths

As with the nonreacting results, reacting cases that correspond to low Reynolds numbers (4,300-6,800) were found to have a different momentum flux ratio scaling than the high Reynolds number cases (13,000-75,000). All Reynolds numbers are cold flow values calculated at the jet exit. As expected the high Reynolds number data were independent of Reynolds number, while the low Reynolds number results did depend on Reynolds number. In the nonreacting results, this Reynolds number dependence was shown to be due to a delay in the spreading in the outer shear layer which lengthened the outer potential core and resulted in increased mixing in the inner shear layer and therefore a shorter mixing length. This result is opposite to the standard effect of Reynolds number in a single jet. In a single jet reducing the Reynolds number results in less turbulence and hence reduced mixing resulting in longer jets. One effect of heat release in the reacting cases is to greatly increase the temperature, resulting in large increases in the fluid viscosity which decreases the effective Reynolds number. So for identical shear flows, the nonreacting case can

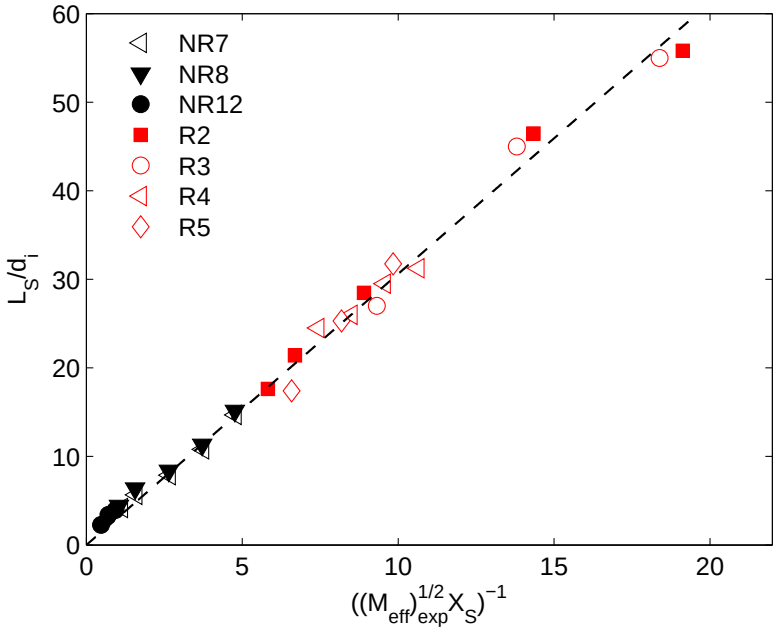

(a)

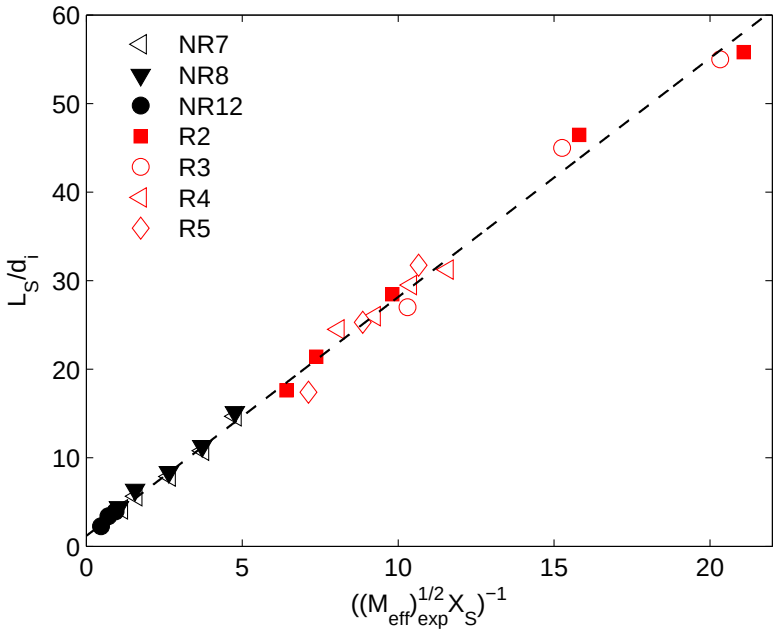

(b)

Figure 6.10: Correlation of the measures nonreacting and reacting stoichiometric mixing lengths (L_S) with the effective momentum ratio parameter $[(M_{eff})^{1/2}_{exp}X_S]^{-1}$ using experimentally measured effective density ratios $[(\rho_e)_{eff}/\rho_e]_{exp}$. Linear best fit with zero offset (a) and linear best fit with offset (b) for high Reynolds number data set (13,000-75,000). Calculated effective density ratios used to the collapse that data to a single curve are provided in Table 6.1.

be fully turbulent, while the reacting case can have a lower local Reynolds number and can become transitional or even laminar. Figure 6.2*c* shows an instantaneous OH contour from data set R1 which corresponds to H_2 / O_2 jets for a Reynolds number range of 4,300-6,800. In addition to the thickened OH layers, it is clear the jet appears much less turbulent than the higher Reynolds number cases. However, Fig. 6.11*a* shows that data set R1 still scales linearly with the momentum flux ratio parameter $(M^{1/2}X_S)^{-1}$ but the curve shown has a smaller slope than that of the higher Reynolds number H_2/O_2 data sets R2 and R3. The same best fit procedure was used as was used for the high Reynolds number data. For the nonreacting low Reynolds number data with a linear fit with offset, an outer effective density ratio of 0.106 was obtained. The result is shown in Fig. 6.11*b*. This collapse of the data is reasonable, however there is still a substantial difference in slopes between the reacting and nonreacting date which is likely to be due to the relatively small effective Reynolds number in the reacting case.

6.4 Assessment of the Tacina-Dahm Equivalence Principle

In the previous sections it was shown that there is an effective density ratio which can be used to relate turbulent coaxial jet flame lengths to nonreacting coaxial jet stoichiometric mixing lengths. The values of this effective density ratio were obtained and are listed in Table 6.1. However, this ratio is a function of the heat release which differs depending on the reaction and to a lesser extent the pressure through the chemistry and is not universal. Therefore a theoretically based method which can predict $(\rho_e)_{eff}/\rho_e$ for any propellent combination and chamber pressure is desirable to make the results as general as possible. One method which has shown promise in

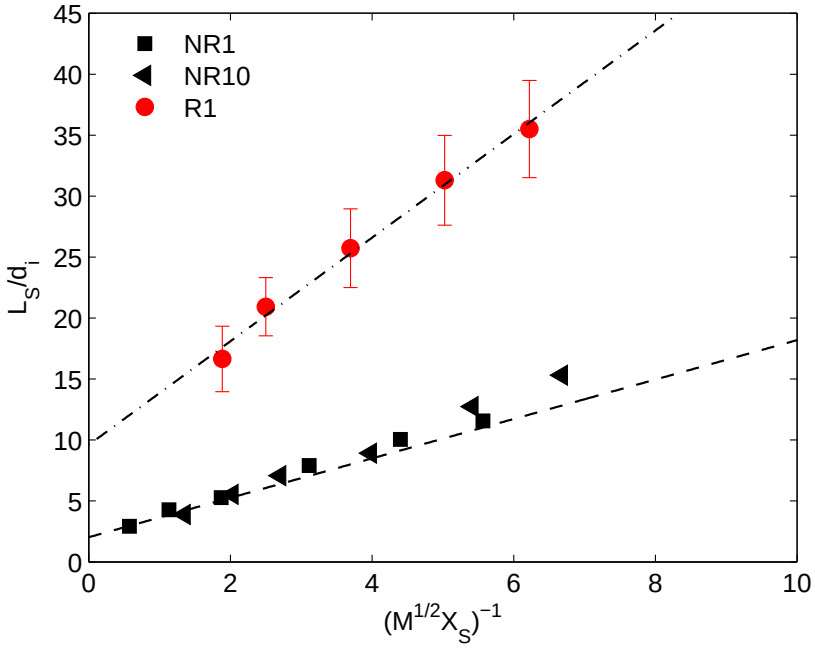

(a)

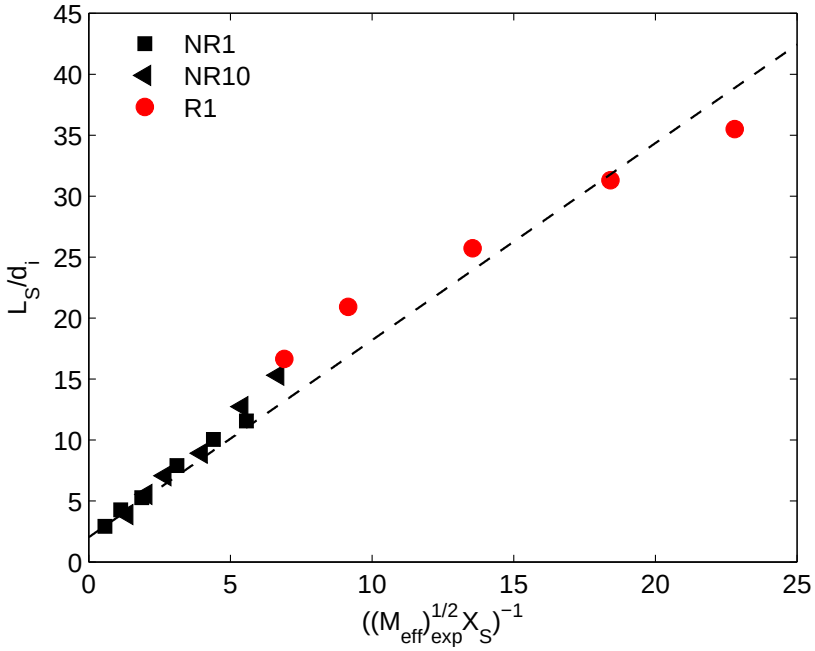

(b)

Figure 6.11: Comparison of low Reynolds number reacting flame lengths with non-reacting stoichiometric mixing lengths for the cold flow momentum flux ratio scaling (a) and collapse of data using the effective momentum flux ratio scaling obtained from the best linear fit with offset. Error bars are one standard deviation of the individual image flame lengths. R1 are H_2 / air with a Reynolds number range of 4,300-6,800. All data sets taken at 1 atm.

other turbulent shear flows is the equivalence principle of Tacina and Dahm (2000), which is outlined in Chapter III. In this section the three methods to calculate $[(\rho_e)_{eff}/\rho_e]_{theory}$ using the equivalence principle are applied to the flame length data and evaluated, based on their ability to collapse the measured coaxial jet flame length to the cold flow momentum flux ratio scaling, using the constants obtained in Chapter V. Subscript "theory" is used to denote effective values calculated using the equivalence principle.

The three methods were described in detail in §3.1.2 and are summarized as follows. With method 1, $[(\rho_e)_{eff}/\rho_e]_{theory}$ is calculated by fitting a straight line to the computed state relation for temperature (T) versus inner jet mole fraction. A straight line fit also is used to represent $MW(X_i)$. With method 2, the average slopes of the equilibrium state relations for large values of X_S are used to calculate $[(\rho_e)_{eff}/\rho_e]_{theory}$. With method 3, the effective temperature and molecular weight ratios are calculated using a best fit to the inner jet fluid equilibrium density profile. Note that if the equilibrium temperature and molecular weight profiles were exactly piecewise linear, all three methods would produce identical values of $[(\rho_e)_{eff}/\rho_e]_{theory}$.

The experimentally obtained high Reynolds number flame lengths are plotted against the effective momentum flux ratio parameter calculated using method 1 (Fig. 6.12*a*) and method 2 (Fig. 6.12*b*). Figure 6.12*a* shows that method 1 shifts all reacting data sets in the correct direction, but underpredicts the effects of heat release for H_2 / O_2 (R2 and R3) and H_2 / air (R4), but greatly overpredicts the effects of heat release for CH_4 / O_2 (R5). Given the large nonlinearities in the equilibrium state relations for oxygen enriched combustion it is entirely expected that using T_S as the reference point would fail. However, in the case of H_2 / air the equilibrium state relations are nearly piecewise linear and thus method 1 should work reasonably well

(see Fig. 3.4), but as Fig. 6.12a clearly shows the general equivalence principle underpredicts heat release effects for this data set. Method 2 performs only marginally better. As seen in Fig. 6.12b data set R2 and R3 are less underpredicted and data set R5 is less overpredicted then with method 1, but only slightly. The dashed line in Fig. 6.12 is the linear best fit with zero offset calculated for all high Reynolds number nonreacting mixing lengths in §5.5.1 ($C_1 = 3.06$).

In §3.1.3 it was shown that for all reactions that method 3 did the best job of approximating the inner jet density profile and hence should do the best job of accounting for heat release effects. Figure 6.13 shows that method 3 does a reasonable job of collapsing all of the reacting data sets to each other, but does not collapse the reacting flame lengths to the nonreacting stoichiometric mixing lengths. The data set R5 (CH_4 / O_2) falls slightly below the rest of the nonreacting data, but this is well within what can be explained from differences in the flame length definitions. The reacting flame lengths can then be made to collapse to the nonreacting mixing lengths by using a correction constant C_R of 2.6 and 2.9 for the linear fit with zero offset and the linear fit with offset respectively as shown in Fig. 6.14. The scatter in Fig. 6.14 is well within that seen in the centerline conserved scaler collapse of reacting and nonreacting simple jets using the equivalence principle (Tacina and Dahm 2000). While the reacting correction constant (C_R) was calculated for all high Reynolds number data it can be approximately related to the ratio of the theoretical and experimental effective density ratios,

$$C_R \approx \left[\frac{[(\rho_e)_{eff}/\rho_e]_{theory}}{[(\rho_e)_{eff}/\rho_e]_{exp}} \right]^{1/2}. \tag{6.1}$$

Table 6.2 compares the effective density ratios measured experimentally, calculated from the equivalence principle, and the corrected equivalence principle values for the

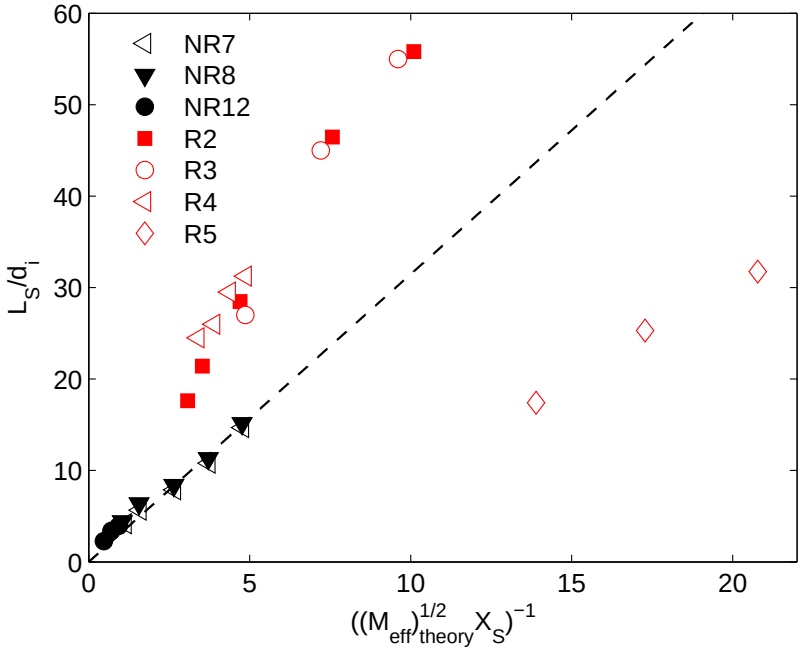

(a)

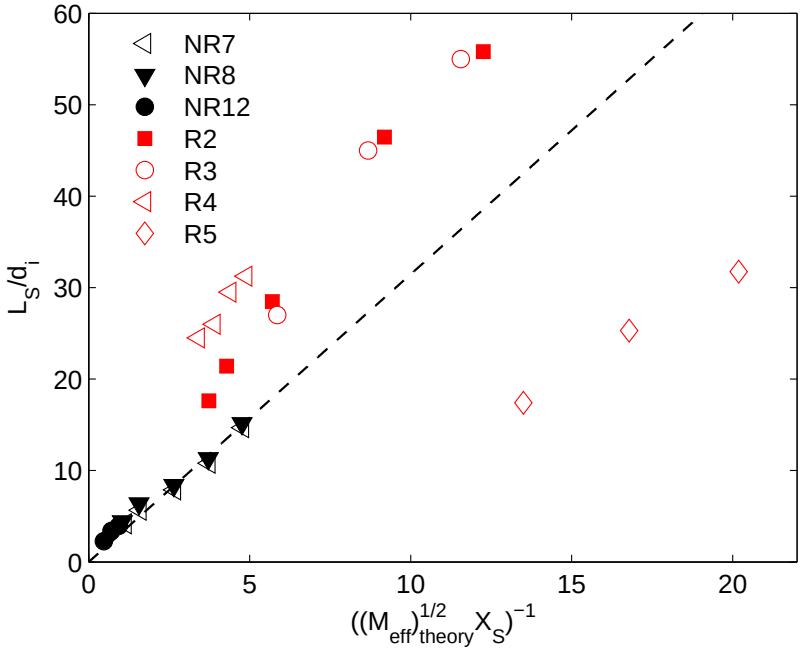

(b)

Figure 6.12: Flame length scaling for reacting and nonreacting high Reynolds number coaxial jets against the momentum flux ratio scaling with the equivalent principle correction using method 1 (a) and method 2 (b). Method 1 uses the linear relationship between T_i and T_S and between MW_i and MW_S and method 2 uses the slopes of the temperature and molecular weight equilibrium state relations for X values far from X_S to calculate $[(\rho_e)_{eff}/\rho_e]_{theory}$.

linear fit with offset. Table 6.3 does the same except for the linear fit with zero offset.

For the equivalence principle to be deemed successful in accounting for heat release in turbulent coaxial jet flames, the reacting correction constant must be accounted for theocratically. Possible ways to theoretically account for this constant are discussed in the following section.

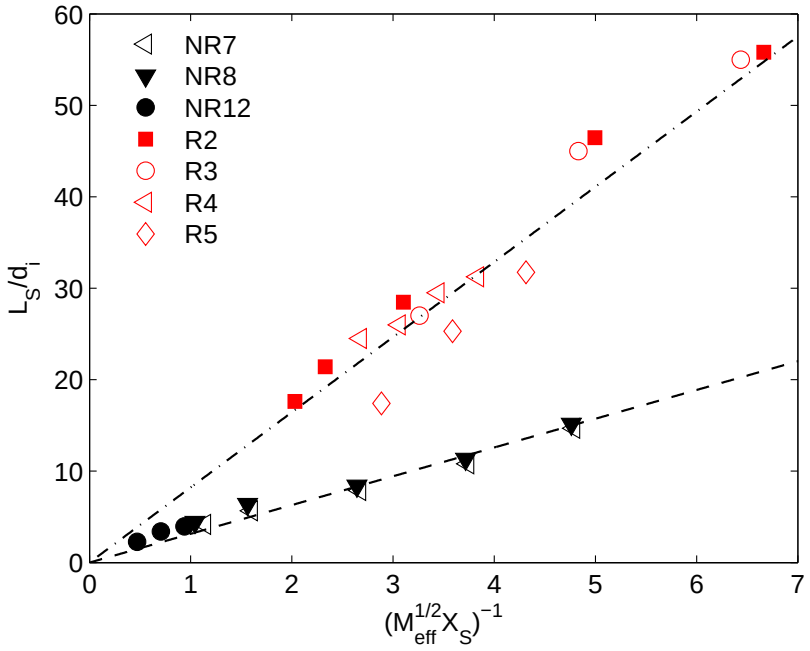

Figure 6.13: Flame length scaling for reacting and nonreacting high Reynolds number coaxial jets against the momentum flux ratio scaling with the equivalent principle correction using method 3.

Table 6.2: Outer fluid effective density ratios calculated directly from experimental flame lengths for the linear best fit with offset.

Group	$[(\rho_e)_{eff}/\rho_e]_{exp}$	$[(\rho_e)_{eff}/\rho_e]_{theory}$	$C_R^{-2}[(\rho_e)_{eff}/\rho_e]_{theory}$
R2	0.048	0.483	0.057
R3	0.048	0.469	0.056
R4	0.048	0.438	0.052
R5	0.014	0.086	0.010

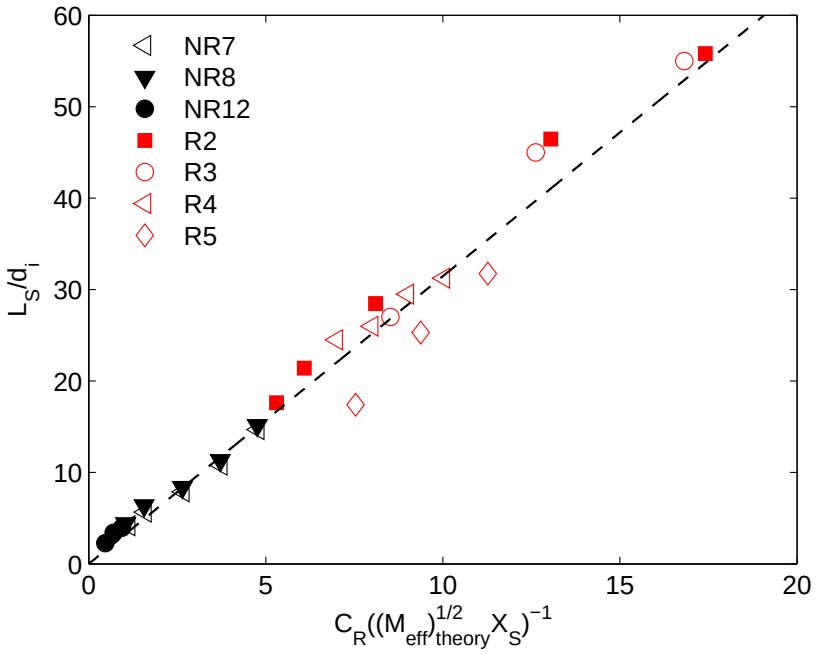

(a)

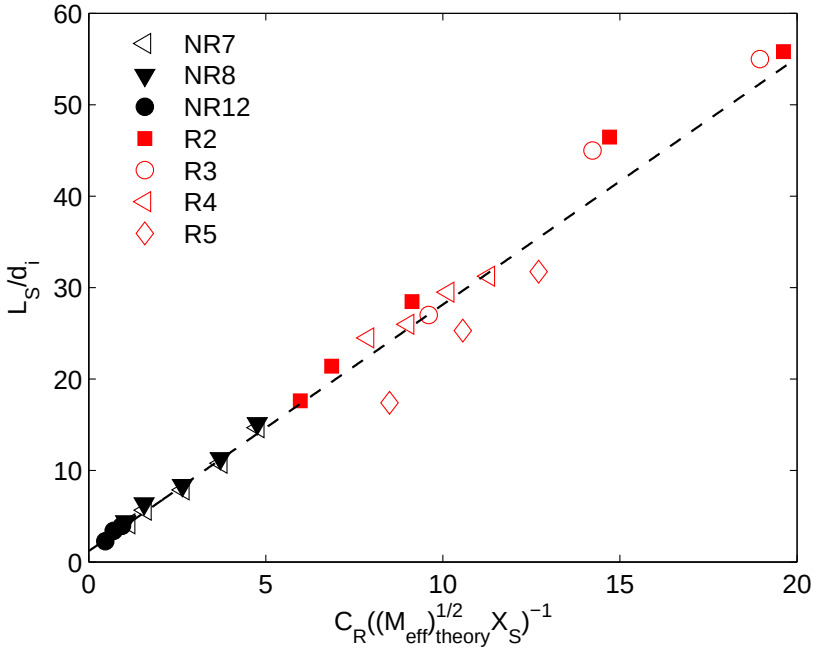

(b)

Figure 6.14: Flame length scaling for reacting and nonreacting high Reynolds number coaxial jets against the momentum flux ratio scaling with the equivalent principle correction using method 3 with a correction constant (C_R). In (a) the linear best fit with zero offset is used and $C_R = 2.6$. In (b) the linear best fit with offset is used and $C_R = 2.9$

Table 6.3: Outer fluid effective density ratios calculated directly from experimental flame lengths for the linear best fit with a zero offset.

Group	$[(\rho_e)_{eff}/\rho_e]_{exp}$	$[(\rho_e)_{eff}/\rho_e]_{theory}$	$C_R^{-2}[(\rho_e)_{eff}/\rho_e]_{theory}$
R2	0.059	0.483	0.071
R3	0.057	0.469	0.069
R4	0.057	0.438	0.064
R5	0.017	0.086	0.012

6.4.1 Applicability of Equivalence Principle to Reacting Coaxial Jets

As pointed out in Chapter III the equivalence principle only accounts for heat release effects that alter the density field. Buoyancy and differential diffusion were mentioned as two additional heat release effects which could cause the equivalence principle to fail, however both effects were argued to be negligible in this work and hence are unlikely to be causing the correction constant between the reacting and nonreacting data after the equivalence principle is applied in the previous section.

One component of the correction constant C_R can be traced to the different ways in which the stoichiometric mixing length (L_S) was obtained for the nonreacting and reacting cases. In the nonreacting cases the stoichiometric mixture fraction was used while in the reacting cases the mixing length was based on OH signal which does exist past the stoichiometric contour. An estimate of the contribution to C_R from this difference in definitions can be obtained by using the simulated OH PLIF signals obtained in §4.3.2. From the simulated OH PLIF signals the mixture fraction that corresponds to the edge of the OH contour can be found. Assuming that the momentum flux ratio scaling is correct, the scaling constant due to the difference in definitions is the ratio of the actual stoichiometric mole fraction to the mole fraction calculated using the mixture fraction that corresponds to the rich edge of the OH signal and Eq. 2.29. Using this method a factor of 1.94, 1.44, and 1.35 was calculated

for H_2/O_2, H_2/Air, and CH_4/O_2 respectively. Given these values it is clear that a significant portion of the correction constant C_R can be explained by the difference in the definitions of L_S in the nonreacting and reacting cases. However, the remaining portion of C_R must be account for by other means.

In Chapter III the equivalence principle was shown to be based on momentum conservation in turbulent shear flows and the goal was to equate the nonreacting and reacting flow by creating an imaginary nonreacting flow that had the same momentum flux density profile ($\rho * u$) as the reacting flow over the mole fractions values where $\rho * u$ is large. Two issues were mentioned in Chapter III with regards to applying this method to coaxial jets. First, in certain cases it is unclear if one side of flow is dominant over the other in a momentum flux density sense and second since the velocity profiles in the near field and transitional region of coaxial jets are not self-similar it is unclear if setting the density field in the nonreacting case to the reacting guarantee that the velocity profiles will match as it does in self-similar flows. Collapsing all of the reacting flame lengths to a single line suggests that using method 3 ensures all reacting cases have the same $\rho * u$ profiles, but not the same as the nonreacting.

Using method 3 and the equivalence principle ensures that the inner jet density profile is well approximated, however, any additional effects of heat release that might or might not act on the velocity field are left unexplored. Unfortunately, the velocity field in coaxial jets with velocity ratios greater than one are very complex due to their bimodal shape. In fact it has been shown that in large velocity ratios cases the centerline velocity can decrease from the exit value up to a certain distance, reach a minimum and then accelerate (Favre-Marinet et al. 1999). Velocity fields for reacting and nonreacting turbulent coaxial jets were not obtained in the current

study, making it difficult to investigate if or how the velocity field is altered. LDV was used only in the nonreacting cases to look at the injector inlet velocity profiles, but not further downstream. Also while near field velocity measurements do exist for nonreacting (Favre-Marinet and Camano-Schettini 2001 and Buresti et al. 1998) and reacting turbulent coaxial jets (Moser et al. 1993) these measurements are limited to a few sparse downstream locations at different momentum flux ratios and geometries making direct comparisons extremely difficult.

The second difficultly when applying the equivalence principle to coaxial jets with velocity ratios greater than one and density ratios less than one is deciding which fluid density should be altered. The experimentally obtained flame lengths show that for all reacting coaxial jets in this work the effect of heat release is to decrease entrainment and mixing and hence increase the flame length. Since the effective fluid density is always less than the actual fluid density switching which side of the equilibrium state relation is used as the effective fluid changes the effect of heat release when inserted into the nonreacting momentum flux ratio scaling. Using the inner jet as the effective fluid results in a decrease in flame length being predicted, while using the outer jet fluid as the effective fluid results in an increase in flame length which corresponds to experimental measurements. However, the equivalence principle states that the momentum flux density profile in the equivalent nonreacting flow should be matched as close as possible to the reacting $\rho * u$ profile. In plain jets and shear layer this is accomplished by matching the $\rho * u$ profile between the fluid mole fraction and the stoichiometric mole fraction where $\rho * u$ is large. Significant errors are possible if neither side is dominate.

The coaxial jet flames studied in this work all have density ratios less than one and velocity ratios greater than one and therefore which side of the equilibrium

state relation is dominate is not immediately obvious. An additional complication arises since the velocity profiles are not self-similar and vary considerably in the downstream direction along the length of the flame. A simple approach to estimate the relative significance of $\rho * u$ in both branches of the equilibrium state relations is to calculate the momentum flux density ratio by integrating the equilibrium density state relation for the two sides of the stoichiometric value. Since the velocity profile is unknown, the velocity is assumed constant and equal to the injection velocity which allows the momentum flux density ratio to be approximated as,

$$M_\rho = \frac{u_e \int_0^{X_S} \rho(X) dX}{u_i \int_{X_S}^1 \rho(X) dX}. \tag{6.2}$$

Assuming constant velocity profiles will over predict $\rho * u$ in the outer fluid since the narrow gap thickness of these jets cause the velocity in the outer fluid to decrease quickly, while the inner fluid velocity will decrease much slower. Applying this to the H_2 / O_2 data sets (R1,R2, and R3) values were found to vary between 0.2 and 0.88 which suggests that using the outer fluid as the effective fluid is appropriate. In these cases the higher outer velocity is counteracted by $S \approx 1/16$ and $X_S = 0.33$ favoring the inner fluid. H_2 / air (R4) cases similarly have a low S value, but X_S shifts to favor the outer fuel jet (0.71) and values of the momentum flux density ratio vary between 2.3 and 1.6. CH_4 / O_2 (R5) has neither a very low density ratio ($S \approx 1/2$) or a stoichiometric mole fraction ($X_S = 0.67$) to counteract the large velocity ratio and values of the momentum flux density ratio vary between 4.5 and 2.3. Therefore, for H_2 / air and CH_4 / O_2 this analysis indicates that the outer fluid is dominate and that the effective fluid should be the inner. This result is opposite of what experimental measurements indicate with the problem likely lying in the use of the constant velocity assumption. In reality the small gap thickness of the outer jet

compared to the inner jet diameter causes the outer jet velocity to decrease quickly resulting in most of inertial effect of heat release being in the inner jet and why the experimental results indicate the outer fluid should be used as the effective fluid.

These results indicate that the equivalence principle shows promise in being able to predict the flame lengths of turbulent coaxial jets with velocity ratios greater then one and density ratios less then one. A significant portion of the correction constant C_R can be explained by differences in the nonreacting and reacting definition of L_S. However, the remaining portion of C_R must be theocratically accounted for the equivalence principle to be deemed completely successful in accounting for inertial heat release effects in turbulent coaxial diffusion flames.

CHAPTER VII

Conclusions

An experimental study of the mixing in nonreacting and reacting turbulent coaxial jets has been described. This study focused on coaxial jets with properties similar to those of rocket propellent injectors. Outer to inner velocity ratios (r_u) were greater than one and outer to inner density ratios (S) were less than one. Acetone PLIF was used in nonreacting coaxial jets to obtain average and instantaneous mixture fraction fields. From the average mixture fraction fields mixing lengths were obtained based on the stoichiometry of fuel and oxidizer combinations common in rockets and furnaces. Theoretical scaling concepts such as planar shear layer theory and the momentum flux ratio theory were evaluated for their ability to predict the stoichiometric mixing length over a wide range of conditions. These conditions included varying the density ratio by a factor of one half and the momentum flux ratio by an order of magnitude from what previously has been investigated.

Reacting turbulent coaxial jets were investigated using cinema chemiluminescence and OH PLIF. Cinema chemiluminescence was used to investigate the translation of turbulent structures down the length of the flame and the formation of flame pockets at the flame tip. OH radical contours obtained using OH PLIF were used as a marker

of the instantaneous and average flame front. From the average flame front, flame lengths were obtained. Flame lengths were found to scale similarly to nonreacting stoichiometric mixing lengths. Experimentally measured constants were obtained to relate the reacting and nonreacting lengths. The equivalence principle of Tacina and Dahm (2000) was used in an attempt to obtain the experimentally measured scaling constant between the reacting and nonreacting lengths by theoretically accounting for the effects of heat release. A summary of the major conclusions is provided below.

7.1 Nonreacting Coaxial Jet Conclusions

1) The momentum flux ratio scaling $(M^{1/2}X_S)^{-1}$ can be extended beyond the potential core to predict the stoichiometric mixing length of fuel/oxidizer combinations common in rockets and furnaces. These combinations include H_2/air ($f_S = 0.97$), H_2/O_2 ($f_S = 0.89$), CH_4/air ($f_S = 0.94$), and CH_4/O_2 ($f_S = 0.80$).

2) Planar shear layer scaling laws do not accurately predict the inner potential core length of coaxial jets with velocity ratios less than one. The interactions of the vortex structures in the two near field mixing layers alter the normal shear-layer instabilities. This invalidates the empirical relations for vortex passing frequency and growth rate used in the derivation of the planar shear layer scaling laws.

3) The stoichiometric mixing lengths were found to be insensitive to absolute velocity difference, injector geometry and the confinement of the combustion chamber over the values investigated.

4) A decrease in the stoichiometric mixing length compared to the momentum

flux ratio scaling was found at M values of 0.07 to 0.12. This correlates with a change in the mixing layers from being "shear-like" to "wake-like" and represents the lower limit of applicability for the momentum flux ratio scaling.

5) Stoichiometric mixing lengths (L_S) were found to be independent of Reynolds number above a value of 13,000. At low Reynolds number the momentum flux ratio scaling still accurately predicted L_S but with different scaling constants. The low Re cases were found to have shorter mixing lengths then the Re independent cases. This was shown to be due to a delay in the spreading of the outer shear layer which kept the outer jet intact longer increasing the growth rate of the inner layer and therefore shortening L_S.

6) In the high Reynolds number limit he scaling constants for the momentum flux ratio scaling ($L_S/d_i = C_1 \left(M^{1/2} X_S\right)^{-1} + C_2$) were found to be 2.7 and 1.19 for C_1 and C_2 respectively. In the case C_2 is fixed at zero, C_1 was found to be 3.06. The constant C_2 is not universal over all coaxial jets but a weak function of the inlet velocity profiles and the shape of the injector post. However in this study C_2 is a constant and it accounts for what is analogous to the virtual origin in simple jets.

7.2 Reacting Coaxial Jet Conclusions

7) OH radical contours were found to be a good marker of the flame front and therefore the stoichiometric contour in inverse coaxial jet diffusion flames (oxidizer surrounded by fuel). OH PLIF images displayed thin wrinkled layers the length of the flame. Computations showed the relation between the OH signal at the stoichiometric condition and the peak OH signal.

8) Cinema Chemiluminescence and OH contours showed that two instability modes wrinkle and distort the flame front in coaxial diffusion flames which is similar to previous findings in simple jet flames. The asymmetric mode was found to predominately cause pocket formation near the flame tip by thinning the inner jet until it burns through. Symmetrical instabilities also were found to cause the formation of flame pockets, but this occurred infrequently.

9) Flame lengths of coaxial jet diffusion flames were found to scale with the momentum flux ratio parameter, but had different scaling constants than the nonreacting stoichiometric mixing lengths. Scaling constants also were found to differ depending on the fuel/oxidizer combination. Flames lengths were always longer than the stoichiometric mixing length of a comparable nonreacting case.

10) Effective density ratios were measured and these values allowed the flame lengths to be collapsed to the same line that is fit through the nonreacting stoichiometric mixing length data. The measured effective density ratios were not universal and depended on the chemistry of the reaction.

11) The equivalence principle of Tacina and Dahm (2000) was applied to theoretically predict the effective density ratios. These values were found to collapse all of the reacting data to a single line but the line has a different slope than the nonreacting data. The ratio of the theoretical to experimental effective density ratios was found to be a constant value of 2.9.

12) While a significant portion of the constant factor of 2.9 can be explained by the difference in the definitions of L_S between the nonreacting and reacting case, more research is needed to theoretically account for the remaining contribution.

7.3 Future work

Future work on reacting and nonreacting coaxial jets should focus on the effect of heat release on the velocity field. This could provide some insight into the difference between the theoretical effective density ratios obtained using the equivalence principle and the experimentally obtained values. This study is the first in which the equivalence principle has been applied and the effective molecular weight ratio been non-unity and is a possible cause for the scaling constant between the effective density ratio values. A study of a turbulent shear flow such as a simple jet or planar shear layer where the equivalence principle has been demonstrated to work in the unity effective molecular weight ratio case but with a non-unity effective molecular weight ratio could provide some insight into this issue. An example of such an experiment would be an air jet flame in an atmosphere of low molecular weight fuel.

APPENDICES

APPENDIX A

Nonreacting Coaxial Jet Experimental Test Matrix

Table A.1: Nondimensional properties and chamber pressure for all nonreacting coaxial jets in data groups NR1-NR4.

Group	Case	Outer/Inner	S	r_u	M	Re	X_s	P_C, atm
NR1	C1	He/Air	0.118	10.3	12.6	3,700	0.49	0.98
	C2		0.119	5.21	3.24	3,500	0.49	0.98
	C3		0.118	3.20	1.21	3,400	0.49	0.98
	C4		0.118	1.92	0.43	3,200	0.49	0.98
	C5		0.118	1.36	0.22	3,300	0.49	0.98
	C6		0.119	1.07	0.14	3,300	0.49	0.98
NR2	C1	He/Air	0.117	4.61	2.49	5,700	0.49	0.98
	C2		0.118	3.09	1.12	4,000	0.49	0.98
	C3		0.118	2.30	0.62	3,200	0.49	0.98
	C4		0.118	1.87	0.41	2,700	0.49	0.98
	C5		0.118	1.53	0.28	2,400	0.49	0.98
NR3	C1	He/Air	0.117	4.77	2.67	4,300	0.49	0.98
	C2		0.118	3.83	1.73	4,400	0.49	0.98
	C3		0.118	3.18	1.19	4,500	0.49	0.98
	C4		0.118	2.75	0.89	4,600	0.49	0.98
	C5		0.119	2.41	0.69	4,700	0.49	0.98
NR4	C1	He/Air	0.117	4.78	2.67	6,000	0.49	0.98
	C2		0.118	3.20	1.21	4,100	0.49	0.98
	C3		0.119	1.92	0.44	4,000	0.49	0.98
	C4		0.119	1.37	0.22	4,000	0.49	0.98
	C5		0.120	1.07	0.14	3,900	0.49	0.98

Table A.2: Nondimensional properties and chamber pressure for all nonreacting coaxial jets in data groups NR5-NR13.

Group	Case	Outer/Inner	S	r_u	M	Re	X_s	P_C, atm
NR5	C1	He/Air	0.118	4.85	2.78	6,500	0.49	0.98
	C2		0.119	3.23	1.24	4,600	0.49	0.98
	C3		0.120	2.44	0.72	3,700	0.49	0.98
NR6	C1	He/Air	0.119	11.0	14.3	3,700	0.49	0.98
	C2		0.121	5.30	3.40	3,500	0.49	0.98
	C3		0.119	3.21	1.22	3,300	0.49	0.98
	C4		0.119	1.94	0.45	3,200	0.49	0.98
	C5		0.119	1.39	0.23	3,200	0.49	0.98
	C6		0.120	1.08	0.14	3,300	0.49	0.98
NR7	C1	He/Air	0.131	4.69	2.89	14,000	0.52	3.70
	C2		0.132	3.33	1.46	13,000	0.52	3.77
	C3		0.132	1.99	0.53	13,000	0.52	3.78
	C4		0.131	1.43	0.27	13,000	0.52	3.80
	C5		0.133	1.11	0.16	13,000	0.52	3.78
NR8	C1	He/Air	0.134	5.05	3.40	20,000	0.52	5.37
	C2		0.133	3.38	1.52	20,000	0.52	5.43
	C3		0.134	2.00	0.53	18,000	0.52	5.39
	C4		0.133	1.42	0.27	18,000	0.52	5.41
	C5		0.133	1.11	0.16	19,000	0.52	5.42
NR9	C1	H_2/Air	0.059	9.61	5.43	13,000	0.32	0.98
	C2		0.059	3.20	0.61	4,900	0.32	0.98
	C3		0.059	1.89	0.21	3,500	0.32	0.98
	C4		0.059	1.37	0.11	3,000	0.32	0.98
	C5		0.060	1.06	0.07	2,800	0.32	0.98
NR10	C1	H_2/Air	0.059	9.46	5.25	8,300	0.32	0.98
	C2		0.059	6.29	2.33	6,700	0.32	0.98
	C3		0.059	4.72	1.31	5,800	0.32	0.98
	C4		0.059	3.18	0.60	4,900	0.32	0.98
	C5		0.059	2.35	0.33	4,500	0.32	0.98
	C6		0.059	1.90	0.21	4,400	0.32	0.98
NR11	C1	H_2/Air	0.059	9.67	5.53	13,000	0.33	0.98
	C2		0.060	3.21	0.62	4,800	0.33	0.98
	C3		0.060	1.93	0.22	3,500	0.33	0.98
	C4		0.060	1.37	0.11	3,000	0.33	0.98
	C5		0.060	1.07	0.07	2,700	0.33	0.98
NR12	C1	CH_4/Air	0.458	4.80	10.6	35,000	0.65	0.98
	C2		0.465	3.18	4.71	24,000	0.65	0.98
	C3		0.469	2.38	2.66	18,000	0.65	0.98
NR13	C1	CH_4/Air	0.469	1.89	1.67	14,000	0.65	0.98
	C2		0.472	1.59	1.20	13,000	0.65	0.98
	C3		0.471	1.37	0.88	12,000	0.65	0.98

Table A.3: Inner and outer jet velocities and densities for all nonreacting coaxial jets in data groups NR1-NR4.

Group	Case	MW_i, g/mol	u_e, m/s	u_i, m/s	ρ_e, kg/m^3	ρ_i, kg/m^3
NR1	C1	33.8	64.5	6.25	0.16	1.38
	C2	33.6	59.3	11.4	0.16	1.37
	C3	34.1	54.7	17.1	0.16	1.38
	C4	34.1	47.6	24.8	0.16	1.38
	C5	34.1	42.2	31.0	0.16	1.38
	C6	33.9	38.2	35.8	0.16	1.37
NR2	C1	34.0	97.3	21.1	0.16	1.38
	C2	34.0	65.3	21.1	0.16	1.38
	C3	34.1	48.7	21.2	0.16	1.38
	C4	33.8	39.2	21.0	0.16	1.38
	C5	33.9	32.3	21.1	0.16	1.38
NR3	C1	34.1	73.7	15.4	0.16	1.39
	C2	34.0	73.6	19.2	0.16	1.38
	C3	34.0	73.5	23.1	0.16	1.38
	C4	33.9	73.8	26.9	0.16	1.38
	C5	33.8	73.6	30.6	0.16	1.37
NR4	C1	34.1	73.9	15.5	0.16	1.39
	C2	33.9	49.2	15.4	0.16	1.38
	C3	33.8	45.9	23.9	0.16	1.37
	C4	33.8	41.8	30.6	0.16	1.37
	C5	33.7	38.0	35.4	0.16	1.36

Table A.4: Inner and outer jet velocities and densities for all nonreacting coaxial jets in data groups NR5-NR13.

Group	Case	MW_i, g/mol	u_e, m/s	u_i, m/s	ρ_e, kg/m^3	ρ_i, kg/m^3
NR5	C1	33.7	115	23.7	0.16	1.36
	C2	33.6	76.3	23.6	0.16	1.36
	C3	33.5	57.5	23.5	0.16	1.36
NR6	C1	33.6	64.2	5.84	0.16	1.37
	C2	33.1	59.0	11.1	0.16	1.35
	C3	33.7	54.2	16.9	0.16	1.37
	C4	33.6	47.4	24.5	0.16	1.36
	C5	33.6	42.3	30.4	0.16	1.36
	C6	33.6	38.3	35.5	0.16	1.36
NR7	C1	30.4	62.4	13.3	0.61	4.66
	C2	30.3	56.8	17.1	0.63	4.74
	C3	30.4	49.2	24.7	0.63	4.75
	C4	30.4	43.8	30.6	0.63	4.77
	C5	30.3	39.5	35.5	0.63	4.73
NR8	C1	30.0	63.6	12.6	0.89	6.68
	C2	30.1	58.3	17.2	0.90	6.78
	C3	30.0	50.6	25.3	0.90	6.71
	C4	30.1	44.9	31.5	0.90	6.73
	C5	30.1	40.5	36.5	0.90	6.73
NR9	C1	34.0	204	21.2	0.08	1.38
	C2	34.0	67.8	21.2	0.08	1.38
	C3	34.1	40.3	31.3	0.08	1.38
	C4	34.0	29.1	21.3	0.08	1.38
	C5	34.0	22.5	21.2	0.08	1.37
NR10	C1	34.2	151	16.0	0.08	1.39
	C2	34.2	117	18.6	0.08	1.39
	C3	34.2	96.6	20.5	0.08	1.39
	C4	34.1	73.2	23.0	0.08	1.38
	C5	34.2	59.2	25.2	0.08	1.39
	C6	34.0	50.7	26.7	0.08	1.38
NR11	C1	33.8	203	21.0	0.08	1.37
	C2	33.6	67.2	20.9	0.08	1.36
	C3	33.8	40.5	21.0	0.08	1.37
	C4	33.8	28.7	21.0	0.08	1.37
	C5	33.7	22.5	21.0	0.08	1.37
NR12	C1	34.2	103	21.4	0.63	1.38
	C2	34.2	68.0	21.4	0.64	1.38
	C3	34.1	50.0	21.3	0.65	1.38
NR13	C1	34.2	42.7	22.6	0.65	1.38
	C2	34.0	38.8	24.3	0.65	1.38
	C3	34.1	35.7	26.1	0.65	1.38

Table A.5: Injector dimensions and centerline mixing lengths for all nonreacting coaxial jets in data groups NR1-NR4.

Group	Case	d_e, mm	d_i, mm	T_P, mm	$L_{0.95}/d_i$	$L_{0.89}/d_i$	$L_{0.85}/d_i$	$L_{0.80}/d_i$
NR1	C1	7.52	3.00	0.89	2.62	2.92	3.07	3.26
	C2				3.71	4.28	4.59	4.78
	C3				4.46	5.27	5.75	6.21
	C4				5.84	7.91	9.15	10.0
	C5				7.45	10.1	11.3	13.4
	C6				8.50	11.6	13.3	15.9
NR2	C1	7.52	3.00	0.89	3.61	4.24	4.69	4.95
	C2				4.08	5.11	5.55	6.09
	C3				5.04	6.23	6.82	7.82
	C4				5.67	7.37	8.69	9.56
	C5				6.59	8.52	9.87	
NR3	C1	7.52	3.00	0.89	3.66	4.29	4.66	4.93
	C2				4.08	4.74	5.16	5.56
	C3				4.47	5.25	5.63	6.17
	C4				4.69	5.71	6.23	6.76
	C5				5.04	6.21	6.96	7.86
NR4	C1	10.0	3.00	0.89	3.16	3.88	4.31	4.76
	C2				4.03	5.08	5.38	5.90
	C3				5.18	7.17	7.68	8.43
	C4				6.12	9.02	10.0	
	C5				7.44			

Table A.6: Injector dimensions and centerline mixing lengths for all nonreacting coaxial jets in data groups NR5-NR13.

Group	Case	d_e, mm	d_i, mm	T_P, mm	$L_{0.95}/d_i$	$L_{0.89}/d_i$	$L_{0.85}/d_i$	$L_{0.80}/d_i$
NR5	C1	7.52	3.66	0.54	3.75	4.43	4.78	5.14
	C2				4.52	5.35	6.05	6.41
	C3				5.29	6.26	7.19	8.18
NR6	C1	7.52	3.00	0.89	2.27	2.58	2.72	2.90
	C2				3.33	3.84	4.14	4.47
	C3				4.46	5.31	5.70	6.10
	C4				5.92	7.61	8.18	9.46
	C5				6.92	9.24	10.5	12.0
	C6				8.01	10.6	11.7	13.6
NR7	C1	7.52	3.00	0.89	3.43	4.18	4.55	4.90
	C2				4.68	5.66	6.21	6.79
	C3				5.74	7.89	9.38	10.8
	C4				6.85	10.8	13.0	16.0
	C5				10.2	14.7	17.8	
NR8	C1	7.52	3.00	0.89	3.67	4.41	4.78	5.27
	C2				5.14	6.37	6.77	7.46
	C3				6.08	8.38	9.19	11.0
	C4				7.01	11.3	13.5	16.1
	C5				10.8	15.1	18.0	
NR9	C1	7.52	3.00	0.89	3.06	3.77	4.12	4.44
	C2				5.78	7.77	8.61	9.89
	C3				8.10	12.7	15.8	19.4
	C4				9.40	14.9	18.2	
	C5				10.1	16.1		
NR10	C1	6.73	3.37	0.72	3.30	3.88	4.31	4.70
	C2				4.53	5.54	6.23	7.03
	C3				5.42	7.07	8.15	9.54
	C4				6.23	8.91	10.3	12.7
	C5				8.09	12.7	16.2	
	C6				10.0	15.3		
NR11	C1	7.52	3.00	0.89	3.20	3.79	4.11	4.38
	C2				6.17	8.31	9.48	10.5
	C3				8.65	12.2	14.2	16.2
	C4				9.91	13.4	15.2	18.7
	C5				11.4	14.5	16.6	20.0
NR12	C1	7.52	3.00	0.89	1.83	2.08	2.18	2.28
	C2				2.39	2.88	3.10	3.41
	C3				2.48	3.23	3.63	3.96
NR13	C1	6.73	3.37	0.72	2.88	3.83	4.12	4.95
	C2				3.19	4.34	5.13	5.84
	C3				3.05	4.69	5.64	6.33

APPENDIX B

Reacting Coaxial Jet Experimental Test Matrix

Table B.1: Nondimensional properties, chamber pressure and normalized flame length for all reacting coaxial jets in data groups R1-R5.

Group	Case	Outer/Inner	S	r_u	M	Re	X_s	P_C, atm	L_S/d_i
R1	C1	H_2/O_2	0.063	6.27	2.47	6,800	0.33	0.98	16.7
	C2		0.063	4.72	1.40	5,900	0.33	0.98	20.9
	C3		0.063	3.19	0.64	4,900	0.33	0.98	25.7
	C4		0.063	2.35	0.35	4,500	0.33	0.98	31.3
	C5		0.063	1.89	0.23	4,300	0.33	0.98	35.5
R2	C1	H_2/O_2	0.062	8.41	4.42	52,000	0.33	4.66	17.6
	C2		0.063	7.32	3.35	49,000	0.33	4.59	21.4
	C3		0.063	5.49	1.89	42,000	0.33	4.40	28.5
	C4		0.063	3.40	0.73	33,000	0.33	4.33	46.5
	C5		0.063	2.54	0.41	30,000	0.33	4.40	55.8
R3	C1	H_2/O_2	0.063	5.29	1.76	76,000	0.33	8.63	27.0
	C2		0.063	3.57	0.80	60,000	0.33	8.28	45.0
	C3		0.063	2.67	0.45	55,000	0.33	8.55	55.0
R4	C1	H_2/Air	0.070	3.03	0.64	25,000	0.71	5.05	24.5
	C2		0.070	2.65	0.49	24,000	0.71	4.89	26.0
	C3		0.070	2.36	0.39	23,000	0.71	4.77	29.5
	C4		0.070	2.12	0.31	22,000	0.71	4.58	31.3
R5	C1	CH_4/O_2	0.552	2.38	3.14	56,000	0.67	5.27	17.4
	C2		0.553	1.91	2.03	51,000	0.67	5.33	25.3
	C3		0.553	1.59	1.41	45,000	0.67	5.03	31.8

Table B.2: Inner and outer jet velocities and densities along with injector dimensions for all reacting coaxial jets in data groups R1-R5.

Group	Case	d_e, mm	d_i, mm	T_P, mm	u_e, m/s	u_i, m/s	ρ_e, kg/m^3	ρ_i, kg/m^3
R1	C1	6.73	3.37	0.72	119	19.0	0.082	1.30
	C2				98.7	20.9	0.082	1.30
	C3				74.9	23.5	0.082	1.30
	C4				60.3	25.7	0.082	1.30
	C5				51.6	27.2	0.082	1.30
R2	C1	6.73	3.37	0.72	198	23.6	0.386	6.18
	C2				187	25.6	0.381	6.08
	C3				161	29.3	0.366	5.83
	C4				115	33.7	0.362	5.83
	C5				92.7	36.4	0.368	5.74
R3	C1	6.73	3.37	0.72	147	27.8	0.719	11.4
	C2				112	31.3	0.691	11.0
	C3				89.1	33.3	0.715	11.3
R4	C1	5.84	3.37	0.72	82.3	27.1	0.423	6.07
	C2				76.1	28.7	0.410	5.88
	C3				70.8	30.1	0.399	5.73
	C4				67.3	31.8	0.384	5.50
R5	C1	5.84	3.37	0.72	39.2	16.5	3.51	6.36
	C2				34.0	17.8	3.55	6.42
	C3				30.6	19.2	3.35	6.06

BIBLIOGRAPHY

BIBLIOGRAPHY

Au, H., Ko, N. W. M., 1987. Coaxial jets of different mean velocity ratios, Part 2. Journal of Sound and Vibration 116, 427–443.

Barlow, R. S., Collignon, A., 1991. Linear lif measurments of OH in nonpremixed methane-air flames: When are quenching corrections unnecessary. In: Proceedings of the 29th Aerospace Sciences Meeting. No. AIAA 91-0179.

Barlow, R. S., W., R., Chen, J. Y., Lucht, R. P., 1989. Effect of damkohler number on superequilibrium oh concentration in turbulent nonpremixed jet flames. In: Proceedings of the 27th Joint Propulsion Conference. No. AIAA 89-0061.

Becker, H. A., Yamazaki, S., 1978. Entrainment, momentum flux and temperature in vertical free turbulent diffusion flames. Combustion and Flame 33, 123–149.

Beer, J. M., Chigier, N. A., 1983. Combustion Aerodynamics. Krieger Publishing, Malabar, FL.

Beisler, M. A., Pal, S., Moser, M. D., Santoro, R. J., 1994. Shear coaxial injector atomization in a LOX/GH2 propellant rocket. In: Proceedings of the 30th AIAA Joint Propulsion Conference. No. AIAA 94-2775.

Brown, G. L., Roshko, A., 1974. On density effects and large structure in turbulent mixing layers. Journal of Fluid Mechanics 64, 775–816.

Bryant, R. A., Driscoll, J. F., 2001. Structure of supersonic flames imaged using OH/acetone. AIAA Journal 39, 1735–1741.

Buresti, G., Petagna, P., Talamelli, A., 1998. Experimental investigation on the turbulent near-field of coaxial jets. Experimental Thermal and Fluid Science 17, 18–36.

Champagne, F. H., Wygnanski, I. J., 1971. An experimental investigation of coaxial turbulent jets. International Journal of Heat and Mass Transfer 14, 1445–1464.

Chehroudi, B., Talley, D., Coy, E., 2002. Visual charateristics and initial growth rates of round cryogenic jets at subcritical and supercritical pressures. Physics of Fluids 14, 850–861.

Chen, C. J., Rodi, W., 1980. Vertical Buoyant Jets - A Review of Experimental Data, in: The science and Application of Heat and Mass Transfer. Pergamon Press, New York.

Chigier, N. A., Beer, J. M., 1964. The flow region near the nozzle in double concentric jets. ASME Journal of Basic Engineering 4, 797–804.

Clemens, N. T., 2002. Flow imaging. In: Encyclopedia of Imaging Science and Technology. John Wiley and Sons, New York, pp. 390–419.

Clemens, N. T., Paul, P. H., 1995. Effects of heat release on the near field flow structure of hydrogen jet diffusion flames. Combustion and Flame 102, 271–284.

Dahm, W. J. A., 2005. Effects of heat release on turbulent shear flows. Part 2. Turbulent mixing layers and the equivalence principle. Journal of Fluid Mechanics 540, 1–19.

Dahm, W. J. A., Frieler, C. E., Tryggvason, G., 1992. Vortex structure and dynamics in the near field of a coaxial jet. Journal of Fluid Mechanics 241, 371–402.

Davis, D. W., Chehroudi, B., Talley, D. G., 2006. A rocket-like coaxial injector in an acoustic field under sub- and supercritical conditions. In: Proceedings of ICLASS-2006. Kyoto, Japan, No. ICLASS06-270.

Dimotakis, P. E., 1986. Two-dimensional shear-layer entrainment. AIAA Journal 24, 1791–1796.

Ditaranto, M., Sautet, J. C., Samaniego, J. M., 2001. Structural aspects of coaxial oxy-fuel flames. Experiments in Fluids 30, 253–261.

Donbar, J. M., Driscoll, J. F., Carter, C. D., 2000. Reaction zone structure in turbulent nonpremixed jet flames from CH-OH plif images. Combustion and Flame 122, 1–19.

Eckbreth, A. C., 1996. Laser Diagnostics for Combustion Temperature and Species. Gordon and Breach.

Everest, D. A., Shaddix, C. R., Smyth, K. C., 1997. Quantitative two-photon laser induced fluorescence of CO in flickering CH4/air diffusion flames. Symposium (International) on Combustion 26, 1161–1169.

Farhangi, S., Hunt, K., Tuegel, L., Matthews, D., Fisher, S., 1994. Oxygen rich preburner for advanced rocket engine applications. In: Proceedings of the 30th AIAA Joint Propulsion Conference. No. AIAA 94-3260.

Favre-Marinet, M., Camano-Schettini, E. B., 2001. The density field of coaxial jets with large velocity ratio and large density differences. International Journal of Heat and Mass Transfer 44, 1913–1924.

Favre-Marinet, M., Camano-Schettini, E. B., Sarboch, J., 1999. Near-field of coaxial jets with large dendity difference. Experiments in Fluids 26, 97–106.

Forstall, W., Shapiro, A. H., 1950. Momentum and mass transfer in coaxial gas jets. Journal of Applied Mechanics 18, 399–408.

Foust, M. J., Deshpande, M., Pal, S., Ni, T., Merkle, C. L., Santoro, R. J., 1996a. Experimental and analytical characterization of a shear coaxial combusting GO2/CH2 flowfield. In: Proceedings of the 34th AIAA Aerospace Sciences Meeting. No. AIAA 96-0646.

Foust, M. J., Pal, S., Ni, T., Santoro, R. J., 1996b. Gaseous propellant rocket studies using raman spectroscopy. In: Proceedings of the 32nd Joint Propulsion Conference. No. AIAA 96-2766.

Garland, N. L., Crosley, D. R., 1986. On the collisional quenching of electronically excited OH NH and CH in flames. Symposium (International) on Combustion 21, 1693–1702.

Gaydon, A. G., 1957. The Spectroscopy of Flames. John Wiley & Sons, New York.

Ghosh, A., Diao, Q., Yu, K. H., 2007. Experimental investigation of shear-coaxial injector flame stability on flow parameters. In: Proceedings of the 43rd Joint Propulsion Conference. No. AIAA 2007-5569.

Han, D., Mungal, M. G., 2001. Direct measurment of entrainment in reacting/nonreacting turbulent jets. Combustion and Flame 124, 370–386.

Hawthorne, W. R., Weddell, D. S., Hottel, H. C., 1949. Mixing and combustion in turbulent gas jets. Symposium on Combustion and Flame and Explosion Phenomena 3, 266–288.

Hill, B. J., 1972. Measurment of local entrainment rate in the initial region of axisymmetric turbulent air jets. Journal of Fluid Mechanics 51, 773–779.

Hutt, J. J., Cramer, J. M., 1996. Advanced rocket injector development at the marshall space flight center. In: Proceedings of the AIAA Space Programs and Technologies Conference. No. AIAA 96-4266.

Jensen, R. J., Farhangi, S., Tuegel, L., Roberts, T., 1995. Oxygen rich preburner technology for full flow cycle applications. In: Proceedings of the 2nd International Symposium on Liquid Rocket Propulsion. ONERA.

Juniper, M., Tripathi, A., Scouflaire, P., Rolon, J.-C., Candel, S., 2000. Structure of cryogenic flames at elevated pressures. Symposium (International) on Combustion 28, 1103–1109.

Kee, R. J., Rupley, F. M., Miller, J. A., Coltrin, M. E., Grcar, J. F., Meeks, E., Moffat, H. K., Lutz, A. E., Dixon-Lewis, G., Smooke, M. D., Warnatz, J., Evans, G. H., Larson, R. S., Mitchell, R. E., Petzold, L. R., Reynolds, W. C., Caracotsios, M., Stewart, W. E., Glarborg, P., Wang, C., Mclellan, C. L., Adigun, O., Houf, W. G., Chou, C. P., Miller, S. F., Ho, P., Young, P. D., Hodgson, D. W., Petrova, M. V., Puduppakkam, K. V., 2006. Chemkin Release 4.1. Reaction Design, San Diego, CA.

Ko, N. W. M., Au, H., 1985. Coaxial jets of diffferent mean velocity ratios. Journal of Sound and Vibration 100, 211–232.

Ko, N. W. M., Kwan, A. S. H., 1976. The inital region of subsonic coaxial jets. Journal of Fluid Mechanics 73, 305–332.

Konrad, J. H., 1976. An experimental investigation of mixing in two-dimensional turbulent shear flows with applications to diffusion-limited chemical reactions. Tech. Rep. Project SQUID CIT-8-PU, California Institute of Technology, Pasadena.

Koochesfahani, M. M., Dimotakis, P. E., 1985. Laer-induced fluorescence measurements of mixed fluid concentration in a liquid plane shear layer. AIAA Journal 23, 1700–7007.

Kwan, A. S. H., Ko, N. W. M., 1977. The inital region of subsonic coaxial jets. part 2. Journal of Fluid Mechanics 82, 273–287.

Lozano, A., Yip, B., Hanson, R. K., 1992. Acetone: a tracer for concentration measurments in gaseous flows by planar laser-induced fluorescence. Experiments in Fluids 13, 369–376.

Lucht, R. P., 2008. Class notes: Me 687 advanced engineering optics: Laser diagnostics for reacting flows. Website: http://meweb.ecn.purdue.edu/me687, Purdue University.

Lucht, R. P., Laurendeau, N. M., Sweeney, D. W., 1982. Temperature measurments by two-line laser saturarted OH fluorescence in flames. Applied Optics 20, 1156–1166.

Luque, J., Crosley, D., 1999. Lifbase: Database and spectral simulation program (version 2.0.60). SRI International Report MP 99-009.

Maczyński, J. F. J., 1962. A round jet in an ambient co-axial stream. Journal of Fluid Mechanics 13, 597–608.

Marshall, W. M., Pal, S., 2005. Benchmark wall heat flux data for a GO2/GH2 single element combustior. In: Proceedings of the 41st AIAA Joint Propulsion Conference. No. AIAA 2006-3572.

McBride, B. J., Gordon, S., 1996. Computer program for calculation of complex chemical equilibrium compositions and Applications II. Users manual and program description. NASA RP-1311.

Moffat, R. J., 1988. Describing the uncertainties in experimental results. Experimental Thermal and Fluid Science 1, 3–17.

Morton, B. R., 1962. Coaxial turbulent jets. International Journal of Heat and Mass Transfer 5, 955–965.

Moser, M. D., Merenich, J. J., Pal, S., Santoro, R. J., 1993. OH-radical imaging and velocity field measurements in a gaseous hydrogen/oxygen rocket. In: 29th Joint Propulsion Conference. No. AIAA 93-2036.

Moser, M. D., Pal, S., Santoro, R. J., 1995. Laser light scattering measurements in a GO2/GH2 uni-element rocket chamber. In: Proceedings of the 33rd AIAA Aerospace Sciences Meeting. No. AIAA 95-0137.

Mungal, M. G., Karasso, P., Lozano, A., 1991. The visible structure of turbulent jet diffusion flames large-scale organization and flame tip oscillation. Combustion Science and Technology 76, 165–185.

Mungal, M. G., O'Neil, J. M., 1989. Visual obervations of a turbulent diffusion flame. Combustion and Flame 78, 377–389.

Muniz, L., Mungal, M. G., 2001. Effects of heat release and buoyancy on flow structure and entrainment in turbulent nonpremixed flames. Combustion and Flame 126, 1402–1420.

Murakami, E., Papamoschou, D., 2002. Mean flow development in duel-stream compressible jets. AIAA Journal 40, 1131–1138.

Nicoli, C., Haldenwang, P., 2003. Combustion of gaseous coflow jets. Combustion Science and Technology 175, 1143–1163.

Paul, P. H., 1994. A model for temperature-dependent collisional quenching of OH $a^2\sigma^+$. Journal of Quantitative Spectroscopy and Radiative Transfer 51, 511–524.

Rehab, H., Villermaux, E., Hopfinger, E. J., 1997. Flow regimes of large-velocity-ratio coaxial jets. Journal of Fluid Mechanics 345, 357–381.

Rehab, H., Villermaux, E., Hopfinger, E. J., 1998. Geometrical effects on the near-field flow structure of coaxial jets. AIAA Journal 36, 867–869.

Ribeiro, M. M., Whitelaw, J. H., 1980. Coaxial jets with and without swirl. Journal of Fluid Mechanics 96, 769–795.

Ricou, F. P., Spalding, D. B., 1961. Measurements of entrainment and mixing by axisymmetrical turbulent jets. Journal of Fluid Mechanics 11, 21–32.

Santoro, R. J., 1998. Applications of laser-based diagnostics to high pressure rocket and gas turbine combustor studies. In: Proceedings of the 20th AIAA Advanced Measurment and Ground Testing Technology Conference. No. AIAA 98-2698.

Sautet, J. C., Salentey, L., DiTaranto, M., 2001. Large-scale turbulent structures in non-premixed, oxygen enriched flames. International Communications in Heat and Mass Transfer 28, 277–287.

Seitzman, J. M., Üngüt, A., Paul, P. H., Hanson, R. K., 1990. Imaging and characterization of oh structures in a turbulent nonpremixed flame. Symposium (International) on Combustion 23, 637–644.

Singla, G., Scouflaire, P., Rolon, C., Candel, S., 2006. Planar laser-induced fluorescence of OH in high-pressure cryogenic LOx/GH2 jet flames. Combustion and Flame 144, 151–169.

Smyth, K. C., Shaddix, C. R., Everest, D. A., 1997. Aspects of soot dynamics as revealed by measurments of broadband fluorescence and flame luminosity in flickering diffusion flames. Combustion and Flame 111, 185–207.

Sutton, G. P., Biblarz, O., 2001. Rocket Propulsion Elements: An Introduction to the Engineering of Rockets., 7th Edition. Wiley-Interscience.

Tacina, K. M., Dahm, W. J. A., 2000. Effects of heat release on turbulent shear flows. Part 1. A general equivalence principle for non-buoyant flows and its application to turbulent jet flames. Journal of Fluid Mechanics 415, 23–44.

Tanahashi, M., Murakami, S., Choi, G.-M., Fukuchi, Y., Miyauchi, T., 2005. Simultaneous CH-OH PLIF and steroscopic piv measurments of turbulent premixed flames. Proceedings of the Combustion Institute 30, 1665–1672.

Thring, M. W., Newby, M. P., 1953. Combustion length of enclosed turbulent jet flames. Symposium (International) on Combustion 4, 789–796.

Thurber, M. C., Grisch, F., Kirby, B. J., Votsmeier, M., Hanson, R. K., 1998. Measurements and modeling of acetone laser-induced fluorescence with implications for temperature-imaging diagnostics. Applied Optics 37, 4963–4978.

Thurber, M. C., Hanson, R. K., 1999. Pressure and composition dependences of acetone laer-induced fluorescence with excitation at 248, 266, 308nm. Applied Physics B 69, 229–240.

Vaidyanathan, A., Gustavsson, J., Segal, C., July 8-11 2007. Heat fluxes/OH plif measurments in a GO2/CH2 single-element, shear injector. In: Proceedings of the AIAA 43rd Joint Propulsion Conference. No. AIAA 2007-5591.

van Cruyningen, I., Lozano, A., Hanson, R. K., 1990. Quantitative imaging of concentration by planar laser-induced fluorescence. Experiments in Fluids 10, 41–49.

Villermaux, E., Rehab, H., 2000. Mixing in coaxial jets. Journal of Fluid Mechanics 425, 161–185.

Warda, H. A., Kassab, S. Z., Elshorbagy, K. A., Elsaadawy, E. A., 1999. An experimental investigation of the near-field region of a free turbulent coaxial jet using LDA. Flow Measurement and Instrumentation 10, 15–26.

White, F. M., 1991. Viscous Fluid Flow. McGraw-Hill Inc.

Williams, T. J., Ali, M. R. M. H., Anderson, J. S., 1969. Noise and flow characteristics of coaxial jets. Journal of Mechanical Engineering Science 11, 133–138.

Yeralan, S., Pal, S., Santoro, R. J., 2001. Experimental study of major species and temperature profiles of liquid oxygen/gaseous hydrogen rocket combustion. Journal of Propulsion and Power 17, 788–793.

Yuen, L. S., Peters, J. E., Lucht, R. P., 1997. Pressure dependence of laser-induced fluorescence from acetone. Applied Optics 36, 3271–3277.